Spray freeze drying of zirconia nanopowder

by

Bala Praveen Chakkravarthy Raghupathy

A Doctoral Thesis submitted in partial fulfilment of the requirements for the award of Doctor of Philosophy of Loughborough University

(December 2007)

Abstract

Industrial exploitation of ceramic nanopowders is inhibited by their poor flowability and strong tendency to agglomerate. To achieve good flowability and die filling characteristics, controlled agglomeration is required whilst the strength of the agglomerates is minimised so that they crush into primary particles when die pressed. Yttria stabilised zirconia nanopowders with a primary particle size of ~16 nm were obtained through different drying routes from an aqueous suspension and characterised in terms of flowability and agglomerate strength.

The granule crushability was characterised from the fracture surface of the die pressed compacts and porosimetry. Oven drying lead to poor flowability whilst spray drying yielded flowable, but hard agglomerates. Spray freeze drying of low solid content suspensions yielded crushable granules that result in a uniform nanostructure when die pressed. As the solid content of the starting suspension was increased, the strength of the spray freeze dried granules increased. Nitrogen adsorption isotherms confirm the presence of inter-agglomerate pores when hard agglomerates were formed from high solid content suspensions.

The flowability of the granules were characterised using Hall flowmeter, Hausner ratio and model shoe – die filling experiments. The flowability of spray freeze dried granules improved with increase in the solid content of the starting suspension.

The spray freeze dried granules were successfully benchmarked with commercial submicron powders and it is possible to retain a nanostructure when the granulation and sintering conditions were optimised.

Key words: ceramics, zirconia, spray drying, spray freeze drying, die pressing, porosimetry, powder flowability.

Acknowledgements

I would like to register my sincere thanks to Prof. Jon Binner for continuous support and encouragement during these years. His input had been vital in both completing the project and in several other professional grounds; he made this task an enjoyable experience.

Many thanks to the timely assistance and advice from staff and faculty in IPTME and other departments; labware, consumables, brilliant ideas were often borrowed or stolen from them.

PowdermatriX's training and feed back from 'Engineering the green state' meetings are highly appreciated. Funding from EPSRC and provision of experimental facilities by LMCC, MEL, Leicester and Birmingham universities and CERAM are acknowledged.

Help from the other members of the research group and friends in Loughborough are gratefully acknowledged; the former took care of my experiments when I was busy partying with the latter.

I couldn't have done my PhD without the love and care of my parents and sister. I would like to express my gratitude to the relentless support from them.

Bala Raghupathy

Table of contents

Acronyms used

A	-	Hamaker constant
BET	-	Brunauer, Emmett and Teller method
BJH	-	Barret, Joyner and Halenda method
c	-	BET constant
CIP	-	cold isostatic pressing
d	-	lattice spacing
d_p, D	-	size of primary particles
d_{pBET}	-	particle size deduced from BET surface area
FEGSEM	-	Field Emission Gun Scanning Electron Microscopy
IEP	-	Isoelectric point
MIP	-	Mercury Intrusion Porosimetry
p	-	gas pressure of the adsorbate
p_o	-	saturation pressure of the adsorbate
r_p	-	pore radius
SANS	-	Small Angle Neutron Scattering
S_{BET}	-	BET surface area
SFD	-	Spray freeze dried
SD	-	Spray dried
TAC	-	Tri-ammonium citrate
TD	-	Theoretical density
TEM	-	Transmission Electron Microscopy
TMAH	–	Tetra-methyl ammonium hydroxide
YSZ	-	Yttria stabilised zirconia

Greek symbols

γ	-	surface tension of mercury
λ	-	separation distance between surfaces of particles
θ	-	contact angle of mercury in case of porosimetry
θ_B	-	Bragg diffraction angle
σ	-	surface tension of the liquid condensate during BET analysis
σ^*	-	fracture strength of the granule
Γ	-	Work of adhesion of solid surfaces
Γ_b	-	Work of adhesion measured by fracturing contacts between particles
Φ	-	volume fraction of solids
ε	-	porosity
ρ	-	theoretical density

Chapter 1

Introduction

Powder processing plays an important role in ceramic industries. Dry pressing is a well established fabrication technique in ceramic component manufacture based on its attractive attributes like ease of automation, relatively low energy consumption, high material utilization and ability to convert powders into complex shapes with high precision and close tolerances. Die pressed ceramic components are used widely in automotive, aeronautical, nuclear and electronic industries. This technique is versatile and it is possible to achieve good quality components at very high production rates [1].

Nanoparticles and nanostructures, being the building blocks of nanotechnology, are gaining world wide research and development attention in the research scenario based on their potential for commercial exploitation. The effect of nanotechnology is pervasive. Every industry is either contemplating or has realized technical and commercial advantages with the use of the emerging nanotechnology [2]. Nanostructured ceramics have been shown to have low temperature superplasticity and are generally stronger than their coarse grained counter parts [3]. It has also been found that various other properties, such as optical, magnetic and electrical, are influenced by the fine grain structure of these materials [4]. These nanomaterials may revolutionise various industries including high performance engineered ceramics, ion conductors, ferroelectrics, etc., in the near future.

The fabrication of nanostructured ceramics still remains a challenge [4]. Ceramic nanopowders are usually the starting material in nanostructured ceramic fabrication. The major challenges in dry pressing of the nanopowders include poor flowability, increased die wall – particle interaction, high inter-particle friction, agglomeration, etc., resulting in a

low green density for the final compacts [5]. Handling of nanopowders is also potentially a safety hazard.

Controlled agglomeration and tailoring the powder properties are crucial for successful industrial adaptation and commercial exploitation of these enabling technologies. Controlled agglomeration of primary ceramic nanoparticles into weak agglomerates to provide good flowability and compactability has been identified as the key for forming good quality, high density consolidated products. Nanocrystalline zirconia is an interesting material based on its superplasticity and ductility at elevated temperatures as well as its ionic conductivity at elevated temperatures [6]. The present work aims to improve zirconia nanopowders so that nanostructured ceramic components can be fabricated.

This thesis consists of six chapters. Chapter 2 reports on a thorough survey of literature on ceramic powder processing. The theory behind the characterisation of powders, pressing and green compacts is discussed in detail in the same chapter. Chapter 3 provides details of experimental procedures of the current work. Firstly, the method for making nanopowders is discussed, followed by the methodical investigation of the influence of various processing parameters in the final nanostructure. Chapter 4 presents the results and discussion on the experimental findings. The results from every stage are discussed in detail and the powders are compared later. In chapter 5 conclusions are drawn from the results and discussions presented in chapter 4 and suggested ideas for future work are given in chapter 6. A bibliography of the works references in this thesis is presented at the end.

Chapter 2

Literature review

An introduction to nanotechnology and nanostructured ceramics is given in the following section. This is succeeded by an introduction to powder processing routes to fabricate nanostructured ceramics. It follows that die pressing is one of the most lucrative routes for mass manufacturing of ceramic components with simple geometry and the hurdles to commercial exploitation are outlined. The various processing stages including slurry preparation, powder preparation/granulation and consolidation are discussed. The primary characteristic parameters used in the work, viz. powder flowability, powder fill/tap density, agglomerate strength, green compact microstructure, pore size distribution and sinterability, are all reviewed.

2.1 General overview of nanotechnology

Nanotechnology research is attracting increasing investment from government and industry around the world. In general, nanotechnology involves materials with a size less than 100 nm at least in one dimension. Several advancements in nanotechnology: quantum dots; nano-wires; nano-grain metals; fullerenes and carbon nanotubes; nano catalysis; nanostructured ceramics; atom-by-atom assembly of molecules; layer-by-layer assembly of multi-component films; nano-tweezers; nano-scale cantilevers; single-electron transistor; self assembly of molecules; and the possibility of tuning properties of materials such as hardness, melting point, colour and magnetic properties, have progressed at a rate faster than projected a few years ago [2]. The sales of products incorporating the emerging nano-technology are predicted to rise from <0.1% of global manufacturing output today to 15% of output in 2014, totalling US$ 2.6 trillion according to Lux Research Inc., (New York). In 2014, 4% of general manufactured goods, 50% of electronic and IT products and 16%

of goods in health care and life sciences are expected to have incorporated the emerging nanotechnology [7].

A multidisciplinary approach is often required to understand the complex nature of the industrially relevant enabling nanotechnology. Extensive collaborations, partnership and networking between industry, academia and government will accelerate the development of new products [8].

2.2 Nanostructured ceramics

Ceramic materials find diverse applications including traditional tableware, refractory tiles, thermal barrier coatings, catalyst supports, bioceramics, nuclear fuel rods, etc., They include a wide range of materials like oxides, carbides, nitrides and borides. Besides conventional ceramic insulators used in power transmission, electronic ceramics are used in ferroelectric, ferromagnetic and piezoelectric applications [9]. Ceramics with good ionic conductivity are used in electric power applications such as solid oxide fuel cells and batteries, where they are used as solid electrolytes, and in sensors, such as the oxygen sensor used in automotive engines for fuel and pollution control [10]. The other frontiers include superconducting cuprate ceramics [11], zirconia ferrules for optical fibres [12], high performance engine components and many other applications.

Nanocrystalline ceramics have a lower sintering temperature providing new opportunities for co-sintering of thin film structures. Multilayer ceramic device fabrication would be most benefited by this. Nanostructured zirconia has been proved, as has nanostructured Si_3N_4 [13], to display superplastic behaviour at elevated temperatures [14,15]. Alumina can be formed in an unusual translucent state when it is nanocrystalline. It is clear that the increased interest in nanomaterials is not because of the size, but for their properties [16]. Improved electrical properties in various electronic ceramics and enhanced mechanical properties in case of structural ceramics have been predicted when the ceramics are nanostructured. However, commercial exploitation of these

benefits warrant transforming the lab level technology into profitable product lines where mass manufacturing can be done quickly and cheaply.

2.3 Advantages in using nanopowders

Apart from the expected enhancements in properties, the main driving force for using nanopowders is their low temperature sinterability. Yoo et al. [17] showed that nanocrystalline tantalum powders (average particle size of 63 nm) could be rapidly consolidated to high density by Plasma Pressure Compaction at a temperature 250°C lower than coarse tantalum powder (average particle size of 15 μm) due to large intrinsic driving force associated with fine particles.

Zych et al. [18] compared the sintering curves of commercial sub-micron zirconia powder and hydrothermally synthesised zirconia nanopowder compacts having the same starting green density. The nanopowder compact sintered to about 99% theoretical density (TD) whilst the submicron powder reached about 60% of TD under identical sintering conditions at 1200°C. The sintering curve, Figure 2-1, shows that shrinkage starts at as low as 200°C in the nanopowder compact whilst it was about 1000°C in the submicron powder compacts.

Zirconia nanoparticles are interesting materials that have a size dependent phase stability. Zirconia polycrystals can exist in three polymorphs: monoclinic, tetragonal and cubic. The monoclinic phase is stable at room temperature whilst the other two are stable at high temperatures above 1000°C [19] as in Figure 2-2. When the particle size is below a certain critical limit, they exist in their metastable tetragonal polymorph [20]. The tetragonal phase can be stabilised at room temperature by doping ZrO_2 with CaO, MgO, Y_2O_3, Ce, Sc etc., Stabilisation by substitution is preferred because the martensitic transformation from tetragonal to monoclinic involves a 3 – 5% volume change when the sintered body is cooled and this volume change induces cracks and the components shatter on cooling. The possibility of stabilising the tetragonal phase in YSZ with lower amounts of yttria, could potentially make YSZ nanopowders cheaper to produce than the conventional powders.

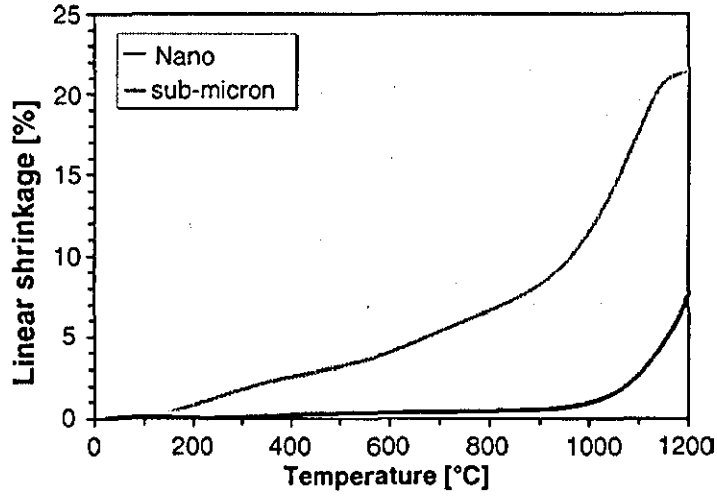

Figure 2-1 Linear shrinkage of sub-micron & nanopowder compacts during non-isothermal sintering, after [18].

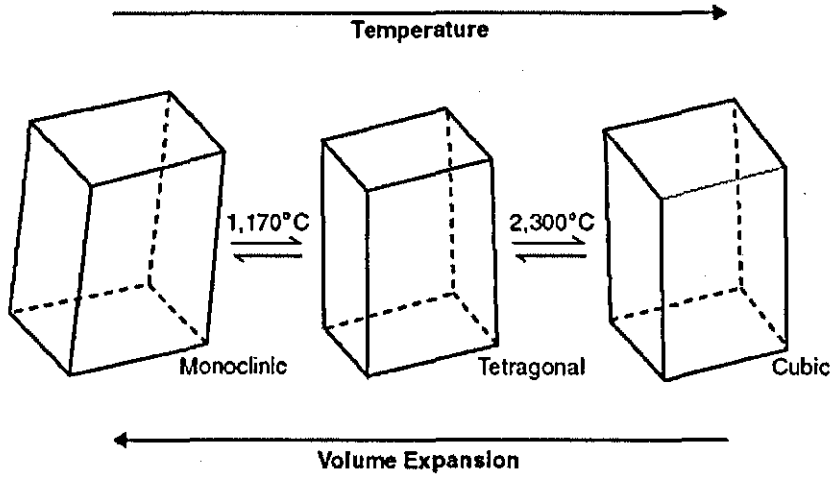

Figure 2-2 Phase transitition in zirconia, after [19].

2.4 Powder processing for ceramics

In general, ceramics are rarely formed by melt casting since they generically have very high melting points and the process often results in uncontrolled grain growth. In addition, some advanced ceramics (e.g. Si_3N_4, SiC) decompose before they melt. The brittle nature of the ceramics precludes the use of deformation techniques commonly used for metals, whilst vapour deposition is uneconomical except for thin films. These limitations combine to make powder processing followed by densification

by sintering the most realistic processing option for most advanced ceramics [21].

Powders exhibit fluid-like characteristics that allow fabrication or processing into a wide variety of shapes. Advanced ceramics' outstanding properties are achieved through special compositions and microstructures that require careful control throughout the successive stages of processing: powder synthesis, powder sizing, rheology / flowability control, consolidation and forming processes, sintering and final machining [22].

The powder forming stage for ceramics can be via dry or wet routes.

2.4.1 Dry routes

Most ceramic components are manufactured using dry processing routes since they do not involve an energy intensive drying step. The process involves shaping the powder with or without the addition of organic additives like binders and lubricants. The shaping proceeds through application of pressure to the loose powder by particle rearrangement, deformation and possibly fractures leading to better particle packing. As the compaction proceeds, the particles slide past each other and the number of contact points increase. At higher pressures, where further rearrangement is not possible, densification proceeds through contact enlargement by plastic deformation. With compaction, there is a reduction in the pore size and porosity. During subsequent sintering, the pores are eliminated and dense structures are formed.

2.4.1.1 Die pressing

Uniaxial die pressing is the most popular dry pressing technique in the ceramic and powder metallurgy industry. In die pressing, the stress is applied by a punch in a mould (die) whose side walls cannot move. The operation can be performed with a single punch movement or double action punch depending on the complexity of the final component to be made. The favourable attributes for die pressing are ease of automation,

high production rates and simplicity. The die pressing of ceramic powders will be dealt with in greater detail in Section 2.6.

2.4.1.2 Cold isostatic pressing

Isostatic pressing is commonly done by placing powder in a sealed elastic bag (rubber or urethane), immersing it in a suitable hydraulic fluid and pressurising the fluid. The technique was developed initially for spark plug manufacturing. As in Figure 2-3, the pressure is applied uniformly throughout the sample using hydrostatic pressure, the density distribution is more uniform than in die pressing. There is less die-wall friction and hence density variations are minimised. As the process is more complex, the production rates are generally low compared to die pressing. Larger samples than for die pressing, with higher length to thickness ratios, can be fabricated satisfactorily using isopressing.

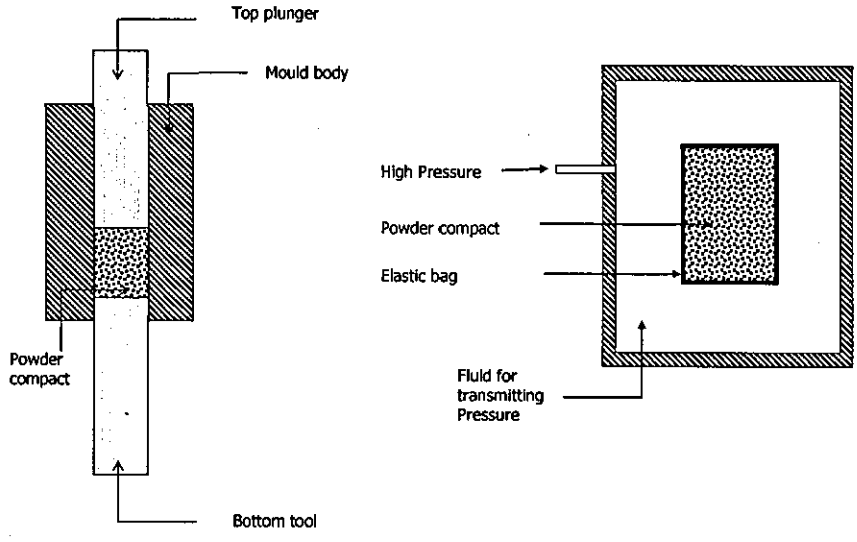

Figure 2-3 Schematic representation of die pressing and isopressing, after [23].

2.4.2 Wet routes

The reliability of dry pressing ceramics is limited by defects due to agglomerates. This can be avoided by using colloidal forming, where ceramic powders can be deagglomerated. Moreover, wet forming routes provide complex shape forming capabilities.

2.4.2.1 Slip casting

Slip casting is one of the widely used wet processing techniques especially in tableware and sanitary ware manufacture. In slip casting, the water is removed from the powder suspension through a filtration process. This is a highly efficient method for producing rather large components and is a stress-free compaction technique. Traditionally, the suspension is poured into a plaster mould that absorbs the water, leaving the powder particles to consolidate into layers on the mould surface, Figure 2-4. The minute pores in the plaster provide the capillary forces necessary for removing the water from the slurry. When the necessary thickness is achieved, the excess slip is removed (drain casting) or the casting proceeds until the casting fronts approach each other (solid casting) [24]. In modern industrial practice, the plaster can be replaced by a porous polymer mould and an external pressure applied to drive out the water through the pores. This increases the production rates to a large extent but at a greater fabrication cost. Further, the maintenance costs associated with the maintenance and replacement of less durable plaster moulds is reduced by substitution with polymeric moulds though the purchase price of the moulds is considerably higher, necessitating the use of long production runs.

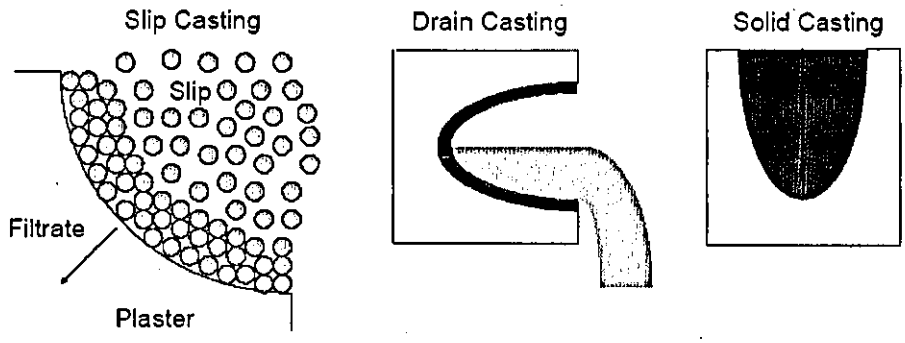

Figure 2-4 Slip casting of ceramics, after [25].

To avoid defects introduced by differential sedimentation due to the particle size distribution of the starting powders, it is desirable to use high solid content slurries. Often, high green density, >60% of TD [26], are

achievable and complex shape geometries can be produced economically using slip casting.

2.4.2.2 Tape casting

Tape casting is used for forming thin and flat ceramics. The technology was developed to meet the needs of the electroceramics industry where thin layers of dielectric substrates were needed for making multilayer capacitors. Thin layers of the order of 6 μm to 1 mm can be achieved using tape casting [27]. The slip consists of a thoroughly dispersed de-agglomerated suspension along with certain binders to have the desired rheological properties. The slip is cast in the form of a thin film using a reservoir and doctor blade arrangement, Figure 2-5. Lindqvist et al [28] used tape casting to produce ultrafiltration membranes from alumina slip.

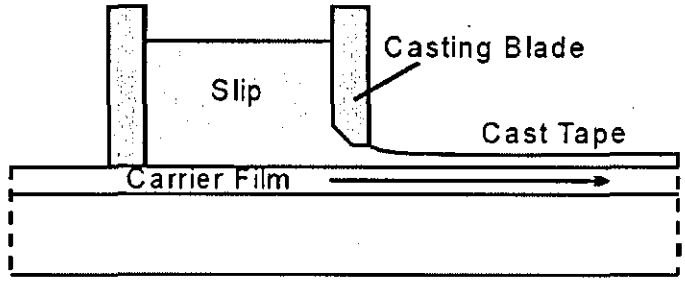

Figure 2-5 Tape casting of ceramics, after [27].

2.4.2.3 Coagulation casting

Coagulation casting can be used to produce ceramic green bodies starting from a de-agglomerated suspension. The process is based on the destabilisation of an aqueous suspension by internal reactions leading to decreased surface charge on dispersed particles either by a pH change or increase in ionic strength. In a polar solvent (like water) the suspended solid ceramic particles carry a charge. In acidic pH regimes, the particles are positively charged and are negatively charged in basic pH values for many ceramics. If the particle surface charge is high, then the repulsive forces prevail over the van der Waals forces resulting in a stable, low viscosity suspension. When the surface charge is reduced and brought near the isoelectric point (IEP), the particles become attracted to each

other (coagulate) and form a stiff, wet solid with a homogeneous microstructure. Enzyme reactions and pH changing coagulants have been very successfully used to do coagulation casting of a wide range of ceramics including Al_2O_3, ZrO_2, SiC etc., with specific surfactants [29, 30].

2.4.2.4 Electrophoretic deposition

The electrophoretic deposition (EPD) system works by applying an external dc field to a slurry, the field promoting the migration of particles (electrophoresis) and their subsequent deposition onto the oppositely charged electrodes. The colloidal parameters (zeta potential, viscosity and electrophoretic mobility) play an important role in EPD, while the electric ones (conductivity) determine the viability of the process [31]. Problems that could be faced during the EPD process are: unwanted water electrolysis, galvanic reactions and water electro-osmosis. However the simplicity of the process and the capability of depositing metals, ceramics and polymer by electrophoresis opens great possibilities for application in different fields such as electroceramics (SOFC, multilayered capacitors, sensors, actuators, etc), structural ceramics (layered composites, long fibre CMC, functionally graded materials, laminated ceramic composite tubes, etc.) and protective coatings onto metals (EPD of sol-gel solutions or suspensions) [32]. This technique is already used commercially for some traditional ceramics (electrophoretic spray coating of sanitary wares, enamel electrophoretic deposition, etc.) [33].

2.4.2.5 Powder injection moulding

This is a plastic forming method where a thermoplastic binder is added to the ceramic powder, heated to a temperature above the glass transition temperature of the binder and injected into a mould as a paste. After cooling, the green body is subjected to dewaxing or binder removal, followed by sintering to form ceramic parts. Complex shapes can be moulded with high precision and low dimensional tolerances [34]. The process can be readily automated, although since large amount of binder needs to be removed before firing, the process can be time consuming and lead to unfavourable pollution.

2.5 Ceramic nanopowders

Ceramic powder is a necessary ingredient for most structural ceramics, ceramic composites, electronic ceramics and ceramic coatings. Nanopowders, the building blocks for ceramic nanomaterials, can be produced either through a bottom-up (inert gas condensation, sol-gel, chemical processing e.g hydroxide precipitation or hydrolysis of alkoxide, spray pyrolysis, hydrothermal routes, emulsion process, vapour deposition, electodeposition [35] etc.) or top-down approach (plasma processing, mechanical milling [36]). The projected U.S. markets for ceramic powders was over US$ 2 billion in 2007, with about 12% being for nanosized ceramic powders. The annual average growth rate for the latter is predicted to have been 9.3% over 2002-07 [22]. As mentioned in Section 2.3, technological advancements in nanosized powder production and use heralds a new era of engineered materials. For example, several researchers have reported that the sintering temperature is lower for ceramic nanopowders [18, 37]. Hence, they could form the basis for easier ceramic fabrication (faster sintering). A major drawback in using nanopowders to form ceramic components is their agglomeration, Figure 2-6, which will be dealt with in detail in the later sections.

Figure 2-6 TEM image of calcined ZrO_2-CeO_2 nanopowder, after [38].

2.6 Die pressing of ceramic powders

Dry pressing is the most common forming route for manufacturing ceramic components with simple shapes like those shown in Figure 2-7.

As stated in section 2.4.1.1, it involves compacting a powder in a die to form a nominally defect-free powder compact to near-net-shape with minimal density gradients [39]. Economically, net shape forming is desirable because it eliminates expensive final machining. The aim in die pressing is to achieve a green compact with:

(i) a high density
(ii) uniform pore size distribution
(iii) minimal density gradients or localised density variations
(iv) good green strength so that handling and green machining (if needed) is possible.
(v) good dimensional tolerance.

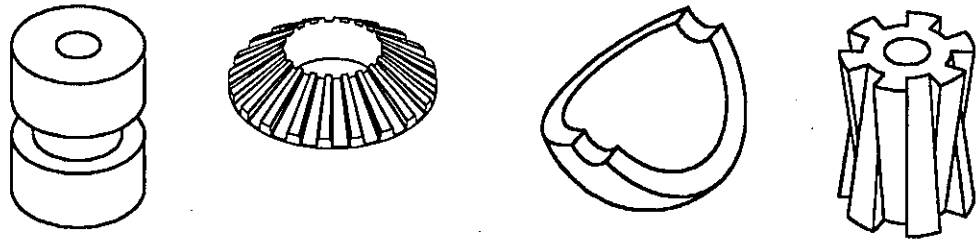

Figure 2-7 Various shapes formed by die pressing, after [40].

An economical industrial process would require all the above attributes to be achieved at the minimum possible applied pressure. Achieving this depends on the quality of the powder that is used.

2.6.1 Various stages in die pressing

The various stages in the conversion of powders into ceramic components through die pressing, Figure 2-8, are:

(i) Powder formulation
(ii) Die filling
(iii) Powder transfer inside the die
(iv) Compaction
(v) Ejection
(vi) Green machining and
(vii) Sintering.

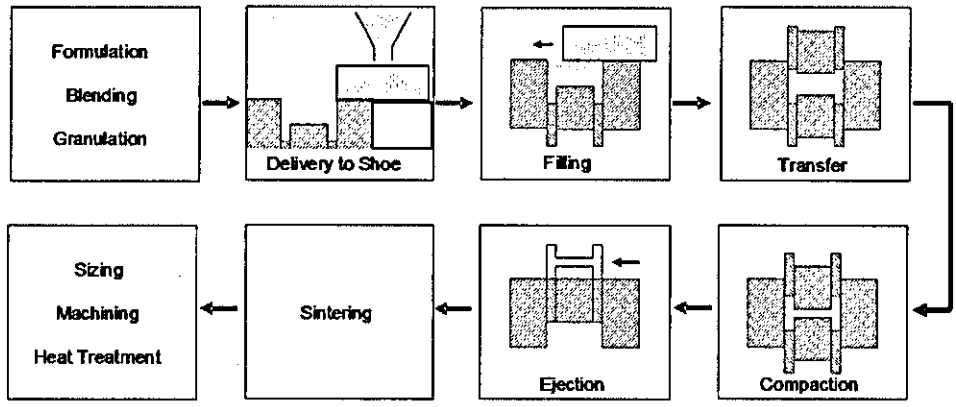

Figure 2-8 Process steps in ceramic component manufacture through die pressing, after [1].

2.6.1.1 Powder formulation

The powder formulation step involves mixing, blending, granulation and addition of binders. Powders can undergo segregation during transportation, handling and storage. Segregation leads to compact to compact variability in production batches. To meet the quality standards, homogeneous mixing with uniform size and compositional distribution should be achieved during powder formulation. Lubricants that can reduce the particle – particle friction and particle – wall friction can also be added to the powder at this stage. Granulation is usually done in ceramic powders to improve powder flowability and die filling characteristics.

2.6.1.2 Die filling

The free flowing powder is fed into a shoe (with open base) from the silo. The shoe traverses over the die at a specified velocity and powder flows into the die under gravity or suction. During die filling, the powder must flow freely and rearrange to fill the die uniformly.

2.6.1.3 Powder transfer

Powder transfer can be intentional or part of the process. For multilevel parts, blocks of material are intentionally translated past each other after filling to create a complex shape. This can effect the density distribution significantly, both initially and throughout subsequent stages [41]. If the punch kinematics of a multi-action punch are poorly designed or a single action punch is used to manufacture a component, intense

shear deformation of the green body can occur during compaction as the powder is pressed, leading to cracks.

2.6.1.4 Compaction

During powder compaction, a high pressure is applied to the powder which results in powder consolidation. At low pressure, densification is through granule rearrangement. When the applied pressure is more than the granule yield point, the granules crush into smaller fragments. At high pressure, the granules are completely crushed or plastically deformed and density increase is through the rearrangement of the primary particles. Lubricants reduce the friction between particles and aid the particles to slide past each other and rearrange.

2.6.1.5 Ejection

This is last step in the compact formation. The compact is ejected by the movement of the bottom punch. Careful control is needed to avoid cracking of the green compacts.

2.6.1.6 Green machining

Green machining is optional in most ceramic component fabrication, it is done, when necessary, to improve the dimensional tolerances. As sintered ceramic components are hard and brittle, machining of green compacts is a cheaper alternative.

2.6.1.7 Sintering

Sintering is the bonding together of particles at high temperatures. It can occur at temperatures below the melting point by solid-state atomic transport events, but in many cases involves a liquid phase. On a microstructural scale, bonding occurs due to the formation of cohesive necks between particles.

2.6.2 Challenges in die pressing fine powders

Most of the problems faced in the die pressing industry have been solved using a trial and error approach. The major problems are:

(i) Powders with poor flowability do not fill the die homogeneously resulting in localised density variations and cracking.

(ii) Low green density can lead to uneven shrinkage during sintering and warpage of the samples.

(iii) The presence of agglomerates leads to increased grain growth during sintering [18].

(iv) End capping, lamination and the formation of cones can result if the applied pressure is not appropriate, Figure 2-9.

(v) Compaction in rigid dies leads to nonisotropic green densities, with gradients in both the axial and radial directions [23].

A high green density is preferable for higher densification kinetics, taking advantage of an increased number of contact points and therefore a greater number of transport points [35]. In ceramic materials, poor compressibility inhibits pressing to high densities. The residual pores left after sintering act as incipient cracks to degrade the strength substantially. Consequently, full density is most useful for competitive mechanical properties of ceramics.

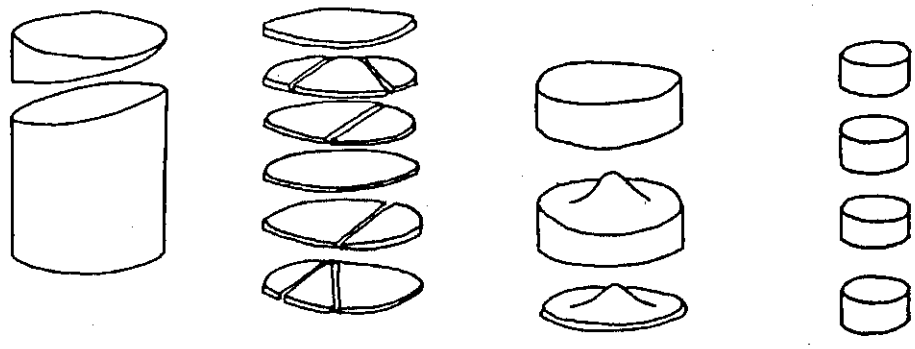

Figure 2-9 Common defects in dry pressed samples (a) end capping; (b) lamination; (c) formation of cones and (d) fracture of an isostatically pressed cylinder, after [23].

High pressures on the order of 350 MPa were needed to achieve green densities in the order of approximately 42% of theoretical density in the case of zirconia nanopowders [42]. Densification by sintering

progresses through pore elimination. A low initial packing density results in a considerable dimensional change before the desired high final densities are obtained. It is the dimensional change that warps many sintered structures as in Figure 2-10. This constraint often leads to an emphasis on high green density.

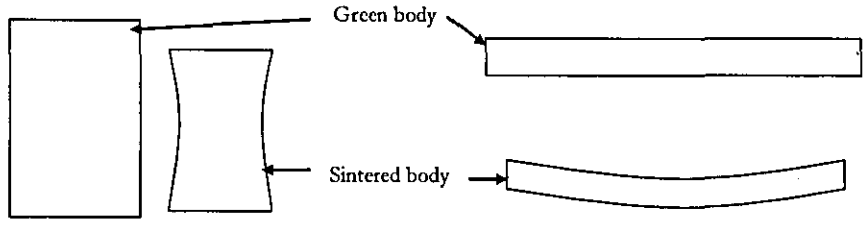

Figure 2-10 Uneven shrinkage during firing due to density gradients, after [23].

However, Bromley [43] showed that 'near net shape' forming of ceramics is possible by optimising die pressing parameters. He showed that small nuclear fuel rods could be formed with a precision of ±12.5 μm using proper lubricants and loading conditions.

The major industrial concerns in component manufacture are reproducibility, minimised flaws, dimensional and compositional control and production efficiency. A higher green density is often preferred as it translates into less shrinkage (and warping leading to non-uniform dimensions), smaller pores and higher final density after sintering. But, compaction at higher pressures introduces density gradients which lead to cracking during subsequent sintering stages.

The creation of an inhomogeneous stress distribution within the compact is an inherent problem in the dry pressing technique. A nominal uniaxial pressure applied from one end of the die containing the powder will be dissipated by the wall and inter-particle friction so that a substantial portion of the powder will experience a lower compressive pressure than the applied pressure [44]. Naturally, these areas will compact to a lower density than those areas exposed to a higher pressure, Figure 2-11. This effect is more pre-dominant when the compacts are long, Figure 2-12. In practice, the use of suitable binders and lubricants can reduce the density variations within the compacts.

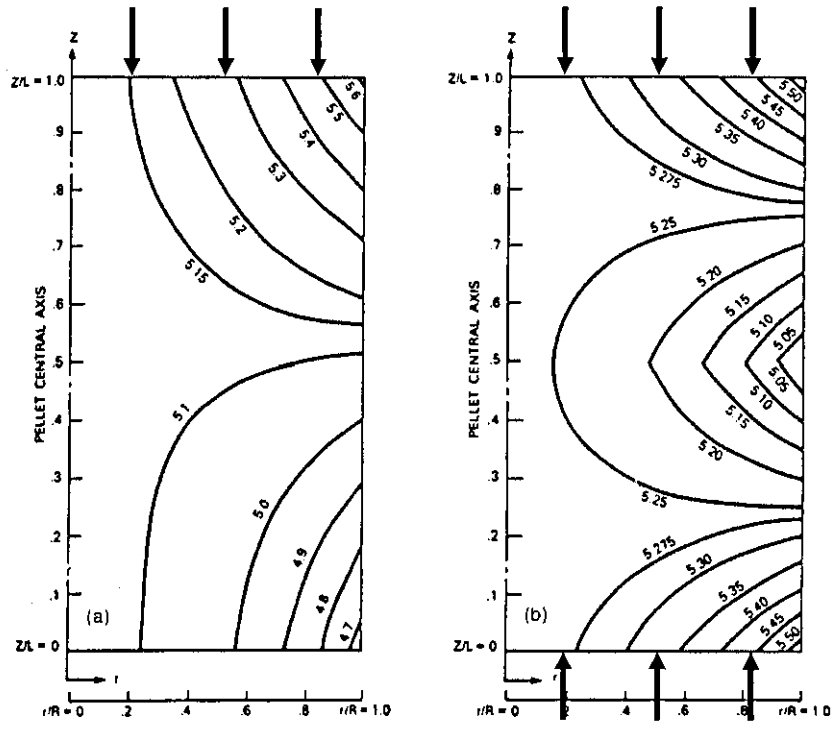

Figure 2-11 Density distribution in green compact with single action and double action pressing, after [23].

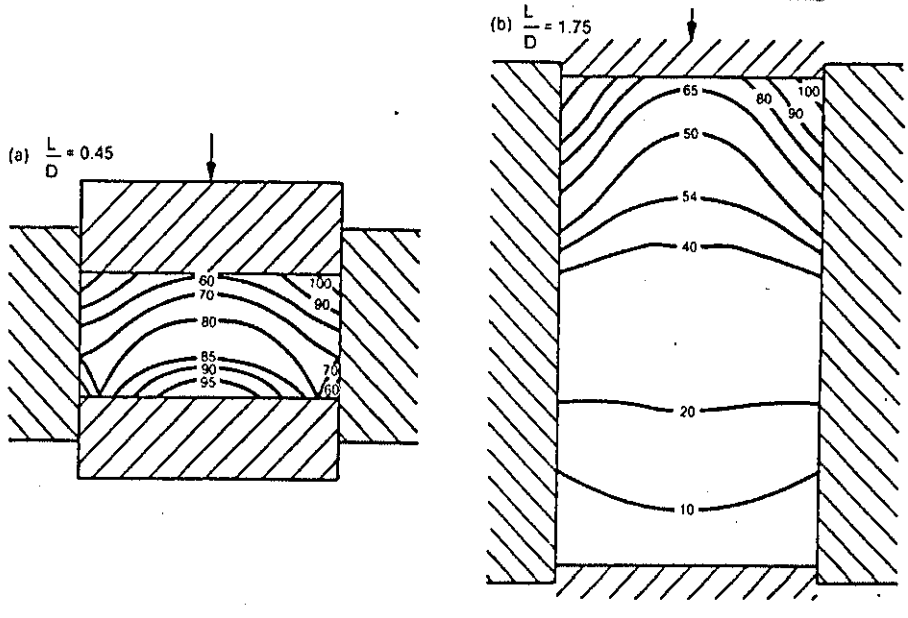

Figure 2-12 Density distribution in die pressed compacts with different aspect ratios.

2.6.3 Hurdles in fabrication of nanostructured ceramics

Apart from the generic difficulties in die pressing, several other issues need to be addressed for the successful application of die pressing to nanopowders. Their unique mechanical, optical, magnetic and electrical properties largely depend on the consolidation of powders into engineered components that will preserve their initial metastable nanostructure [35].

For fine particles of less than 100 μm in size, weak forces like van der Waals and electrostatic forces can be more crucial than for coarser particles. Feng et al. [45] studied the packing efficiency of mono-sized spheres of different sizes, Figure 2-13. They reported that the porosity increased with decreasing particle size, below a certain critical size. If the particle diameter was greater than this critical value, the porosity was constant and independent of particle size.

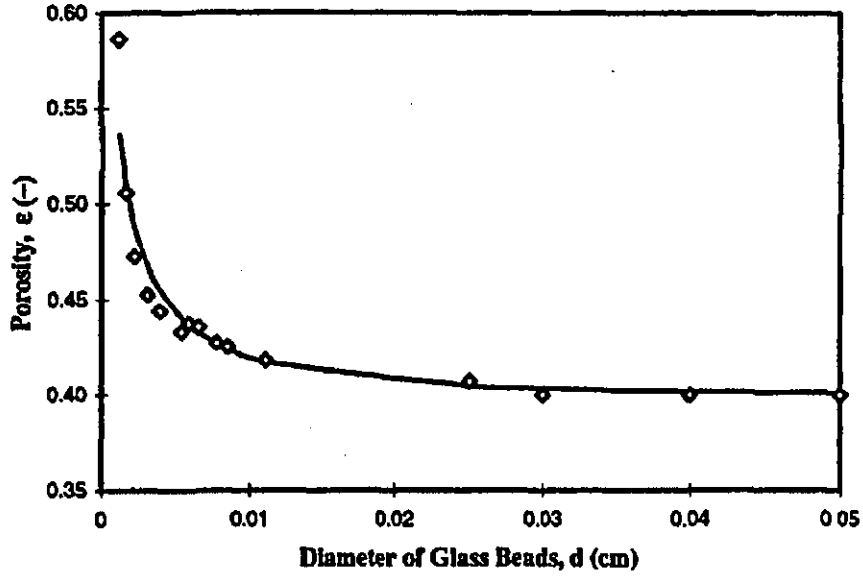

Figure 2-13 Dependence of porosity on particle size, after [45]

Nanosized powders have a higher tendency to form agglomerates [46]. If these agglomerates are not broken down, it will not be possible to obtain a uniform nanostructure at the end of green forming [47]. Rather, it there will be differential densification [48], intra-agglomerate coalescence and grain growth during sintering [18]. The presence of hard agglomerates also reduces the green density [49]. As indicated earlier, a

high green density is preferred at the end of the die pressing since it reduces shrinkage, and hence there is the possibility of warping as well as reducing the energy spent on sintering. If the green density is low, longer sintering durations and higher temperature will be required to eliminate all the pores in the green body, which generally leads to undesirable grain growth.

The compaction efficiency is found to be low in the case of fine powders [50]. Under similar consolidation conditions, coarse powders were shown to achieve higher green densities than their finer counter parts when die pressed. This is attributed to the high surface area which in turn translates into higher inter-particle friction and powder – wall friction co-efficient.

In the absence of a proper grain growth controlling mechanism during sintering, the finely divided active nanopowders can undergo extensive (even more than 10 fold) grain growth wherein the final microstructure will have a grain size in the range of microns. When compacts made of zirconia nanopowders with a crystallite size of 30 nm were sintered, the final sintered body (>98% density) had an average grain size of 5 μm [51]. According to Chen's work [52], a two stage sintering technique wherein the kinetics of grain boundary diffusion and grain boundary migration were controlled could be used to achieve fully dense ceramics with an average grain size of <100 nm.

2.7 Granulation of ceramic powders

Loose nanopowders have a very low bulk density (around 10% of theoretical). As a result, the punch will have to travel a long distance during a die pressing operation. In addition, since they have poor flowability, they do not fill the die uniformly, resulting in density gradients in the final compact. Further, nanopowders have a strong tendency to agglomerate owing to their high surface area. Fine powders used in dry pressing are generally granulated to micrometre size for improved flowability [53]. Granulation is the process of intentionally agglomerating fine particles into larger particle cluster (i.e., agglomerates) that exhibit improved handling and flow. The challenge lies in controlling the granule

strength. Granules should be strong enough to facilitate easier handling and allow rearrangement prior to granule deformation/fracture, but weak enough to completely break down, deform and knit together during compaction. Excessively hard granules can retain their character in a pressed and sintered body resulting in inter-granular pores and low density, low strength components on sintering.

The benefits associated with granulation can be summarised as:

- Control of size distribution
- Increase in bulk density
- Improved flow characteristics
- Minimal dusting.

The most widely used granulation technique in the ceramics industry is spray drying. Other options include freeze drying, fluidised bed granulation and high speed shear granulation. The spray drying of technical ceramics is dealt with in detail in Section 2.8 and freeze drying is discussed at some length in Section 2.9.

2.7.1 Fluidised bed granulation

Fluidised bed granulators are used in pharmaceutical industries for production and drying of granules. The powder is placed in a porous base in the bottom of the drying tower. Through the bottom of the fluidised bed reactor, the product compartment is fed a constant temperature controlled airflow, Figure 2-14. The binder fed to the product via a spray nozzle contributes to the increasing size of the dispersed particles until they can no longer be carried by the airflow and fall to the vessel bottom. The hot air carries the excess moisture away and the dried granules are left below. As the drying and wetting is repeated, an onionskin structure is built up. This is called layering [54]. Owing to the nature of the process, shape control is poor and hence the process leads to powders with poor flowability.

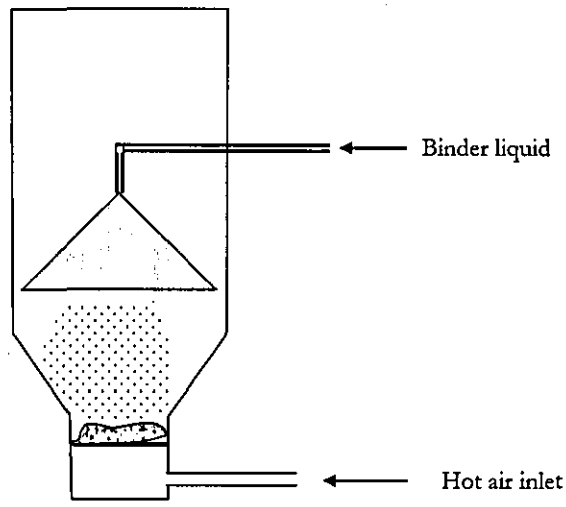

Figure 2-14 Fludised bed granulation, after [54].

2.7.2 Mechanical shear granulator

Some processes, such as milling or plasma synthesis, yield dry powders that are too fine to handle and need granulation. Size enlargement of the finer powders can be done using high shear rate mechanical mixers without converting them into slurries. A small amount of binder liquid is added to the powder and it is mechanically agitated at a very high speed. The shear and normal forces are generated in the powder by rotating tools called impellers and choppers. Impellers are large metallic arms, usually situated at the bottom of the vessel, that rotate relatively slowly and induce an overall motion of the powder inside the granulator. Choppers are much smaller tools fixed to the sides of the machine that rotate much faster and are there to disrupt the flow, disperse binder and disintegrate large chunks of material that may form [55]. The impeller blade tip velocities typically rage between 5 – 10 ms^{-1}. The fine powder is converted into a dense granule due to the mechanical agitation. This process is used widely in pharmaceutical and detergent manufacturing units. Compared to fluidised bed drying, which also operates on the basis of agitation, the high shear mixer granulators are more rugged, more productive and can handle cohesive powders [56]. It has been shown [57] that the high shear granulation yields high density granules with better flowability compared to that of fluidised bed

granulation. However, the median granule diameter (d_{50}) and the span ((d_{90} – d_{10})/ d_{50}) of the granule size distribution was larger.

Granulation using mechanical shear mixers can be an alternative to produce weak ceramic granules. As this process does not involve redispersing the powders, there is a greater possibility to control agglomeration. This operation can be completed at room temperatures and hence eliminates the higher capital costs involved in freeze drying. The size distribution of the granules depend on a number of factors such as the uniformity of distribution of binder liquid, the rate of redistribution of liquid between the granules and the kinetics of the process of granule breakage and size enlargement [58]. These parameters depend on the granulator design. An American patent [59] describes a method to uniformly disperse the liquid binder into the powder during granulation. Hoornaert et al [60] studied the agglomeration behaviour of powders in a Lödige mixer granulator, one variant of the high shear granulator, Figure 2-15. Keningly et al [61] established that a minimum binder viscosity is needed to initiate granulation and this is dependant on the primary particle size. They showed that the minimum viscosity for granulation to form was 1 mPas for 8 μm particles and was of the order of 1 Pas for a particle size of 230 μm. Small particle size and low viscosity can facilitate an improvement in granule sphericity [62]. The explanation is that small particle size enhances granule strength to an extent that it is sufficient to resist deformation from impeller impact and a low viscosity provides granules with sufficient deformability to become more rounded.

The disadvantages of the high shear granulator are (i) poor shape control & (ii) the process is not continuous (it is a batch process), although Werani et al [63] demonstrated that high shear granulation can be made semi-continuous with an improvement in overall productivity.

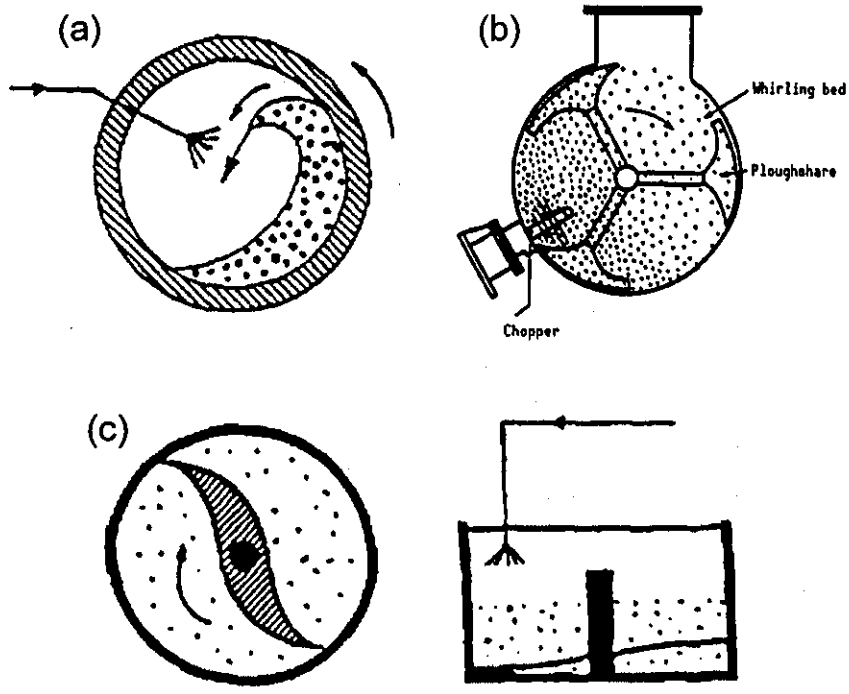

Figure 2-15 Different configurations of industrial granulators (a) rotary drum, (b) Lödige mixer and (c) high shear mixer granulator, after [60].

2.8 Spray drying of ceramics

Spray drying is by far the most widely used granulation technique for ceramics. Continuous operation, flexibility in granule size control, ease of automation and high production rates with minimal wastage makes spray drying a lucrative option for mass producing large quantities of spherical shaped ceramic powders. Spray drying is by definition a one step, continuous particle processing operation with the transformation of feed from a fluid state into a dried particulate form by spraying the feed into a hot drying medium [64]. Granulation of ceramics by spray drying involves atomisation of the feed (ceramic slurry) into fine droplets and contact between the spray and hot drying medium resulting in moisture evaporation.

2.8.1 Types of spray dryers

Spray dryers are classified by the air flow type and the atomiser type [64]. The three most common configurations are (i) cocurrent, (ii) countercurrent and (iii) mixed flow type, describing the relationship

between the direction of flow of air and product in the drying chamber, as in Figure 2-16. The commonly used atomisers are (i) rotary, (ii) nozzle type and (iii) ultrasonic.

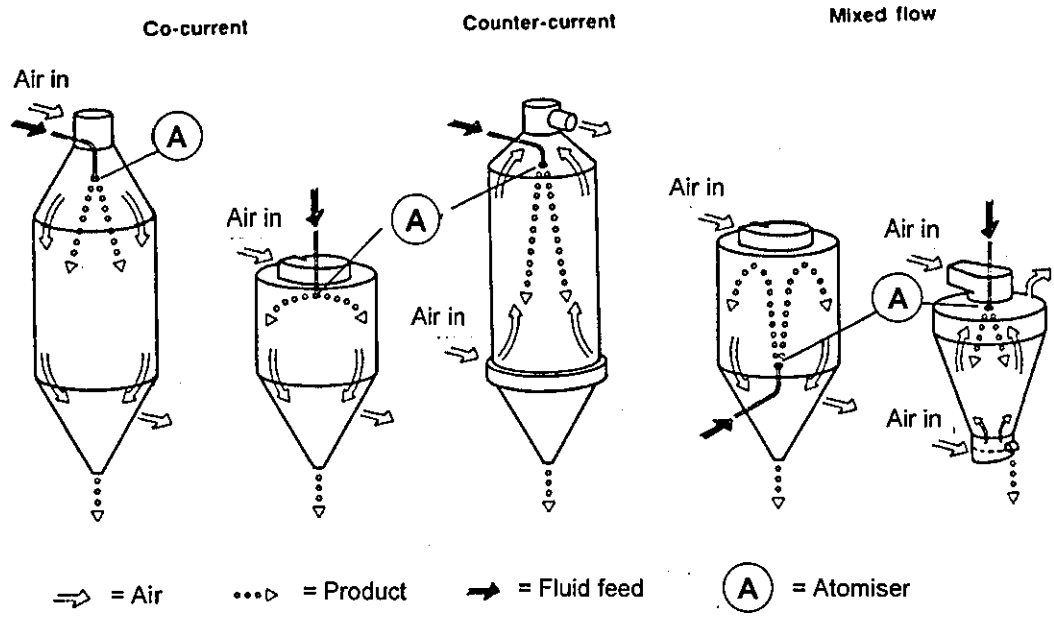

Figure 2-16 Classification of spray dryers based on flow pattern, after [64].

In a rotary atomiser, the feed is introduced centrally onto a wheel or disc rotating at a controlled speed. The feed flows outwards over the surface, accelerating to the periphery. Feed on leaving the periphery readily disintegrates into spray droplets. The spray droplet trajectory from the rotary atomiser demands a large diameter for the dryer. The droplet diameter is typically 20 – 150 μm. The merits of this type of atomiser are less clogging and easier control of particle size simply by controlling the wheel rotation speed.

The nozzle type atomiser can be either a pressure nozzle or two-fluid (pneumatic) nozzle system. In the pressure nozzle, the pressurised feed concentrate is fed into the nozzle where pressure energy is converted into kinetic energy and the feed emanates from the orifice as a high speed film. This disintegrates instantaneously into fine droplets inside the drying chamber. In a two-fluid system, the feed is mixed with high velocity air which breaks the feed into fine droplets when atomised into the dryer. The

nozzle type atomisers yield a wider droplet size distribution. The typical particle size range will be 120 - 300 μm. Sometimes, more than one nozzle atomiser is used to enable high feed rates.

The ultrasonic atomisers use high frequency ultrasound to create fine droplets from the suspensions. The droplet size is dependant on the frequency of the ultrasound used. For a given slurry, the size of the droplet decreases with an increase in ultrasound frequency. The ultrasonic atomiser is more suitable for producing small quantities of spray dried powders.

A cyclone separator or bag filter is normally used to separate the powders from the product stream. Occasionally, electrostatic precipitators are used to separate the fines.

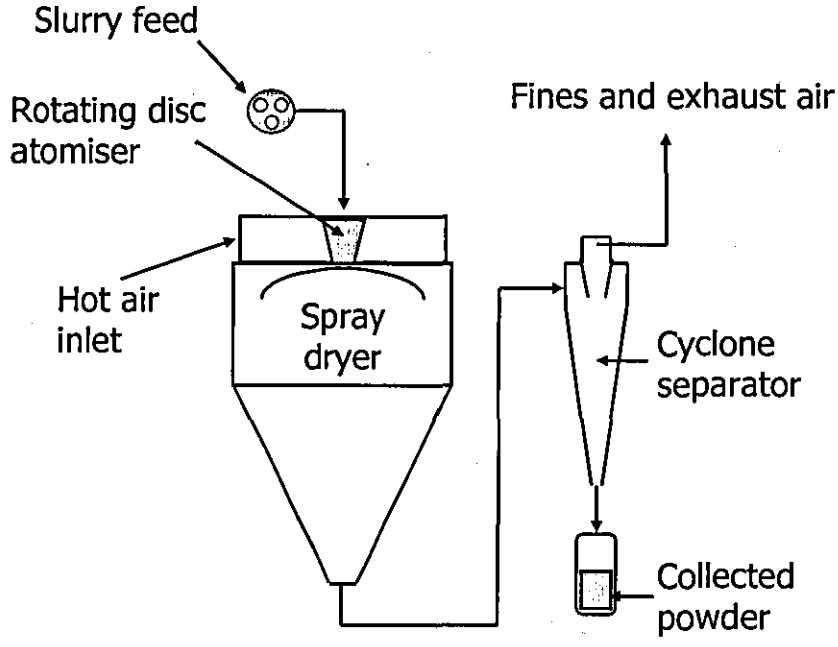

Figure 2-17 Schematic representation of a spray dryer.

2.8.2 Morphology control in spray drying

For good flowability, the ideal spray dried granule must be dense and spherical. Depending on the drying conditions and the slurry characteristics, the dried granules can be spherical or irregular - donut shaped, hollow, elongated, etc [65]. If a rigid surface layer forms before atomisation is complete, needle shaped granules can result. The

morphology and particle packing of the spray dried granules also depends on the state of dispersion of the slurry used. Ceramic slurry can be either in a flocculated or dispersed state depending on the pH, presence of dispersants, de-flocculating agents, steric stabilisers, etc. When the slurry is well dispersed, the viscosity and the slurry yield stress is low.

Walker et al. [66] found that a high deflocculant level, which corresponds to a low slurry yield stress, results in hollow granules. Bertrand et al [67] studied the correlation between slurry characteristics and granule properties for zirconia and alumina. They used sedimentation ratio as a measure of the state of dispersion of the slurry and showed that dispersed slurries result in hollow granules while flocculated slurries yield solid granules, Figure 2-18. The different morphologies were explained on the basis of mobility of the particles in dispersed and flocculated slurries [68].

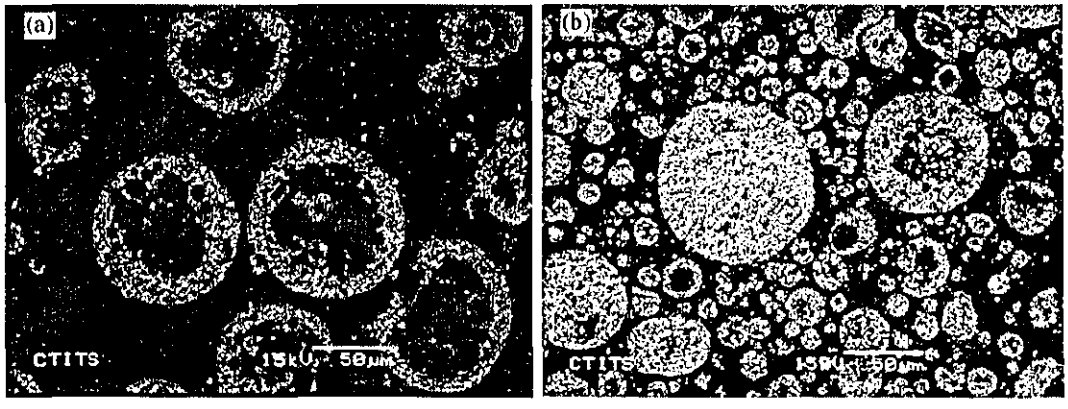

Figure 2-18 Polished cross sections of spray dried alumina from (a) dispersed suspension and (b) flocculated suspension, after [67].

The four different mechanisms proposed for the formation of hollow granules during spray drying of ceramics were [66]:

(i) ballooning, where internal pressure causes the droplet to expand.

(ii) as the rigid surface layer is formed, the moisture evaporates at a faster rate than diffusion of solids back into the droplet interior, leaving air voids

(iii) suspended solids being drawn to the droplet surface as liquid migrates because of capillary action of the solid and

(iv) entrained air in the feed slurry persisting as voids.

Ballooning can produce thin walled hollow spheres that are larger than the original droplets. Because of the partial vacuum created during the flow of materials towards the surface, the granule can collapse inward resulting in a large crater on the surface of the granule. The tendency to form hollow granules can be lowered by using suspensions with high solid contents and lower amounts of soluble material.

The granule morphology of spray dried alumina powders with different deflocculant level, solid content and binder concentration was reported along with a model for granule formation [66], Figure 2-19. As per this model, Figure 2-20, the degree to which particles are able to rearrange during drying influences the final granule density and shape and is determined by the strength of the floc structure, as indicated by the slurry yield stress. When the yield stress is low, a crater may form from the inward collapse of the surface of a forming granule when the particle packing density in a droplet continues to increase after the droplet size becomes fixed by the formation of a rigid shell, leaving an internal void. Konsztowicz et al. [69] introduced surface tension of the slurry as a parameter in determining the conditions for formation of 'donut' shaped granules.

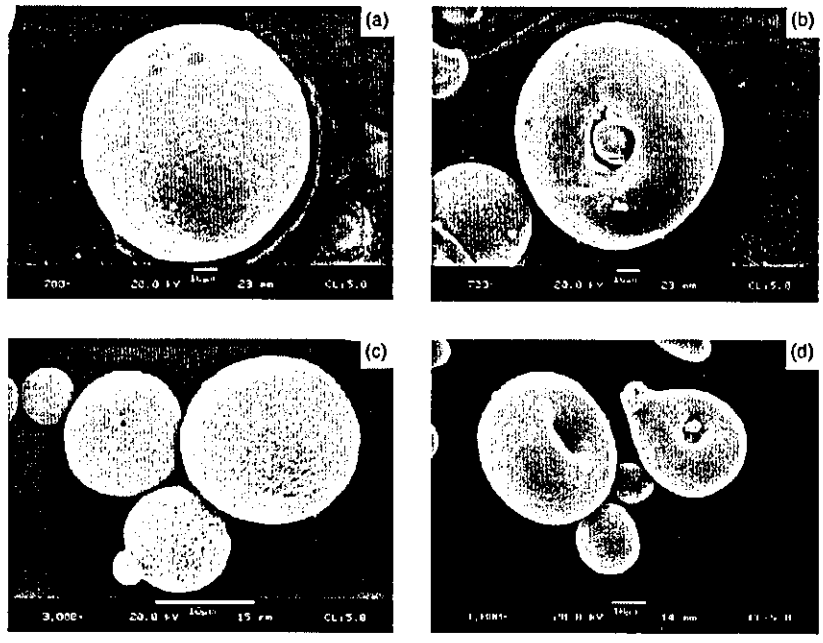

Figure 2-19 Typical spray dried granules from a mixed flow spray dryer (a) flocculated slurry (b) dispersed slurry; and from a concurrent spray dryer (c) flocculated slurry and (d) dispersed slurry, after [66].

Mahdjoub et al [70] used a single droplet drying device to study the spray drying behaviour of yttria stabilised zirconia suspensions with a solid loading of 14.3 vol%. The results were similar to those obtained by Walker and co-workers [66] i.e. dispersed slurries lead to hollow granules whilst flocculated slurries yielded solid granules. The ammonium salt of polyacrylic acid, molecular weight ~7000, was used as a dispersant in this study. Further they showed that the use of different binders, e.g. latex based on a copolymer of styrene and acrylic ester and polyvinyl alcohol, lead to different shell thickness in the hollow granules. They correlated the difference in shell thickness to the sedimentation ratio of the suspension for various pH, dispersant levels and binder addition.

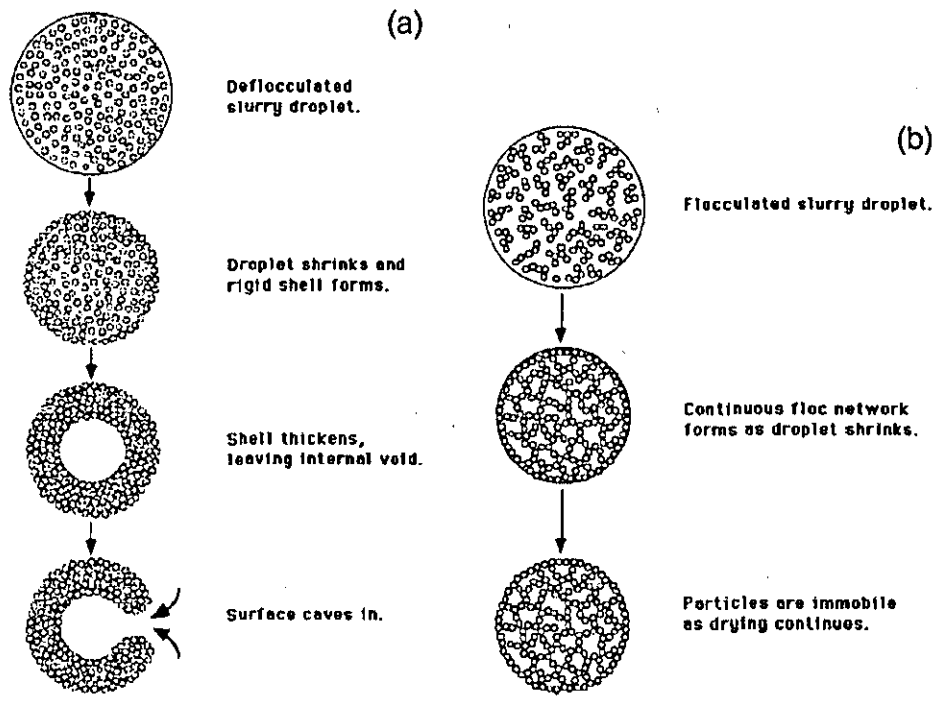

Figure 2-20 Model of granule formation from (a) dispersed slurry and (b) flocculated slurry, after [66].

Takahashi et al. [71] showed that the porosity of the granules can be altered by changing the pH of the spray drying slurry. By progressively decreasing the pH of a well dispersed alkaline slurry (from 10.8) to near the IEP (pH = 7.9) by spray drying at four different pH, they obtained granules of different density and crushability. The pore size distribution was markedly different in each of the batches, as presented in Figure 2-21. Higher capillary forces and clustering of primary particles govern the shrinkage of droplets during granule formation. Interestingly, the porous granules compacted better and resulted in better ceramics after sintering.

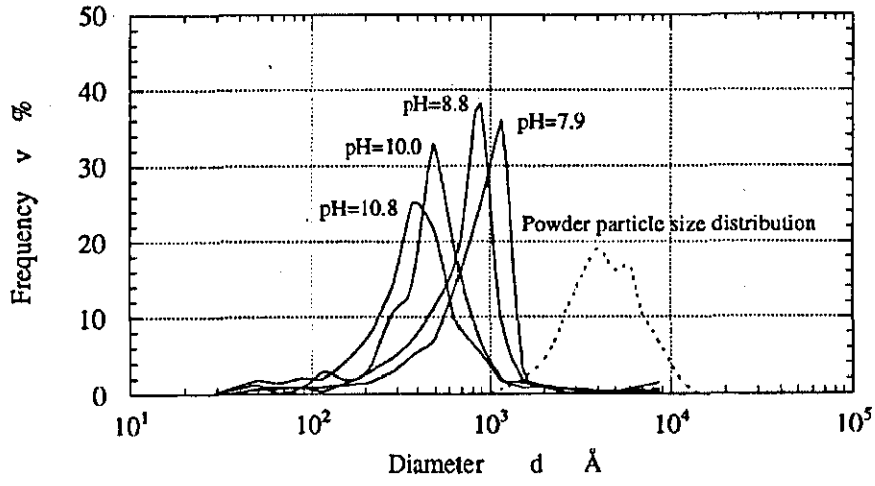

Figure 2-21 Pore size distribution in silicon nitride granules prepared from slurries at different pH, after [71].

2.8.3 Strength of spray dried granules

Spray drying can often produce hard agglomerates; addition of binders and exposure to high temperatures being blamed as the root cause. Binders are often used in ceramic dry pressing operations to increase the green strength of the compacts formed. The most common binders are PVA, PEG and latex based. Binder selection involves techo-commercial issues like cost, ease of availability, compatibility with the system, environmental hazards related to thermal removal and sensitivity to processing conditions.

A homogeneous distribution of the binder in the powder is preferred and this may be achieved by adding the binder to the slurry that is to be used for spray drying. The addition of binders to slurry changes its rheology and affects the state of dispersion of the powder. Binder segregation can occur in the granule even when it was homogeneously dispersed in the slurry before spray drying. When a droplet is introduced into the drying chamber, the droplet dries by loosing moisture from its outer surfaces through mass transport between the droplet surface and drying medium. As the droplet travels further in the drying medium, the surface is completely dried while the centre of the droplet still has moisture. This provides the driving force for the water inside the granule to migrate to its surface. During this process, the soluble species or fine

particles tend to migrate with the solvent to the surface of the granule. As a result, the binder forms a thin layer around the shell of the granule and leads to uneven distribution of the binder. Baklouti et al [72] estimated that the thickness of the layer which contains about 50% of the binder introduced to be a few percent of granule radius. The heterogeneous distribution of binder on the sample is detrimental for the mechanical properties of the compact [73].

The effect of latex binder in spray dried zinc oxide granules was studied by Begum et al. [74]. They evaluated the effect of various organics in the form of binder, plasticizer, dispersant and lubricant in terms of powder flowability, granule density, green density and compressibility. A combination of three dispersants and four binder systems were evaluated in an attempt to optimise alumina and titania slurries for spray drying by Tsetsekou et al [75]. They were successful in identifying the optimum amounts of binder and dispersant to get mixing of alumina and titania in the granules.

Heat treatment can influence the characteristics of spray dried granules to a great extent. Shinohara et al. [76] claimed that the heat treatment (binder removal at 500°C for 5 h) of spray dried alumina granules resulted in better microstructure. The heat treated agglomerates were hard and brittle resulting in rearrangement of the fragmented particles during consolidation, while the 'as spray dried' granules deformed plastically, Figure 2-22. The initial granular structure was still identifiable, showing a clear interface between the granules in the isopressed compacts and acted as crack initiation sites. The fracture strength and fracture toughness were greater for the fired bodies made of heat treated powder, as they had smaller pores and fewer defect sites.

Ceramists resort to plasticisers and polymer blends to improve the granule deformability [77]. Balasubramanian et al. [78] studied the effect of externally applied plasticiser to spray dried alumina. The presence of plasticizer on the surface of the granule resulted in softer and deformable granules, with better breaking and knitting. However, the addition of plasticizer reduced the green strength of the samples, as determined by the diametral compression test. According to Lukasiewicz [79], excessive

drying temperatures can lead to hard agglomerates that resist deformation during the compaction stage.

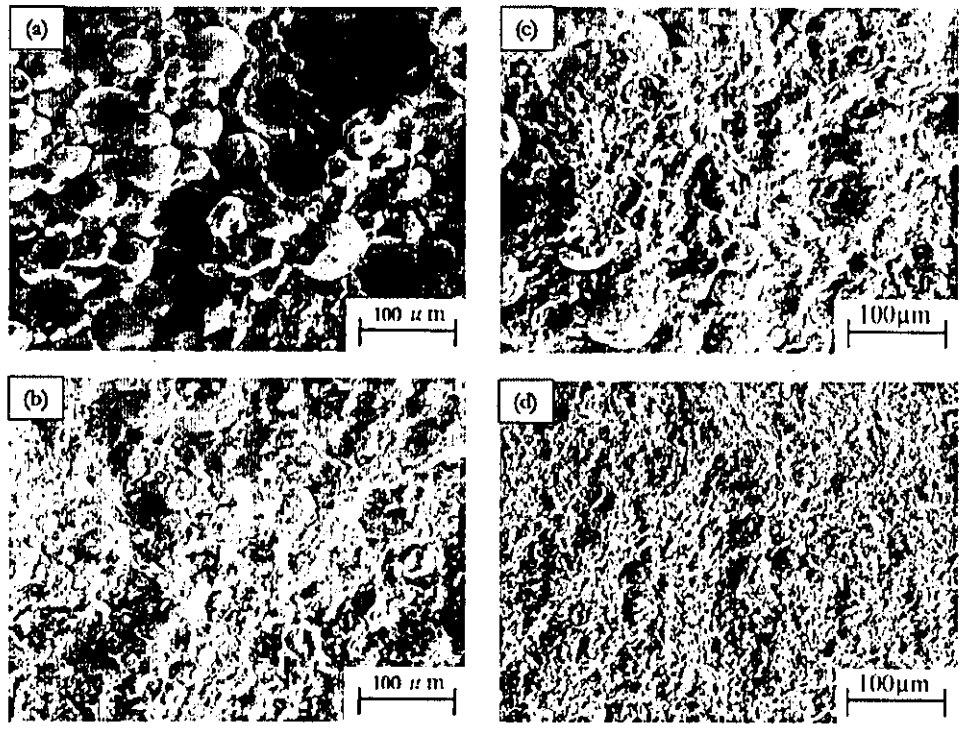

Figure 2-22 SEM micrograph of fracture surface of cold-isostatically pressed green compacts (a) and (c) by pressing at 9.8 MPa, (b) and (d) by pressing at 176 MPa; compacts (a) and (b) were made from as spray dried granules and compacts (c) and (d) were made from heat treated granules, after [76].

Advantages of spray drying powders for ceramic processing:

(i) The granule shape can be controlled to achieve good flowability,

(ii) The powder quality can be controlled and maintained constant throughout the batch used in the entire operation by keeping the conditions constant.

(iii) The operation is continuous with high yield and can be automated.

Disadvantages of spray drying are:

(i) High installation costs associated with the large structures needed to support the spray dryer setup.

(ii) Low thermal efficiency.

(iii) Hard agglomerates.

2.9 Spray freeze drying

Spray freezing combined with subsequent freeze drying is called spray freeze drying. This process is also known as lyophilisation and is widely used in the pharmaceutical industry for drying temperature sensitive materials like proteins, hormones, serums, antibiotics, etc. Nescafė Gold, a popular brand of instant coffee, is a classical example of a spray freeze dried product [80].

A typical freeze drying operation consists of three stages: freezing, primary drying and secondary drying [81]. In case of spray freeze drying, the slurry is sprayed into a cold chamber that typically contains liquid nitrogen and hence frozen as droplets. Freezing is an efficient desiccation step where most of the solvent, typically water, is separated from its solute to form ice. As freezing progresses, the solute phase becomes highly concentrated and is termed the "freeze concentrate". Primary drying, i.e. sublimation, begins when the chamber pressure is reduced to well below the vapour pressure of ice and the latter is transferred from the product onto the cold coils/plates in the condenser. Secondary drying is the stage where water is desorbed from the freeze concentrate, usually at elevated temperature and low pressure, to form dry granules. A schematic expression of the processing path is shown in Figure 2-23 after Rigterink [82].

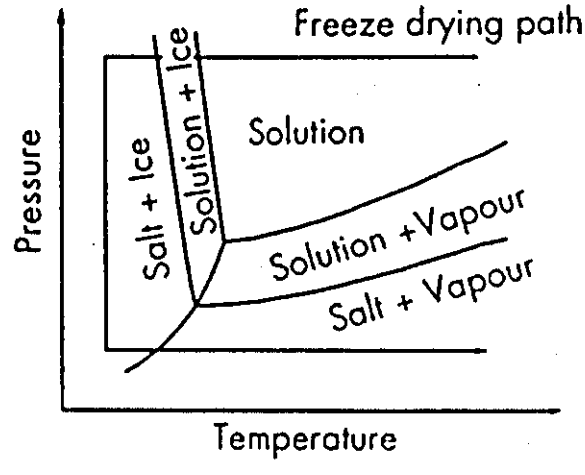

Figure 2-23 Temperature- pressure diagram for an aqueous salt solution and the processing path for freeze drying, after [82].

The concept of freeze drying was adopted for ceramic powder manufacture in the mid 70s. Continued research efforts in the Swedish ceramic institute showed that spray freeze drying can be an alternative for making soft, spherical agglomerates [83], Figure 2-24. They also showed that the spray freeze granulated powders showed better sinterability and higher sintered densities could be achieved as compared to spray dried granules with the same green density, Figure 2-25. It is envisaged that production and granulation of nanomaterials via spray freeze drying will be on demand in the years to come [84].

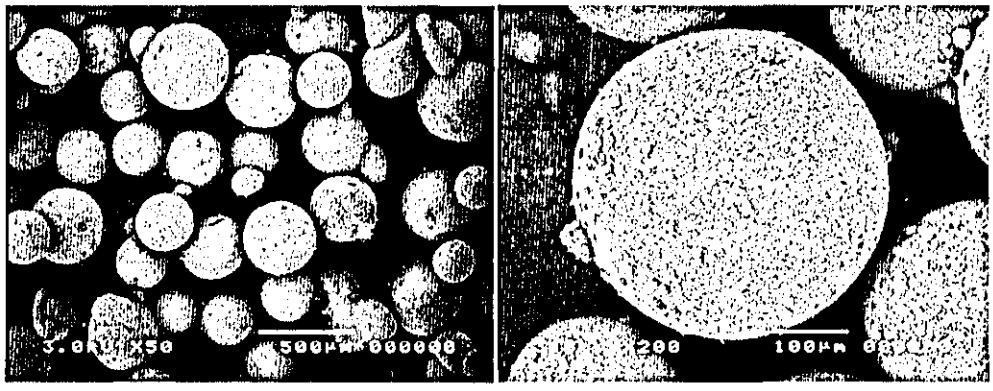

Figure 2-24 Freeze dried ceramic composite granules, after [85].

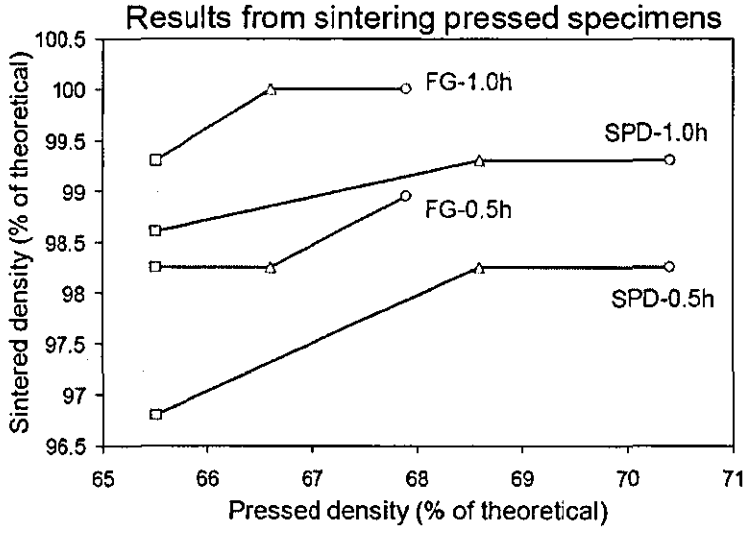

Figure 2-25 Comparision of green and sintered densities for freeze dried & spray dried granules, from [83]. SPD-1.0h – spray dried and 1 hour sintering; SPD- 0.5h – spray dried and 0.5 hour sintering; FG-1.0h – Freeze dried and 1 hour sintering and FG-0.5h – Freeze dried and 0.5 hour sintering.

The advantages of spray freeze granulation can be:

(i) Improved flowability compared to 'as synthesised' powder

(ii) Soft granules that can be easily crushed in a pressing operation or easily dispersed into a suspension

(iii) Homogeneous distribution of binder inside the granule as binder migration is avoided.

(iv) Uniform pore size distribution and hence improved sintering kinetics of the green compacts.

(v) The granule density can be controlled by controlling the solid content of the slip.

(vi) No cavity in the granules.

The spray freeze dried granules can yield higher sintered densities than spray dried granules under similar sintering conditions [86], probably due to lack of hard agglomerates and uniform green microstructure, which results in improved densification kinetics.

In the ceramics industry, freeze drying is also used during synthesis [87 - 97] and green forming [98 - 106] apart from granulation. Itatani et al. [88] reported the preparation of calcium phosphate powders by an ultrasonic spray freeze drying technique. Ultrasonics were used to achieve a fine droplet size in the range of 1 μm to 2 μm in this case. Amato et al. [89] evaluated spray freeze drying and spray drying as options for dispersing MgO in alumina starting powders to obtain transparent ceramics and concluded both to be efficient. Synthesis of YSZ [90], $La_{0.7}Ca_{0.3}MnO_3$ [91], lanthanum doped lead zirconate titanate [92], nanocrystalline $BaTiO_3$ [93], NASICONs [94] and superconducting cuprates [95, 96] by spray freeze drying (followed by calcination) of appropriate precursors has been reported. The synthesis of γ-Al_2O_3 nanopowders by spray freeze drying was reported recently [97]. The dried granules had a typical microstructure, as shown in Figure 2-26, rising from the ice formation and subsequent removal by sublimation from the starting suspension.

Spray freeze drying has the following disadvantages:

(i) The tap density is low and requires a large fill volume

(ii) It is an energy intensive and time consuming batch process

(iii) Scaling up to tonnage quantities has not yet been demonstrated for ceramics.

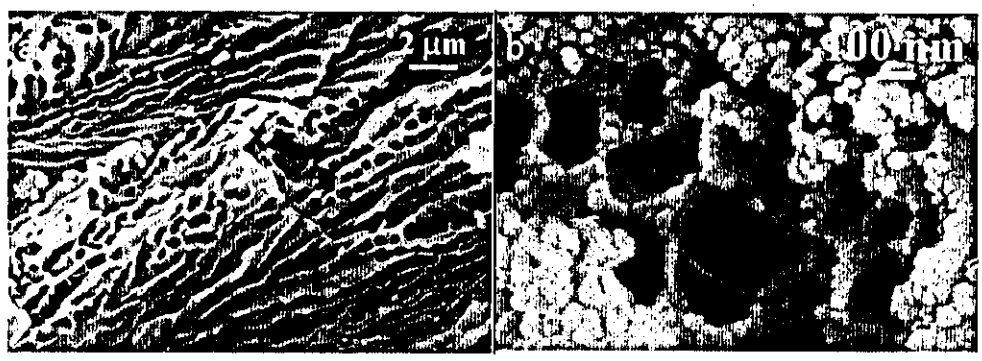

Figure 2-26 Micrograph of freeze dried powder (a) before and (b) after heat treatment, after [97].

2.9.1 Freeze casting

Freeze casting, a green forming route can also be done either from an aqueous suspension [98, 99] or with the aid of sublimable material like camphene [100, 101]. Complex shapes such as zirconia dental implants encapsulating steel rods [102], bilayered ceramic composites [103] and porous bioactive glass-ceramics [104] have all been freeze cast for specific applications. The ability to tailor porosity [105, 106] is a distinct advantage and can be exploited for various applications such as catalyst supports, gas filters and bone scaffolds.

2.9.2 Density of SFD granules

Spray freeze drying (SFD) and freeze casting does not involve the capillary forces that are common in spray drying and slip casting [107]. As a result, there is a direct dependence between the initial solid loading of the suspension and the porosity of the SFD granules / green bodies. The work of Koh et al. [108] deals with the relation between porosity and solid loading for freeze cast alumina bodies from alumina-camphene slurries. The fabricated bodies with three dimensionally interconnected pore channels show a linear relation between porosity and initial vol% solid loading, Figure 2-27 and Figure 2-28. As the physical processes involved in this case are the same as those of the spray freeze drying of aqueous

ceramic slurries, a similar trend would be the norm in the later case as well.

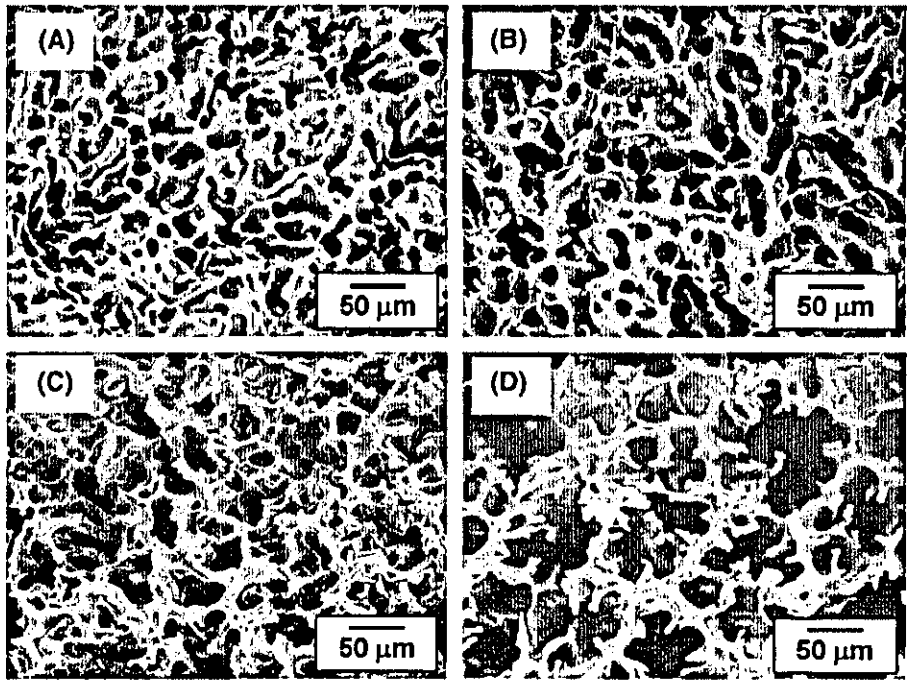

Figure 2-27 Micrograph of porous alumina ceramics sintered from freeze casts starting with a (A) 20 vol%, (B) 15 vol%, (C) 10 vol% and (D) 5 vol% slurry, after [108].

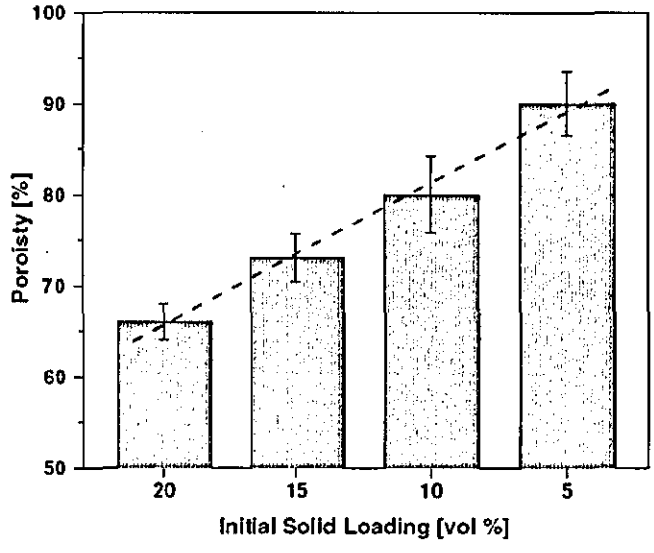

Figure 2-28 Measured porosity in sintered alumina ceramics as a function of initial solid loading, after [108].

Distortion from the shape of the atomised output is uncommon in spray freeze granulation. As a consequence, even suspensions with high deflocculant level yield spherical SFD granules. However, if the atomisation does not yield spherical droplets, the end product will also be the non-spherical.

2.9.3 Strength of SFD granules

The strength of the SFD granules depends on the freezing rate, organics / moisture present, granule size and granule density. The drying rate does not have any significant effect as capillary forces and shrinkage are not present.

2.9.3.1 Effect of freezing rate

In spray freezing, when the atomised slip droplets come in contact with liquid nitrogen, freezing proceeds through a sequence of steps. Nucleation sites are formed first and then propagation of ice crystals occur. If the rate of freezing is high, more nucleation sites are formed and polycrystalline structures result. Accordingly, the ice structure is more disjointed and the dispersed phase is homogeneously distributed within the ice framework. If the freezing is slow enough, the dispersed phase is excluded (seggregated away from the ice phase) and eventually leads to aggregation. Lee and Cheng's paper [109] discusses the effect of freezing rate on the aggregation and redispersibility of poorly water soluble pharmaceutical ingredients. They showed that the quick frozen nanocrystals on redispersion break down readily into primary particles whilst slow freezing leads to less redispersible powder. Unimodal particle size distribution at 0.2 and 9 μm corresponding to primary particles and aggregates formed at different freezing rates were evident, Figure 2-29. They defined a critical freezing rate as the rate of cooling below which the powder looses its redispersibility.

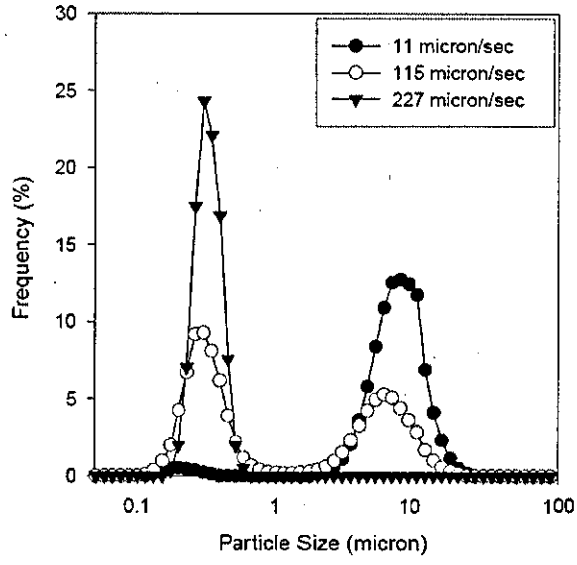

Figure 2-29 Particle size distribution of redispersed nanocrystals frozen at different rates, after [109].

2.9.3.2 Effect of binders / dispersants

The preponderant mechanism for strengthening of SFD granules is the binding of primary particles by organic moieties. Often, the dispersants/binders glue the nanoparticles together and reduce the crushability. The fracture strength of single SFD granules was found to be too low [110] before the addition of PVA. With increase in PVA content, the agglomerates became harder to crush, as shown in Figure 2-30. They remarked that the granules with 0.5 and 1% PVA were too weak to be tested with their kit whilst those with 2 and 3 mass% PVA were weaker than spray dried granules. Moritz and Nagy [107] reported an increase in granule strength distribution with the addition of dispersant on high surface area fumed silica nanopowder, Aerosil 90, with a mean particle size of 20 nm, Figure 2-31.

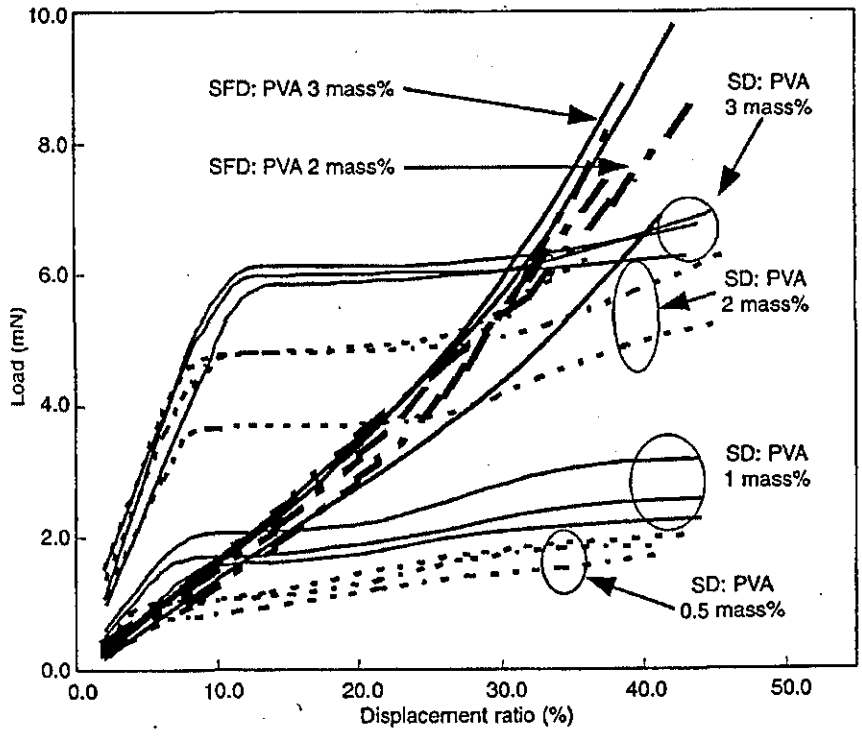

Figure 2-30 Load-displacement curves of fracture strength test of single granules. Three runs are shown for each set of granules, after [110]. SD=Spray dried, SFD=Spray freeze dried.

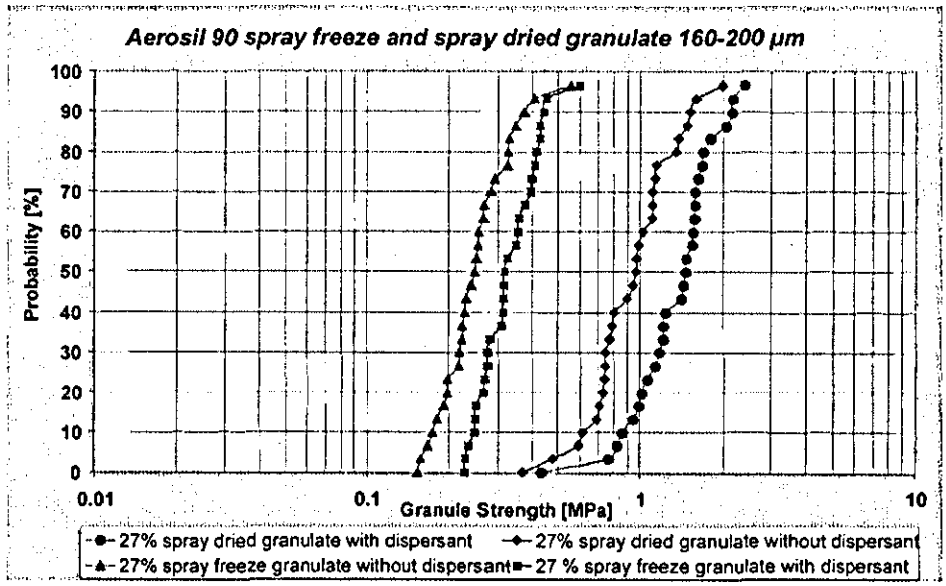

Figure 2-31 Functions of single granule strength of different SFD & SD Aerosil 90 granules with and without addition of organics, after [107].

2.9.3.3 Relation between granule size, density & crushability

A granule can be visualised as an ensemble of several tiny particles bound together to form a bigger lump. In a typical case, the primary particles, either nanosized or sub-micron sized, make up granules with sizes in the range of <10 to 200 μm.

There can be at least two reasons for the increase in granule strength with increase in granule density. Higher granule density implies that the particle packing is better and the inter-particle distance is reduced. This would elevate the effect of van der Waals forces. At the same time, the probability of bridging between the particles by dispersants and binders increase. Two popular theories for estimating the van der Waals forces in agglomerates are by Rumpf [111] and Kendall [112].

According to Rumpf's model, the normal stress σ^* that is applied to the agglomerate made of spherical particles of diameter d_p is distributed over all the individual inter-particle contact points [113]. Rumpf's theory assumes that the failure occurs simultaneously across the granule [114] and the limiting strength of a granule is reached when the separation force imposed by the normal stress equals the adhesion forces. The rupture stress σ_r^* can be expressed as

$$\sigma_r^* = n F_a \qquad \text{..... (1)}$$

where n is the average number of particle - particle contact points per unit area in the cross-section of the granule and F_a is the particle-particle adhesion force.

The parameter n is given by

$$n = \frac{1.1(1-\varepsilon)}{\varepsilon d_p^2} \qquad \text{..... (2)}$$

where d_p is the diameter of the particle and ε is the agglomerate porosity. The van der Waals forces, F_w, for two dry, identical spheres of diameter d_p can be given by

$$F_w = \frac{Ad_p}{24\lambda^2} \quad \text{..... (3)}$$

where A is the Hamaker constant and λ is the separation distance between the surfaces of the particles.

Assuming that the other binding forces are absent, we can equate the rupture stress to van der Waals forces combining Eq (1) and (3) as follows:

$$\sigma_r^* = \frac{nAd_p}{24\lambda^2} \quad \text{..... (4)}$$

Rewriting this equation, we get

$$\sigma_r^* = \frac{1.1(1-\varepsilon)A}{24\varepsilon\lambda^2 d_p} \quad \text{..... (5)}$$

This equation was used by Song et al. [115] as the tensile strength of the particle assembly.

As the granule size increases, a reduction in the single granule strength has been predicted [116] and demonstrated [107]. This is attributed to the smaller flaw sizes associated with smaller granules.

According to Kendall et al. [116], the ultimate fracture strength, σ*, of an agglomerate can be estimated as

$$\sigma^* = 15.6\ \varphi^4\ \Gamma_b^{5/6}\ \Gamma^{1/6}\ (d_p c)^{-1/2} \quad \text{..... (6)}$$

where φ is the volume fraction of solids in the agglomerate, Γ_b is the work of adhesion as measured by fracturing the contacts between the particles as opposed to the equilibrium value of adhesion energy Γ measured in elastic modulus tests, d_p is the primary particle size and c is the flaw size. Kendall's theory assumes a fracture mechanism similar to that of brittle materials. The Φ used in Equation 6 is equal to (1-ε) of Equation 5.

Direct experimental evidence of these theories are difficult to find owing to the difficulty in finding parameters λ and c for Rumpf's theory and Kendall's theory respectively [113]. However, trends that prove the increase in granule strength with increase in granule density have been demonstrated. In Figure 2-32, the plot shows an increase in granule strength with an increase in starting suspension solid content. It is

rational that the difference in starting solid content leads to difference in the density realised.

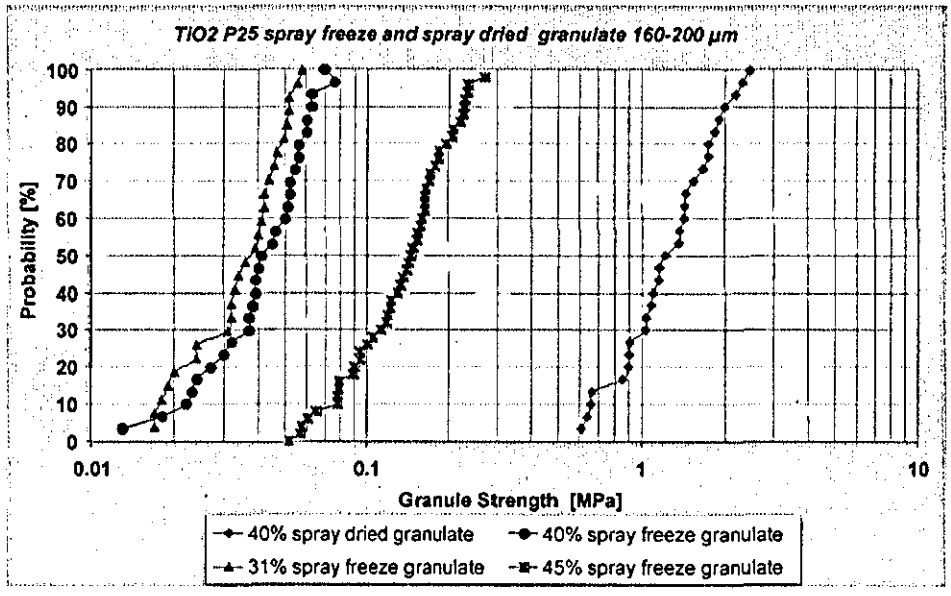

Figure 2-32 Single granule strength as a function of starting suspension solid content for SFD granules, after [107].

2.9.4 Comparison between SD & SFD granules

During spray drying, the spray droplets are subjected to higher temperatures, at least to above 100°C, whereas spray freeze drying is done below room temperature. The binder often migrates from the bulk of the granule to the outer surface during spray drying forming a thin layer enriched with binder. This affects the granule deformation characteristics.

The straight forward approach to quantify granule crushability is by finding the fracture strength of single granules. The load-displacement curves for individual granules prepared by spray drying and spray freeze drying show interesting trends. Uchida et al. [110] analysed alumina granules from the above mentioned routes. Four batches with different amounts of binder (0.5, 1, 2 and 3 mass%) were prepared from submicron alumina powder having a mean particle size of 0.56 µm. The solids content of the slip was maintained at 30 vol%. All four batches were both spray dried and spray freeze dried and their load-displacement curves were shown in Figure 2-30. Interesting features are (i) the SFD

granules show a monotonous increase in the force with displacement, (ii) the SD granules show a distinct breaking point which correspond to the breaking of the outer rigid PVA layer and (iii) the granule strength increases with the increase in the amount of binder in both cases.

For a given slip, the SD granule density is higher than that of the SFD granules owing to shrinkage in the former case [110]. The tap density was 0.61 and 1.1 g cm^{-3} for SFD and SD granules respectively for a 30 vol% alumina slip [107]. The higher density is often advantageous as it enhances the flowability and fill density.

2.10 Powder fill density

Die fill density is a measure of the volume that a given mass of powder occupies when the die is filled before compaction. A high fill density corresponds to a low compaction ratio (i.e., the ratio of the fill density to the compact density). The higher the compaction ratio, the more the punch will have to transverse to achieve the desired compact density. Fluffy powders, irregularly shaped granules, hollow agglomerates and fine powders with high inter-particle friction all have very low fill densities and are generally not suitable for dry pressing.

The control of fill density is conceptually easier in the case of spray freeze drying. As there is no granule shrinkage during drying, an increase in the solid content of the starting suspension steers towards a higher fill density. In contrast, the granule density in spray drying depends on various parameters including slurry viscosity, state of dispersion, inlet and outlet temperatures and starting solid content.

2.11 Slip preparation for granulation

Granulation is carried out either directly from the 'as synthesised' suspension or from an aqueous suspension containing the calcined powder. In the latter case, the powder is dispersed with suitable pH modifiers, dispersants, binders, plasticisers, defoaming agents, etc., and then ball milled or ultrasonicated to obtain a uniform dispersion. In the earlier sections, it was shown that the suspension characteristics affect

the granule characteristics; hence the factors that are of importance will be discussed here.

2.11.1 *Effect of solid content*

The solid content of the slurry is the percentage of the ceramic with respect to that of the complete slurry. This can be expressed either in weight % or volume %. In a typical ceramic suspension, there are several ingredients, viz. the dispersing medium (typically water), dispersant, pH modifiers, binders, defoaming agents, etc. The solid content of the slurry can be found by evaporating off the water and burning away the organics at high temperatures. The ability of the organic additives to burn off completely without leaving any residue in the sintered body is one of the major considerations for advanced ceramics.

For spray drying of ceramic suspensions, a higher solid content slurry is preferred; this reduces the total amount of water to be evaporated and hence the operating costs due to energy consumption. As the amount of water to be removed is low, a higher production rate is achievable with a spray dryer of fixed evaporative capacity [79]. The increase in solid content of the starting suspension increases the granule density in spray freeze drying. However, the viscosity of the suspension increases as the solid content is increased. The particles are packed more closely in higher solid content suspensions, which in turn increases the particle–particle interaction. This hinders the pumpability and sprayability of the suspension. Therefore, the aim is to push the solid content to a maximum whilst the viscosity is still low enough to allow atomisation during spraying.

There is an inherent problem with the colloidal stabilisation of nanopowders when steric dispersants are used. The adsorbed molecules form a layer of a few nanometres thickness. For particles bigger than 100 nm, the volume increase associated with this is negligible, but it is significant in case of nanoparticles [117]. The estimated maximum vol % solids with a particle size D and adsorbed layer thickness δ is plotted in Figure 2-33.

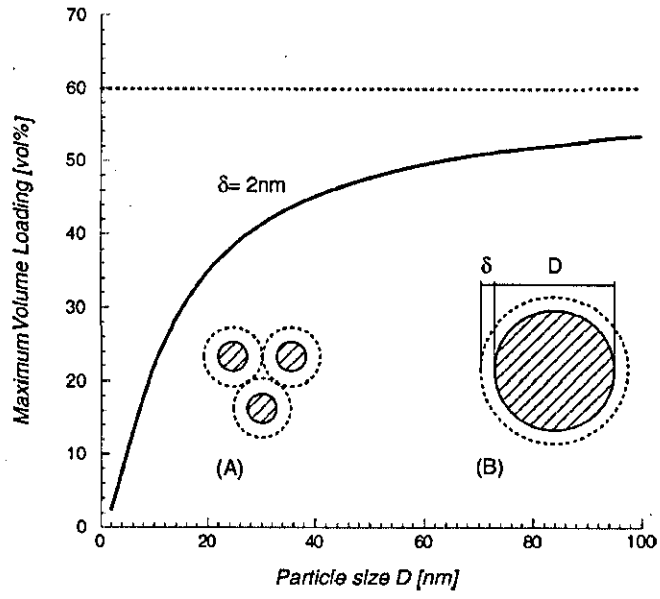

Figure 2-33 Maximum acheivable solid loading for small (A) and large (B) particles in suspension, after [117].

2.11.2 *Viscosity*

As shown in the earlier sections, the viscosity is one of the deciding factors for feasibility of the spray granulation operation. The particle size has a marked influence on the viscosity at a fixed concentration. For a fixed viscosity limit of 1 Pa s, the highest solid content was about 57, 53 and 46 wt. % for ZrO_2 with mean particle sizes of 2.78, 1.08 and 0.53 μm respectively [118]. Additionally, in the case of aqueous ceramic slurries, the rheological properties at a given solid content depend on the surface chemistry of the powder. Flocculated suspensions have a higher viscosity than the dispersed suspensions [119, 120] and are difficult to pump. Further, dispersed suspensions exhibit nearly Newtonian flow behaviour in contrast to the pseudoplastic behaviour of flocculated slurries [121]. The viscosity of the Newtonian fluid is constant and independent of the shear rate; in a pseudoplastic system, the viscosity decreases with increasing shear rate.

Ceramic particles in polar medium such as water are charged and may be colloidally stabilised by introducing repulsive forces between the particles. These forces can be either electrostatic, steric or electrosteric. The electrostatic forces between particles are caused by excess electric

charge on the particle surface. Steric stabilisation provides an alternative method of controlling the colloidal stability as the adsorbed organic molecules induce steric repulsion between the particles. Polyelectrolytes like the ammonium salt of poly acrylic acid and poly ethylene amine are examples of anionic and cationic electrosteric dispersants. The adsorption of dispersants on to the ceramic particle surface is pH dependant.

Cationic dispersants are effective in acidic pH whilst anionic dispersants improve suspension stability in the basic regime. Increase in the amount of dispersant reduces the viscosity to a given limit [122]. Addition of binders like poly vinyl alcohol (PVA) generally increases the viscosity and hence reduces the maximum usable solid content. Anklekar et al. [86] reported that the maximum solid content of pumpable alumina slurry was 50 vol% using tri ammonium citrate (TAC), against 40 vol% in the case of Darvan C. This can be explained on the basis of zeta potential and hydrodynamic radius of the particles as explained briefly in the following section.

Some dispersants work well with a given system whilst others do not [53]. A variety of reasons including the chemistry of the powder, surface characteristics, impurity levels, etc., affect the effectiveness and is beyond the scope of the current work.

2.11.3 Zeta potential

Zeta potential is the difference in the potential between the immovable layer attached to the surface of the dispersed phase and the dispersion medium. This arises from the surface charge on the particles. The latter may change as a function of pH where the oxide surface is generally hydrated.

$$MOH_2^+ \underset{pH < IEP}{\overset{H^+}{\rightleftharpoons}} MOH \underset{pH > IEP}{\overset{OH^-}{\rightleftharpoons}} MO^- + H_2O$$

where M stands for a cation such as Al^{3+}, Zr^{4+}, Y^{3+} or Si^{4+}.

At particular values of the pH the net surface charge is zero, it is known as the isoelectric point (IEP). Repulsive inter-particle potentials are needed to mitigate the attractive van der Waals forces. When the

positively or negatively charged polyelectrolyte is adsorbed on the surface of the particles, the zeta potential is altered and the IEP is shifted. The higher the zeta potential, the higher will be the stability and hence lower the viscosity [118, 123]. Near the IEP, the suspension is flocculated and hence the viscosity is higher. The particles are attracted to each other because of weak van der Waals forces. When such a suspension is granulated, the granule formation proceeds through floc rearrangement as opposed to primary particle rearrangement in case of well dispersed slurries.

Electrostatic dispersion of YSZ in acidic pH is risky as yttria dissolves in acidic solutions and destabilizes the colloid [123]. Therefore, stabilising with the use of anionic dispersants at high pH is the norm. Specific cases relevant to the current work are discussed here. Several researchers have reported the shift in IEP and magnitude of the zeta potential with the addition of dispersants. This is because the adsorbed ionic species alters the surface properties of the particles in the suspension. For instance, in Figure 2-34 it can be seen that the IEP shifts towards the acidic regime with the addition of poly methyl methacrylate. When cationic dispersants are used, the IEP shifts towards the higher pH [124].

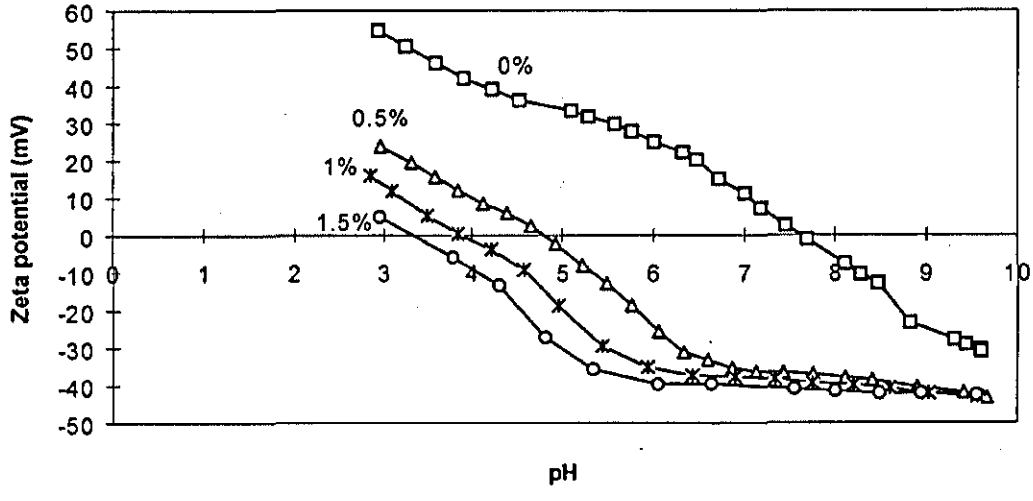

Figure 2-34 Zeta potential as a function of pH for different addition of dispersant (poly methyl methacrylate) given in wt% of dry powder, after [123].

The use of TAC to obtain high solid content zirconia suspension with low viscosity was reported by Ewais et al. [125]. The suspension was more stable in the basic pH as illustrated in Figure 2-35.

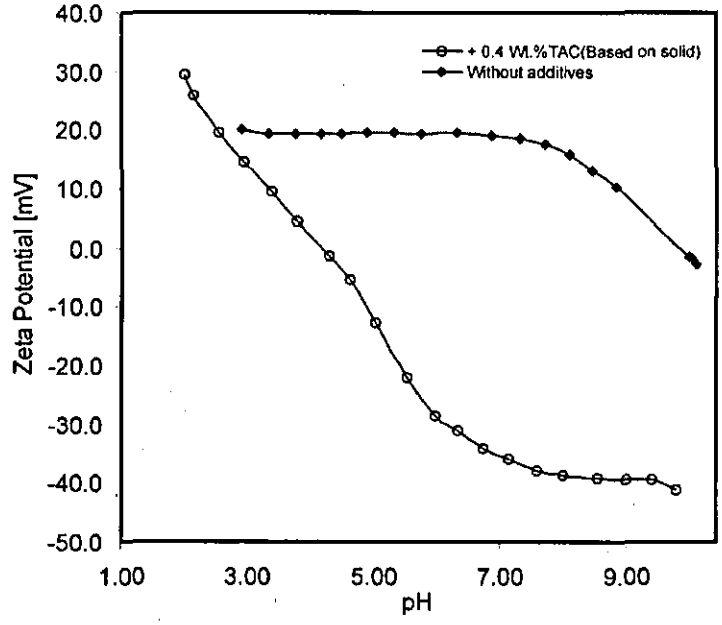

Figure 2-35 Zeta potential as a function of pH with and without the addition of TAC, after [125].

2.12 Relation between inter-particle force and flowability

The inter-particle attractive forces make the powder cohesive and adversely affect the flowability. The effect of inter-particle force on the angle of repose of spherical granular powder was studied by Forsyth et al. [126]. It was shown that the angle of repose increased approximately linearly with the increase in attractive interparticle force that was induced on spherical magnetic particles using a homogeneous magnetic field. Fine powders are always associated with poor flowability [127].

2.13 Impact of powder properties on compaction

The forces that hold the fine powders into specific shapes, say porous agglomerates or granules, are the inter-particle forces. These forces can be of different origin and can be either strong or weak. Forces

of physical origin, like the van der Waals forces, are considered weak. Solid bridges arising from hydroxide functional groups and polymer chains can lead to hard agglomerates. The granule strength arising from van der Waals forces can be calculated using Rumpf's theory (Equation 5) and Kendall's theory (Equation 6). It can be easily interpreted that the granule strength increases with decrease in the primary particle size and increase in the granule density.

In the case of nanopowders the agglomerate strength should be low to ensure that all the granules are crushed during the compaction stage and this demands a processing route where hard agglomerates are not formed at all. Powders with reduced granule density are likely to have a lower diametral compression strength. As the open structure in the granule readily crushes, it helps in eliminating the large, hard granule related pores in the sintered body [128].

2.14 Powder flowability

Powder handling is extremely important in a variety of industries such as the food, pharmaceutical, ceramic and metallurgic industries. Powder flowability affects various stages including blending, storage, feeding into the die and compaction. However, powder rheology is a less developed field as compared to liquid or suspension rheology. In ceramic die pressing, the powder flow characteristics decide the uniformity and reproducibility of the die filling process [129] and hence that of the final compacts. The effect is more important in the case of stepped dies.

2.14.1 The nature of powders

Powders behave like fluid in that they can take the shape of the mould in which they are introduced. Yet, they are rigid and can be compressed under the application of a load. A wide spectrum of internal and external factors can influence the powder flowability [130].

Internal factors:

- Particle size
- Size distribution
- Shape

- Surface texture
- Cohesivity
- Particle interaction
- Electro-static charges

External factors:

- Vibration
- Temperature
- Humidity
- Aeration
- Container surface effects
- Compaction condition due to handling and transportation

Poor powder flowability can result in hopper failure, a typical industrial scenario. Adsorbed moisture can lead to cohesive powders.

2.14.2 Measuring powder flowability

There is no universally accepted method for measuring powder flowability [131]. Each method has its own advantages and disadvantages. The most commonly used methods for powder flow characterisation are

- Angle of repose
- Flow through orifice
- Compressibility index and Hausner ratio
- Jenike shear cell tester
- Annular shear cell tester
- Aeroflow® equipment
- Helix method equipment
- Model Shoe - die filling

The flow behaviour of the same powder may differ depending on application. Therefore, each of the powder handling operation requires appropriate experimentation to characterise and predict actual powder flow behaviour in the equipment.

2.14.2.1 Angle of repose

The angle of repose defined as the angle to the horizontal plane of a conical pile of a powder, can be measured using a variety of different

techniques, Figure 2-36 [131 - 133]. In pharmaceuticals, this method is used to determine the influence of additives on powder flow. Cohesive powders pose problems in achieving a reproducible measurement of the angle of repose. Hence, samples with a varying, and known, ratio of free flowing to cohesive powder are made and the angle of repose is measured. Then, the data is extrapolated to 100% of the cohesive powder.

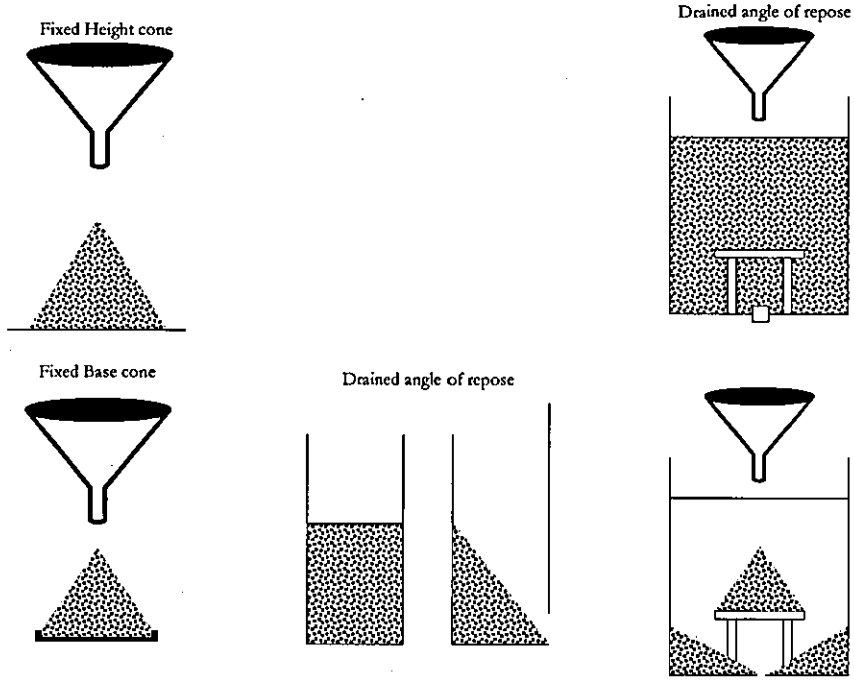

Figure 2-36 Methods of measuring angle of repose, after [132].

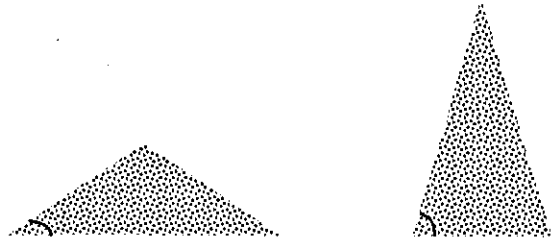

Figure 2-37 Powder with different flow properties have different angle of repose, after [133].

Powders with different flowability produce different cones. Powders with good flowability generally have a smaller angle of repose and poorly flowing powders have a greater angle of repose.

2.14.2.2 Flow-through-orifice

The flow-through-orifice technique is similar to that used for viscosity measurements of suspensions or liquids using the Ford cup. As in Figure 2-38, the Hall flowmeter has a calibrated orifice at the bottom through which the powder flows under gravity. The time required for the flow of a specific amount of powder is noted and the results are expressed in grams per second. This is applicable only for free flowing powders. Ceramic granules and metal powders are often characterised using this technique [134,135]. In some cases, the orifice diameter can be varied and the minimum diameter at which the sample freely flows under gravity is noted.

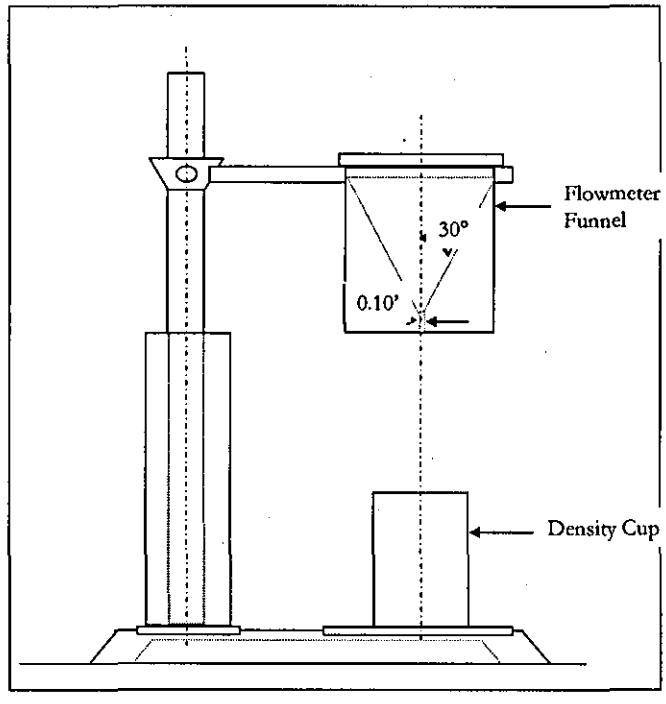

Figure 2-38 Hall flowmeter funnel, after [135].

2.14.2.3 Compressibility index and Hausner ratio

The relative magnitude of friction between particles in a powder mass can be estimated by the ratio of the tap density (D_f) to the apparent

density (D_o) of the powder. The ratio D_f / D_o is termed the Hausner ratio and is small for free flowing powders. The apparent density is the density of a powder after it is poured into a cylinder without applying any external force or vibration. The tap density is the density of the powder after tapping it until there is no volume change. The 'as synthesised' ceramic powders often have a higher Hausner ratio compared to spray dried powders, which have good flowability [136]. BS EN ISO 787-11: 1995 [137] gives the procedure for measuring the tap density. A schematic representation of the setup is shown in Figure 2-39. This method was compared with other commercially available techniques for assessing the flowability of porous and non-porous powders by Abdullah et al. [138]. A Hausner ratio of <1.2 generally represents a free flowing powder whilst values >1.5 represent poor flowability.

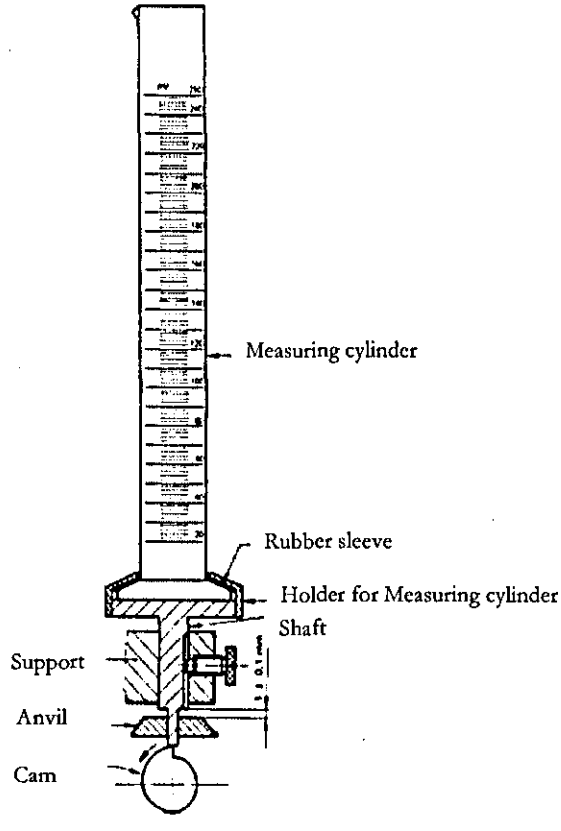

Figure 2-39 Tamping volumeter set-up, after [137].

The % compressibility of a powder is the measure of the potential powder arch or bridge strength, i.e the possibility of inconsistent hopper flow. It is derived from apparent density and tap density as follows:

$$\% \text{ compressibility} = \left(\frac{D_f - D_o}{D_f}\right) \times 100 \quad \text{..... (7)}$$

Carr developed a generalised relationship between % compressibility and flow description [133, 139] as in Table 2-1.

Table 2-1 Relationship between powder flowability and % compressibility after [133, 139].

% compressibility	Flow description
5 – 15	Excellent (Free flowing granules)
12 -1 6	Good (Free flowing powdered granules)
18 – 21	Fair (Powdered granules)
23 – 28	Poor (Very fluid powders)
28 – 35	Poor (Fluid cohesive powders)
35 – 38	Very poor (Fluid cohesive powders)
> 40	Extremely poor (Cohesive powders)

2.14.2.4 Jenike shear cell tester

The Jenike shear cell is the most widely accepted standard method in industry and research for measuring the cohesive properties of powders [131]. The instrument is used for direct shear tests, where the powder sample is consolidated in the vertical direction and then sheared on the horizontal plane. The equipment consists of a circular, open-ended shear box split horizontally; the base is immobile and the ring slides freely horizontally, Figure 2-40. The normal stress, N, is first used to consolidate the powder and then to load it during testing. After a predetermined consolidation time, the ring is pushed horizontally at a constant velocity to a final translation of 6 mm. Initially, the material deforms elastically and the shear force increases rapidly. Beyond a certain shear force, the material reaches a maximum elastic deformation and then the shear force

decreases while the material deforms plastically. The maximum shear force required to initiate movement is measured. The shear stress is the shear force per unit area needed to move the ring at a constant velocity while the normal stress is the force per unit area loaded. The shear stress / normal stress diagram is referred to as a Jenike yield locus. The diagram is useful in determining the flowability under free and forced flow conditions during the design of silos, Figure 2-41.

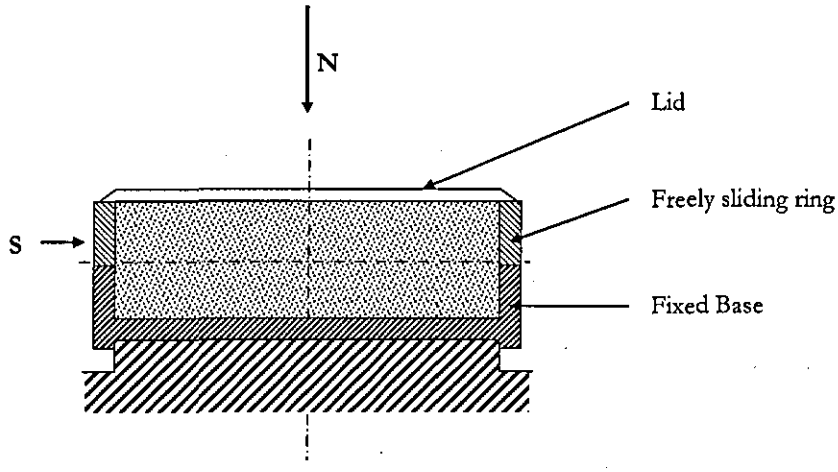

Figure 2-40 Schematic diagram of the Jenike Shear cell, after [131].

A modification of the Jenike direct shear cell tester by replacing the base with the silo wall material can be used to study the particle – wall friction behaviour. The friction decides whether the particles will slide over the wall surface (mass flow) or adhere to the wall and preferentially slide on itself (funnel flow) [140]. Funnel flow, Figure 2-42, leads to first in – last out, flooding and material consolidation.

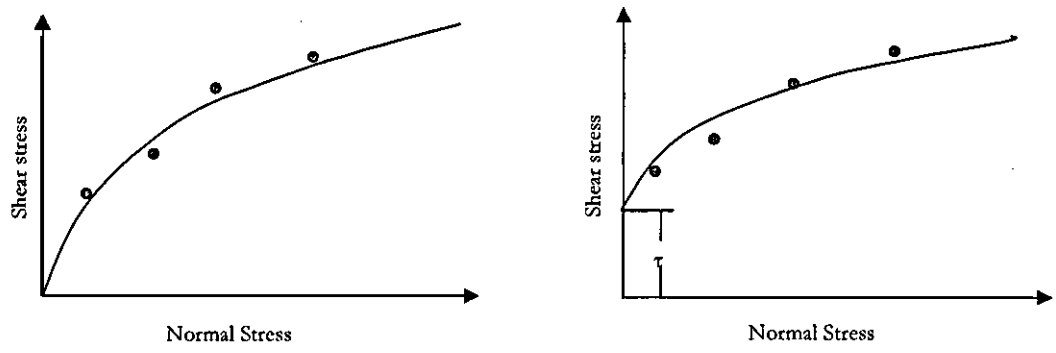

Figure 2-41 Jenike shear stress/ normal stress diagram for cohesive and non-cohesive powder.

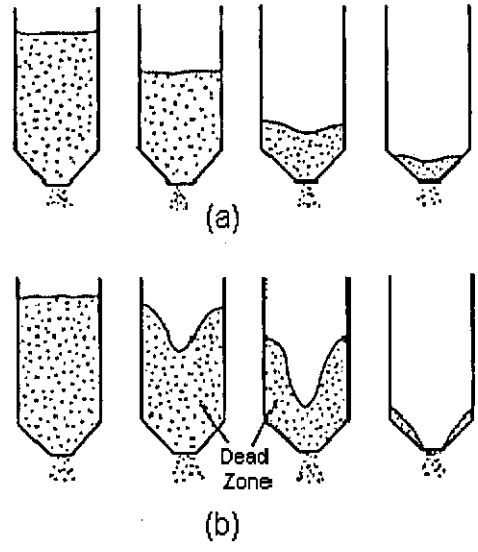

Figure 2-42 (a) mass flow and (b) funnel flow in silos.

2.14.2.5 Annular shear cell tester

The annular shear cell, also known as the rotational shear box is an alternative for the Jenike shear cell (translational shear box) for engineering design and is used widely. The shear stress is applied by rotating the top portion of the annular shear box, Figure 2-43 [132]. The advantages are (i) unlimited travel (as against 6 mm in the Jenike shear cell), (ii) easier sample preparation and (iii) a constant area of shear.

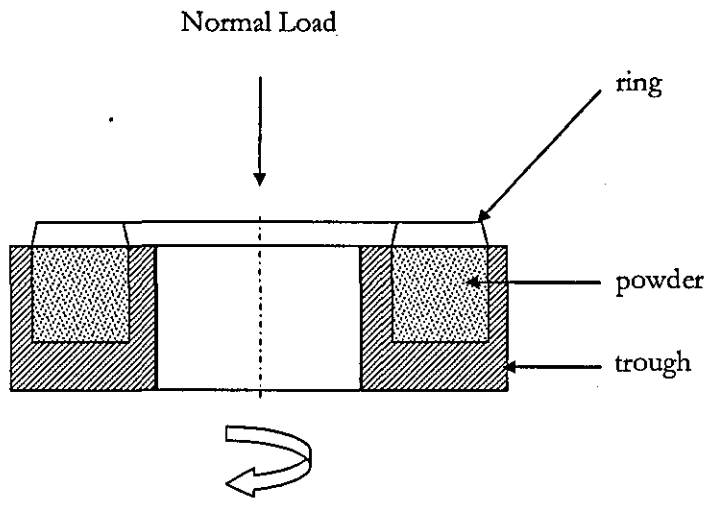

Figure 2-43 Schematic diagram of an annular shear cell.

2.14.2.6 Aeroflow® equipment

The aeroflow® is a commercial powder flow testing equipment that utilises deterministic chaos theory to analyse avalanching behaviour of the powder [141]. These avalanches exhibit a linear relationship dependant on the flowability of the powder. Being automated, the equipment reduces the chances of operator error to a great extent. The powder is placed in a transparent cylindrical cavity and rotated slowly. A light source is placed in front of the cylinder as showed by Figure 2-44 and a photodetector is set behind the cavity. The amount of light that can pass through the cavity and reach the detector is dependant on the avalanche built up on the cavity. The photodetector responds to the difference in the transmitted light by generating a voltage output proportional to the amount of light transmitted. A Phase Space Attractor map, Figure 2-45, is used to analyse the data. The effect of lubricants, particle size distribution, presence of fines, etc. can be assessed. Hancock et al [142] showed that this equipment can be used to compare powders having a wide range of flowability with good reproducibility.

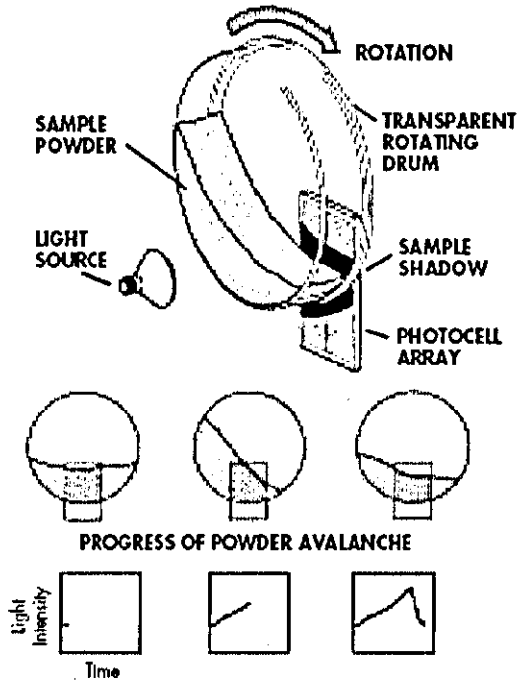

Figure 2-44 Schematic representation of Aeroflow powder flowability analyser, after [143].

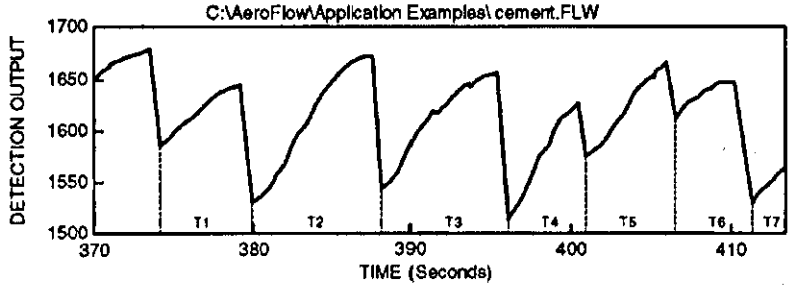

Figure 2-45 Phase Space Attractor map for powder flowability, after [143].

2.14.2.7 Helix method equipment

The helix method equipment measures the axial and rotational forces acting on a blade during the movement of a powder poured into a cylinder, Figure 2-46. The forces are used to determine the work done, or energy consumed, in displacing the powder. A preconditioning cycle can be introduced to the powders to remove the effects due to the history of the powder such as storage, handling etc. The effect of moisture and humidity can also be quantified using this method. Freeman et al [144] patented their powder rheometer that works on this principle recently.

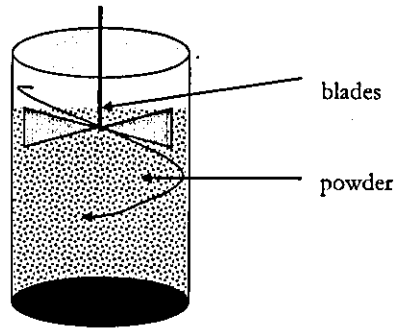

Figure 2-46 Schematic representation of powder rheometer [131].

2.14.2.8 Model shoe – die filling

The model shoe – die filling experiment is a replica of the most common configuration used in powder processing industries, Figure 2-47. The powder is placed in a rectangular shoe which traverses over a simple or stepped die. The shoe velocity is controlled through a pneumatic control unit. The filling rate and the filling ratio for different powders can be studied using transparent dies. The various parameters in this test are: (i) powder characteristics, (ii) shoe kinematics and (iii) die opening. The critical velocity is the maximum shoe velocity in which the die is completely filled with a given powder and die opening. For shoe velocities greater than the critical velocity, the die is partially filled, Figure 2-48. This can be used to find the filling rate in a shoe - die filling test. It has been shown that the powder filling rate can be enhanced by using vacuum suction in the die or vibration or aeration of the powder in the shoe. Very fine powders are displaced (chimney effect) during die filling by the entrapped air inside. This can be avoided by doing the experiments under vacuum.

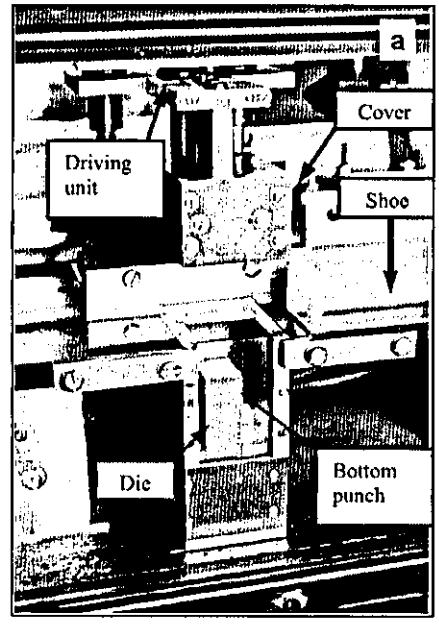

Figure 2-47 Experimental set-up for studying die fill, after [146].

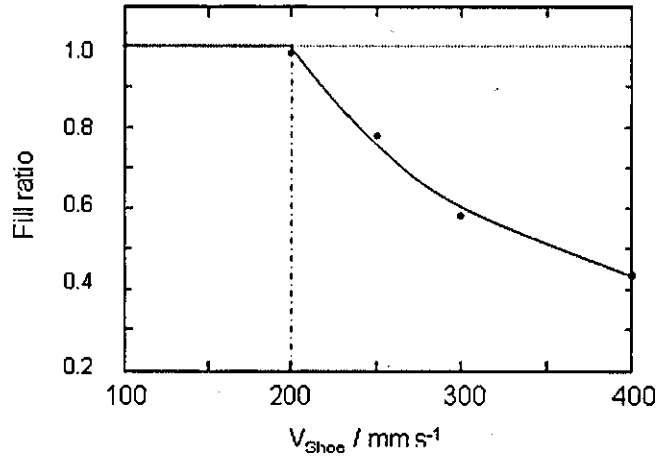

Figure 2-48 Filling ratio for Distalloy AE powder into a narrow cavity at various shoe speeds, after [145].

Wu et al [145] used high speed cameras to observe the die filling inside a simple and stepped die in air and vacuum. The model shoe – die set-up is probably the most suitable experiment for characterising powder flowability in the context of industrial die filling. Sinka [146] used a similar set-up to analyse the flow behaviour of different pharmaceutical powders. Jackson et al. [147] studied the effect of suction on the die filling properties and reported more than a two fold increase in the filling rate when suction was created by the downward movement of the lower punch. A comprehensive study on the flowability of a range of materials

including metallic, ceramic, hardmetal and magnetic powders was done by Schneider et al. [148]. This method has several advantages over the other methods. For example, the measurement of angle of repose is an empirical approach and cannot be used to assess the flow of powder in a bin or press. Further, it is inherently difficult to measure the angle of repose of cohesive powders. Shear cells are versatile in that they can be used to test a range of flowable and non-flowable powders. However, it is unclear if it gives details about the transient or dynamic flow of the powder [149]. The Hall flow meter is widely used, but the results are highly operator dependant unlike model shoe – die fill set up.

The schematic representation of powder flow into a die cavity from a shoe is shown in Figure 2-49. A series of events taking place as the shoe moves on top of the die can be seen. In this case, the shoe transverses from the right to left. As the edge of the powder bed reached the die opening, powder drops down into the die and start filling it. At this stage, the flow is characterised by what is called as 'nose flow' where relatively rapid filling of the die occurs, owing to the relatively easy escape of air from the die cavity. Due to inertia, it can be seen that the powder fills the left side of the die and then flow back into the opposite direction on collision with the wall. As the shoe continues to move, the entire die opening is covered by the sliding powder bed in the shoe. At this stage, the powder flow is called 'bulk flow' where the particles randomly detach from the bottom of the powder bed and fill the die. As powder level increase in the die, the air inside the die is pushed or displaced out. The increase in air pressure forces the air to flow through the powder bed and hinders the die filling. If the powders are light, they are carried away by the air stream escaping from the die. This effect is more pronounced in case of fine powders as coarse particles form a more porous powder bed in which air escape is relatively easy.

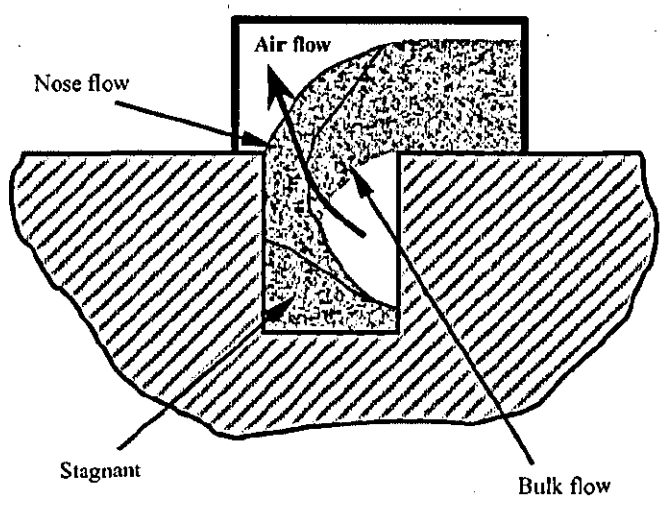

Figure 2-49 General representation of die filling pattern [145]

The mass flow rate into the die is a complex phenomenon and the flow can be predominantly nose flow or bulk flow depending on the shoe velocity. At low shoe speeds, the powder from the edge of the powder bed falls into the die and hence there are less chances of arching above the die cavity. In other words, nose flow is the predominant mechanism of die filling. As the shoe speed increases, the time available for nose flow is reduced and hence bulk flow could be the predominant mechanism. This was demonstrated using powder bed with a lower darker layer and filling the die at high and low shoe speeds by Wu et al. [145]. As a result, of two competing mechanism which describe the die filling, the equations that govern their filling are not linear, as described in the subsequent sections.

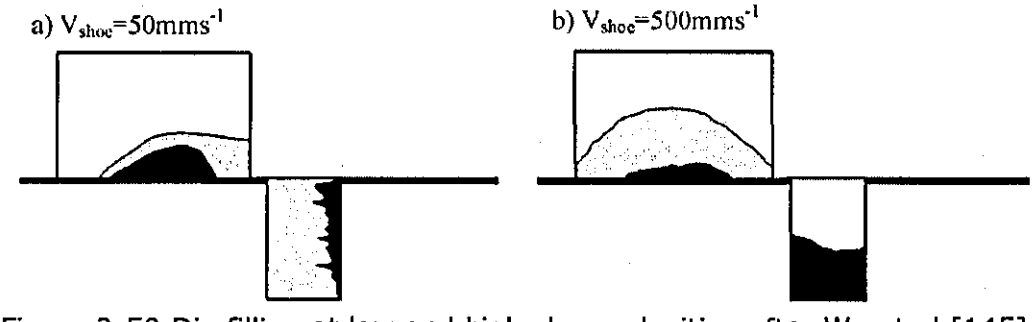

Figure 2-50 Die filling at low and high shoe velocities after Wu et al [145].

2.14.3 Critical velocity

Wu et al. [149] came up with the concept of critical shoe velocity for model shoe-die filling experiments. Critical velocity is defined as the

maximum velocity at which the die is completely filled by powder i.e., when the shoe speed is higher than the critical velocity, the die is partially filled.

According to modified Beverloo equation [149, 150] the hopper flow is given by

$$M = C\rho_0 (gD_H A^*)^{1/2} \qquad \text{Equation 1}$$

where M is the mass flow rate, ρ_o is the bulk density of the loosely packed powder, g is the acceleration due to gravity, D_H is the hydraulic diameter of the hopper opening (four times the cross-sectional area divided by the perimeter), A^* is the effective discharge area (actual cross-sectional area minus 1.4 x d x perimeter), d is the particle diameter and C is a dimensionless constant. The major difference between the hopper flow and the delivery from shoe is that C is not a constant, but a function of velocity. After analysing a wide range of powders [148], it was suggested that

$$C = C_O \left(\frac{V}{gD_H} \right)^{-m} \qquad \text{Equation 2}$$

where C_O is a constant.

Combining Equation 1 and 2 for a shoe of length L and die of depth H, the critical velocity is given by

$$Vc = (gD_H)^{1/2} \left(\frac{C_O L}{H} \right)^{1+m} \qquad \text{Equation 3}$$

At velocities higher than the critical velocity, incomplete filling is expected and the fill ratio, δ is given by

$$\delta = \left(\frac{Vc}{V} \right)^{1+m} \qquad \text{Equation 4}$$

2.14.4 Relevance of powder flow to die pressing

Uniform powder filling into the die is essential for obtaining green compacts [151] with minimal density gradients and uniform shrinkage

during sintering. The powder filling uniformity depends on the flowability of the powder.

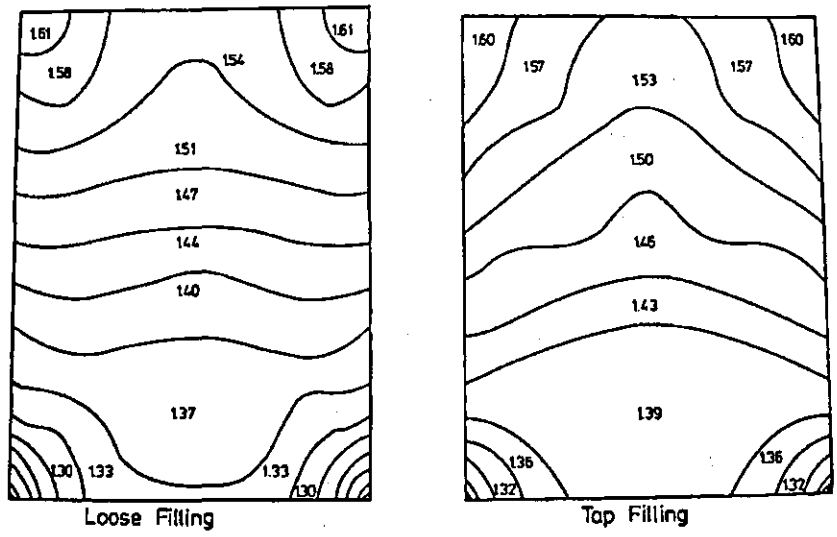

Figure 2-51 Influence of filling on density variations, after [151].

A free flowing powder fills the die cavity uniformly and allows rearrangement of the particles so that localised density variations are minimised.

2.15 Characterization of agglomerates

Ceramic nanopowders derived from aqueous routes inevitably have agglomerates. Despite the fact that the co-precipitation method yields agglomerated powders, it is the most widely used based on its commercial advantages. The forces binding the primary particles in a ceramic powder can be either strong or weak. The particles may be bound together because of weak van der Waals forces or by strong solid bridges. The solid bridges can be permanent (e.g., cementiceous bonds formed by solid bridges) or temporary (e.g., bonds made by a water soluble binder) [152]. In the liquid state, one can employ electrostatic or steric mechanisms to maintain powders in the unagglomerated state, but these mechanisms are ineffective in the dry state. The origin of hard agglomerates can be:

(i) The use of inappropriate binders, especially when the glass transition temperature of the binder is too high;

(ii) Cementation of the primary particles by hydrated phases;

(iii) Calcination at high temperatures, leading to the formation of strong solid bridges between the powder particles.

2.15.1 Importance

The presence of agglomerates reduces particle packing efficiency, suppresses sintering activity and finally deteriorates sintered properties due to the loss of microstructural homogeneity/integrity and crack-like void formation (strength limiting defects) [153]. The agglomerate strength and the deformation characteristics of the agglomerates are crucial in determining the flexural strength of the final component [154]. Staiger et al. [155] showed that the final density of gamma-alumina powder compacts improved from 74% to 99% of theoretical under identical consolidation and sintering conditions by simply attrition milling and eliminating the agglomerates.

The presence of organic additives (binders, plasticizers and lubricants) affect the deformation characteristics of the granules. For example, Shinohara et al [156] studied the effect of modifications to the dewaxing procedure, i.e. removal of binders from the sample for cold isostatically pressed alumina granules. Granules spray dried with PVA and wax as binders were consolidated using a die press at low applied pressure and then cold isostatically pressed (CIP) at higher pressures to prepare green compacts. Dewaxing, before sintering was done either immediately after die pressing or after CIPing. They observed that the sintered compacts made from samples that were dewaxed before CIPing had a finer pore size distribution and higher flexural strength than those which were dewaxed after CIPing. The significant variation in flexural strength was attributed to the granule deformation characteristics. According to the authors, in the sample dewaxed before CIPing the granules underwent brittle fragmentation into smaller particles whilst the other batch of granules underwent plastic deformation, resulting in larger pores and hence reduced flexural strength.

The agglomerate strength decides the compaction behaviour, sinterability, microstructure of the green and fired component and thereby

affects the performance of the structure. Despite the fact that fine powders are always in an agglomerated state, if the agglomerates can be fragmented under the application of a pressure during consolidation, then the compacted green body can yield good quality products after subsequent sintering. Hard agglomerates act as fracture initiating sites in ceramic bodies, whereas fine, fluffy powders can lead to handling problems and inconveniently low densities. Thus, there is a need to tailor the agglomeration state of the powder.

Agglomerates can be characterised by their geometrical and physical characteristics. The geometrical properties of the agglomerates, e.g. size and size distribution, can be characterised through a variety of techniques such as sieve analysis, light scattering, settling velocity and scanning electron microscopy, whilst the latter is the best approach for shape analysis. However, the decisive parameter in powder performance is the agglomerate strength.

2.15.2 Approaches for measuring agglomerate strength

Most of the approaches for characterising agglomerate strength in ceramic powders are indirect methods. The most widely discussed techniques by ceramicists are microstructural analysis using electron or optical microscopy, porosity measurement using mercury intrusion or nitrogen adsorption or small angle neutron scattering (SANS), estimation of granule strength from single granules or compaction curves and sintering curves. The techniques used in this study are microstructural analysis, mercury intrusion porosimetry (MIP), N_2 adsorption isotherms and compaction curves. Although there are other techniques, they are not discussed here.

2.15.2.1 Compaction curves

The particle and granule characteristics, pressing conditions and interparticle and particle – die interactions influence powder compaction. Applied pressure vs. compact density plots are often known as compaction response diagrams or compaction curves. These can be generated from the measured density of individual samples pressed at various pressures

[157] or by measuring the continuous change in density with pressing pressure [158]. It is possible to compare the agglomerate strengths of different powders by conducting this test under uniform and identical conditions for different powders. Thus, compaction curves can be a useful tool for quality control, to optimize pressing, evaluate different binder systems and the environmental effect on powders [159].

In a classical granulated / agglomerated powder, the compaction diagram shows three distinct regions, Figure 2-52 [160]. In region I, there is very little density increase with increase in applied pressure. The densification occurs due to granule rearrangement in this region. As the pressure is increased, there is a second linear region where the density increase is due to crushing of granules. In the third linear portion, the rearrangement of the fragments occurs and this response is similar to that of the ungranulated powder. The junction of the region I and region II is the breakpoint pressure where the granules start crushing down. After the joining pressure, intersection of the regions II and III, the granules loose their individual identity.

Compaction curves for zirconia powders processed differently show different compaction behaviour [161]. Water washed precipitates resulted in hard agglomerates whilst the initial granule crushing pressure was ~72 and ~60 MPa respectively for air calcined and hydrothermally crystallised powders, Figure 2-53. Weakly agglomerated powders had a low break point, ~40 MPa [162].

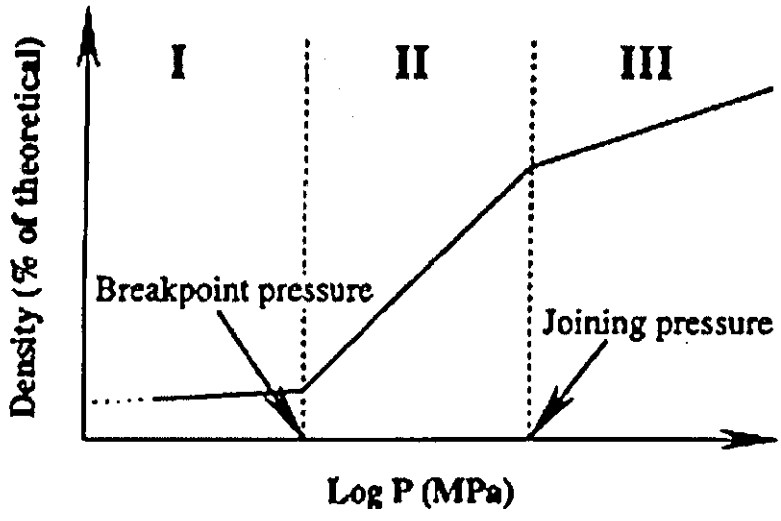

Figure 2-52 Typical compaction response for granulated powder, after [160].

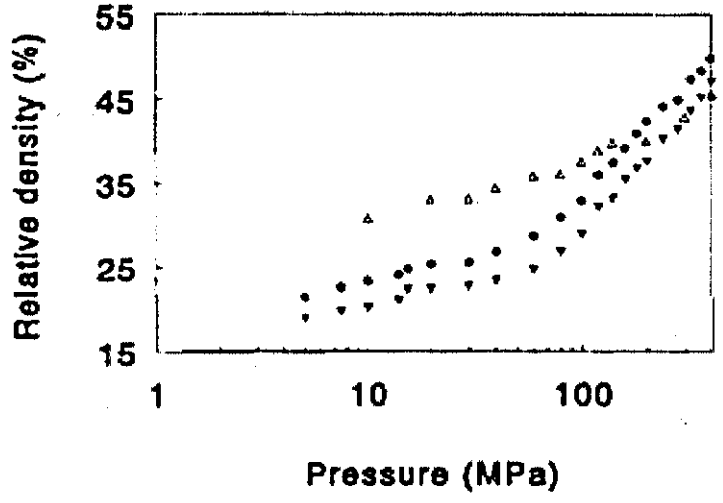

Figure 2-53 Compaction behavior of zirconia nanopowders: Δ water washed, ▼ air calcined and • hydrothermally crystallised, after [161].

A report by Walker et al. [163] on spray dried silicon nitride showed that hollow granules compacted better than the solid ones. The pressing efficiency was higher when NH_4-PAA was not used.

To obtain the true powder compaction response from in-die test data, elastic compliance of the punch and experimental setup must be accounted for in the analysis.

2.15.2.2 Pore size measurements

Pore size measurements using Mercury Intrusion Porosimetry (MIP) or nitrogen adsorption can give quantitative evidence about the presence of agglomerates in ceramic nanopowders. Agglomerated powders have a characteristic multimodal pore size distribution. A schematic representation of the origin of different kinds of pores in agglomerated powders is shown in Figure 2-54. The pore size distribution of powder with a primary particle size of about a few nanometres is shown in Figure 2-55. The peak at <50 nm corresponds to the inter particle/intra agglomerate pores. They are also called as the primary pores. The peak at less than 1 μm are the inter-agglomerate pores, i.e the pores formed between two agglomerates.

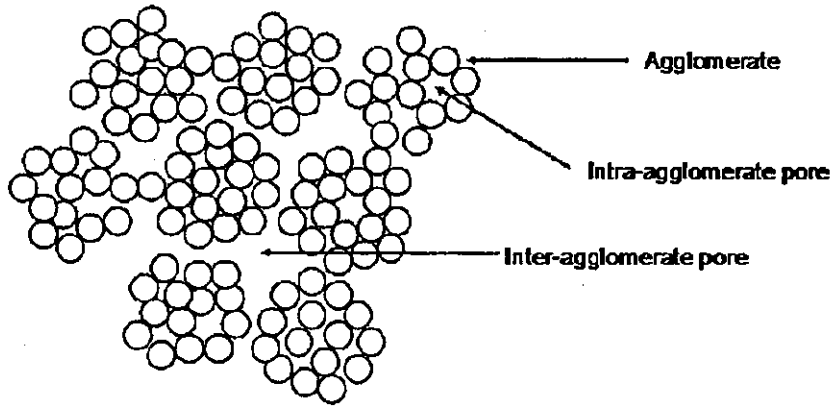

Figure 2-54 Schematic representation of agglomerates in powders.

The agglomerate strength is strongly dependant on the preparation procedure employed [164]. When the powder is compacted (either by uniaxial die pressing or isostatic pressing), the softer agglomerates crush and fragmentation occurs. The softer agglomerates are eliminated at lower pressures whereas the hard agglomerates remain intact even after the application of high pressures on the order of 500 MPa. Figure 2-56 shows the elimination of pores as pressure is applied to a weakly agglomerated powder. When a low pressure of the order of 50 MPa is employed, the agglomerates are not broken and the secondary, inter agglomerate pores are evident. When the pressure is increased to

100 MPa, the secondary pores are slowly eliminated. At 200 MPa, the agglomerates are completely broken down and the remaining porosity is because of the inter particle pores. As the pressure is further increased to 500 MPa, the pore size narrows down as the rearrangement of the fragmented particles is effected.

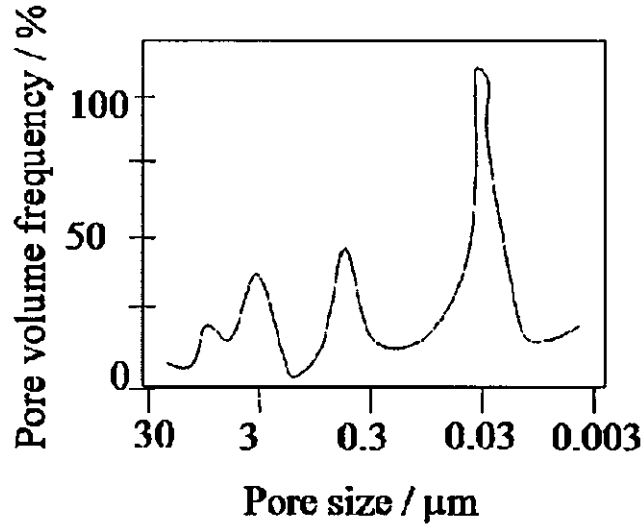

Figure 2-55 Typical pore size distribution in agglomerated fine ceramic powders.

Dúran [162] pointed out that control of powder synthesis and subsequent sintering is essential for achieving an ultrafine grained microstructure in high density ceramic components. They showed that weakly agglomerated nanopowders have a very fine, narrow pore size distribution when compacted, Figure 2-57. The primary particle size in their study was ~10 nm and the pore mode size was 6 nm. Homogeneously distributed pores in the green body are critical for achieving fully dense nanostructured ceramics with acceptable mechanical properties. Fully dense nanoscale ceramics with a grain size below 95 nm was obtained after sintering at 1200°C in their study.

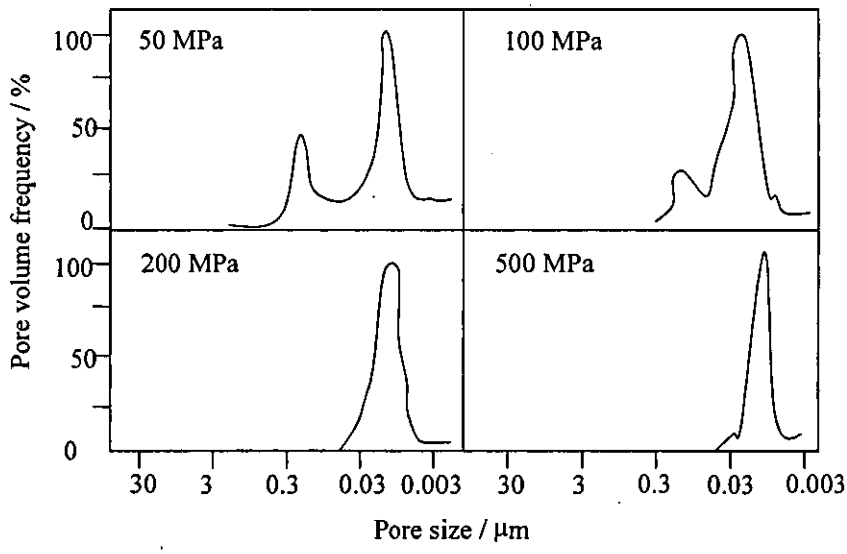

Figure 2-56 Pore size distribution in powder compacts pressed at different pressures from YSZ calcined at 600°C, after [164].

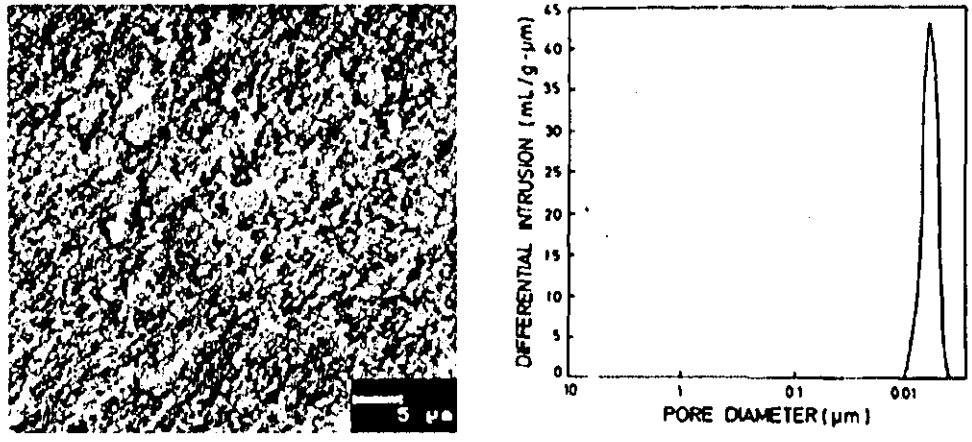

Figure 2-57 Microstructure of fracture surface and pore size distribution in weakly agglomerated nano Y-TZP, after [162].

Hysteresis in the nitrogen adsorption – desorption isotherm has been used to detect the presence of agglomerates formed by partial sintering or cementing of the nanoparticles [38]. Srdic et al. used the same technique for comparing the compactability and sinterability of nanosized zirconia prepared from different routes [165] whilst Tadokoro and Muccillo [166] used it for studying the pore size distribution after azeotropic distillation.

The two techniques extensively used in this thesis are nitrogen adsorption isotherms and mercury porosimetry; the physics of these two processes are detailed in Section 2.16 & 2.17 respectively.

2.15.2.3 Microstructure of green compacts

The granule strength decides the green microstructure formed at the end of cold compaction. Hard granules that resist deformation leave granule relics that are passed on to the subsequent stages of processing. Common microstructural defects from compaction are persistent large pores and poorly joined granule interfaces. These inhomogeneities in the green microstructure transform into strength limiting defects when sintered. The fracture is inter-granular in this case as presented in Figure 2-22 (a and b) and Figure 2-58.

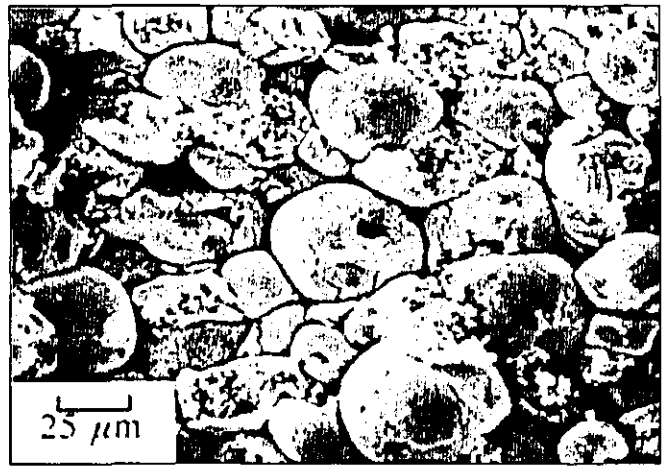

Figure 2-58 Fracture surface of hard spray dried granule compacts, after [79].

When the granules are soft and friable, a uniform microstructure is formed at the end of compaction as illustrated in Figure 2-22(d) and Figure 2-57. With the aid of a high refractive index liquid, the microstructure and the persistence of granular relics have been studied [167, 168]. The visual observation had a quantifiable correlation to the flexural strength of the sintered compacts [169]. Hence, the benefits of observation under a microscope should not be underestimated.

2.15.2.4 Density of green compacts

Green density is one of the most important parameters in the forming of ceramic articles. For a given ceramic powder, a higher green density indicates better packing and results in less shrinkage during sintering [170]. Large voids may be created when hard agglomerates are present. Inter-agglomerate voids tend to reduce the density of the green compacts. When dispersants and binders are added, a lower green density is observed owing to the lower density of the organic phase.

2.15.2.5 Sintering behaviour of agglomerated powder compacts

Sintering is the process of pore elimination and densification at high temperatures. For a given powder, the sintering kinetics are affected by the agglomeration state [155]. A systematic study of the sintering behaviour of zirconia powders with different levels of agglomeration was done by Liu et al. [171]. They proved that highly agglomerated powders sintered to lower final densities and grain coarsening started earlier. This is because of the heterogeneous microstructure and multimodal pore size distribution. In conventional sintering, pores smaller than a critical size shrink, whilst larger pores grow. A higher temperature or longer sintering duration is needed to achieve dense products [172] though at the expense of greater grain growth. To summarise, when powders with varying levels of agglomeration are processed under identical cold compaction and sintering conditions, the final sintered density is generally inversely proportional to the agglomerate strength.

2.16 Nitrogen adsorption Isotherms

When a gas or vapour is brought into contact with a solid, part of it is taken up by the solid. The molecules that disappear from the gas either enter the inside of the solid, or remain on the outside attached to the surface. The former phenomenon is termed absorption (or dissolution) and the latter adsorption. When the phenomena occur simultaneously, the process is termed sorption. The solid that takes up the gas is called the adsorbent, and the gas or vapour taken up on the surface is called the

adsorbate. Nitrogen is the most commonly used adsorbate for finding pore size distribution in ceramic powders.

The adsorption is dependant on the gas pressure and temperature and is reversible. The progressive formation of adsorbed layers with gradual increase in the gas pressure under isothermal conditions in a typical mesoporous ceramic surface can be visualised as shown in Figure 2-59. Mesopores are defined as pores ranging between 2 to 50 nm in width/diameter.

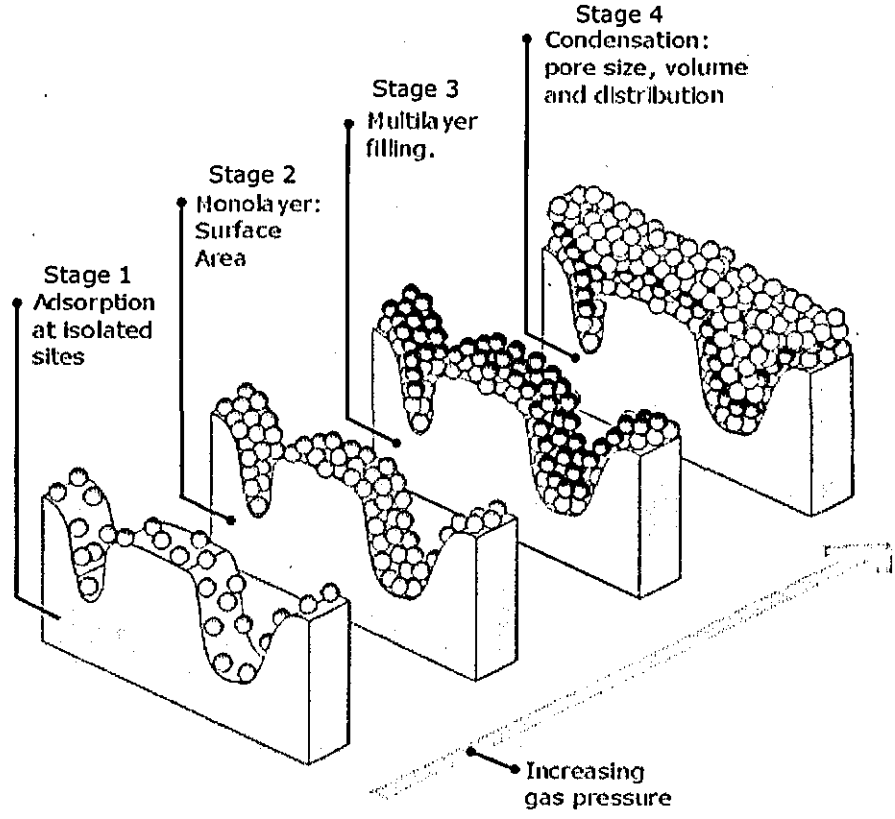

Figure 2-59 Progressive filling of pores with increasing gas pressure, modified from [173].

2.16.1 Types of isotherms

Adsorption isotherms are conventionally plotted as relative pressure, p/p_o (x-axis) versus amount adsorbed, $cm^3\ g^{-1}$ (y-axis), where p_o is the vapour pressure of the gas at the sample temperature and p is the absolute pressure inside the sample chamber. Depending on the surface characteristics the plot can have different shapes which normally fall under one of the six types shown below [174]. Type I corresponds to

microporous materials. Type II and Type III are characteristic of non-porous materials. The difference in shape (amount of adsorption) originates from the adsorbent-adsorbate interactions. Mesoporous surfaces exhibit a hysteresis loop as in Type IV and Type V, Figure 2-60. Type VI isotherms can occur only on extremely homogeneous surfaces where adsorption of the second layer happens only after the complete formation of first layer and so forth.

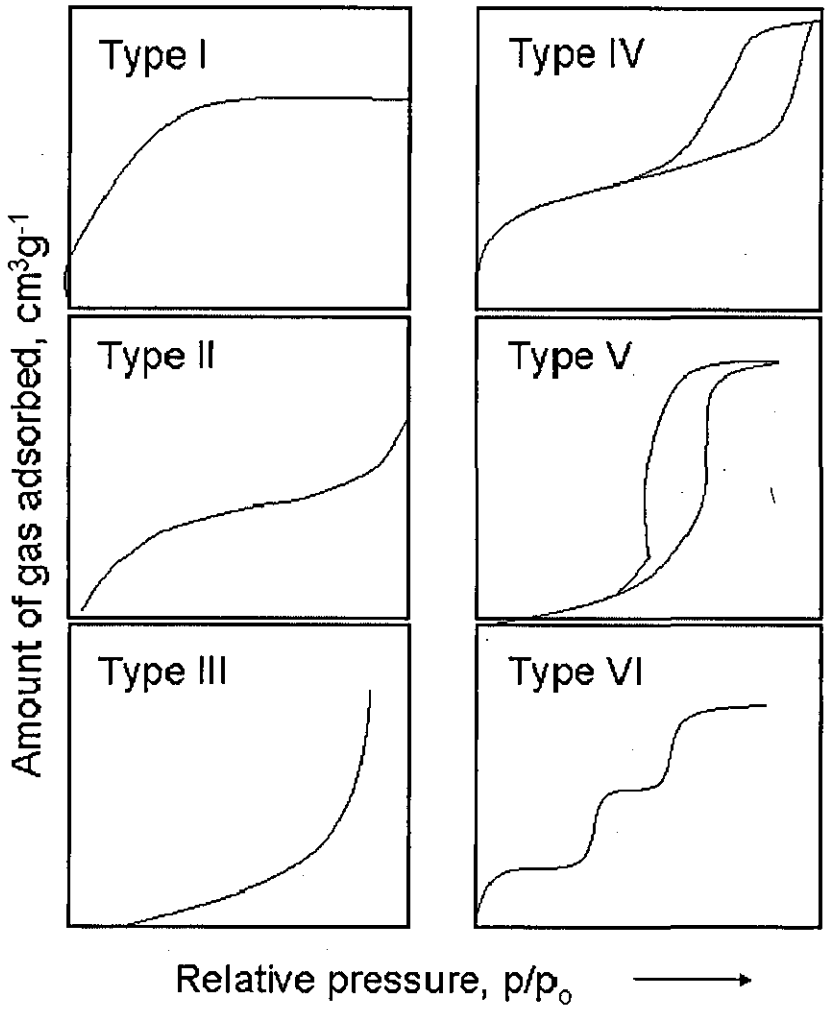

Figure 2-60 Types of adsorption isotherms according to IUPAC.

The ceramic materials used in this study had a Type IV isotherm and this is discussed in detail in the latter sections. The important information that can be obtained from isotherms are surface area and porosity of the material under consideration.

2.16.2 BET analysis

Brunauer, Emmett & Teller put forward a theory to derive the surface area from adsorption isotherms. Between p/po range of 0.05 to 0.3, the adsorption behaviour can be statistically converted into monolayer coverage using the BET equation given below.

$$\frac{x}{x_m} = \frac{c(p/p_o)}{\{1-(p/p_o)\}\{1+[c-1](p/p_o)\}} \quad \text{..... (8)}$$

where c is a constant that depends upon the adsorbate, adsorbent and temperature, x is the volume of gas adsorbed per gram of material and x_m is the amount of gas corresponding to 1 monolayer on solid surface. The area of cross section of N_2 molecule is 0.162 nm and the surface area of the sample, S_{BET}, can be deduced from the volume of monolayer N_2 adsorbed obtained from the BET equation.

The average particle size, d_p can be estimated from this surface area using the following expression:

$$d_{pBET} = \frac{6\times10^3}{\rho S_{BET}} \quad \text{..... (9)}$$

where ρ is the density of the material.

2.16.3 Kelvin's equation

Mesoporous solids with high 'c' constant values exhibit Type IV isotherms. The increase in adsorbed volume at higher p/p_o is caused by capillary condensation below the expected condensation pressure of the bulk of adsorbate. Capillary condensation is a secondary process that requires the preformation of an adsorbed layer on the pore walls formed by multilayer adsorption. Both processes generally occur simultaneously in the region of 0.3 to 1 p/p_o [175]. The curvature of the meniscus present in a pore to the p/p_o value associated with condensation is given by Kelvin's equation as follows:

$$r_K = \frac{-2\sigma v_l}{RT\ln(p/p_o)} \quad \text{..... (10)}$$

where r_K is the Kelvin radius, v_l the molar volume of the liquid condensate, and σ the surface tension of the liquid condensate. The pore radius of a cylindrical pore is deduced from the Kelvin radius and the film thickness of the adsorbed multilayer, t, as shown below

$$r_p = r_K + t \qquad \text{..... (11)}$$

where r_p is the pore radius and t is the statistical thickness of the adsorbed film. Values for t can be derived from standard isotherms. The mesopore size distribution can be calculated using the computational methods based on the BJH model by Barrett, Joyner and Halenda [176].

From the Kelvin equation (10), it can be inferred that the condensation occurs in the finer pores at low gas pressures. In the adsorption leg of the test, as the gas pressure is increased incrementally, condensation occurs at pores of relatively larger radius (still within the mesoporous range). The pore coarsening during calcination of nanopowder was reported by Hung et al. [177]. Intuitively, the hysteresis loop shifts towards the high pressure range with increase in calcination temperature as in Figure 2-61.

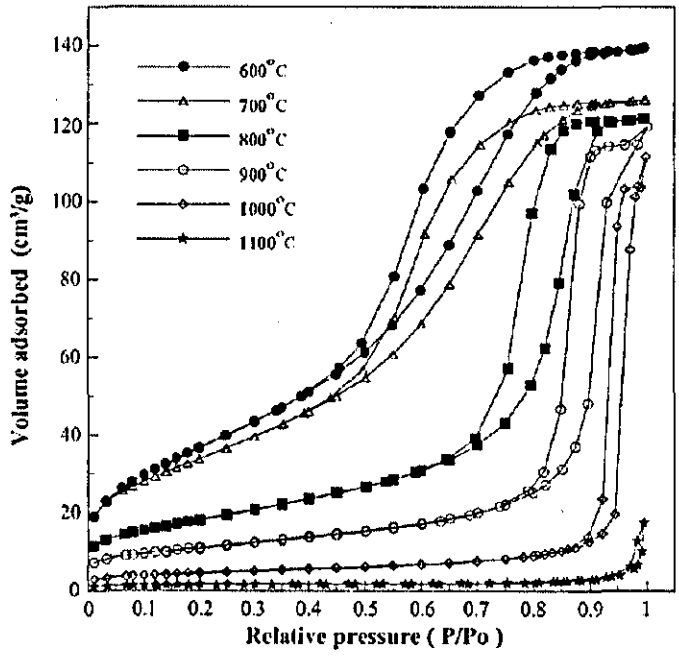

Figure 2-61 Nitrogen adsorption/desorption isotherms for YSZ powders calcined at different temperatures, after [177].

Pores of size up to around 200 nm can be found using this technique. The difference in the porosity from geometrical measurement of the sample density and the cumulative porosity from nitrogen adsorption isotherms can be used to estimate the volume of pores having size greater than 200 nm [178].

2.17 Mercury intrusion porosimetry

Mercury intrusion porosimetry enables determination of pore size distributions in the macropore range, where the gas adsorption method breaks down. Since the contact angle of mercury with solids is ~130°, an excess pressure Δp is required to force liquid mercury into the pores of a solid. Therefore, the technique of mercury intrusion porosimetry essentially consists of measuring the extent of mercury penetration into an evacuated solid as a function of the applied hydrostatic pressure.

The Washburn equation can be used to calculate the radius of the cylinderical pore, r_p as follows

$$r_p = \frac{-2\gamma\cos\theta}{\Delta p} \qquad \text{..... (12)}$$

where γ is surface tension and θ is the angle of contact. The most commonly used values are 484 mN m^{-1} for surface tension and 130° for θ.

Different researchers have used values ranging from 130 to 150° for θ. The contact angle of the mercury also depends on whether it is advancing over, or receding from, the solid surface. The values of r_p can vary by many per cent depending on the value of θ that is used as shown in Table 2-2. Shi et al. [164] used 130° in their work with super fine zirconia powder compacts and this value is used in this thesis.

Oya et al. [179] studied the effect of mercury intrusion on the original pore structure. They concluded that the high pressure applied during intrusion does not alter the original pore structure by conducting systematic studies on green samples with binder, after dewaxing and calcination.

Table 2-2 Effect of the value of the contact angle θ of mercury on the calculated value of pore radius at different values of applied pressure ΔP, after [174].

Pressure (atm)	Pore radius / Å		
	θ = 130°	θ = 140°	θ = 150°
1	60.9×10^3	72.6×10^3	82.1×10^3
2	30.5×10^3	36.3×10^3	41.0×10^3
10	6090	7260	8210
100	609	726	821
200	305	363	410
500	122	145	164
1000	61	73	82
2000	30	36	41

A serious set back in using mercury porosimetry is that the sizes of the entry passageways are obtained rather than actual pore sizes, causing errors in the case of inkbottle shaped pores [163]. According to Zheng's publication [180], erroneous results are likely when large pores contribute <10% of the compact's porosity. In such a case, the large pores can possibly be entrapped inside the compact and isolated, i.e. connected to the external surface only through particle-particle channels which act as throat or neck, regulating the mercury intrusion. Under these circumstances, high pressure corresponding to fine porosity may be needed to intrude and fill these pores. This can result in the observed pore size distribution skewed towards the smaller pore size.

2.17.1 Comparison of pore size distribution by MIP and nitrogen adsorption isotherms

Tristar™ is a commercial surface area analyzer which can measure the BET surface area, and micro- and meso- pore size distribution. Micro-porosity in the range of 0.35 nm to 2 nm is not considered in this study. The mesoporous range detectable by using the BJH method based on Kelvin's model is valid from 2 nm to ~100 nm pore radius. Above this

limit, the control of the gas pressure becomes practically difficult and flooding was often observed. Mercury intrusion porosimetry is effective in the range between 3 nm to 6 μm. Beyond these limits, the values obtained from these techniques become increasingly uncertain. Rigby et al. succeeded in integrating Hg intrusion porosimetry and N_2 sorption to find the pore size distribution in catalyst supports having a wide pore size distribution [181, 182].

In general, both these techniques are used complementary to each other. An overlap is generally expected in the range that is common between these two techniques. However, several researchers have found that there can be significant differences between the distributions as calculated from these two techniques for various reasons [183]. The distribution obtained from mercury intrusion is influenced by the channel effect. Due to the sequential nature of porosimetry, some pores are not measured at their corresponding pressure until mercury reaches there through one of the largest accessible throats at a given pressure [184]. A continuum of mercury is essential for the pore to be filled. On the other hand, the small size of the nitrogen molecules enables it to reach all the mesopores. Pore filling by condensation occurs instantaneously once the gas pressure reaches the value corresponding to the pore diameter. In short, nitrogen sorption based porosity measurement is free of 'shadowing' effects.

2.18 Objectives of the present work

Nanoparticles with potentially extremely useful properties are now being made worldwide, sometimes in large quantities. However, the production of nanostructured engineered components is still a major challenge. This work aims to investigate and improve the processability of nanopowders by die pressing with a view to achieving homogeneous and uniform green bodies of high density. One of the reviews [4] remarks that the scientific emphasis has been on improving performance of engineering ceramics whereas the technical difficulty lies in the handling of nanoscale powders.

Wet synthetic routes still remain as the most efficient method to prepare nanoscale powders [185]. This inevitably results in agglomerated powders on drying. Dry attrition milling can break down the agglomerates if they are soft. However, the end product of milling is fluffy and exhibits poor flowability. This powder cannot fill the die reliably and hence the green compacts formed from these powders on an industrial scale is prone to have defects and inconsistencies. Controlled agglomeration with tailored agglomerate size, shape and strength is the key to success. The agglomerate should essentially have excellent flowability, uniform die filling characteristics and above all, the ability to crush down into primary particles when die pressed.

This work aims in identifying and optimising a suitable granulation technique for an yttria stabilised zirconia nanopowder. To circumvent the problems associated with industrial mass production of die pressed components using submicron powders, spray drying is commonly used. The same technique can be applied for nanopowders. Spray freeze drying is another granulation technique which has been found to be useful during the course of the work. Both spray drying and spray freeze drying are studied in this project.

After granulation, the powders are characterised for their suitability. Flowability and crushability are studied using various techniques. The ability of the granules to form a uniform green nanostructure has been evaluated. To the best of the author's knowledge, this is the first work carried out on spray freeze drying of high solid content suspensions with a primary particle size less than 30 nm. In both the spray granulation techniques under consideration, increasing the solid content of the starting suspension reduces the amount water to be removed and, as a result, reduces the operating costs. For example, increasing the starting solid content from 50 wt% to 75 wt% triples the amount of powder produced [79] while the amount of water removed remains same.

Apart from powder flowability and crushability, the third parameter of interest is the fill density of the granules. Higher granule density is often associated with better flowability in gravity fed systems. High fill density is also favoured as faster production rates as possible when the

compaction ratio is reduced. In the case of spray freeze drying, the bulk density almost doubles when the starting solid content increases from 50 wt% to 70 wt%.

Examination of the published work indicates a clear gap in the literature. Whilst many of the publications point out the disadvantages associated with formation of hard agglomerates in spray drying, few have investigated the advantages of controlled agglomeration using spray freeze drying. However, low fill density was invariably reported in almost all literature concerning spray freeze dried nanopowders. A systematic study of the effect of solid content of starting suspension on the SFD granule characteristics has not been done so far. These issues are addressed in the current work.

In an industrial context, YSZ is one of the most widely used ceramics, with excellent mechanical properties and ion conduction characteristics. Generally, 3 mol% yttria stabilised zirconia is used for structural applications and 8 mol% yttria stabilised zirconia has maximum ionic conductivity. The fundamental properties which make zirconia an interesting candidate are [186]:

- High strength
- High fracture toughness
- High hardness
- Wear resistence
- Good frictional behaviour
- Non-magnetic
- Electrical insulation
- Low thermal conductivity
- Corrosion resistance in acid and alkali
- Modulus of elasticity similar to steel
- Co-efficient of thermal expansion similar to steel.

This knowledge gained in this study will be applicable to optimise the processing conditions in an industrial scenario.

Chapter 3

Experimental

All the key experiments were designed having in mind the final product – a free flowing, crushable, reasonable high fill density granule from nanometric YSZ suspension.

3.1 Suspension preparation and characterisation

A well dispersed suspension of 3 mol% yttria stabilised zirconia with an average particle size of ~20 nm was supplied by MEL Chemicals, UK. According to the manufacturer, it had ~26 wt% (5.5 vol%) zirconia in water and no other additives. The pH was between 2 to 3. The technique for making high solid content suspensions was developed by co-workers within the group [186]. To prepare high solid content suspensions from the as-received suspension, the pH was initially changed using tetra-methyl ammonium hydroxide (TMAH) procured from Aldrich Chemicals Ltd., Dorset, UK. When the pH has reached a value of ~10, Dispex A40 from Allied Colloids, Bradford, UK or tri-ammonium citrate (TAC) from FSA Laboratory, Loughborough, UK was added as the dispersant. Dispex A40 is a solution of ammonium salt of an acrylic polymer in water. The active material is 43% by weight. Typically 1.5 wt% of active material of Dispex A40 or 2.5 wt% of TAC with respect to zirconia was used and a pH of 9 to 11 was found to be suitable for these anionic dispersants to be effective. After adding appropriate amounts of the pH modifier and dispersant, the suspension was heated gently at 60°C in a water bath until the solid content of the suspension reached the desired value. Throughout the concentration process, the suspension was kept under vigorous stirring to maintain homogeneity.

After the suspension had reached the desired solid content, ultrasonication with an amplitude of 12 μm was used to break down any agglomerates into primary particles. Typically a 2 minute ultrasound for

every 30 ml of the suspension was found to be sufficient. Soniprep 150 (MSE Scientific Instruments, Manchester, UK), a commercial ultrasonic disintegrator with an ultrasonic frequency of 23 kHz and maximum power of 150 W, was used for this purpose. The viscosity of the suspension was required to be lower than 1 Pa s to be able to spray the suspension.

The Soniprep 150 transmitted sound energy to the medium through high frequency vibration at the tip of an interchangeable probe. The effect of this was to create many micro-cavities in the dispersion medium. The rapid alternation of positive and negative pressure produced by the sound waves travelling through the liquid caused these minute gas filled bubbles to disintegrate implosively during the rarefaction phase of the sound pressure wave. This produced intense local shock waves in which the pressure may have reached several thousand atmospheres and rapid microstreaming of the liquid will have occurred around the point of collapse. The intense localised sheer gradients so generated combined, in part, with the transient regions of high pressure, resulted in the agglomerate-disruptive capabilities of this instrument.

3.1.1.1 Determination of solid content of the suspension

The YSZ content of the suspension was calculated from the weight loss on heating to 700°C. The heating and the cooling rates were 5°C/min. Thermogravimetric analysis was carried out on one representative suspension to study the weight loss behaviour on heating.

$$Weight\ \%\ of\ YSZ = \frac{Weight\ of\ powder\ after\ heating\ to\ 700°C}{Weight\ of\ initial\ suspension} \times 100$$

3.1.1.2 Zeta potential measurements

The electrokinetic behaviour of the suspensions were characterised using an AccoustoSizer II. This equipment facilitates automatic measurement of zeta potential over a wide range of pH from 2 to 13. Dilute suspensions with 5 wt% zirconia were used; pH modifying agents were dosed in small quantities to achieve any desired value. 0.1 M HCl/NaOH solution (Fischer, UK) were used for decreasing/increasing the

pH respectively. An equilibration time of 180 seconds was used to ensure that the pH modifier was mixed homogeneously within the system before every zeta potential measurement at different pH.

As a general practice, the pH was incrementally taken to the nearest extreme and then traced back to the other extreme pH in small steps where the zeta potential measurement was required. For instance, the suspension without any dispersant had a natural pH of 2 to 3. Therefore, the pH was slowly increased to 11 and zeta potential data was collected at regular intervals. Since the nanosuspension containing TAC or Dispex A40 was dispersed at pH 9 to 10. In this case, the pH was increased to 11 in one leg and then reduced in steps to about 2 to yield the zeta potential curve.

3.1.1.3 Viscosity measurements

Suspension flow behaviour was monitored using a Bohlin Visco 88 viscometer (Bohlin Instruments UK, Cirencester, UK), a controlled speed device that measures shear stress and viscosity as a function of shear rate. A concentric cylinder (C30) measuring system was used. About 20 ml of the suspension was needed for each test and a 30 second ultrasound treatment was used before testing. The slurry was presheared for 60 seconds at 100 s^{-1} to neutralise any effects due to suspension storage. Viscosities were recorded in a sweep cycle of continuous increasing and then decreasing shear rate ranging from 56 s^{-1} to 1000 s^{-1}. All measurements were carried out at room temperature; three trials were carried out for each suspension.

3.1.1.4 Thermogravimetric analysis

The weight loss from the suspension over a temperature range from 25°C to 700°C was studied using a thermogravimetric analyser (TA Instruments Inc., Delaware, USA) at a heating rate of 10°C per minute.

3.2 Powder preparation

Powders were obtained by drying well dispersed suspensions; oven drying, spray drying and spray freeze drying were done as explained in the subsequent sections.

3.2.1 Oven drying

Oven dried powder was obtained by drying the as-received suspension in a glass tray at 60°C for 48 hours. After drying, the flaky powder was collected and micronised for 4 minutes in a micronising mill (McCrone Scientific, London, UK).

3.2.2 Spray drying

Spray drying of two dispersed suspensions were carried out at MEL Chemicals Ltd., Manchester, UK in a Niro spray dryer with a rotary atomiser with the inlet and outlet stream temperatures maintained at 210°C and 120°C respectively. The hot air and the suspension were fed cocurrently from the top of the chamber. The inlet air pressure was maintained at 5 bar and the liquid flow rate was controlled using a peristaltic pump. The two suspensions used were (i) as-received nanosuspension of YSZ having 5.5 vol% solids supplied by MEL and (ii) a 14.3 vol% YSZ suspension stabilised with an electrosteric dispersant (Dispex A40). The dried powder was collected from the outlet stream using a filter bag arrangement and the hot air escaped out through the exhaust.

3.2.3 Spray freeze drying

The SFD powder was prepared by spray freezing an aqueous suspension into liquid nitrogen followed by drying the frozen granules in a freeze dryer. Thus, it necessarily involves

(i) making well dispersed aqueous suspensions with the required solids content (Section 3.1)

(ii) spray freezing the suspension to form frozen granulates of the required size (Section 3.2.3.1),

(iii) removing the water from these granules by sublimation (Section 3.2.3.2) and

(iv) sieving the dried granules to remove the fines and big agglomerates (formed by suspension which was not atomised properly), Section 3.2.3.3. The yield on sieving was about 75% of the total dried powder.

3.2.3.1 Spray freezing

Ultrasonic atomisation was used to spray the high solid content suspensions on to liquid nitrogen. The suspension was slowly delivered on a vibrating ultrasonic horn (Soniprep 150, MSE Scientific Instruments, Manchester, UK) using a plastic pipette. The ultrasonic frequency was 23 kHz and amplitude maintained at 12 μm. Due to the high frequency agitations, the liquid that was fed in to the horn was broken down into fine droplets and ripped into finer fragments. The distance between the ultrasonic horn and the liquid nitrogen was 15 cm. This height was found be sufficient for the droplet to become spherical. The droplet size depended on parameters including solid content and viscosity for a given frequency [188]. The distribution was a bell-shape with the particle size on a logarithmic scale.

The fine droplets thus created were collected in a beaker filled with liquid nitrogen (boiling point -196°C), converting them into frozen granules instantaneously. At the end of this process, the excess nitrogen was evaporated off and the frozen granules were freeze dried.

3.2.3.2 Freeze drying

Freeze drying was carried out in a benchtop freeze drier (Virtis® Benchtop SLC, New York, USA) backed up with a Leybold® D2.5B double stage oil-sealed rotary vane vacuum pump (Leybold vacuum GmbH, Germany) with exhaust filter. The condenser capacity, i.e., the maximum volume of water that could be condensed from the product before defrosting was required, was 2.5 litres. The frozen granules were placed in borosilicate glass flasks connected to the kit through a stainless steel manifold which featured four 1.89 cm (¾ inch) ports. The water vapour

from the frozen sample reached the condenser through the manifold and was converted to ice there, as shown in Figure 3-1.

The condenser was cooled down to -50°C and evacuated to vacuum levels below 13.33 Pa (100 milli Torr) before connecting the samples. As soon as the frozen sample was connected, vacuum was created in the flask. Owing to the temperature gradient between the frozen sample and the ambient air, the heat required for sublimation was obtained from the ambience. The low pressure inside the flask ensured that the sample did not melt back into liquid stage. If the sample melts, the granules will no longer have a spherical shape. Sample melt back was avoided by either decreasing the amount of product (water content) or by slowing down the heating rate by insulating the product from ambient heat sources.

The water vapour thus created by sublimation tended to increase the pressure within the flask. As the vacuum pump continually tried to maintain the vacuum levels, the water vapour migrated towards it. The chilled condenser module acted as a cold trap and ensured that the moisture did not reach the vacuum pump. Ice was formed on the condenser walls. All this happened at pressures below the triple point of water.

During the initial stages, the frozen granules were observed to be a cohesive mass. As drying proceeded, powder fluidization was visible. The end point was determined by visual examination of the powder. By the end of the process, there was no further condensation from the ambient to the external surface of the flask. Typically, the powder was ready within 48 hours of drying.

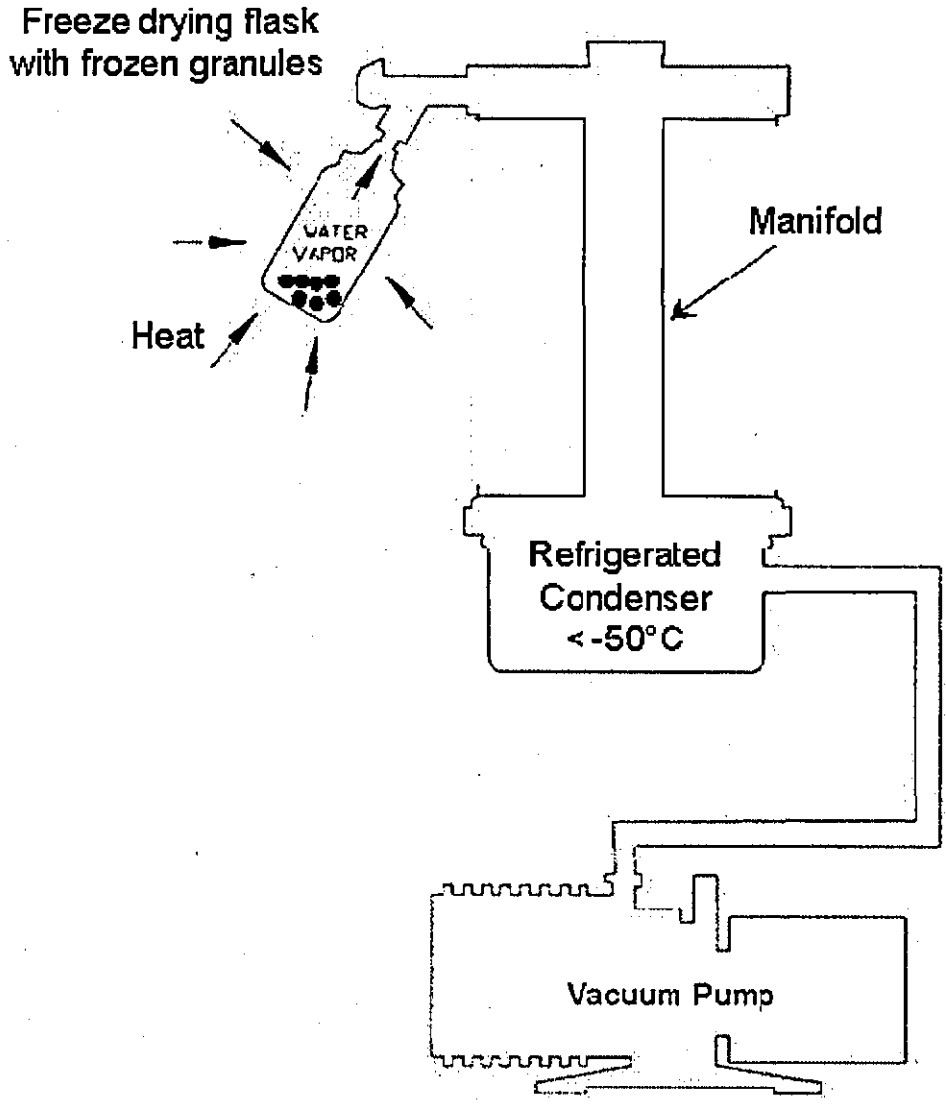

Figure 3-1 Schematic diagram of the freeze dryer setup.

3.2.3.3 Sieving

Sieving was done to separate out the granules into different size fractions. Test sieves made as per BS 410/1986 with mesh sizes of 250 μm and 125 μm were used.

3.2.4 Benchmark powder

The benchmark spray dried submicron YSZ powder (TZ-3YSB-C) was procured from TOSOH, Japan. According to the manufacturer, the crystallite size was 37 nm; loss on ignition was 5.4 wt% and 5.18% Y_2O_3.

The total amount of impurities including SiO_2, Fe_2O_3 and Na_2O was less than 0.3 wt%.

3.3 Powder coding

Based on the starting suspension used, the powders were coded as follows in Table 3-1.

Table 3-1 Coding for different powders used in this study.

Powder code	Drying route	Solid content of starting suspension
OD	Oven dried	5.5 vol%
SD5	Spray dried	5.5 vol%
SD14	Spray dried	14.3 vol%
SFD5	Spray freeze dried	5.5 vol%
SFD14	Spray freeze dried	14.3 vol%
SFD16	Spray freeze dried	16.3 vol%
SFD20	Spray freeze dried	20 vol%
SFD21	Spray freeze dried	21.4 vol%
SFD24	Spray freeze dried	24.4 vol%
SFD28	Spray freeze dried	28 vol%
TOSOH	Spray dried	Unknown

3.4 Powder characterisation

3.4.1 X-ray diffraction studies

Powder X-ray diffraction (Bruker AXS D8 Advances, Karlsruhe, Germany) was used to identify the crystallite phases. The scanning rate was 2° 2θ per minute and Cukα radiation with wavelength of 1.5406 Å was used. The lattice spacing, d, was calculated using Bragg's law:

$$n\lambda = 2d.\sin\theta_B \qquad \text{.....Equation 3-1}$$

where n is an integer, λ is the wavelength of x-ray source and θ_B is the angle between the incident ray and scattering plane.

X-ray line broadening was used to find the crystallite size [188] assuming that the crystals were free of strains or faulting, the crystallite size was found using the Scherrer formula:

$$L = (0.9\,\lambda) / (\theta * \cos\theta_B) \qquad \text{..... Equation 3-2}$$

where L is the crystallite domain size in nm, λ the wavelength in nm, θ the full width at half maximum, FWHM – in radian, and θ_B the Bragg diffraction angle in degrees. L is considered as an average crystal dimension perpendicular to the reflecting planes.

3.4.2 Thermogravimetric analysis

The weight loss from the powder over a temperature range from 25°C to 600°C was studied using a thermogravimetric analyser (TA Instruments Inc.,) at a heating rate of 10°C per minute.

3.4.3 Electron microscopy on powder

A Leo 1530VP Field Emission Gun Scanning Electron Microscope (FEGSEM) was used to observe the powder agglomerates at different magnifications. The powder was sprayed on the conducting carbon tab mounted on an aluminium stub for observation under the microscope; the specimen was gold coated by sputtering to avoid charging of the particles.

A JEOL JEM 2000FX transmission electron microscope (TEM) was used for looking at the primary particles at higher magnifications. Only the oven dried powder was observed using a TEM.

3.5 Powder flowability

The powder flowability was measured using (i) a Hall flowmeter, (ii) the Hausner ratio and (iii) Model shoe – die filling experiments.

3.5.1 Hall flowmeter

The powder flowability was measured using the Hall flowmeter for freely flowing powders [79, 129]. The powder flow rate was assessed using three different orifice diameters, 2.5 mm, 5 mm and 7.5 mm. The powder was poured into the funnel and collected in a density cup placed on top of a weighing balance. The microbalance had an accuracy of 0.001 g and was interfaced with a computer which records the mass at an interval of 0.1 second. The test was repeated 3 times for each powder for a given orifice diameter. The SFD5, SFD14 and SFD28 powders were sieved to get the 125 to 250 μm fractions whilst Tosoh and SD5 were used as such.

3.5.2 Hausner ratio

A custom built setup, shown in Figure 3-2, was used to find the Carr Index and Hausner ratio of the powders. The untapped volume and tapped volume after 1250 ± 10 tapings for the known mass of powder was used to find the untapped and tapped density. The use of compressibility of the powder as a measure of powder flowability was discussed in a previous section, 2.14.2.3. The weight and volume of the powder were measured to ±0.01 g and 0.5 cm^3 accuracy. The tapping cam rotated at 75 revolutions per minute and the dropping height was 3 mm. Each test was repeated three times to get the average and standard deviation of untapped and tapped densities. The SFD5, SFD14 and SFD28 powders were sieved to get the 125 to 250 μm fractions whilst Tosoh and SD5 were used as such.

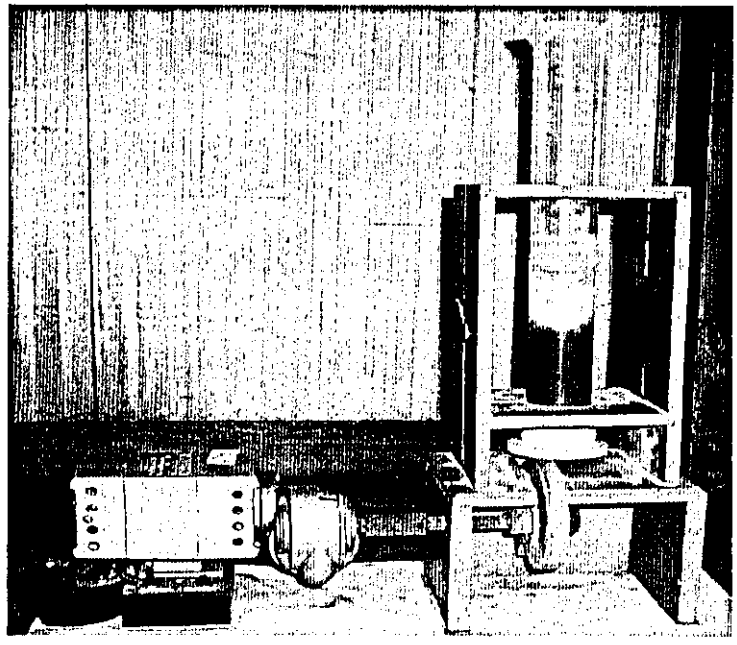

Figure 3-2 Experimental setup for finding powder flowability.

3.5.3 Model shoe – die filling experiments

The model shoe-die filling rig consisted of a pneumatically driven shoe, the velocity and acceleration of which could be controlled using a microprocessor. The powder was delivered to the die from the powder filled shoe as it traversed over the fixed die cavity. A rectangular shoe of size 60 mm x 40 mm was used. The height of the powder bed was 10 mm when filled. The die opening was 14 mm x 14 mm and a constant height of 20 mm was used in all the experiments. The set-up is shown in Figure 3-3 [145] and is located in Leicester University, UK.

The acceleration was fixed at 50 m s^{-2} and the weight of the powder in the die was noted for 7 different shoe speeds viz., 50, 100, 150, 200, 300, 500 and 750 mm s^{-1}. The powder filled shoe was moved from left to right on top of the die. The shoe was programmed to have five quick shakes of ±5 mm before it was translated over the die. The shakes would nullify any effects due to manual powder filling into the shoe and aid in achieving a reproducible initial state of material inside the die. The shoe velocity profile for the die filling is pictorially depicted in Figure 3-4. This profile had a initial acceleration period, (0 - t_a), where the shoe started from rest and reached a steady state velocity, V_{shoe}, as programmed; the

shoe continued to travel at the predefined speed until it reached the other side of the die and started decelerating at time t_d. Finally, at time t_f, the entire operation was completed and the shoe came to rest.

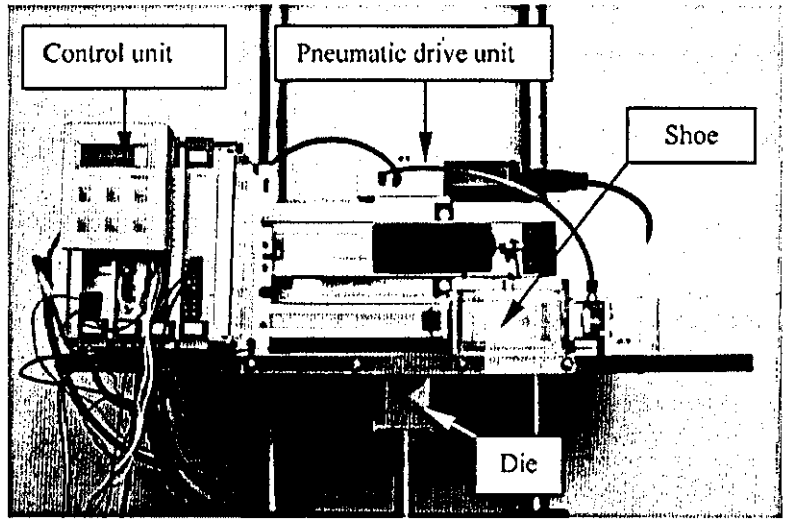

Figure 3-3 Experimental set-up used for die filling studies.

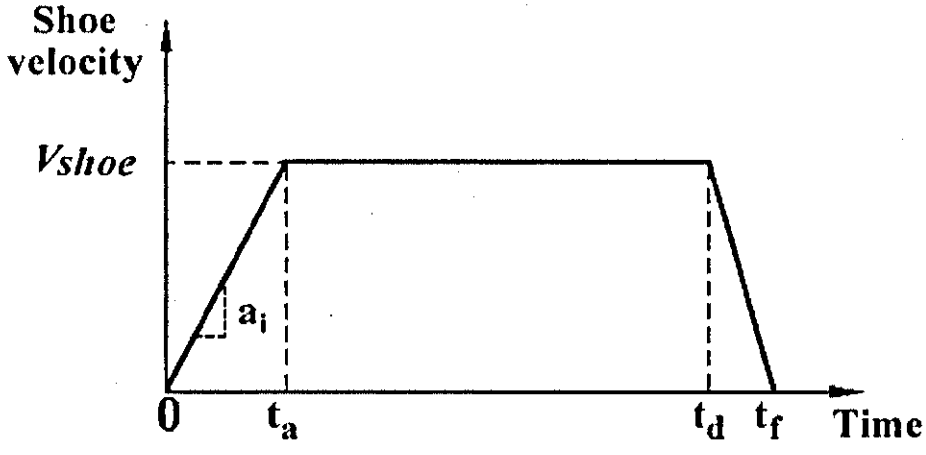

Figure 3-4 The shoe velocity profile [145].

The shoe and the die were all made of transparent material so that the whole process could be captured using a high speed camera and qualitative comparisons made. The images were captured at 1000 frames per second using an Olympus i-SPEED (Olympus corporation, USA), a high speed digital video camera. The weight of the powder in the die after the

shoe made one pass over it at the programmed velocity was measured for each of the powders to make quantitative comparisons.

The SFD5, SFD14 and SFD28 powders were sieved to get 125 to 250 μm fractions whilst Tosoh and SD5 were used as such for testing. Only one trial was possible for each powder at a given shoe velocity. The obtained experimental data of fill ratio at different shoe velocities was fit using a power law relationship and used to deduce the critical velocity from the experimental data.

3.6 Die pressing

Green compacts were die pressed using a Lloyds mechanical testing machine (L10000 Tensometer, Lloyds Instruments, Fareham, UK) in a single-action, hardened steel die with a diameter of 10 mm. Before every pressing, the die and the punch wall were thoroughly cleaned, polished and washed with acetone. About 1 g of powder was used for every pellet. The ram (top punch) speed was 1 mm min^{-1} and was held at the consolidation pressure (125 MPa or 380 MPa) for 1 minute. The discs thus made were slowly ejected from the die and used for further testing.

3.7 Compaction curves

Compaction curves were generated to study the granule yielding behaviour. The die and punch were cleaned thoroughly before every test using acetone. About 1 g of a powder was used in each test. The powder was filled into a 10 mm diameter hardened steel die and a load was applied onto the top punch using a Lloyds mechanical testing machine with a computer interface to continuously record load versus cross head position. The rate of displacement was fixed at 1 mm min^{-1}. The density of the compact at any given pressure was deduced from the data on elastic compliance of the testing system and cross head position at the particular load. The maximum pressure applied was 380 MPa. The green density of the pellet was measured after ejecting the pellet from the die.

3.8 Green density of pellets

The green density of the die pressed compacts was calculated from the weight of the sample (measured to ±0.001 g) and the dimensions of the compact (measured to ±0.01 mm). The dimensions were measured in at least three locations within the sample and averaged out for calculations. Five green bodies were made and densities measured for each powder compact.

3.9 Fracture surface analysis by electron microscopy

A Field Emission Gun Scanning Electron Microscope (FEGSEM, Leo 1530VP FEGSEM, LEO Elektronenmikroskopie GmbH, Oberkochen, Germany) was used to analyse the fracture surface of green bodies at different magnifications. The diametrally cracked pellets were glued on conducting carbon tabs mounted on aluminium stubs; gold was coated by sputtering to avoid charging of the particles before observation under the microscope.

3.10 Nitrogen adsorption isotherms

An automated gas adsorption analyser (Tristar™ 3000, Micromeritics Instrument Corporation, Norcross, USA), was used for finding the BET surface area and mesoporosity of the powders and compacts. All powder and compacts were heated to 400°C in air and then degassed in a nitrogen atmosphere for 30 minutes at 400°C before testing. During the testing, the sample was evacuated to less than 20 μmHg vacuum, cooled down to 77K and then high purity nitrogen (>99.99% pure) was dosed in a predefined manner. The experimental procedure involved the use of relative pressure, p, where the pressure was expressed with respect to the saturation vapour pressure, p_o, at a constant temperature of adsorption. 40 adsorption and desorption points were selected with p/p_o values in the range 0.05 to 0.99. Equilibration was reached when the pressure change per equilibration time interval (10 seconds) was less than 0.01% of the average pressure during the interval. The Tristar™ 3000 had a resolution within 0.05 mmHg and accuracy 0.5%

of full scale [190]. Three samples could be tested simultaneously in this equipment.

The adsorption-desorption isotherm, i.e. plot of p/p_o vs. volume of N_2 adsorbed, was the basic data gathered during the standard test. The other parameters, viz., BET surface area and pore size distributions were derived from this data.

3.11 Mercury intrusion porosimetry

Mercury intrusion porosimetry was carried out using a poresizer, (Model 9310, Micromeritics Instrument Corporation, Norcross, USA). The powder compacts were heated to 400°C for 1 hour before the porosimetry measurements to remove the organics i.e. dispersants and TMAH. The sample was then placed on the penetrometer, outgassed to less than 2 mPa (200 μmHg) and mercury was filled into the penetrometer. The penetrometer with sample and mercury was introduced into the high pressure chamber. The hydraulic pressure was increased from ~0.15 MPa (15 psi) to ~100 MPa (15000 psi) which corresponded to a pore size of ~10 μm to ~12 nm. Data was collected in the equilibration mode where the pressure was held at each data point for a specific time period of 180 seconds.

The volume of mercury (Hg) taken up by the solid was measured as the applied pressure Δp was gradually increased. The relation between the pore size and pressure of intrusion is given by the Washburn equation as described earlier in Section 2.17.

3.12 Sintering

The nanopowder compacts were uniaxially pressed at 380 MPa and sintered isothermally at 1100°C for 1 hour in a conventional furnace. The heating and the cooling rates were set at 20°C min^{-1}. The benchmark TOSOH powder was also pressed at 380 MPa, but sintered at 1400°C for 1 hour.

Chapter 4

Results and Discussion

The results are arranged and discussed in the sequence of processes involved in powder processing. The slip characterisation, micrographs of prepared powders, powder flowability, compaction curves, green density and porosimetry on powder compacts are given in order.

4.1 Nanosuspension characterisation

The nanosuspensions were characterised before the spraying stage. The prepared suspensions were stable up to at least one week after preparation and no sedimentation was observed.

4.1.1 Zeta potential measurement

From Figure 4-1, it is clear that the IEP shifted towards lower pH with the addition of anionic dispersants. It can be inferred that the suspension without any dispersant had a higher zeta potential in acidic pH. As the pH is increased, the zeta potential slowly decreased and the suspension flocculated when the pH reached approximately 8.3. With further pH increase the polarity of the particle charge reversed and increased in magnitude. The shift in the IEP with the addition of TAC and Dispex A40 compares well with those reported in the literature. When di-ammonium citrate, a carboxylic group containing analogue of TAC, was used, Fengqiu et al. [124] observed the IEP shift towards acidic pH. In the same paper, Darvan C, a chemically identical species to Dispex A40 showed a similar behaviour. The increase in the magnitude of zeta potential in the high pH with the addition of TAC as presented in Figure 4-1 was also in line with those reported in the literature [125]. The shift in zeta potential shows that the dispersant had adsorbed on the nanopowder. At least 5 measurements were made on each suspension at a given pH and the reproducibility was within ± 5 mV.

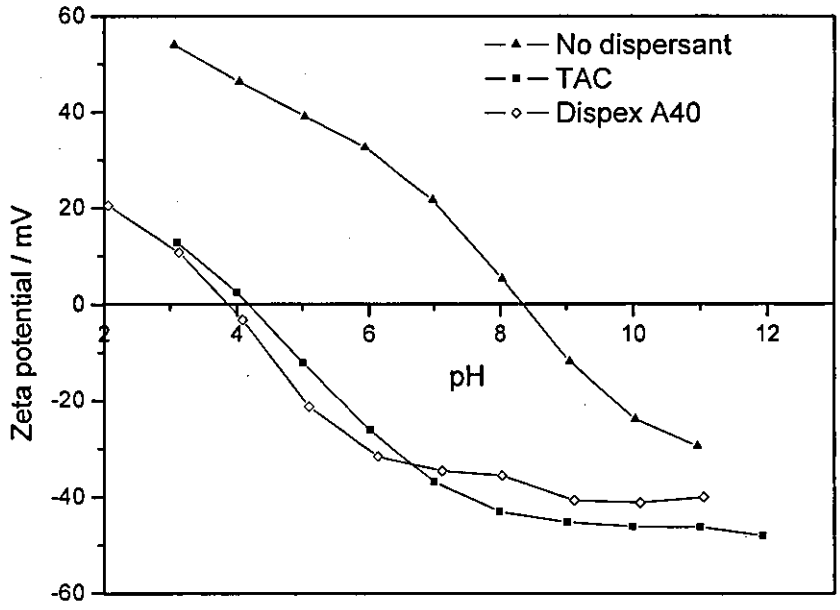

Figure 4-1 Zeta potential for different nanosuspensions.

As a rule of thumb, a suspension with zeta potential higher than |30 mV| is considered stable [53]. Thus, all granules prepared in this study were from stable, well dispersed suspensions.

4.1.2 Viscosity measurements

In Figure 4-2, the 5.5 vol% ZrO_2 suspension without dispersant had viscosity similar to that of 14.3 vol% ZrO_2 suspension with the addition of TAC. All the TAC based suspensions had a near Newtonian flow behaviour, a characteristic of well dispersed suspensions. The viscosity remained constant over a wide range of shear rates. At any given shear rate, for suspensions containing TAC, the viscosity followed the trend of the solid content. TAC was more effective than Dispex A40 in reducing the viscosity of this system. Note that the viscosity measurement for the suspension without dispersant was carried out in the acidic pH (pH = 3) whilst the suspensions with deflocculants (TAC and Dispex A40) were done at pH~9.5 i.e., respectively in their useable pH range.

When the suspension was concentrated without the addition of dispersants, the viscosity increased very significantly. This can be attributed to the lack of repulsive forces that are required to keep the

particles apart in the suspension. When uncharged particles come in contact, they cling together because of the attractive van der Waals forces and flocculate. This effect is greater when the suspension is near the IEP.

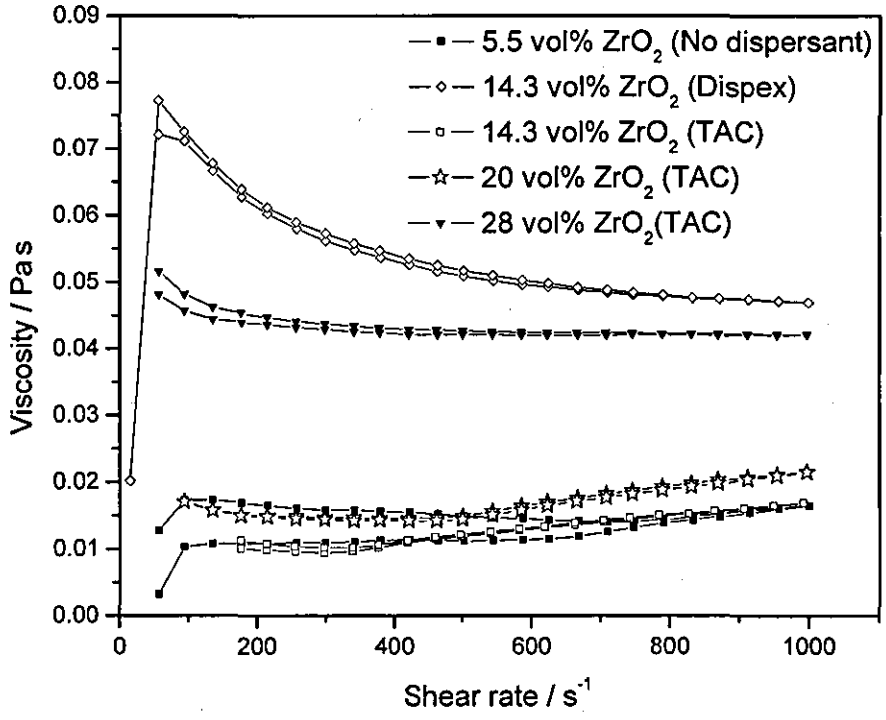

Figure 4-2 Viscosity data on different suspensions.

For comparison, the viscosity of different suspensions at a shear rate of 200 s^{-1} is plotted in Figure 4-3. The nanosuspension with TAC had a much lower viscosity compared to that of the Dispex A40 based dispersion of same solid content (14.3 vol% oxide). The absolute value of the zeta potential was higher for the TAC based suspension than the Dispex A40 based suspension whilst the viscosity showed an inverse trend. This explains the relation between these two parameters. However, another reason for the higher viscosity for Dispex A40 based suspension was the size of the adsorbed molecule. From the literature [117], it can be inferred that the size of the adsorbed molecule has an impact on the maximum solid content for stable nanosuspensions. Well dispersed suspensions with high zeta potential can be achieved when the surface charge density is high enough to generate a strongly repulsive double layer. The chemical structure of Dispex A40 is shown in Figure 4-4; it has

an average molecular weight of 4000. TAC has a molecular weight of 243. The long polymer chain of Dispex can orient in several ways depending on the charge in the polymer backbone [122] and provide electrosteric stabilisation. The adsorption of TAC electrostatically disperses the YSZ particles. The difference in the dispersion mechanism affects the zeta potential and viscosity of the suspensions. As expected, the viscosity of the suspension increased with the increase in solid content for dispersions where TAC was used.

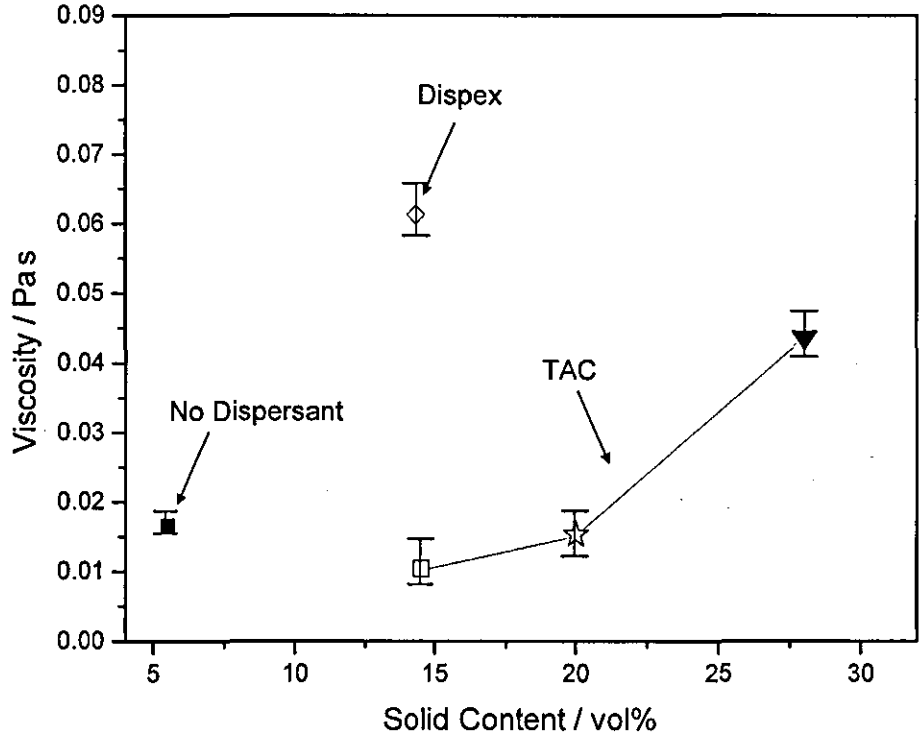

Figure 4-3 Viscosity of different suspensions at shear rate = 200 s^{-1}

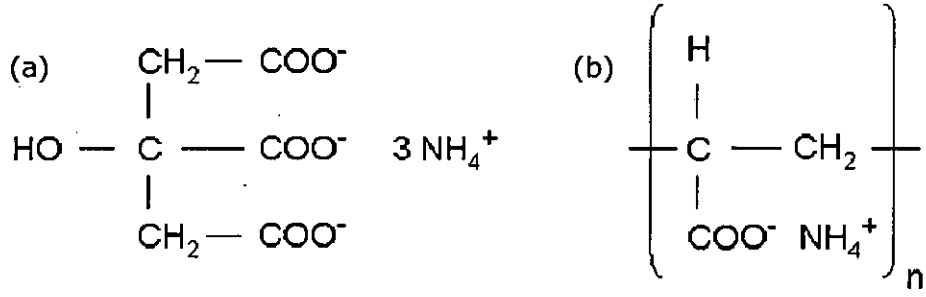

Figure 4-4 Chemical structure of (a) TAC and (b) Dispex A40.

4.1.3 Thermogravimetry on the suspension

The thermogravimetric analysis of a typical suspension used in this study is presented in Figure 4-5. It can be seen that much of the weight loss occured at around 100°C. At higher temperatures, around 250°C, a small peak in the rate of weight loss can be attributed to the decomposition and removal of the added organics. There was negligible weight loss after 400°C and the mass remained almost constant. This corresponds to the weight of YSZ in the suspension.

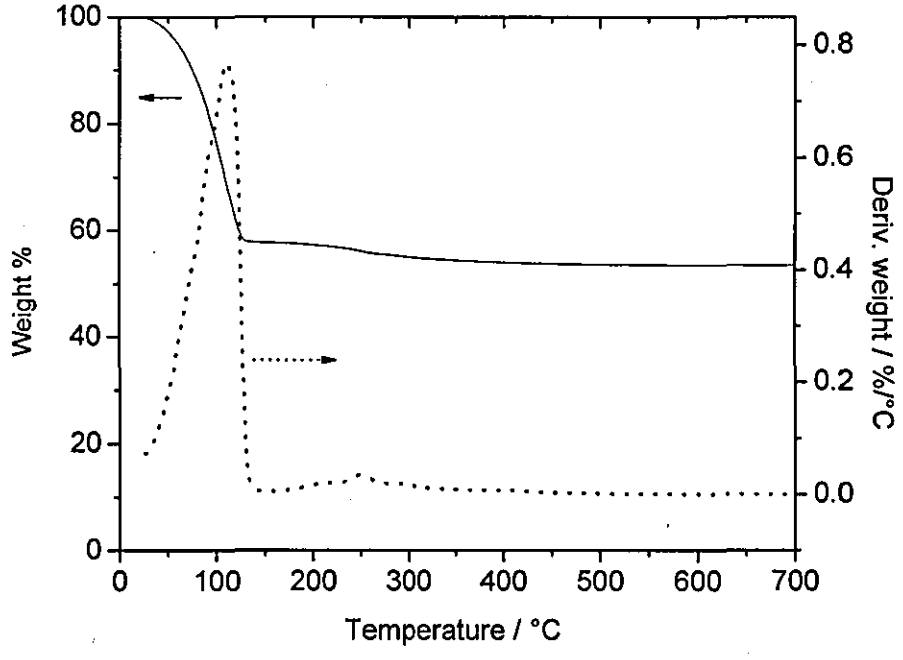

Figure 4-5 Thermogravimetric analysis on a typical nanosuspension.

Accurate control of the solids in the suspension was found to be difficult. The high solid content suspensions were prepared by concentrating the well dispersed low solid content suspension received from the supplier. The estimate of the solid content based on the volume and density of the suspension was not better than ±2% accurate. Therefore, the concentrated suspension had to be taken to 700°C to know the exact oxide content.

4.2 Powder characterisation

4.2.1 Phase identification

The XRD patterns of the nano- and submicron powder are shown in Figure 4-6 and Figure 4-7 respectively. The peaks marked 't' correspond to the tetragonal/cubic peaks and 'm' correspond monoclinic peaks as reported in JCPDS file 79-1769 and 78-1807 respectively (see Appendix 1). The nanopowder was completely tetragonal/cubic, as expected based on the yttria content and particle size [20]. The benchmark submicron powder had both tetragonal and monoclinic peaks. The nanopowder peaks were broader in contrast to the sharper peaks of the submicron powder, Figure 4-7. The crystallite size calculated using the Scherrer formula for the nanopowder was ~12.8 nm.

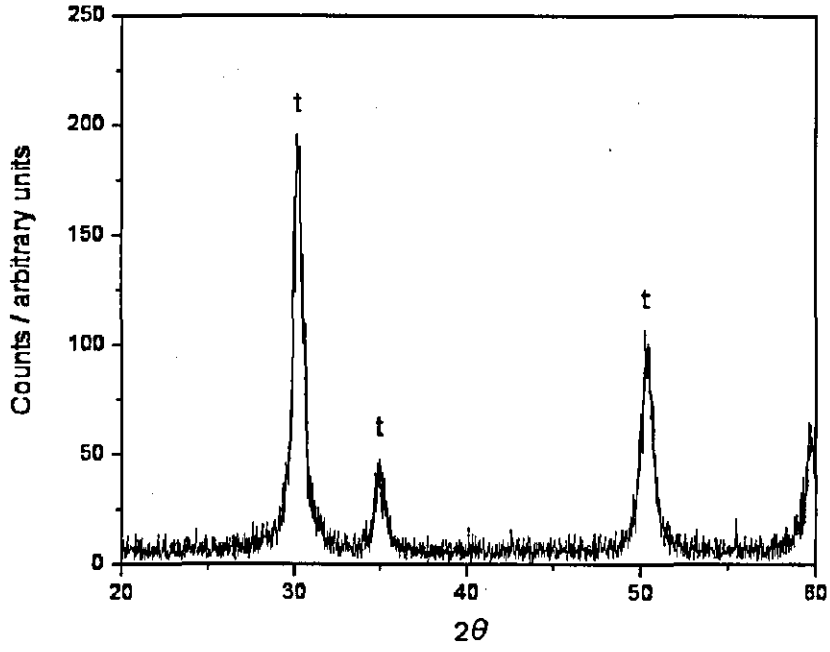

Figure 4-6 X-ray diffraction pattern for 3 YSZ nanopowder.

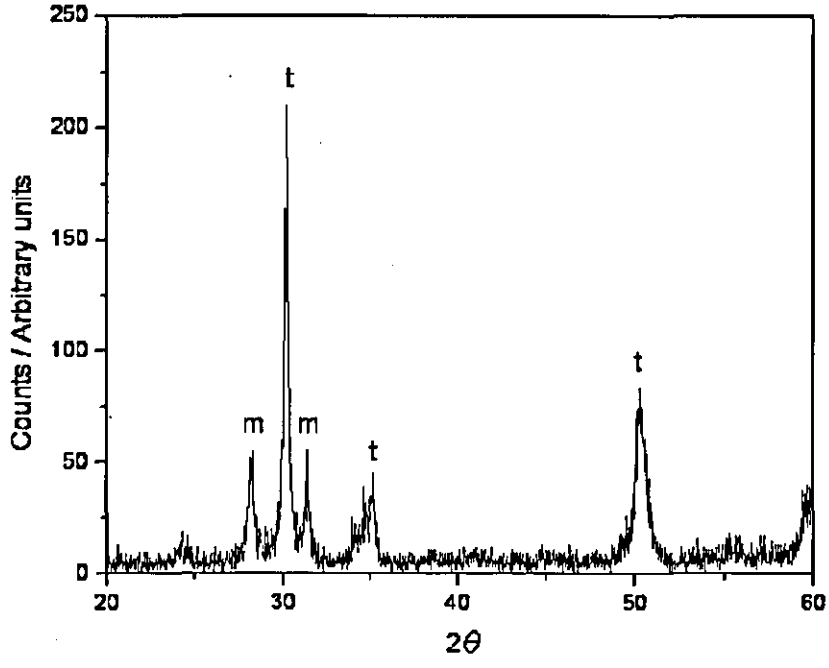

Figure 4-7 X-ray diffraction pattern for TOSOH submicron YSZ.

4.3 Powder preparation

Powder preparation required various parameters to be optimised. Oven drying was the simplest and it involved drying the powder in an

oven at 60°C. The dried powder was in the form of flakes which on micronising formed a fluffy powder consisting of irregularly shaped and sized agglomerates.

The drying paths for spray drying and spray freeze drying are shown in Figure 4-8. In spray drying, the suspension temperature was raised and water removed as vapour, the nanopowder being collected in a cyclone separator. The suspension required a low viscosity so that it could be pumped and atomised; high viscosity slurries can clog the nozzles. The development of a low viscosity, high solid content nanosuspension by other colleagues within the research group was vital in making this project feasible. The use of a co-current spray dryer with a rotary atomiser had several advantages over other models. First, rotary atomisers can yield spherical granules with a narrow size distribution. Secondly, with co-current systems the slurry and the hot drying air are fed simultaneously from one direction. As a result, with heat transfer between the two streams, the temperature of the hot air stream reduces and equilibrates with that of the liquid stream and water from the slip is converted into vapour. Therefore, the maximum temperature the granules experience is lower than that of the inlet temperature of hot air stream. In the case of counter current systems, the hot air and the liquid stream are fed from opposite directions so the drying granules are subjected to higher and higher temperatures as drying proceeds. This enhances the chances of formation of hard agglomerates.

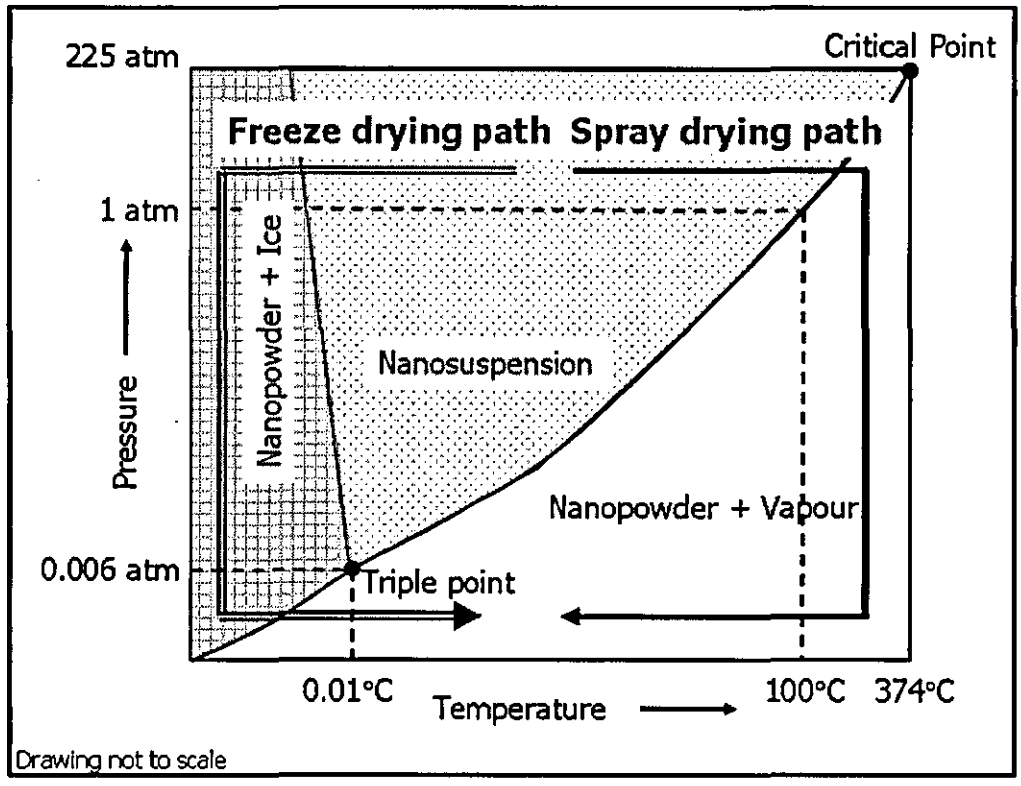

Figure 4-8 Phase diagram for different drying paths.

For spray freeze drying, the various parameters to be optimised were (i) spray freezing conditions viz., spraying technique, spraying rate, height of the spraying etc., and (ii) freeze drying conditions, i.e. drying temperature, drying pressure, height of drying powder bed etc. To make spray freeze dried granules, the solid content of the starting suspension was systematically varied keeping the level of the organics constant. As a result, the viscosity of the suspension increased with increasing solid content. The use of twin fluid spraying nozzles was restricted by the experimental setup, which was more suitable for lab scale trials; it was found to be practically difficult as the suspension froze and clogged in the nozzle tip due to extreme temperatures. Further, the high pressure stream coming of the nozzle would spatter liquid nitrogen. Therefore, ultrasonic atomisation was selected.

An ultrasonic horn with a fixed frequency of 23 kHz was used. In this setup, the droplet size distribution depends on the viscosity of the suspension. If the viscosity was too high, the droplets stuck to each other

and proper atomisation could not be achieved. Since clustered granules have poor flowability, flocculated suspensions could not be used. The height between the tip of the horn and the surface of the liquid nitrogen was also important. If this distance was short, the liquid fragments were frozen before they take the preferred spherical shape. A distance of 15 cm was found satisfactory for dispersed suspensions.

Ultrasonic spray nozzles can operate over a wide range of slurry feed rates. There exists a maximum suspension feed rate beyond which the suspension forms a continuous liquid stream while spraying into the liquid nitrogen bath. To get spherical agglomerates with controlled size, the slurry feed rate should be less than this critical value. This limit was found to be approximately 10 ml min^{-1} for the setup used in the present work. The amplitude of the horn is also an important parameter. At low vibrational amplitudes, the energy was insufficient to produce any atomised drop. At very high amplitudes, the liquid was ejected as large cluster, a phenomenon called cavitation. With low power, a mist of fine droplets was formed.

It was observed that the drying time was less when the solid content of the starting suspension was higher. To obtain 100 g of powder from 5.5 vol% YSZ suspension, the amount of water to be removed is ~284 g whereas, for the same amount of powder, a 28 vol% ZrO_2 suspension would have only ~43 g of water. This large decrease in the amount of water to be sublimed can be realised as decrease in the overall operating cost. On similar lines, it is preferable to use high solid content suspension for spray drying also. However, the pumpability and sprayability criterion restricts the maximum useable solid content.

4.3.1 Thermogravimetry on the powders

The TGA trace of the spray freeze dried granules, Figure 4-9 showed that there were two clear temperature regimes where the weight loss occured. As in the suspension, the loss around 100°C was attributed to residual/reabsorbed moisture removal whilst the peak at ~265°C can be assigned to burning out of the dispersant and pH modifiers. The total weight loss was about 14% at 600°C. The split up of the weight loss can

be as follows: ~8 wt% TMAH, ~2.5 wt% dispersant and ~3.5 wt% moisture. The amount of organics lost on ignition was consistent with those added in the preparation stage. The moisture removed was similar to the weight loss from oven dried nanopowders and this is attributed to surface 'bound' water molecules that are released from the YSZ particles at temperatures above 100°C.

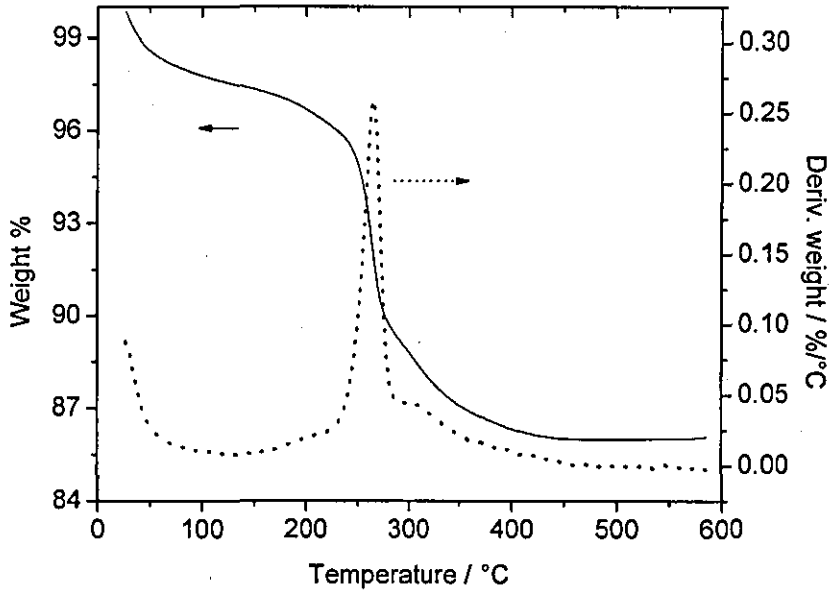

Figure 4-9 Thermogravimetric analysis on a typical SFD powder.

The TOSOH powders had a total weight loss of only 5% of the initial mass of the powder, Figure 4-10. This proves that the amount of organic additives used in this powder is much less than the granules made in this study. The lower amount of organics might have been achieved as: (i) lower levels of dispersants are needed in stabilising submicron powder suspensions in comparison with the nanopowders and (ii) lower levels of tailored binders can give satisfactory performance in submicron powders. It is also important to note that the release of binders is slow and spanned a wide temperature range in the case of TOSOH powders. In ceramic processing, a slow and controlled decomposition of the organics during sintering is preferred as this reduces the chances of sudden release of gaseous species and possible damage to the formed compacts.

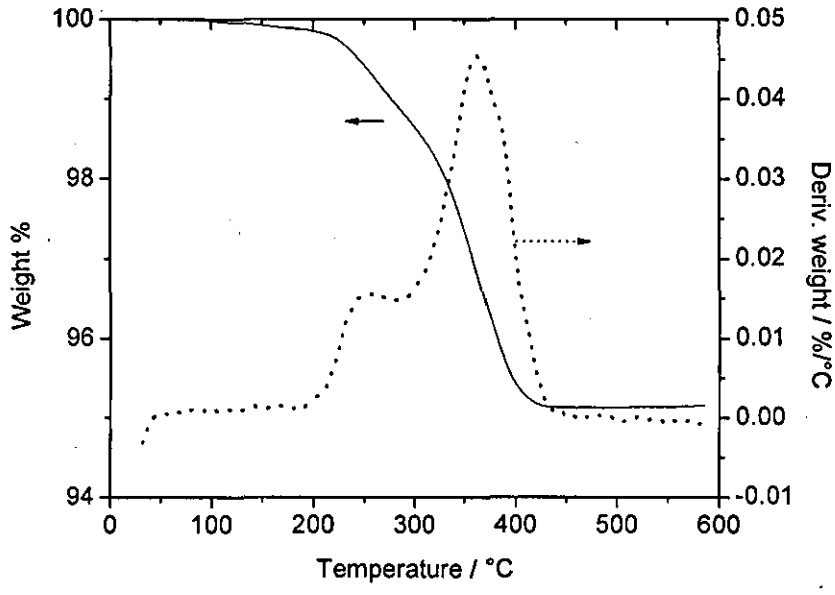

Figure 4-10 TGA on TOSOH powder.

4.3.2 Electron microscopy powders

4.3.2.1 Oven dried powder

The FEGSEM image of powder obtained by oven drying the powder followed by micronising using the Mcrone micronising mill is shown in Figure 4-11a. The powder was heavily agglomerated with the agglomerates having an irregular shape and a wide particle size distribution with some granules of upto 50 μm in size. At higher magnifications, the primary particles in the oven dried powder were visible, Figure 4-11b.

Figure 4-11 Oven dried and micronised zirconia nanopowder (a) at low magnification and (b) high magnification showing multiple levels of agglomeration.

The TEM revealed that the particles were weakly agglomerated when dispersed, Figure 4-12. Solid bridges and necks between particles were not evident in the micrographs.

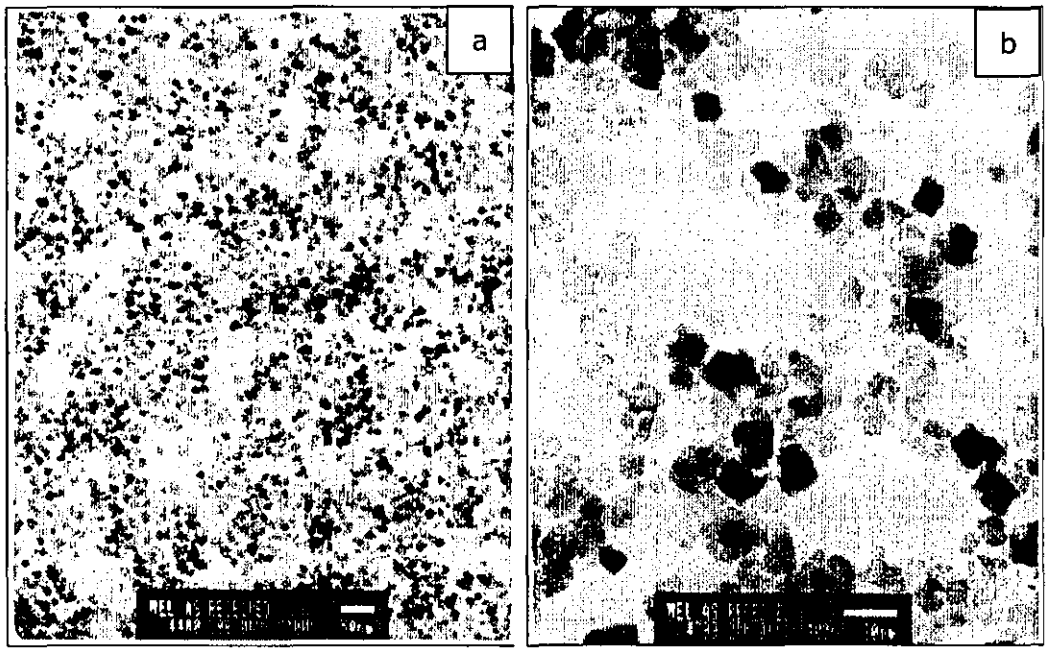

Figure 4-12 TEM image of oven dried zirconia nanopowder (a) low magnification and (b) high magnification.

4.3.2.2 Spray dried granules

The spray dried powder from 5.5 vol% ZrO_2 nanosuspension without any dispersant consisted of dense granules as shown in Figure 4-13. These agglomerates were spherical with some having a small dimple. The 14.3 vol% ZrO_2 suspension made with Dispex A40 as dispersant, Figure 4-14, formed donut shaped agglomerates. The two major differences between the starting suspensions for these powders are (i) solid content and (ii) amount of dispersant. The increase in viscosity with increase in solid content is predictable; however, the addition of dispersant offsets it so that it can be sprayed. The formation of donut shaped granules with the addition of deflocculant agrees well with those presented in the literature [66 - 70]. These are formed by the inward collapse of the granule shell as the droplet dries. For better flowability, solid spherical granules are needed.

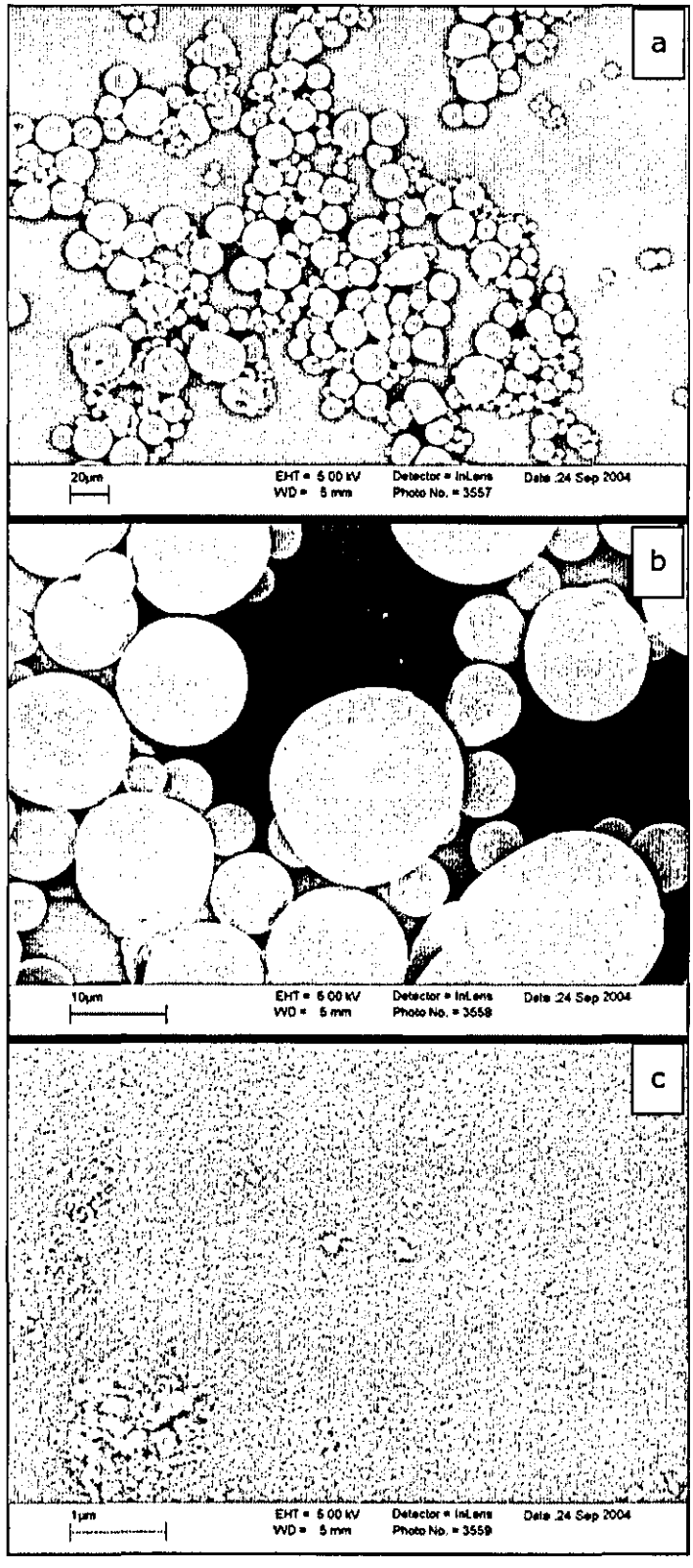

Figure 4-13 Spray dried nanopowder obtained from the 5.5 vol% suspension without dispersant showing (a) spherical granules at low magnification, (b) crater in granules and (c) high magnification showing dense packing of primary particles.

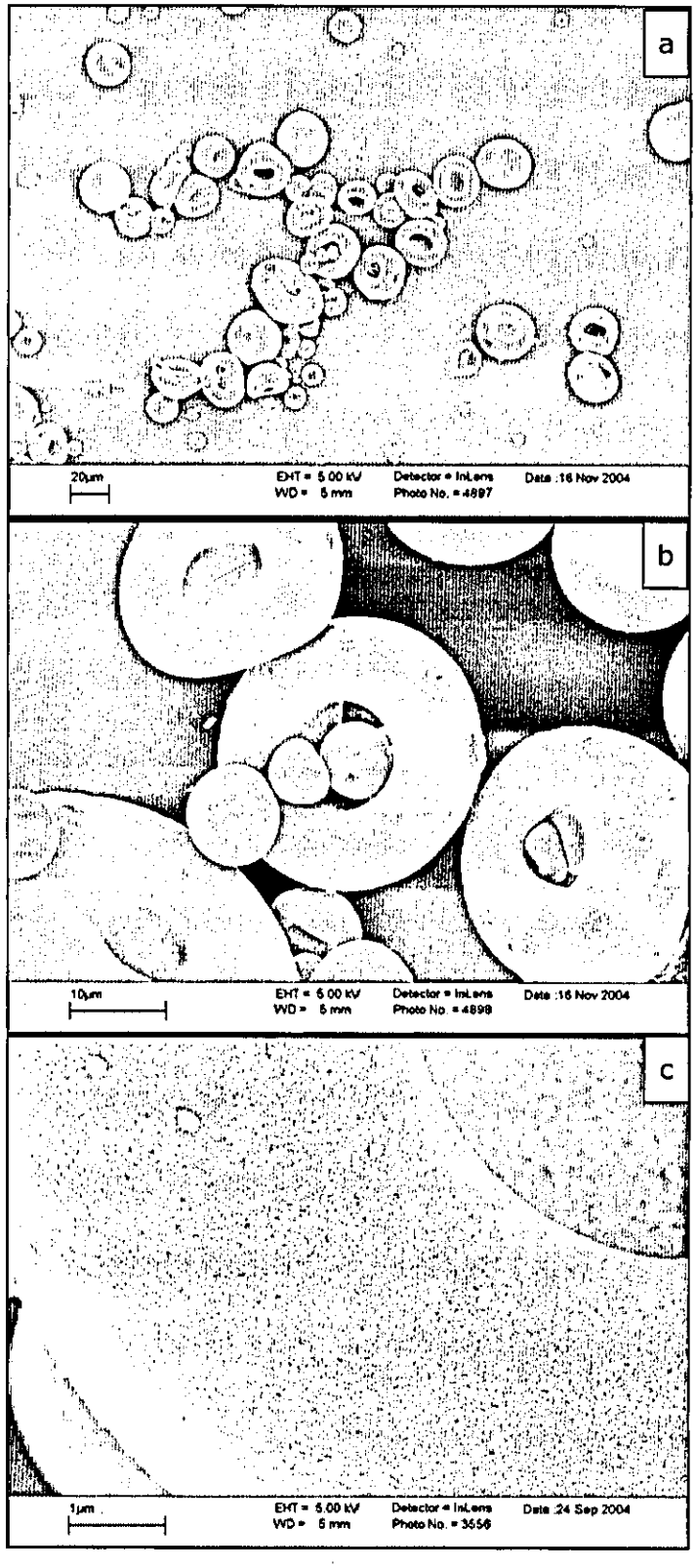

Figure 4-14 Spray dried powder obtained from 14.3 vol% nanosuspension using Dispex as dispersant showing (a) donut shaped granules at low magnification (b) higher magnification and (c) high magnification.

4.3.2.3 Spray freeze dried powders

The powder obtained by spray freeze drying of the as-received suspension is shown in Figure 4-15a. The granules were spherical in shape and porous. A high magnification showed that the granules had a flaky structure, shown in Figure 4-15b. The freeze drying process guarantees that >99% of the moisture is removed during the operation. The porosity in these granules was about 95% and its structure may be seen even more clearly in Figure 4-15c.

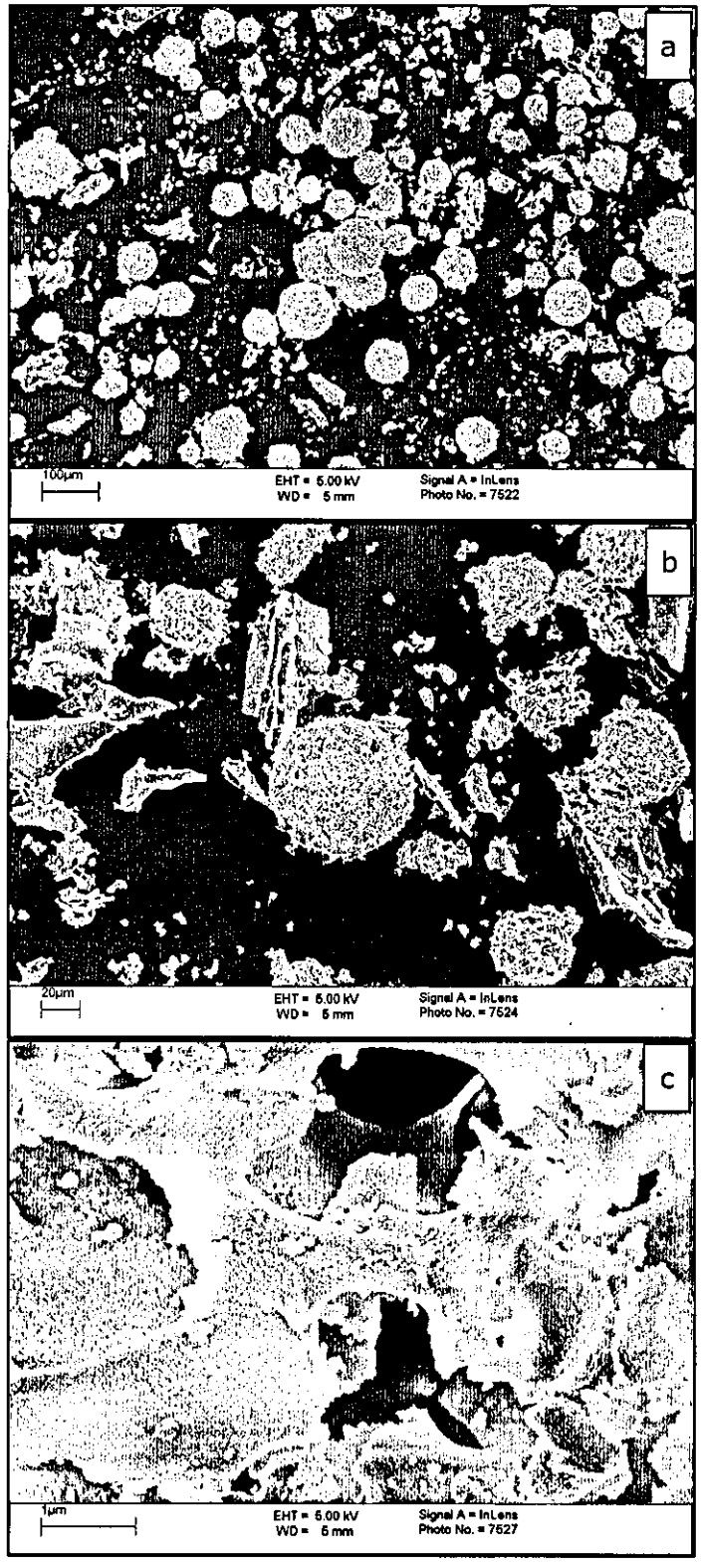

Figure 4-15 Spray freeze dried powder obtained from 5.5 vol% solids suspension without dispersant showing (a) spherical granules at low magnification, (b) higher magnification and (c) intra-granular porosity at high magnification.

As the solid content of the suspension was increased, the granules showed better packing of the primary particles and became denser. The micrographs from spray freeze dried powder obtained from 14.3 vol% solids suspension is shown in Figure 4-16. The powders made from suspensions having starting solid content of 16.3, 20, 21.4 and 24.4 vol% are shown in Figure 4-17 to Figure 4-20. It can be seen that the flaw size in the granules decreased with increasing solid content.

The spray freeze dried granules had no craters, unlike the spray dried granules. The micrograph revealed that the primary particles were more loosely packed and the pore structure was different from each other. It was also possible to achieve a better control on the granule shape compared to micronising oven dried powder when either spray drying or spray freeze drying was used.

The droplet size from ultrasonic atomisation is dependent on the slip viscosity and sonic frequency. For the given selection of suspension and frequency, a median droplet size of >70 μm can be expected [187]. Freeze drying works by sublimation, a process where the product is taken from frozen state to gaseous state directly, by-passing the liquid stage. As there is no liquid phase involved, the size and shape of the granules remain the same as that of the initial frozen state. Spherical granules with a wide size range were prepared and then sieved off fractions were used in the study.

The porous structure of these granules was similar to that reported by Tallon et al. [97]. The decrease in porosity with the increase in solid content matches the trend observed in previous work done by Koh et al. [108] on freeze cast bodies. The macropores slowly disappeared in the FEGSEM images, Figure 4-16 to Figure 4-21, as the oxide content increased. Quick freezing with liquid nitrogen precludes any changes in concentration of the constituents of the colloid by segregation [109]. The difference in dried microstructure between the powders from different solid contents was probably because of the difference in the formation of the frozen microstructure. When the suspension is quick frozen, more nucleation sites are formed and hence dendrite like structures are formed.

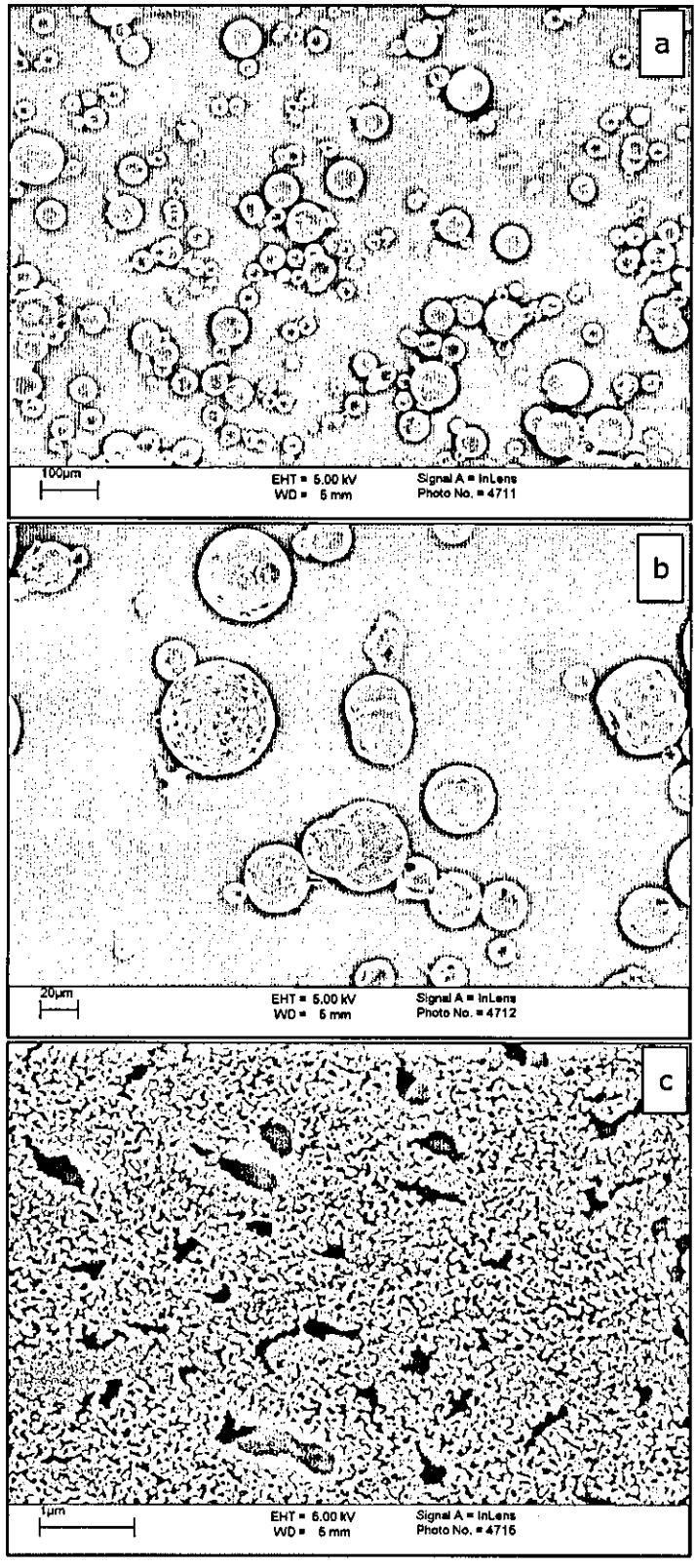

Figure 4-16 Spray freeze dried granules obtained from 14.3 vol% ZrO_2 suspension using TAC as the dispersant (a) low magnification, (b) higher magnification and (c) high magnification showing porosity.

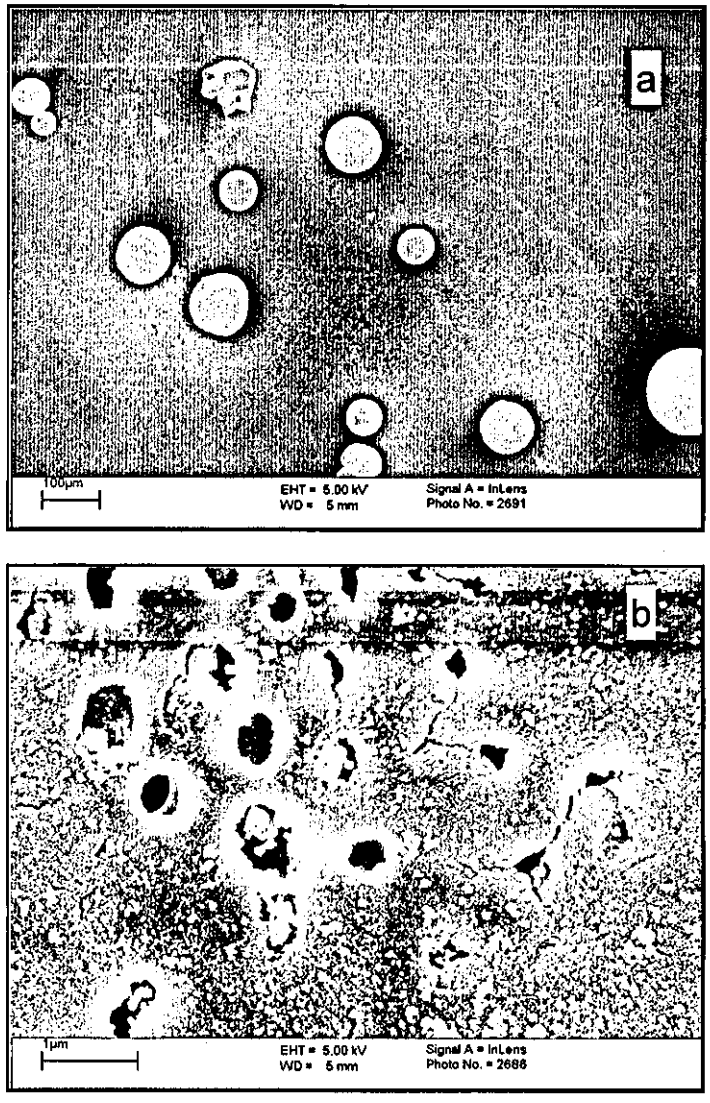

Figure 4-17 Spray freeze dried powder obtained from 16.3 vol% solids suspension using TAC as dispersant at a) low magnification and b) high magnification.

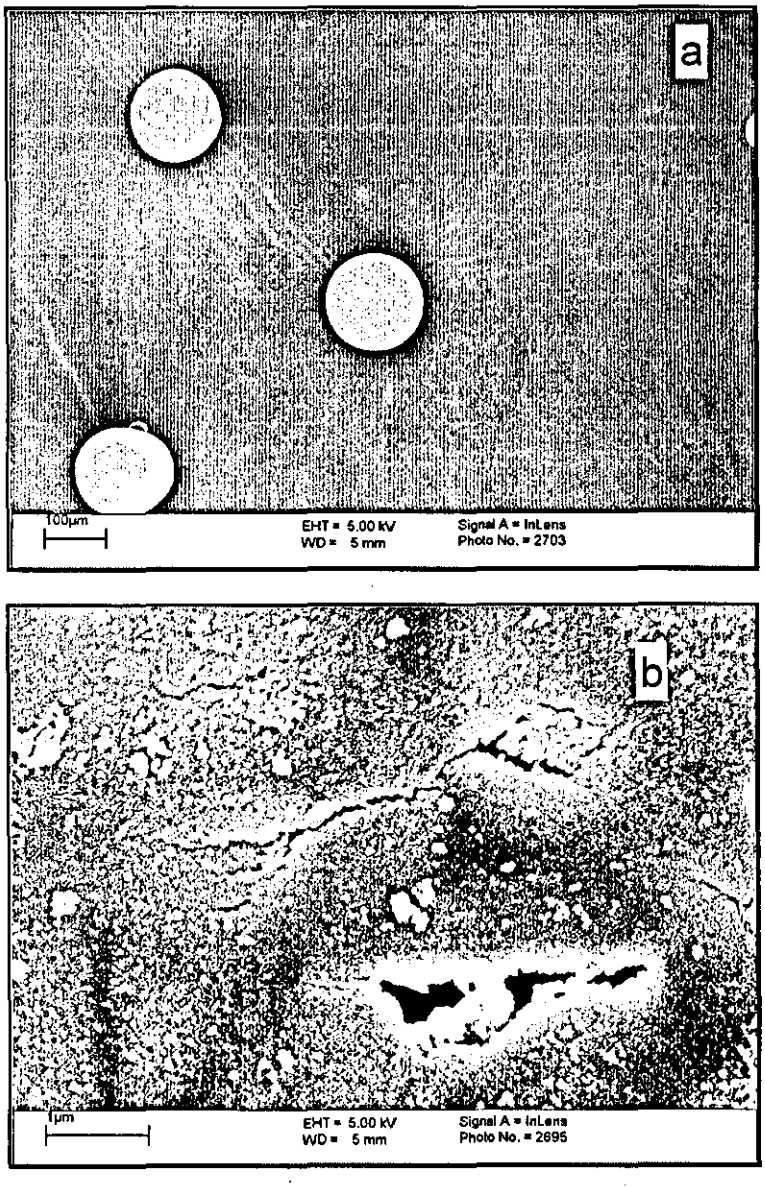

Figure 4-18 Spray freeze dried powder obtained from 20 vol% solids suspension using TAC as dispersant at a) low magnification and b) high magnification.

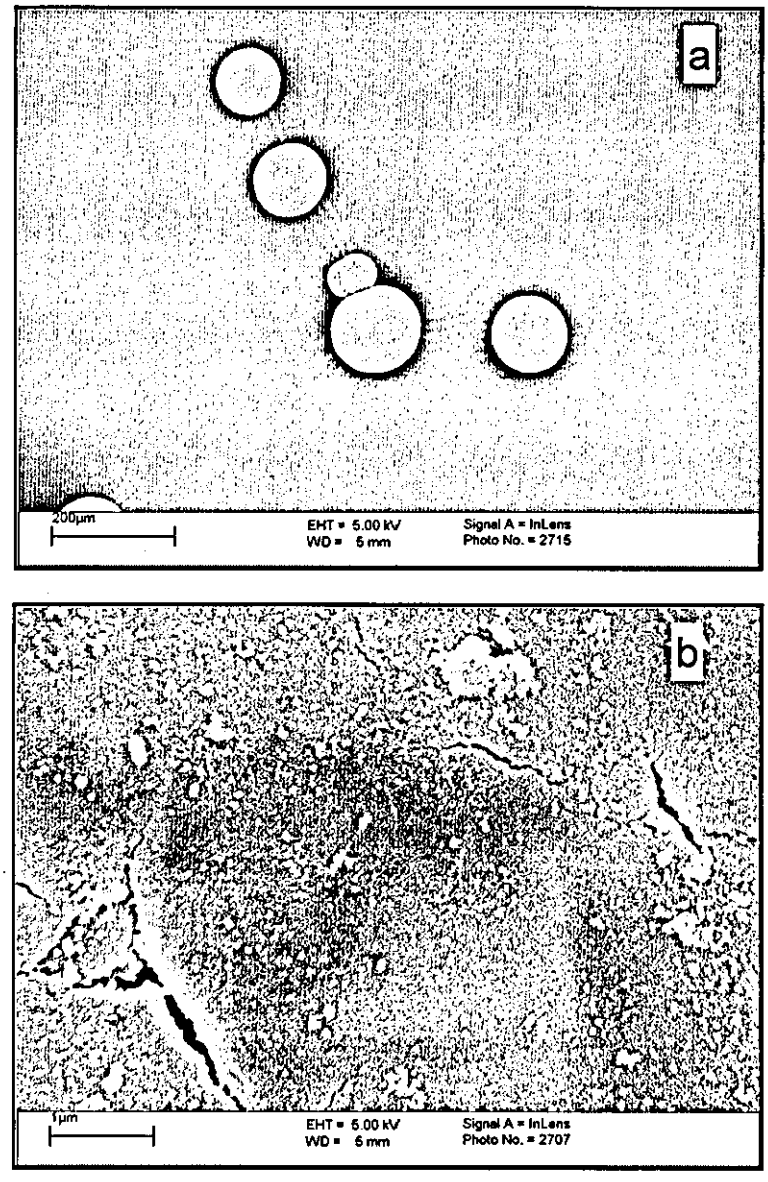

Figure 4-19 Spray freeze dried powder obtained from 21.4 vol% solids suspension using TAC as dispersant at a) low magnification and b) high magnification.

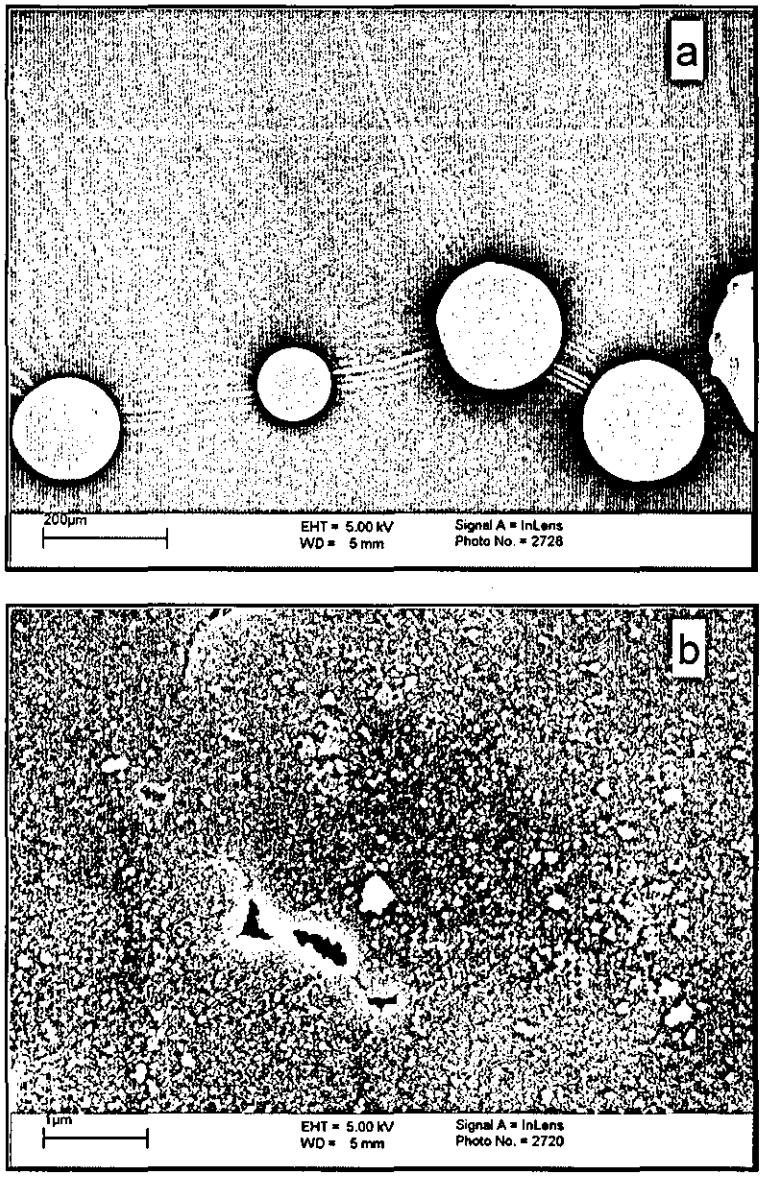

Figure 4-20 Spray freeze dried powder obtained from 24.4 vol% solids suspension using TAC as dispersant at a) low magnification and b) high magnification.

The maximum solid content at which spraying was possible due to the viscosity was 28 vol% of zirconia.

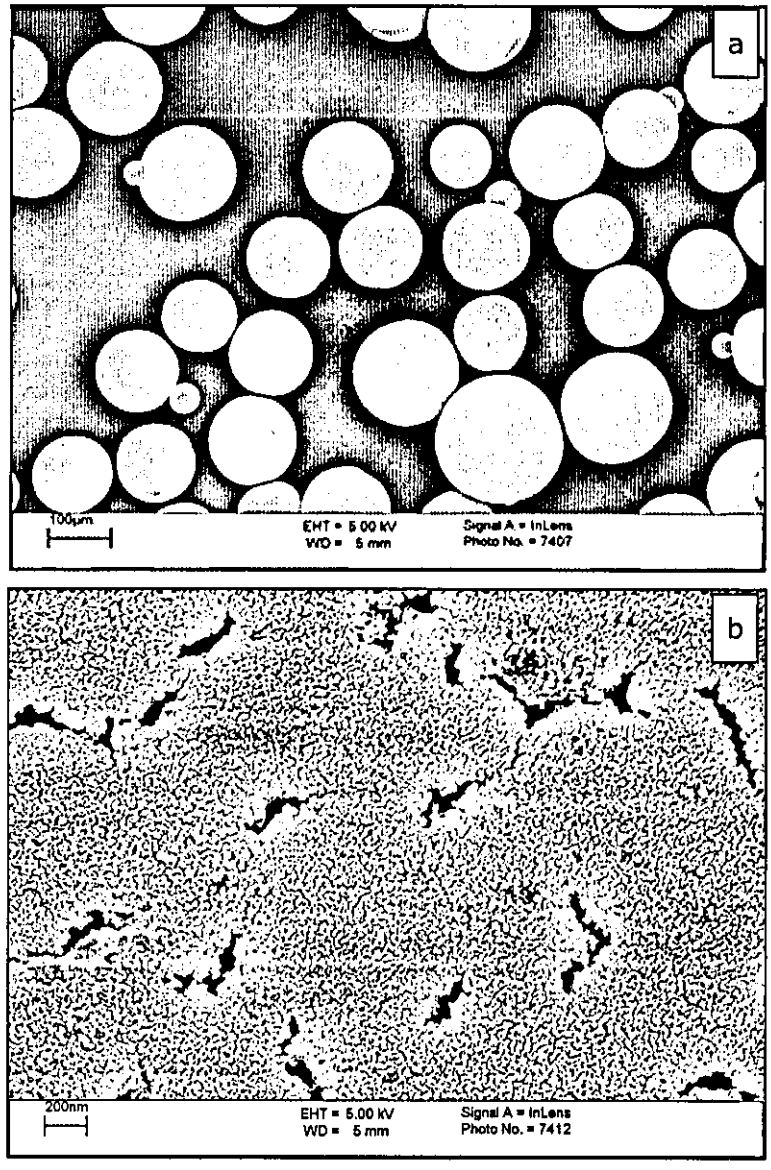

Figure 4-21 Spray freeze dried powder obtained from 28 vol% solids suspension using TAC as dispersant at a) low magnification and b) high magnification.

4.3.2.4 Benchmark submicron powder

The benchmark TOSOH powder is shown in Figure 4-22. These granules also had a crater in the centre similar to SD14 powders.

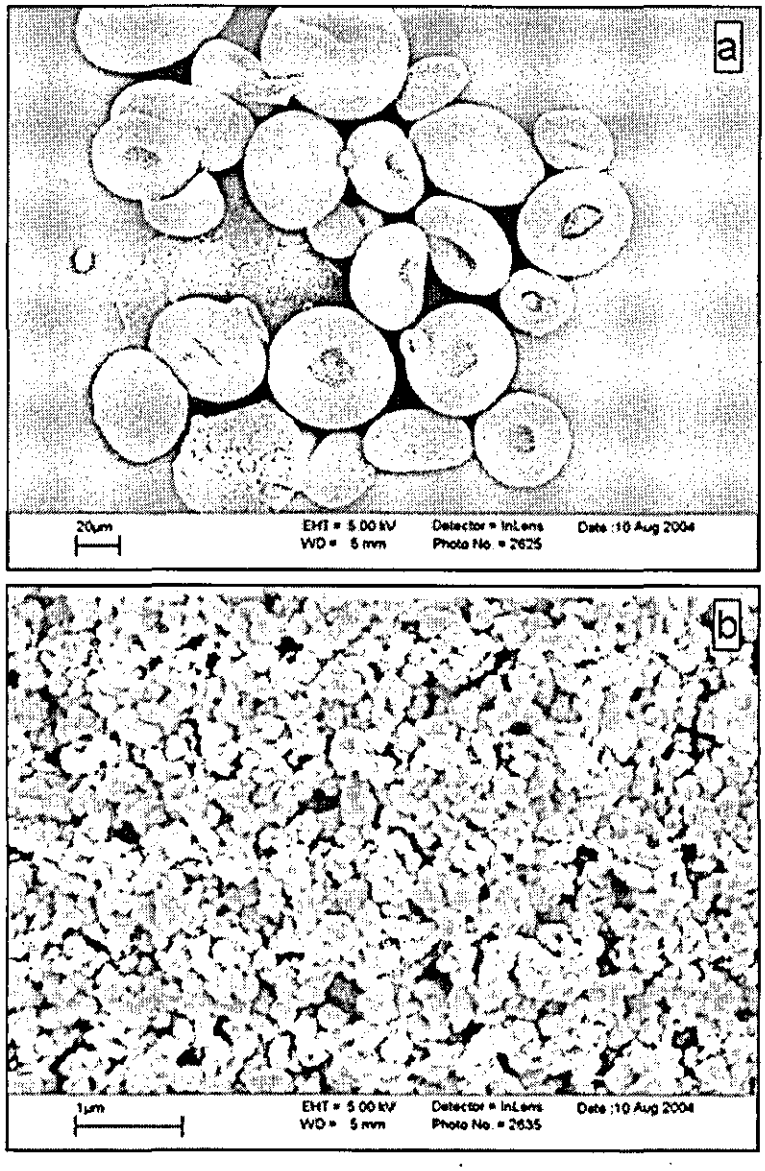

Figure 4-22 Benchmark submicron TOSOH powder at a) low magnification and b)high magnification.

4.4 Powder flowability

4.4.1 Hall flowmeter

Denser granules made from high specific gravity slips had a better gravimetric flow rate (gs^{-1}) in the Hall flowmeter [129]. The mass and volumetric flow rates of the powders are presented in Figure 4-23. It can be seen that the flow rate increased with increase in the orifice diameter as expected. Intermittent / poor flow was observed for spray freeze dried

granules from 5.5 vol% suspension through the 2.5 mm diameter orifice and hence the exact flow rate could not be measured. The flow rate of spray dried granules from the as-received, 5.5 vol% ZrO_2 suspension and spray freeze dried granules from 28 vol% suspension were comparable to that of the benchmark TOSOH powder. The oven dried powder was cohesive and did not flow through the Hall flowmeter setup at all. Flowability measurements were not carried out on spray freeze dried granules from nanosuspensions with solid content in the range 14.3 vol% to 28 vol% owing to the limitations on the amount of powder needed for such tests. For spray freeze dried granules, sieved fractions were preferred to subvert effects arising from differences in granule size distribution.

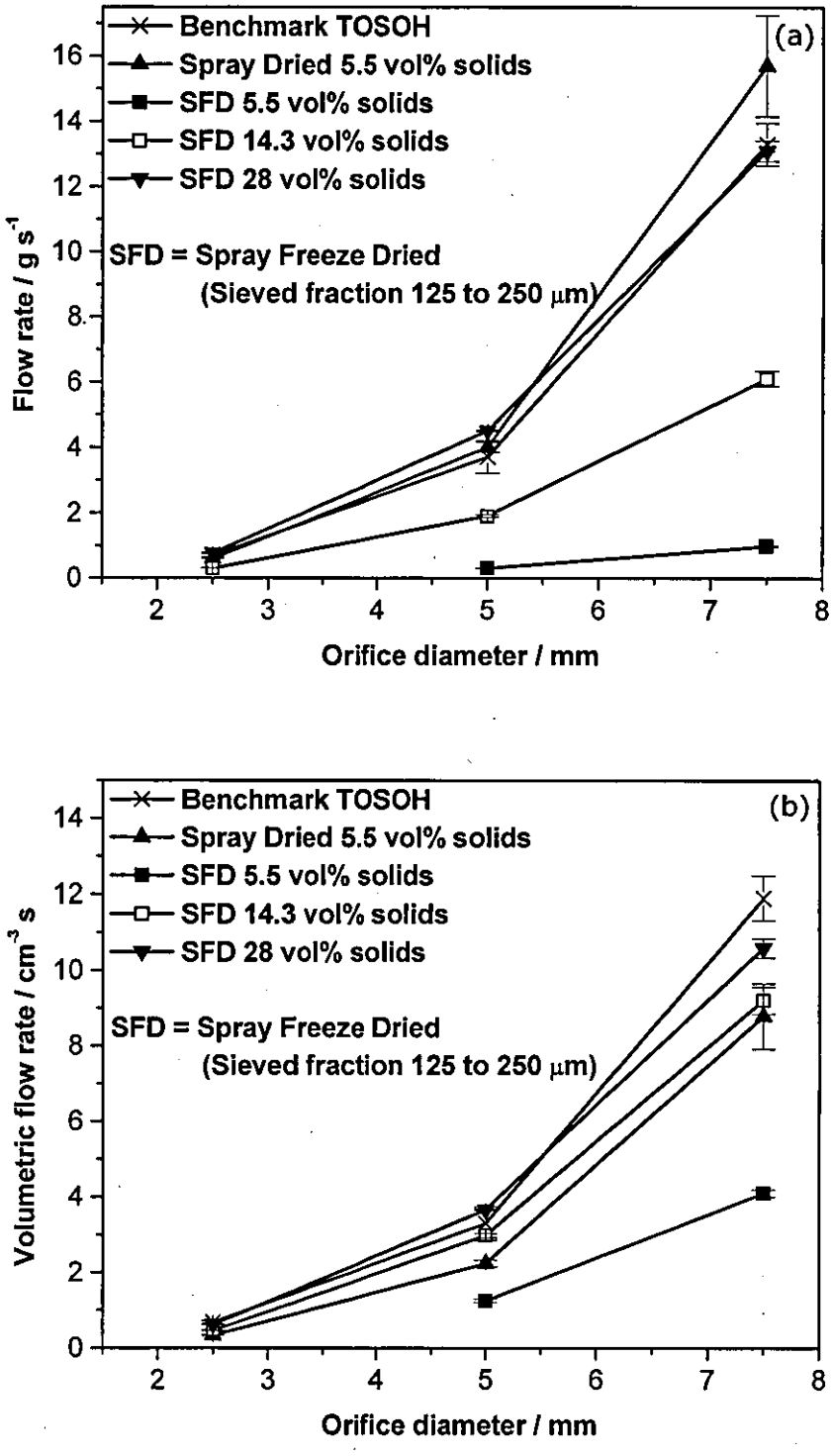

Figure 4-23 a) Mass flow rate and b) Volumetric flow rate for different powders.

4.4.2 Hausner ratio

The other technique used to characterise powder flowability utilised the fill density and tap density as given in Table 4-1. A Hausner ratio near unity would mean excellent powder flow characteristics. The increase in tap density of the powder with increase in solid content of the suspension is evident for the spray freeze dried granules. The errors were within 5% of the stated mean value.

Table 4-1 Flowability of different powders

Powder Description	Fill density, g cm^{-3}	Tap density, g cm^{-3}	Hausner ratio	%Compressibility	Flowability
Oven dried	0.95	1.62	1.7	41.1	Poor
SD from 5.5 vol% suspension	1.79	2.06	1.15	13.3	Good
SD from 14.3 vol% suspension	1.19	1.45	1.22	18.18	Fair
SFD from 5.5 vol% suspension	0.22	0.35	1.57	36.45	Poor
SFD from 14.3 vol% suspension	0.65	0.71	1.1	9.09	Good
SFD from 28 vol% suspension	1.24	1.31	1.02	5.76	Excellent
Benchmark TOSOH	1.24	1.52	1.22	18.51	Fair

The increase in fill density on spray drying was brought about by closer packing aided by the spherical shape of the granules (Table 4-1). The reason behind the lower bulk density of the SD14 granules compared to SD5 granules is two fold, (i) the addition of the organics reduced the theoretical density of the mixture and (ii) these granules were either hollow or had a donut shape which packed poorly in comparison to the denser, spherical, SD5 granules. Although denser granules are generally obtained in spray drying when the specific gravity of the slurry is higher

provided the other parameters do not change [129], in this case, the increase in viscosity with the increase in solid content of the suspension effectively reduced the granule density.

The relation between solid content of the starting suspension and the tap density of the spray freeze dried granules is shown in Table 4-2. The theoretical deduction is based on the following assumptions: (i) the air inclusion during spraying was negligible, (ii) there was no shrinkage of the granules during drying, (iii) the packing efficiency of the granules was 60% at the end of tapping and (iv) all the granules were equisized spheres. As in Figure 4-24, it can be seen that the experimentally obtained tap densities were higher than theoretically predicted. This was because of the wide granule size distribution normally realised in practice. The calculations agree with reported experimental values for other materials in the literature [46].

Table 4-2 Theoretical and realised tap density of SFD granules.

Solid content, Wt%	Solid content, vol%	Expected tap density /g cm^{-3}	% theoretical density	Realised tap density /g cm^{-3}
26	5.5	0.19	3.16	0.22
50	14.3	0.51	8.57	0.65
60	20	0.72	12	-
70	28	1.00	16.8	1.24
80	40	1.44	24	-

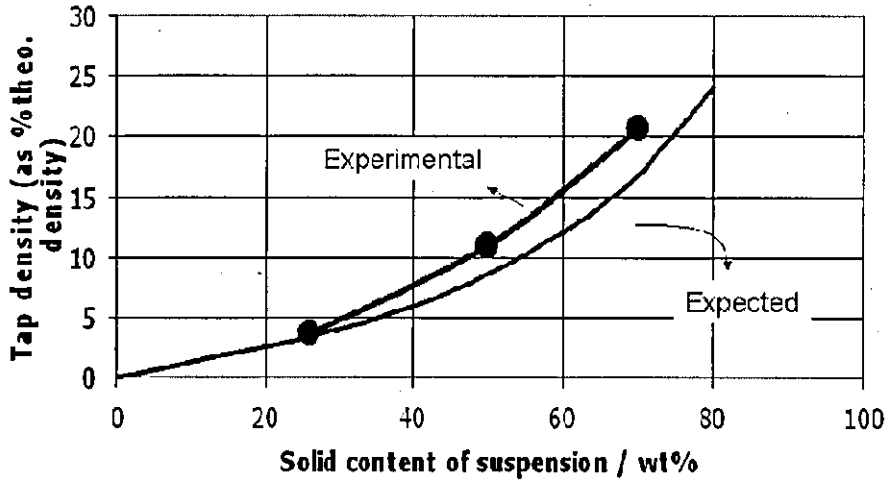

Figure 4-24 Tap density of SFD granules.

4.4.3 Powder flowability by Hall Flow and Hausner ratio

The powder flowability data in Figure 4-23 is derived from one set of experiments. The volumetric and gravimetric flow rates can be related to two distinct powder flow properties. The gravimetric flow rate of SFD5 and SFD14 powders were low in comparison with the benchmark. The SD5 powder and SFD28 powders had good flowability. High mass flow rates can be beneficial for faster die filling and hence higher production rates. In this aspect, the SFD14 powder was not on a par with the industrial benchmark. At the same time, another important parameter is the volumetric flow rate. Higher volumetric flow rate corresponds to good granule rearrangement and hence uniform die filling. In other words, powders with good volumetric flowability homogeneously fill the die and hence the chances of formation of density gradients on consolidation are minimised. Consistent die filling can also be expected in this case. In this regard, the SFD14 powder matched with the benchmark. The lower mass flow rates of SFD5 and SFD14 were caused by low granule density.

In essence, the SFD14 powder had a flowability comparable to that of benchmark powder in most criteria. SFD28 and SD5 granules have slightly better flowability than the industrial benchmark. This would imply that the existing industrial setups can potentially be used for die filling

during nanostructured ceramics mass production. The Hausner ratios confirm these findings.

4.4.4 Model shoe – die filling

This technique was capable of clearly demarcating the flowability of the different powders. The oven dried nanopowder was cohesive and had poor flowability. Even when the shoe was held stationary on top of the die opening, there was no continuous flow or complete die filling, Figure 4-25. Instead, there was random detachment of particles from the bottom of the powder bed in the shoe. This behaviour was called intermittent flow by Schneider et al. [190].

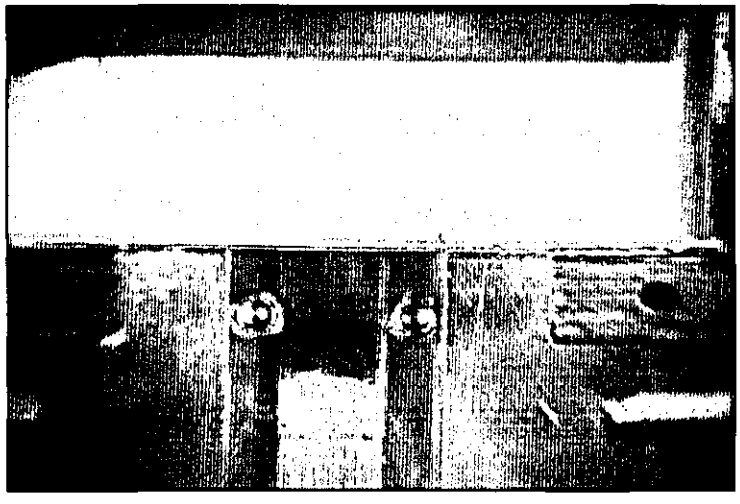

Figure 4-25 Intermittent/poor flow in oven dried nanopowder.

For all the other five powders tested, the die was found to be completely filled when a slow shoe velocity of 50 mm s^{-1} was used. As the speed was increased, there was partial die filling in some cases. The fill ratio at various shoe velocities for different powders is shown in Figure 4-26 to Figure 4-30. The spray dried powder from the as-received 5.5 vol% ZrO_2 based suspension had a comparable critical velocity (and hence flowability) as that of the benchmark TOSOH powder, Figure 4-26 and Figure 4-30.

The spray freeze dried powder from the 5.5 vol% ZrO2 based suspension had improved flowability compared to oven dried powder, but

was not good enough to fill the die completely at a shoe velocity of 100 mm s^{-1}. The critical velocity of the spray freeze dried granules increased with increasing solid content of the starting suspension, i.e. the flowability of the spray freeze dried granules from high solid content suspensions was better than those of low solid content suspensions, a trend also observed in the Hall flowmeter and Hausner ratio based measurements.

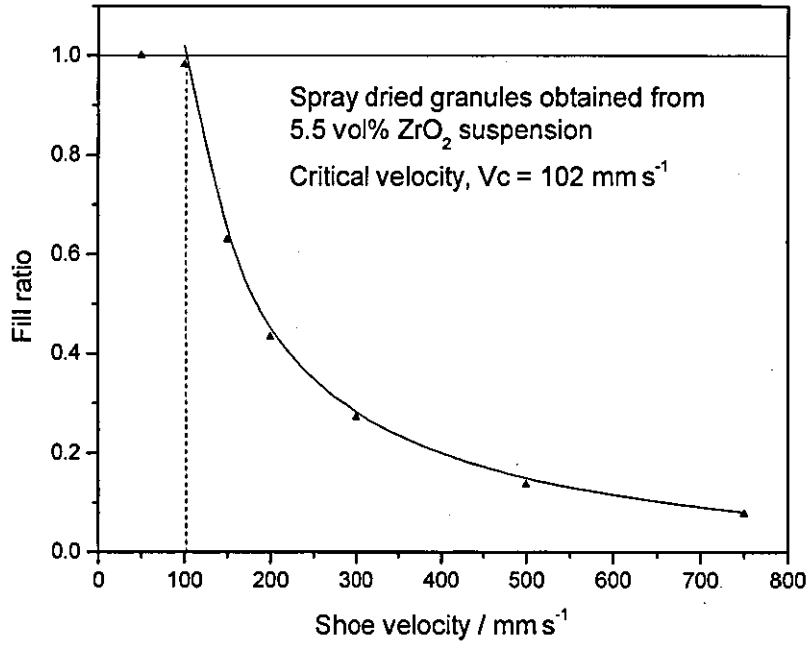

Figure 4-26 Fill ratio at different shoe velocities for SD5 powder.

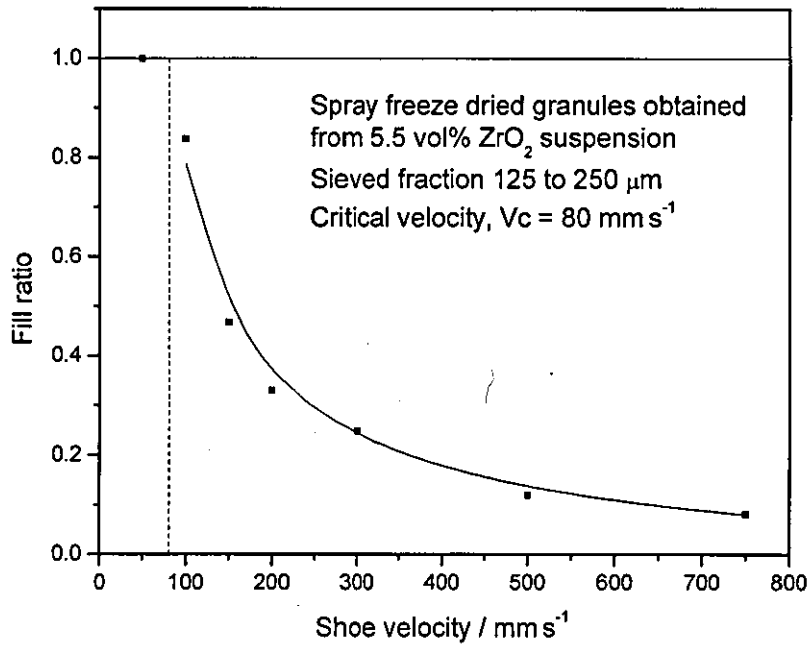

Figure 4-27 Fill ratio at different shoe velocities for sieved SFD5 powder.

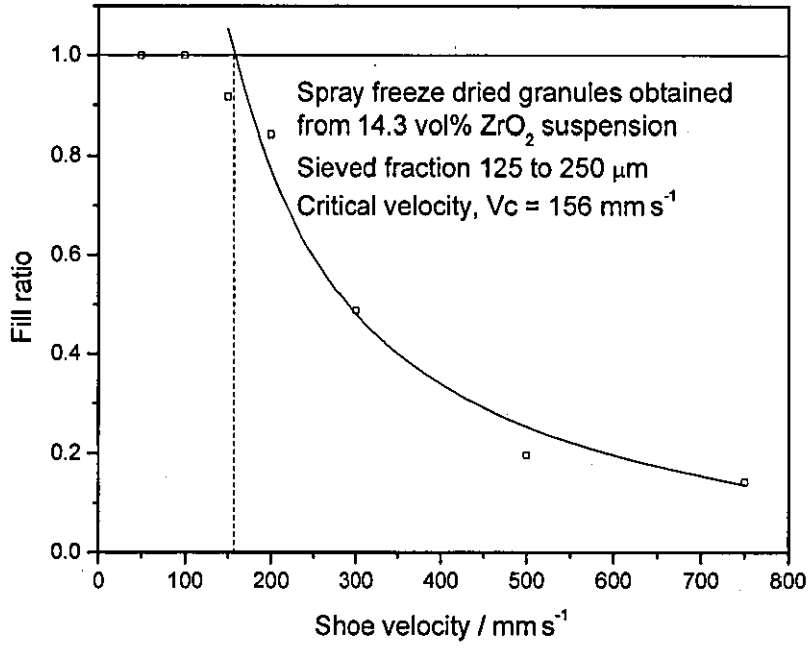

Figure 4-28 Fill ratio at different shoe velocities for sieved SFD14 granules

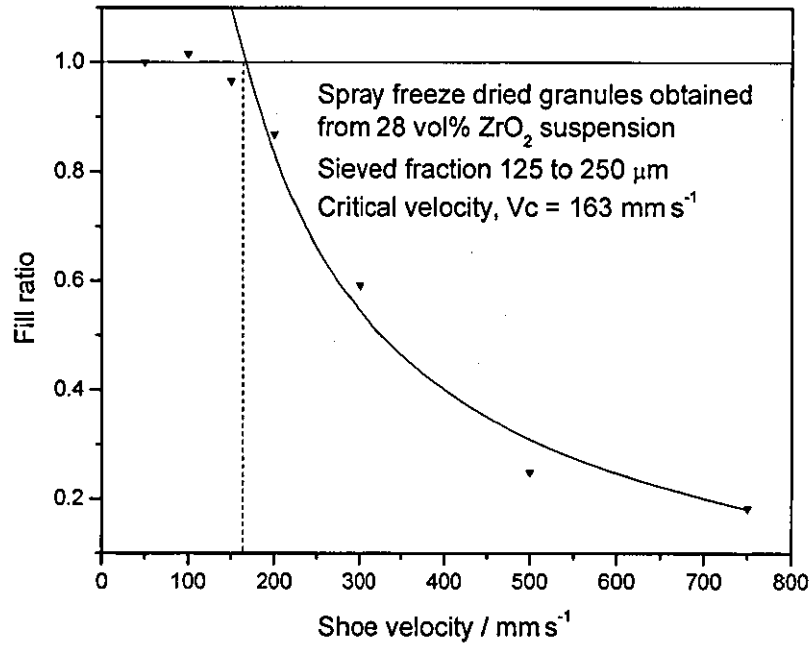

Figure 4-29 Fill ratio for different shoe velocities for sieved SFD28 granules.

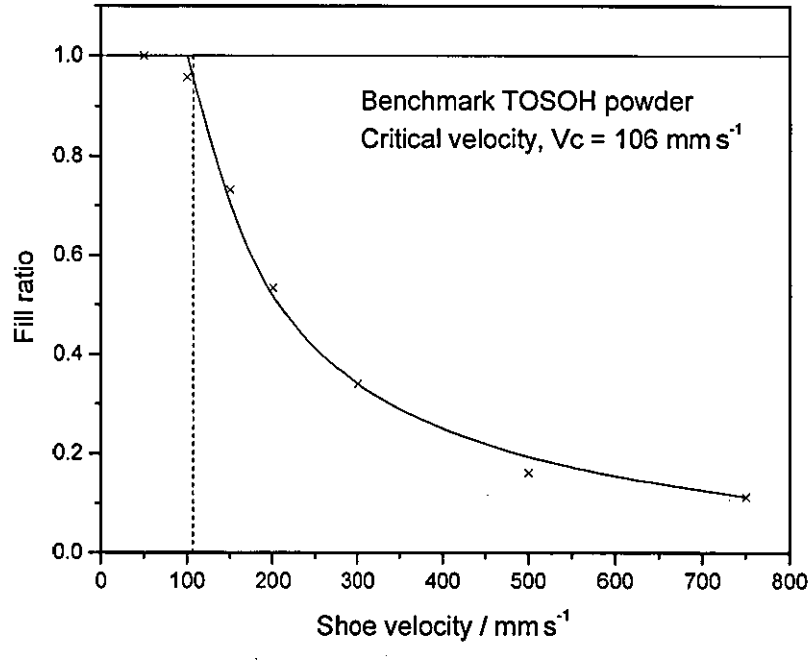

Figure 4-30 Fill ratio for benchmark submicron TOSOH powder.

Various other methods to improve the powder flow are known. Modification can be done in the shoe delivery system (vibration, fluidising

the powder bed, force feeding by rotating paddles etc.,) or the die (by providing channels for air escape and suction filling). However, granulation overcomes the problems associated with poor die filling directly. The increase in filling rate by granulation can be attributed to several factors including (i) increase in the "particle" size (ii) spherical shape and (iii) increase in granule density in some cases. The size increase also greatly reduces the health risks associated with air borne nanopowders. Aeration can improve segregation and suction filling of complex shaped moulds is severely restricted.

As shown in Figure 4-31, the die filling of the SFD5 powders was affected by the upcoming stream of escaping air. Incidentally, these were the lightest powders and were affected the most.

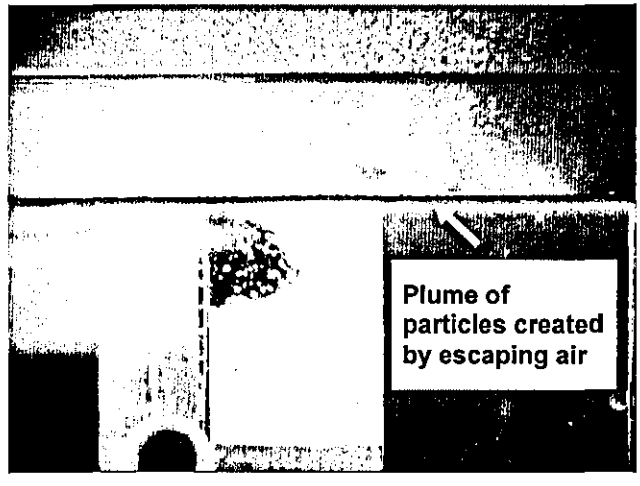

Figure 4-31 Air effect in the flow pattern of SFD5 powder.

The critical velocity for the various powders in the study is presented in Table 4-3. At a slow speed of 50 mm s^{-1}, the die was completely filled for all the flowable powders (i.e. except the oven dried powder) used in the tests. This was taken as the base value for complete die filling, i.e., this corresponds to a fill ratio of unity.

Table 4-3 Critical velocity of zirconia powders.

Powder Description	Critical velocity, Vc / mm s^{-1}
SD5	102
SFD5	86
SFD14	156
SFD28	163
Benchmark TOSOH	106

The critical velocity of the powders showed several interesting features. These powders had different bulk densities; the spray dried powders were typically fine particles whilst the spray freeze dried powders were sieved fractions with a narrow particle size distribution of 125 to 250 μm. As shown in Table 4-1, the spray dried powders had a higher granule density. In general, the powder flowability increases with increasing granule density as denser particles can accelerate faster under the influence of gravity and will have lesser influence because of the escaping air stream. However, the spray dried granules from 5.5 vol% ZrO_2 suspension had a finer particle size as shown in Figure 7-1. Finer particles are lighter and are easily carried away by air than the coarse ones. As a result, the increased flowability that could be achieved in the denser granules was offset by their finer particle size for the SD5 powders.

In the case of spray freeze dried powders, the critical velocity, and hence the flowability, increased with increasing solid content as expected. The spray freeze dried powders from different solid content suspensions had different granule size distributions on granulation. As the powder flowability is influenced by the granule size as well as size distribution, it was essential to sieve the powders in to a narrow size distribution; this helped in clearly visualising the effect of granule density on the powder flow. However, the Tosoh and SD5 powders could not be sieved owing to their finer granule size and were used as such. One of the major concerns

for the die pressing industry is to increase productivity. This can be achieved by quicker die filling and higher compaction speed. Therefore, the increase in powder flow rate is preferred and achieved here. Another important observation was that the powder from high solid content suspensions was less influenced by escaping air. Figure 4-32 shows the powder flow pattern for the two SFD powders at the same time frame with a shoe speed of 100 mm s^{-1}. The SFD28 granules had a good flowability and, as a result, the predominant flow mechanism was nose flow. In case of the SFD14 powders, the flow seems to be a combination of bulk and nose flow at the same time.

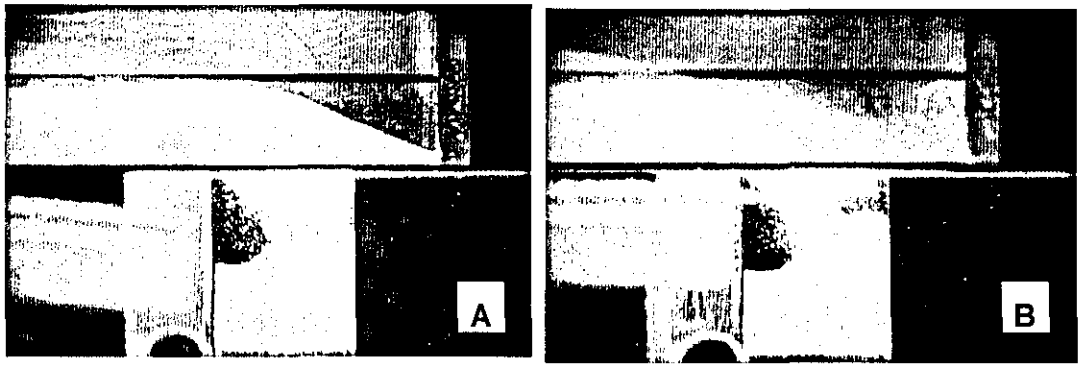

Figure 4-32 Die filling for (a) SFD14 and (b) SFD28 powders.

Figure 4-33 shows the die fill at different shoe velocity for the various powders used in this study. The slope of the powder bed is typical based on the direction in which the shoe travels. It can be seen that the volumetric die fill is comparable for a given velocity for different powders. However, the actual weight of the powder filled in the die varied from powder to powder, Figure 4-34, owing to the difference in their granule density, Table 4-1. For instance, the total weight of the powder in a completely filled die for SFD5 powder was ~0.92 g whilst that of SFD28 granules was ~5.3 g and that of SD5 granules was ~7.1 g. As expected, this difference is in proportion with that of their respective granule densities.

A variety of other experimental conditions are possible. The orientation of the die, shape of the die opening, powder bed height in the shoe, total height of the die, etc., affect the filling characteristics. Suction,

presence of vibration and force feeding also influence the powder flow greatly. However, the aim of the exercise was to benchmark and compare the powders' flowability against the industrially established TOSOH powder. It was demonstrated beyond doubt that granulation by spray freeze drying improved the powder flowability and bettered the commercial submicron granules for solid contents >14.3 vol%.

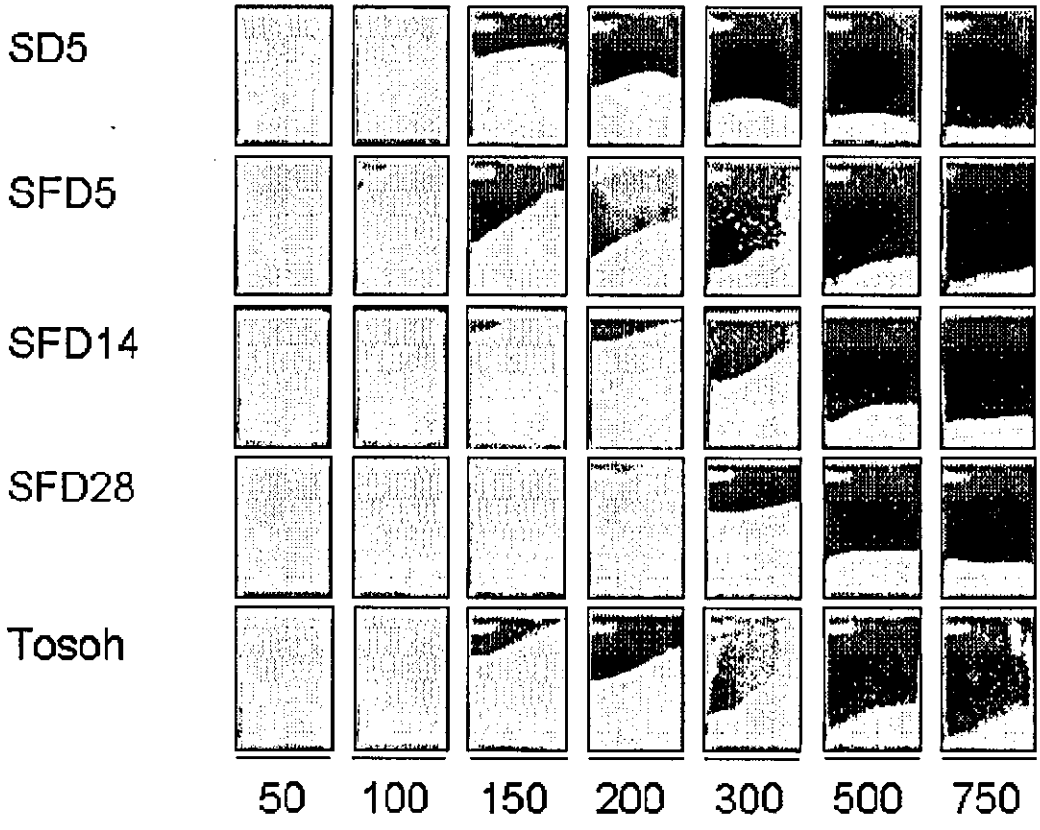

Figure 4-33 Die fill for granulated powders at different shoe velocities.

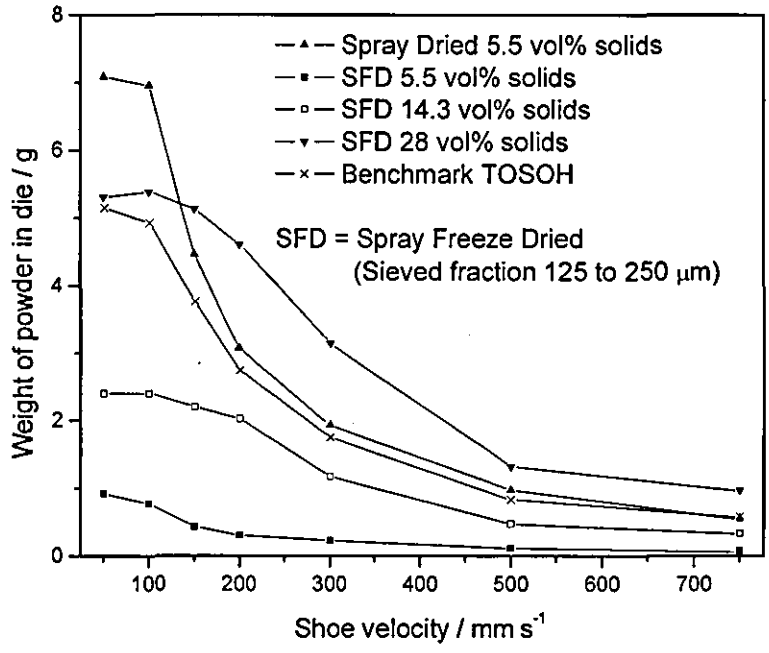

Figure 4-34 Comparision between die filling of different powders.

4.5 Compaction curves

The process of consolidating the powders into compacts was characterised using compaction curves. The increase in density with increase in pressure varied between the powders. The starting point of the curve where the applied load was low approximated to the tap density of the powder. At low pressures, there was a little increase in density till the joining pressure. After this point, the density increased steeply with pressure. The compaction curves for the various powders used in this study are plotted in Figure 4-36 to Figure 4-39. In Figure 4-37, it can be seen that the fill densities of the powders were lower when the solid content of the starting suspension is low. The weight of the pellet used in constructing the compaction curves was that before any binder removal stage. The results were reproducible within 1% error between three runs for each powder.

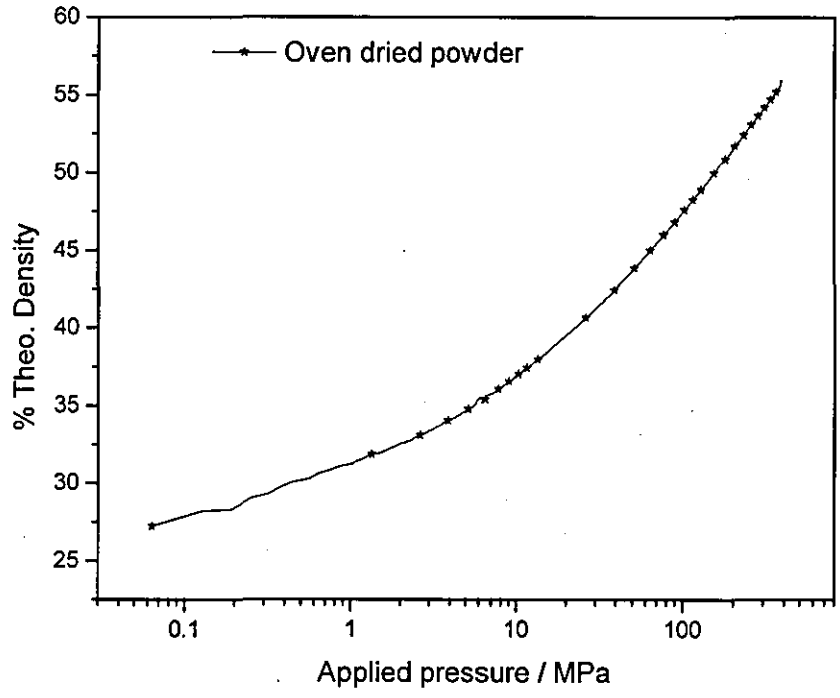

Figure 4-36 Compaction curve for the oven dried

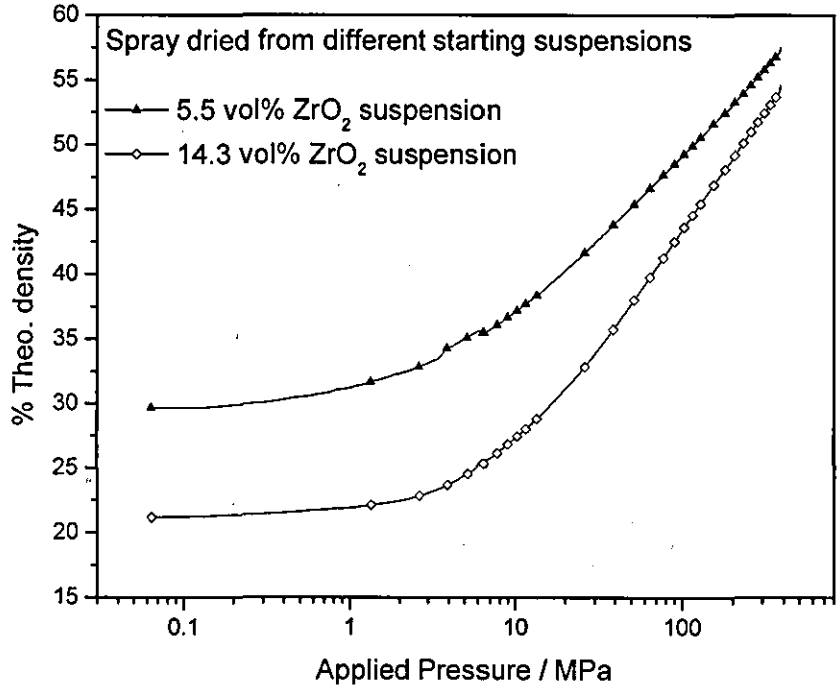

Figure 4-35 Compaction curve for spray dried granules.

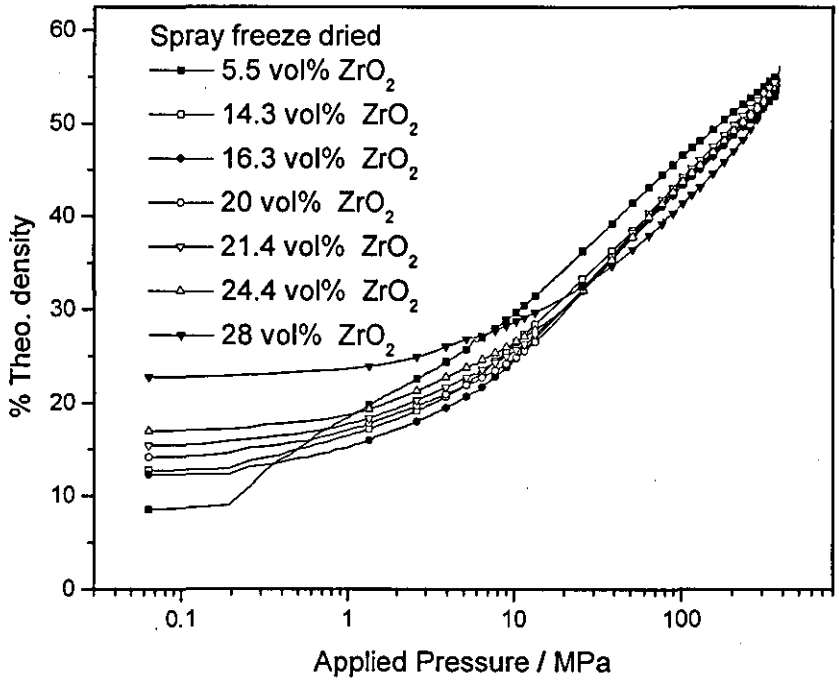

Figure 4-37 Compaction curves for spray freeze dried granules from different solid content suspensions.

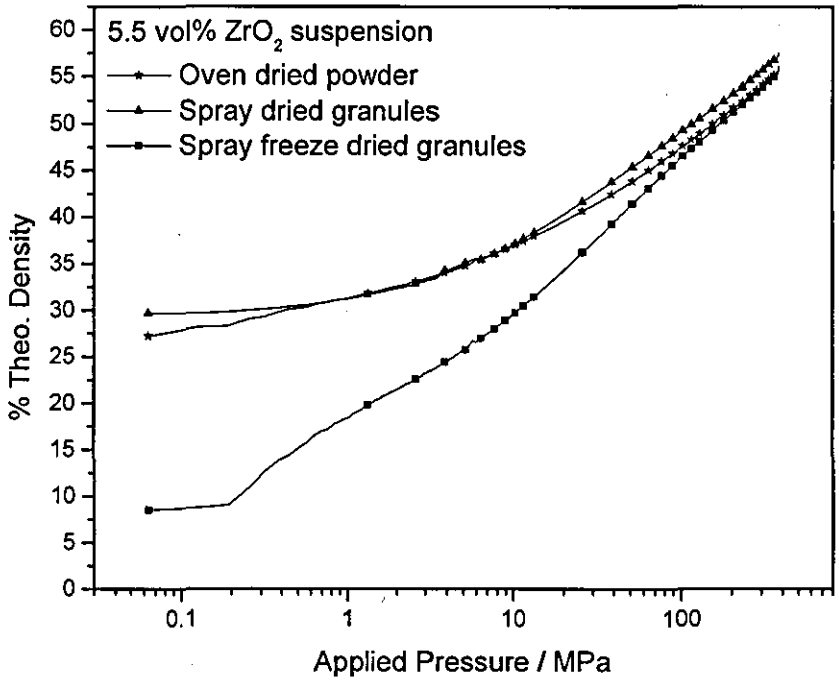

Figure 4-38 Compaction curves for granulated nanopowders obtained from as-received 5.5 vol% nanosuspension by different routes.

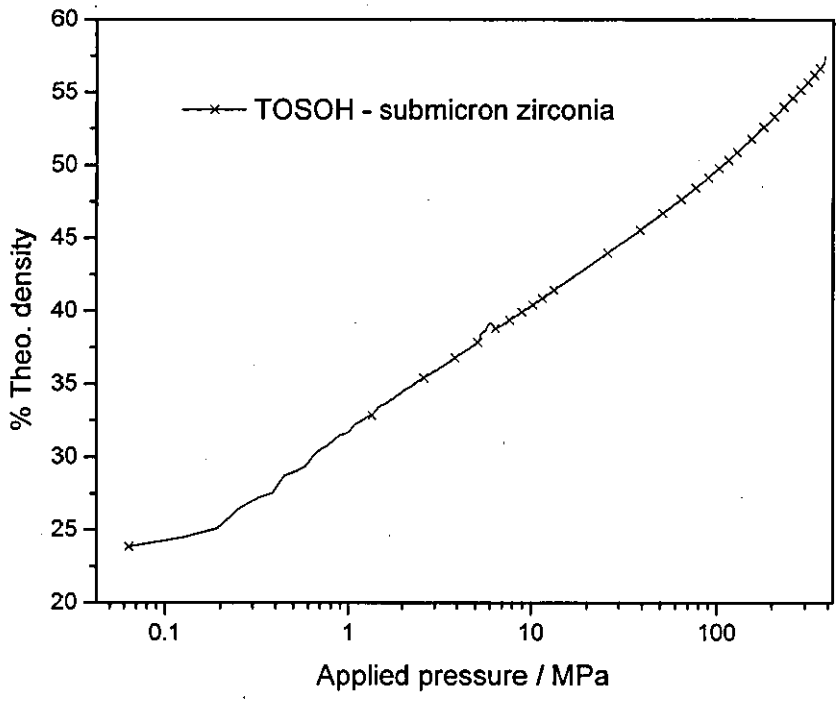

Figure 4-39 Compaction curve for the benchmark TOSOH submicron powder.

In Figure 4-35, the compaction curves for spray dried granules show their deformation and subsequent compaction behaviour. As detailed in the tap density data in Table 4-1, the SD5 granules had a higher density to start with. As consolidation proceeded the density increased rapidly after a certain point. In contrast to most submicron systems, the nanopowders required higher consolidation pressures. The density increased at pressures even beyond 380 MPa, but the cylindrical compacts would show cone formation defects if higher pressures were used. The lower starting density and final density obtained from SD14 granules is attributed to the presence of organic additives.

As the applied pressure was increased for SFD5 granules, these porous granules yielded and collapsed; this is reflected by the rapid increase in the density even at low pressures in Figure 4-37. With the increase in solid content of the starting suspension, the starting density indeed increased. Interestingly, all these compaction curves merge at higher pressures and reach almost same final density. The absence of a knee in the case of the spray freeze dried granules other than SFD5 is probably a result of the pore structure of the granules. These granules

have meso and macropores. As a result the crushing down of these granules does not happen in a single step. Instead, the granules slowly deform as the pressure was increased. As most of the macropores were eliminated, at higher pressures the deformation behaviour of these compacts merged with each other.

The TOSOH powders compacted nicely. As in Figure 4-39, they show a knee point at much lower pressures and the final density attained is higher than those of nanopowder compacts. The clear knee point implies that the granules were weak and had uniform crushing behaviour. The submicron powders have a lower surface area, the inter-particle friction is less and hence they compact to a higher density than their nanosized counterparts.

4.6 Characterisation of green bodies

The green density of the pellets after binder removal at 400°C is given in Figure 4-40. The density of the green compacts was around 53% of theoretical after pressing at ~380 MPa. Oven dried powder with uncontrolled agglomeration lead to a non- uniform microstructure on consolidation at 380 MPa, Figure 4-41. By definition, the granules are intermediates and hence must be destroyed during the subsequent changes. Figure 4-42 show granule relics formed from hard spray dried agglomerates. A similar micrograph is frequently encountered in the literature too. In the case of SD5 granules, the tap density was above 2 g cm^{-3}, this corresponds to a granule density of about 55% of the theoretical value of YSZ. The compact density was not very different from this value. Hence, it can be said that the granules had undergone more rearrangement than deformation during the consolidation stage. Interestingly, this is reflected in the nitrogen adsorption based porosity measurements as well, Figure 4-62, which will be discussed later.

Spray drying involves capillary forces which pull the primary particles closer to each other and cause undesirable agglomerate strengthening. Freeze drying, on the other hand, forms soft agglomerates. With a porosity of 80 – 90%, the single granule strength can be 20 to 50 times lower than that of the conventional powders [46]. Porous granules

yielded deformable granules, which, in turn, formed a homogeneous nanostructure on compaction.

In contrast to the spray dried granules, spray freeze dried granules crushed down into primary particles and left a homogeneous microstructure as in Figure 4-44 and Figure 4-45. This could have been possible considering the friable nature of the SFD5 and SFD14 granules. Evidence of hard agglomerates start emerging in Figure 4-46, where granule-like circular features are seen in the microstructure at low magnifications. The fracture was intra-granular, unlike the spray dried powder compacts. This is probably because of the good knitting of the particles at some points in the granule surface. Also, the low granule density necessitated a lot of particle rearrangement before the final dense body was obtained. Figure 4-47 and Figure 4-48 show clear signs of microscopic density gradients developed in the compact. More granule relics are visible in this case.

Yet another important parameter is the strength of the green compacts. The pressed bodies should have enough mechanical strength to withstand handling and green machining if required. Green machining is preferred over machining of the sintered body owing to the high costs associated with the latter. Die pressing is liable to chipping and capping defects. Improper selection of binders, poor tooling and entrapped air can cause havoc in the production lines. Within this study, capping defects were sometimes observed when a granule with very low fill density, i.e SFD5, was used. When these powders were used, the punch travelled a much longer distance to compact the powder to a given green density. With the increase in solid content, the SFD14 and other granules had better green strength and would withstand handling and sintering. No capping was observed in freeze granulated powders having a starting solid content of greater than 14.3 vol%. As the spray dried powders had higher granule density, they also had good green strength.

The TOSOH powder compact fracture surface was smooth and homogeneous. Very thin lines of separation between granules were visible at higher magnification.

The green density of these nanopowder compacts showed little variation with the difference in granule preparation conditions. This is in contrast with the noticeable microstructural differences. Five green bodies were made and densities measured for each powder.

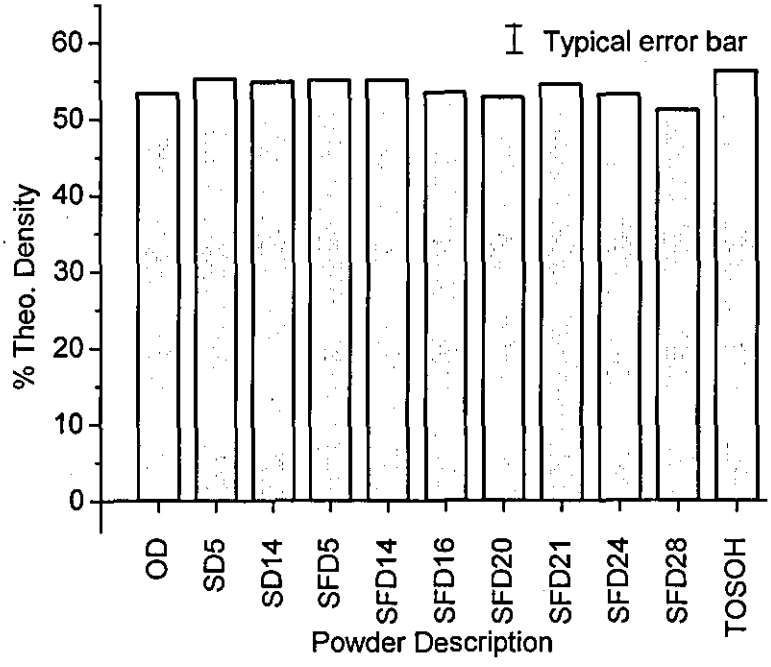

Figure 4-40 Green density of compacts from different powders.

The compacts were obtained from different starting powders by die pressing at ~380 MPa. Oven dried powder compact showed signs of uncontrolled agglomeration carried over from the parent powder, Figure 4-41a, although it was homogeneous in between the uncrushed granules, Figure 4-41b.

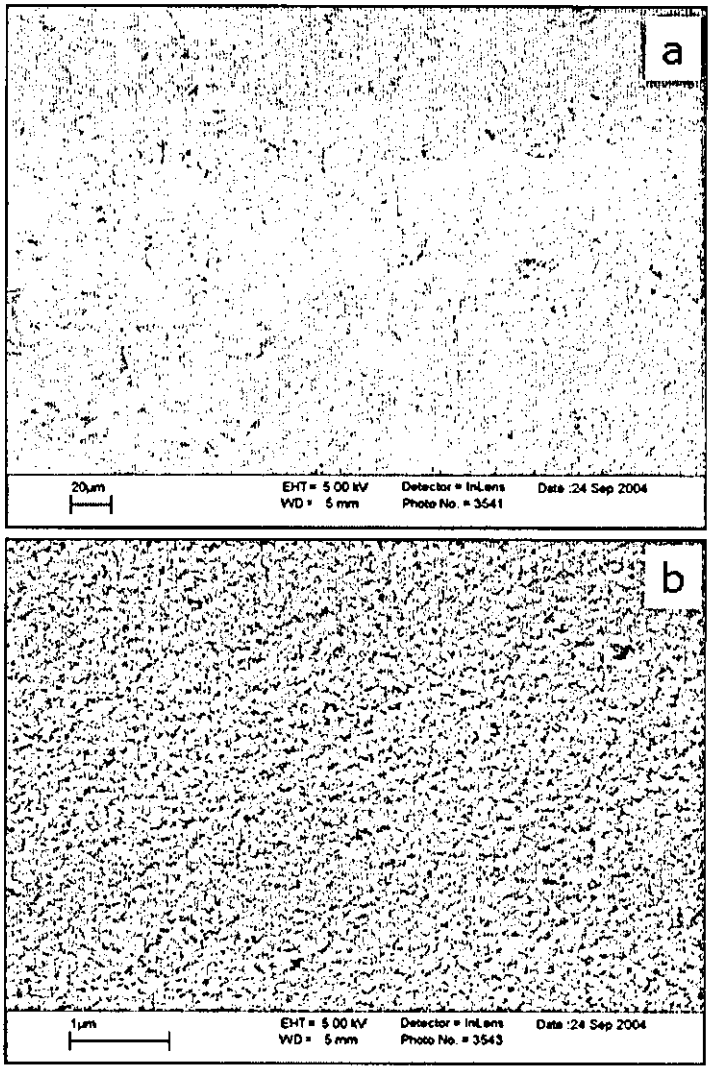

Figure 4-41 Green microstructure observed from the fracture surface of a compact pressed at 380 MPa using oven dried powder obtained from the 5.5 vol% suspension (a) at low magnification and (b) at high magnification between the uncrushed granules.

The spray dried granules on consolidation by die pressing did not yield homogeneous microstructures either. Inter-agglomerate and intra-agglomerate pores were clear in the case of dispersed, 5.5 vol% solids suspension based spray dried granule compact in Figure 4-42. The donut shaped granules from 14.3 vol% solids suspension seem to have broken, but not necessarily into primary particles, Figure 4-43.

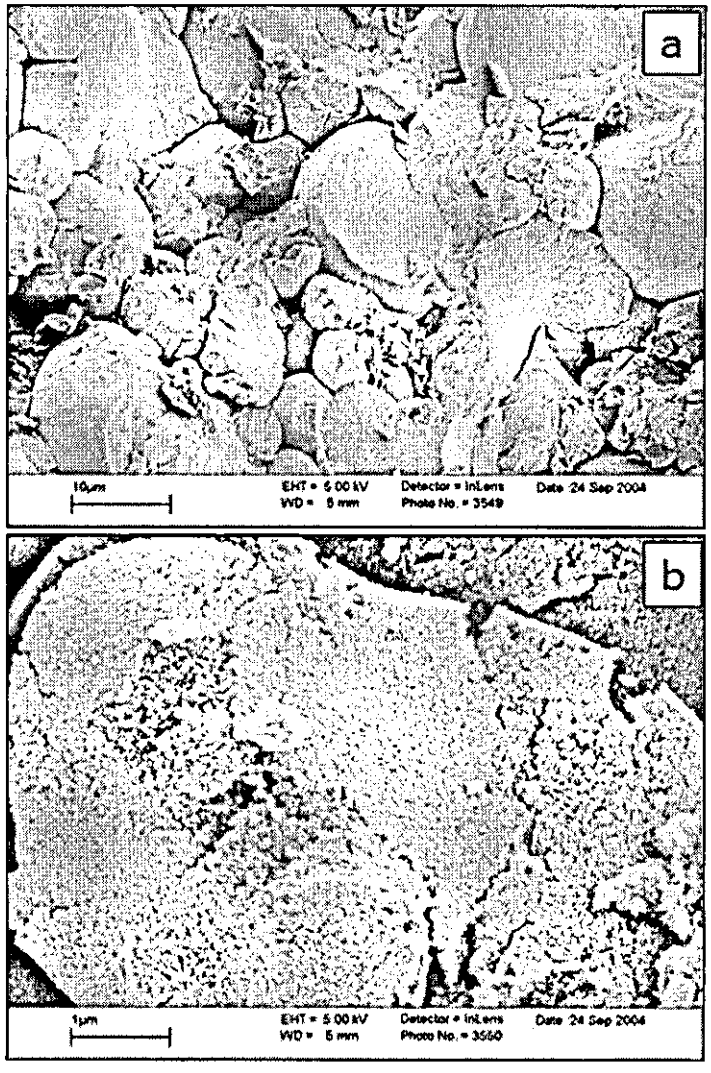

Figure 4-42 Green microstructure observed from the fracture surface of a compact pressed at 380 MPa using spray dried powder obained from the 5.5 vol% suspension (a) at low magnification and (b) at high magnification showing the uncrushed granules.

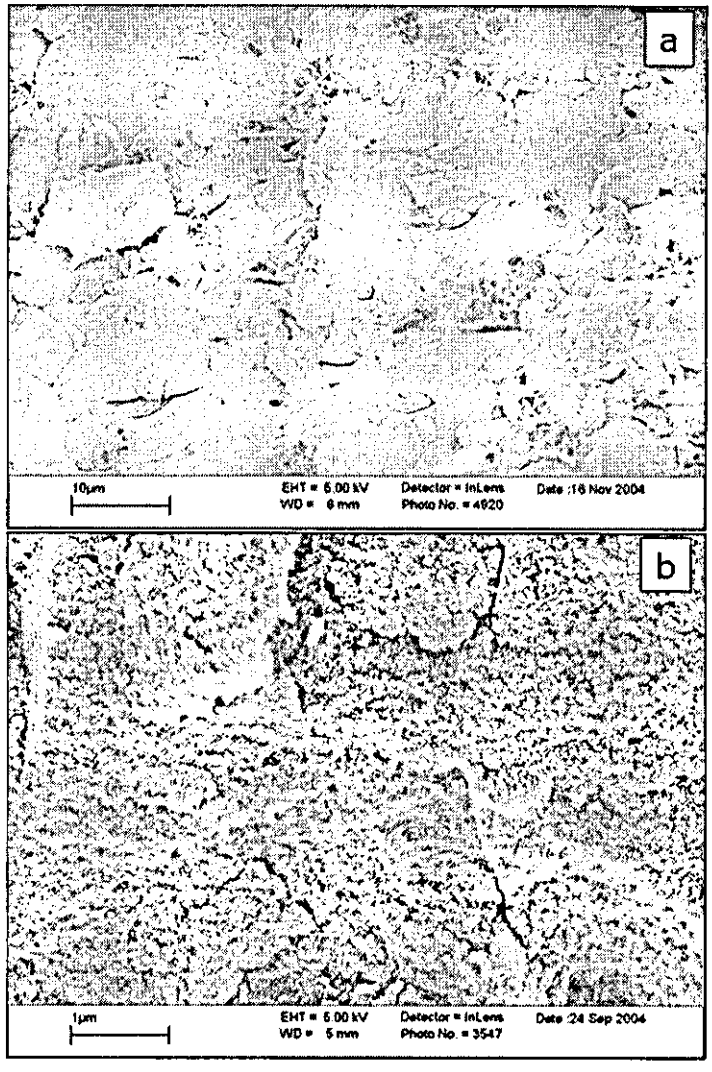

Figure 4-43 Green microstructure observed from the fracture surface of a compact pressed at 380 MPa using spray dried powder obtained from the 14.3 vol% suspension (a) at low magnification and (b) at high magnification showing the partially crushed granules..

As may be seen in Figure 4-44, the fracture surface of the green body pressed at ~380 MPa from the spray freeze dried granules obtained from the as-received 5.5 vol% ZrO_2 suspension was homogeneous. No granule interface was observed. The fracture surface of green compacts made from spray freeze dried granules of different solid content are shown at different magnifications in Figures 4-47 to 4-50. Whilst the microstructure looked homogeneous for the 14.3 vol% solids derived spray freeze dried granules, Figure 4-45, for higher solids contents microstructural heterogeneitioes started emerging. In Figure 4-46,

granule relics were not clearly visible, nevertheless the fracture surface appears different to Figure 4-44 especially at low magnifications.

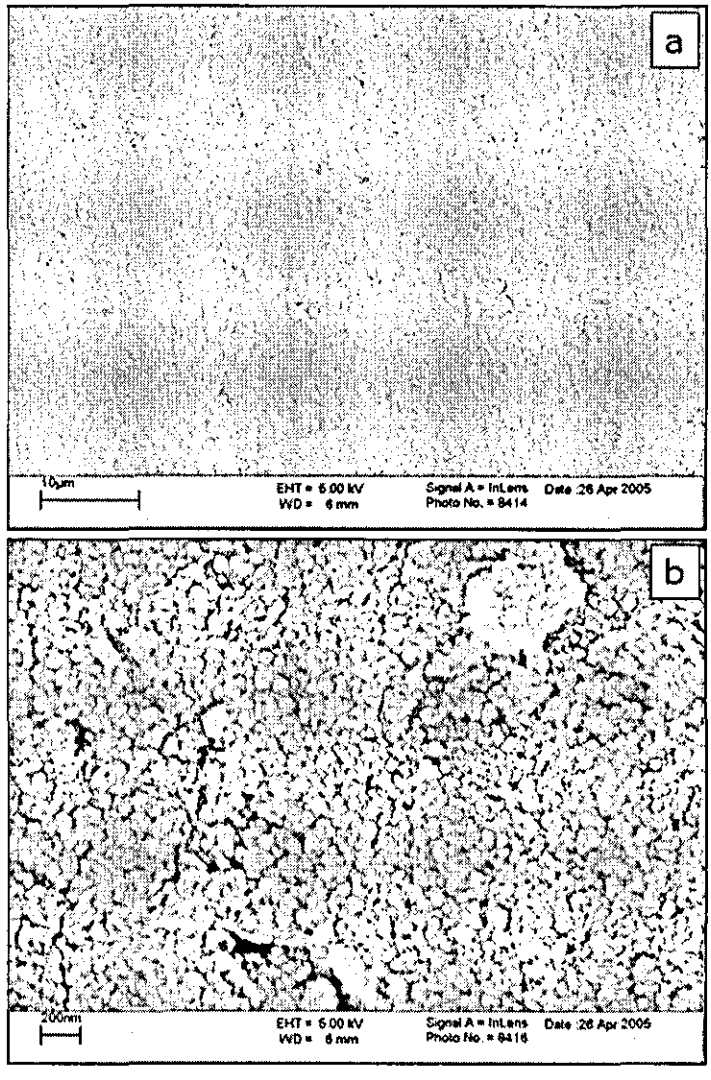

Figure 4-44 Green microstructure observed from the fracture surface of a compact pressed at 380 MPa using spray freeze dried powder obtained from the 5.5 vol% suspension (a) at low magnification and (b) at high magnification showing a homogeneous microstructure.

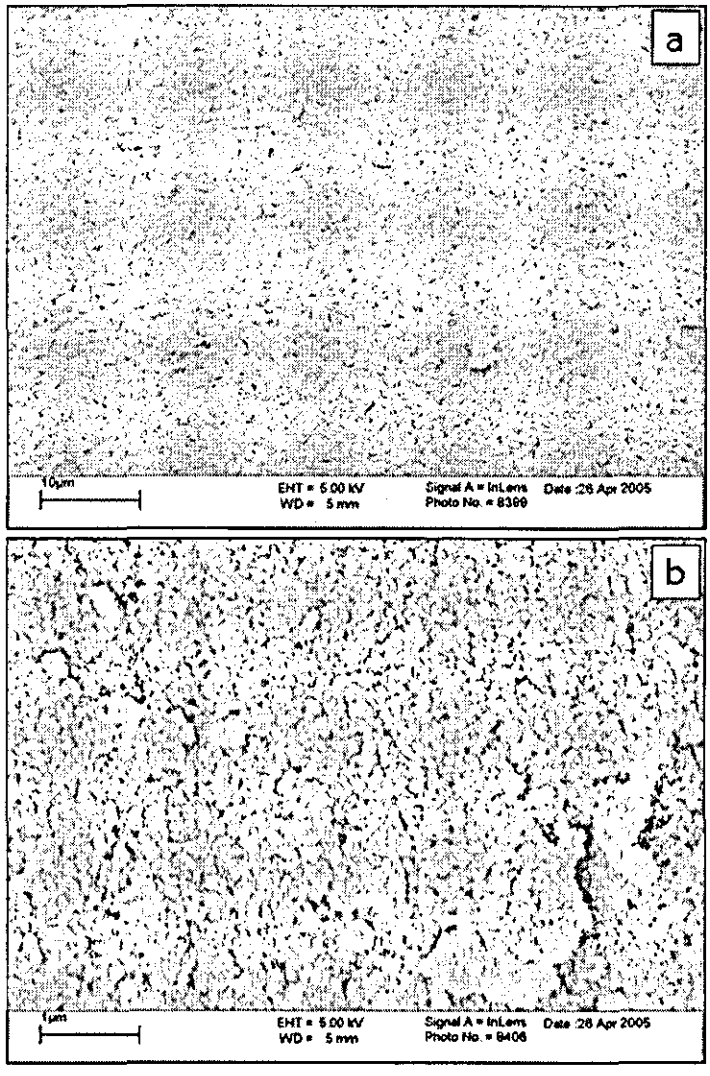

Figure 4-45 Green microstructture observed from the fracture surface of a compact pressed at 380 MPa using spray freeze dried powder obtained from the 14.3 vol% suspension (a) at low magnification and (b) at high magnification showing a homogeneous microstructure.

The granule structure can be better delineated in Figure 4-47, but still the fracture is trans-granular meaning that the granules had knitted well together at the boundaries. In Figure 4-48, the granules had left a clear trace of the rounded shape of the agglomerates.

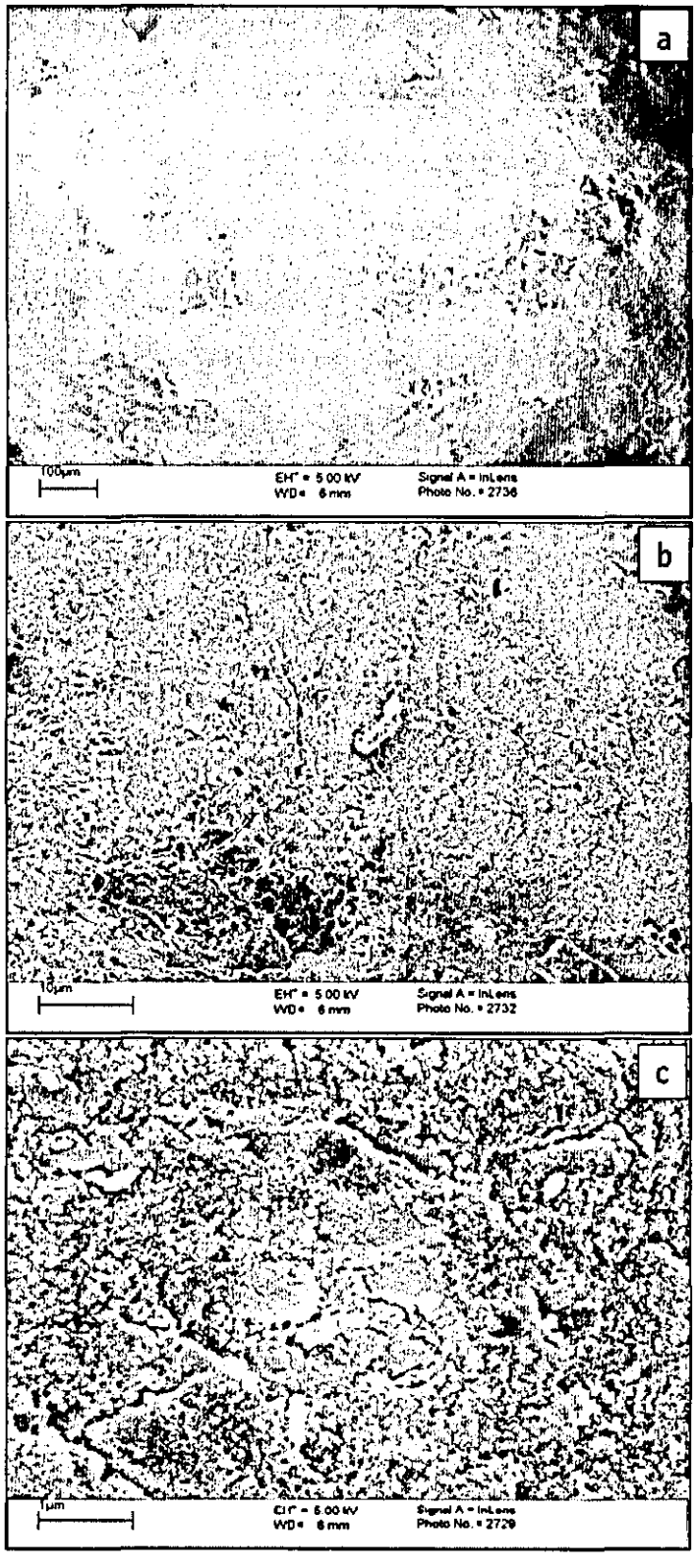

Figure 4-46 Green microstructure of the fracture surface of a compact pressed at 380 MPa using SFD powder obtained from 16.3 vol% suspension (a) at low magnification, (b) higher magnification and (c) high magnification showing agglomerates.

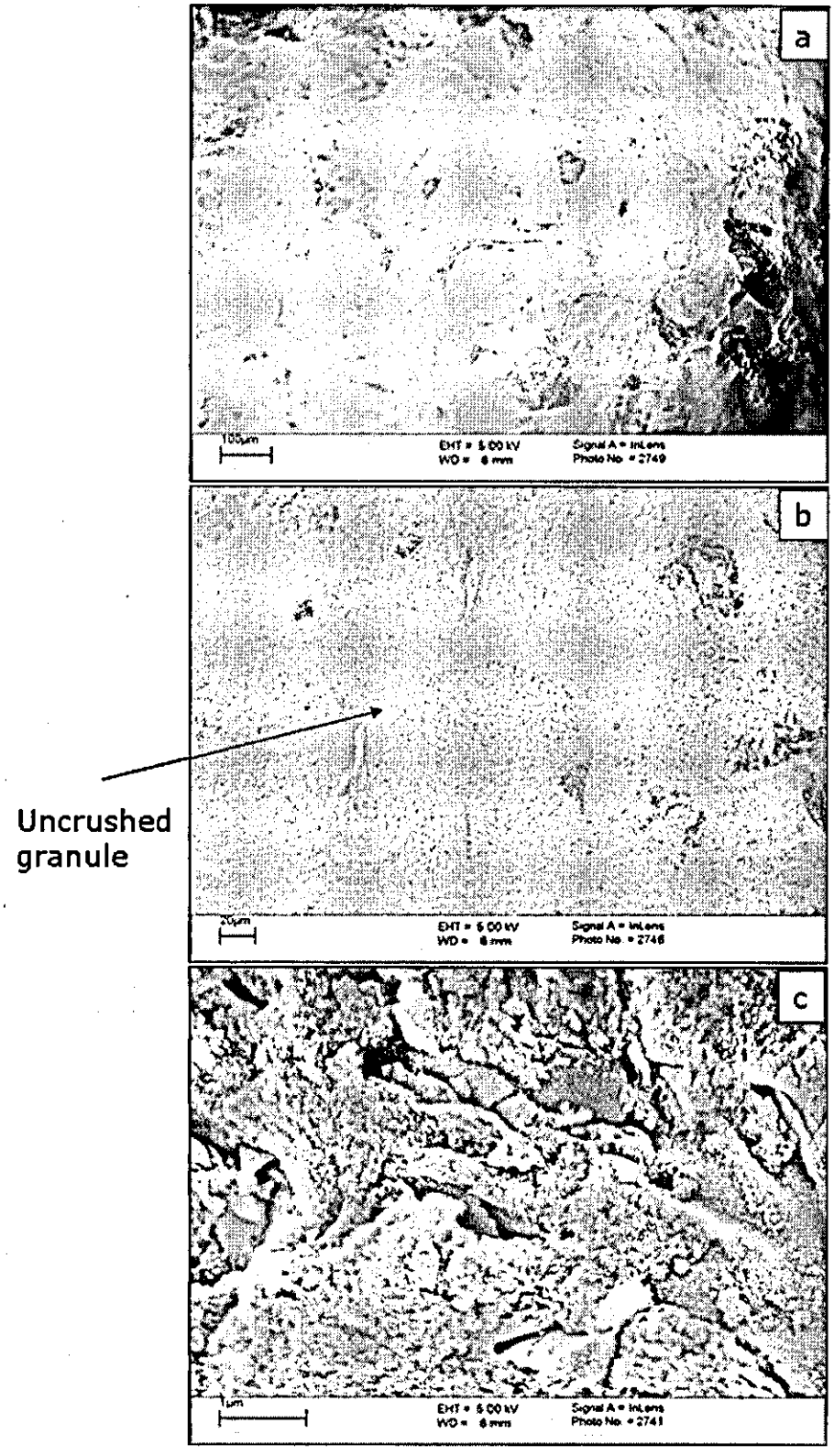

Figure 4-47 Green microstructure of the fracture surface of a compact pressed at 380 MPa using SFD powder obtained from 21.4 vol% suspension (a) at low magnification, (b) higher magnification and (c) high magnification showing uncrushed granules.

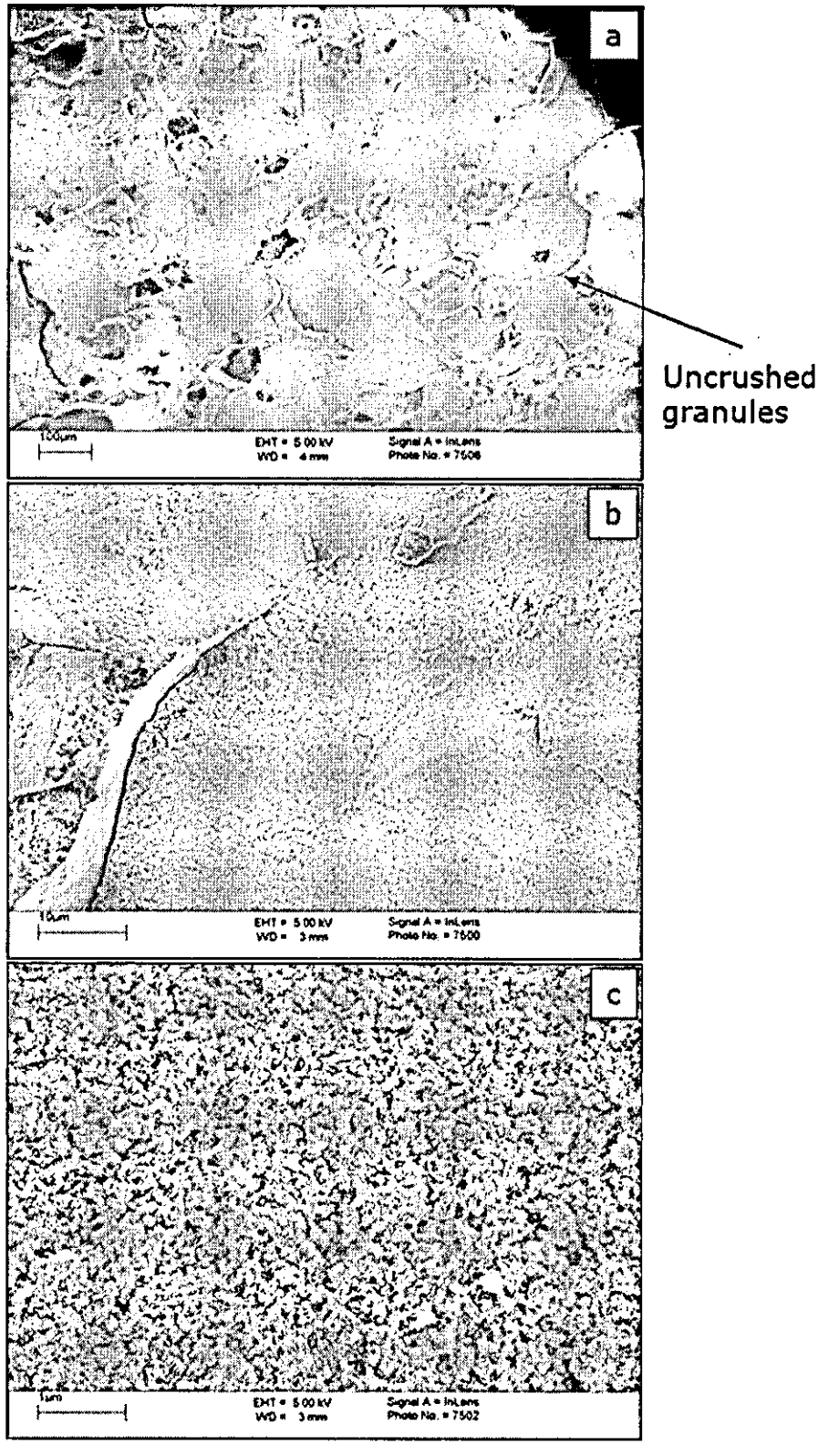

Figure 4-48 Green microstructure of the fracture surface of a compact pressed at 380 MPa using SFD powder obtained from 28 vol% suspension (a) at low magnification, (b) higher magnification and (c) high magnification showing uncrushed hard agglomerates.

The fracture surface of the benchmark TOSOH powder after consolidation at ~380 MPa is shown in Figure 4-49. The microstructure was homogeneous, although the primary particles were rather larger in this case. It is believed that the presence of binders resulted in the 'smeared' looking fracture surface.

In all cases, the inter-granular pores were very elongated; these larger size pores did not seem to be interconnected in a continuous fashion.

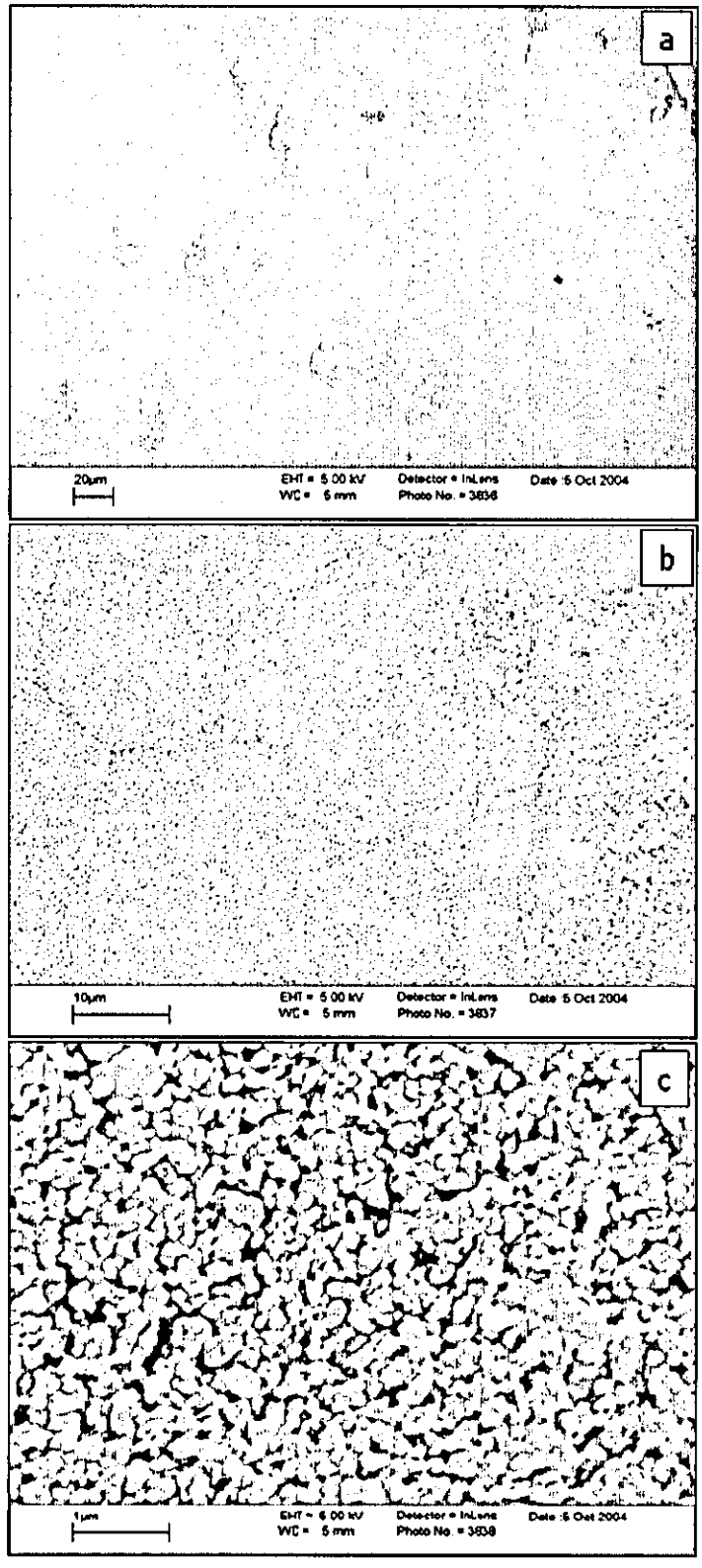

Figure 4-49 Green microstructure of the fracture surface of a compact pressed at 380 MPa using submicron TOSOH powder (a) at low magnification, (b) higher magnification and (c) high magnification showing a homogeneous microstructure.

4.7 Nitrogen adsorption isotherms

Physisorption is defined as the weak bonding of the adsorbate, reversible by small changes in pressure or temperature. The isotherms and the pore size distribution obtained by BJH method for the nanopowders [166] and compacts were similar to those reported in the literature [184, 165]. The nitrogen adsorption - desorption isotherm for the oven dried powder showed a typical Type IV behaviour, Figure 4-50 suggesting that the powders were mesoporous. Type IV isotherms follow the trend similar to Type II in the low pressure region ABC in the curve, but at a certain point, the curve begins to deviate upwards (CDE) until higher pressures, where its slope decreases, see section 2.16.3. As the saturation pressure is reached, the curve may again have an upward turn, mostly due to flooding.

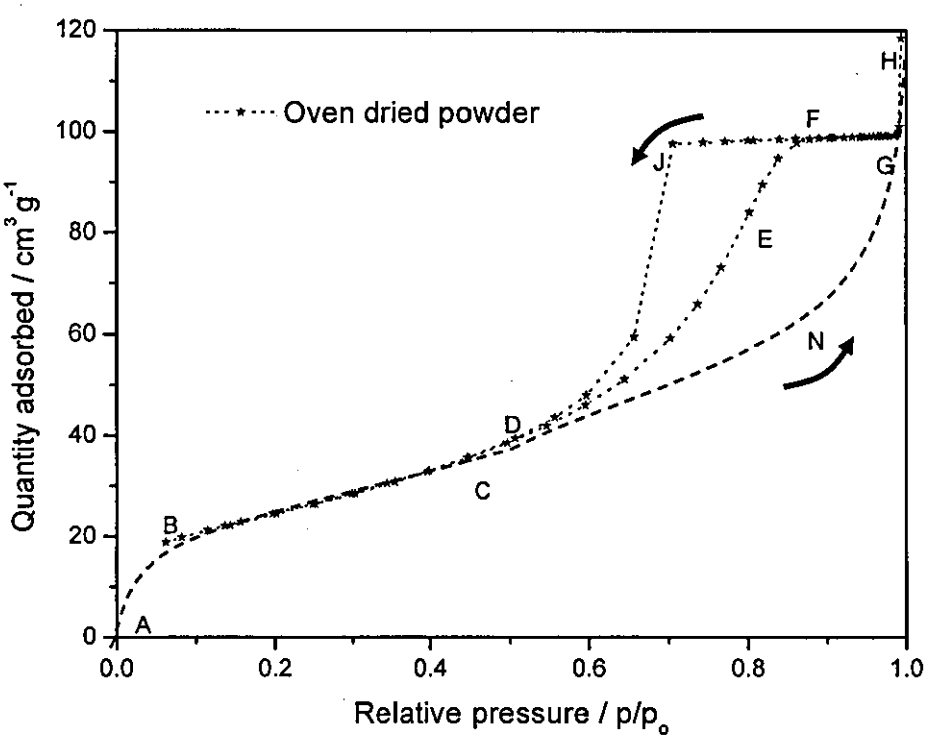

Figure 4-50 Nitrogen adsorption - desorption isotherm for oven dried powder from 5.5 vol% suspension showing Type IV behaviour.

In Figure 4-50, the adsorption leg ABDEGH is significantly different from the dashed lines ABCNG that correspond to adsorption in a non-

porous surface. The increase in adsorption is a function of the mesoporosity within the powder agglomerates. The increased adsorption is attributed to capillary condensation in the pores and is governed by the Kelvin equation. Another important characteristic of this isotherm is its hysteresis loop, which is associated with the filling and emptying of the mesopores [191]. The exact shape of the loop varied between different samples, but as shown in the figure, the desorption branch FJD was always above the adsorption branch. This would mean that the amount adsorbed was always greater at any given relative pressure along the 'desorption' branch than along the 'adsorption' branch. This loop is reproducible as long as the desorption run was started from a point after point F.

The isotherm is the basic data gathered during any nitrogen adsorption tests. Various other parameters like BET surface area and pore size distribution were derived from this data.

4.7.1 BET surface area

A typical fit of linearised BET equation to the data is shown in Figure 4-51. A pressure range from 0.05 to 0.3 of p/p_0 was used. At least 5 data points were used to find the multipoint specific surface area.

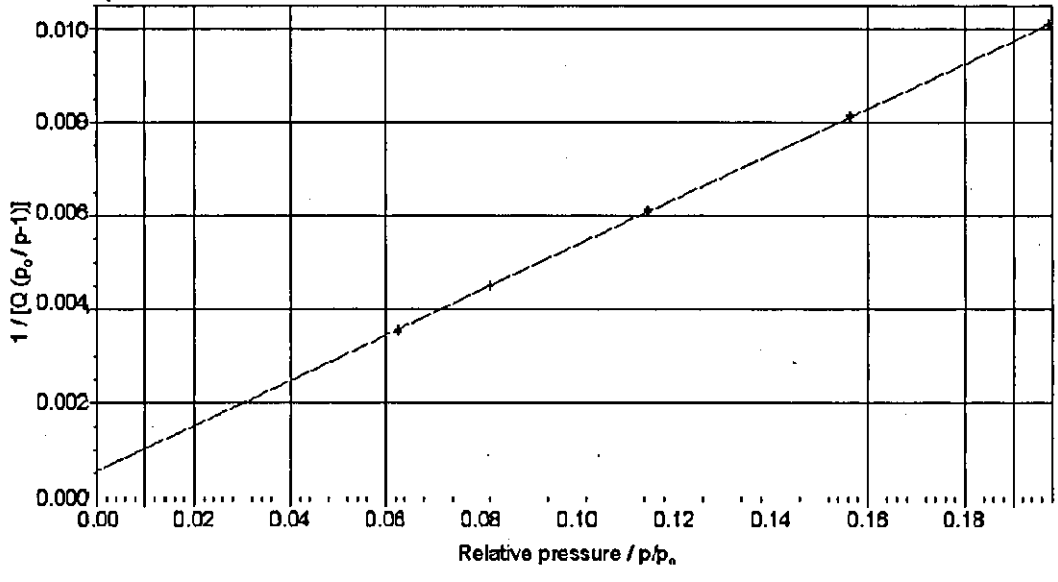

Figure 4-51 BET transform plot for oven dried powder showing good fit with linearised BET equation.

The surface area of the nanopowders obtained from different drying routes and their compacts was 85±3 $m^2 g^{-1}$. This corresponds to a primary particle size of 11.76±0.33 nm, as explained in 2.16.2. The surface area of TOSOH powder and its compact were 3.38±0.1 $m^2 g^{-1}$.

4.7.2 Pore size distribution from nitrogen adsorption isotherms

Though the surface areas were similar, the pore size distribution varied amongst the powders and also between the powder and its compacts pressed at different pressures. The mesoporosity in oven dried powder is shown in Figure 4-52a and b. The maximum pore size that could be probed in this powder system was about 120 nm. Above this limit, the pore size distribution obtained was erratic and not reproducible owing to the limitations of the technique. It can be seen that the majority of the pores were less than 20 nm and the peak was at about 10 nm for the derivative function shown in Figure 4-52b. The minimum pore size that could be detected was 1.7 nm.

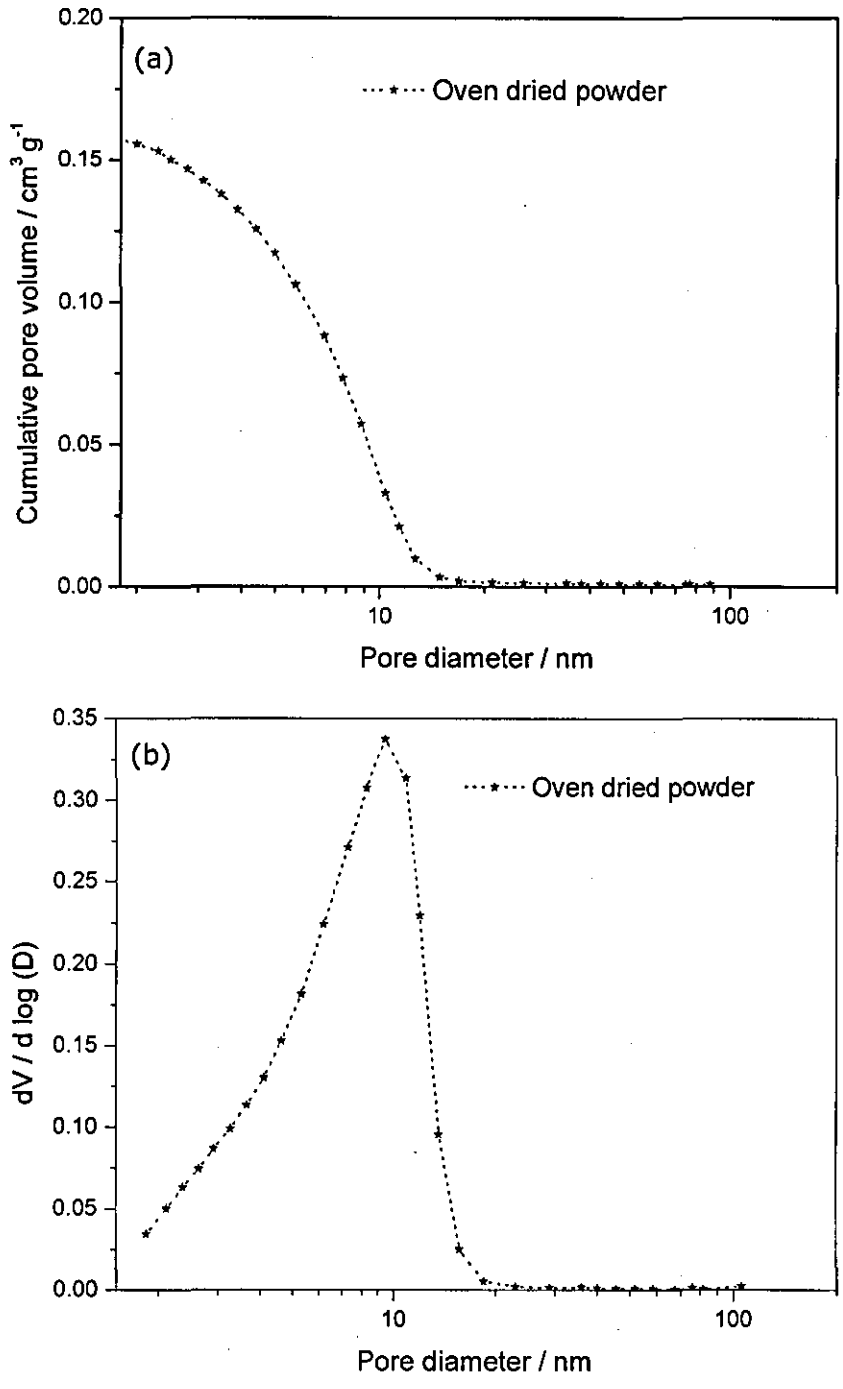

Figure 4-52 Pore size distribution in oven dried powder from 5.5 vol% suspension (a) cumulative and (b) differential showing mesoporosity.

The technique was found to give reproducible results. A plot of the pore size distribution from 2 different runs for a spray freeze dried powder is shown in Figure 4-53.

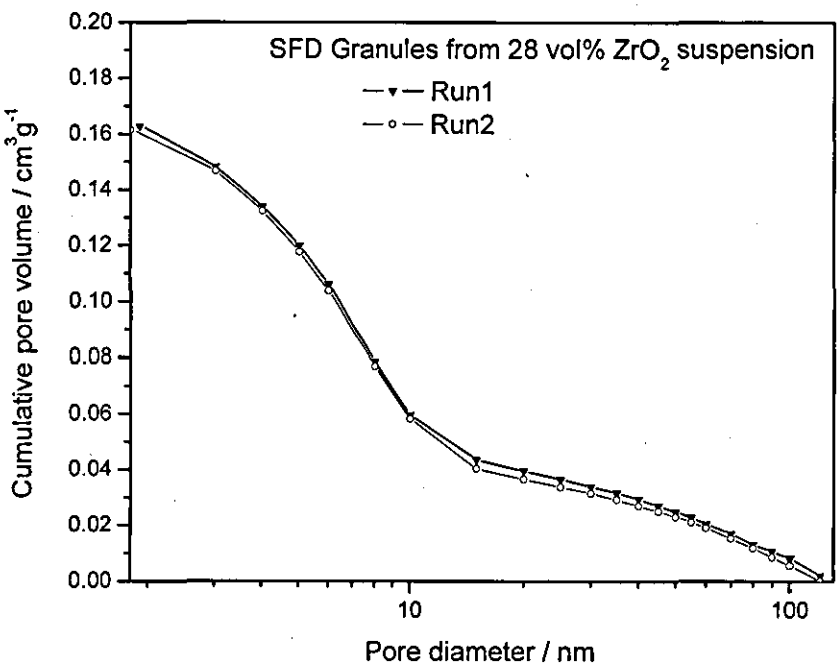

Figure 4-53 Pore size distribution obtained from nitrogen adsorption isotherms for spray freeze dried granules from 28 vol% suspension from two different runs showing good reproducibility .

4.7.3 Pore size distribution in spray dried granules

The SD5 granules were dense and had closely packed primary particles. As a result, the pore diameter was small and the total pore volume was less. In Figure 4-54a and b, the SD14 granules show higher porosity than SD5 granules. As the pore size was measured after degassing at 400°C the organic additives would have been removed, i.e. the dispersant would have decomposed leaving a void in the granule structure. Another possibility is the poorer particle rearrangement due to capillary forces during spray drying. The slip for SD14 powders had a higher viscosity. This would have hindered the shrinkage of these droplets and resulted in higher porosity on drying. However, the reader is reminded that these pores represent only the fraction below 120 nm.

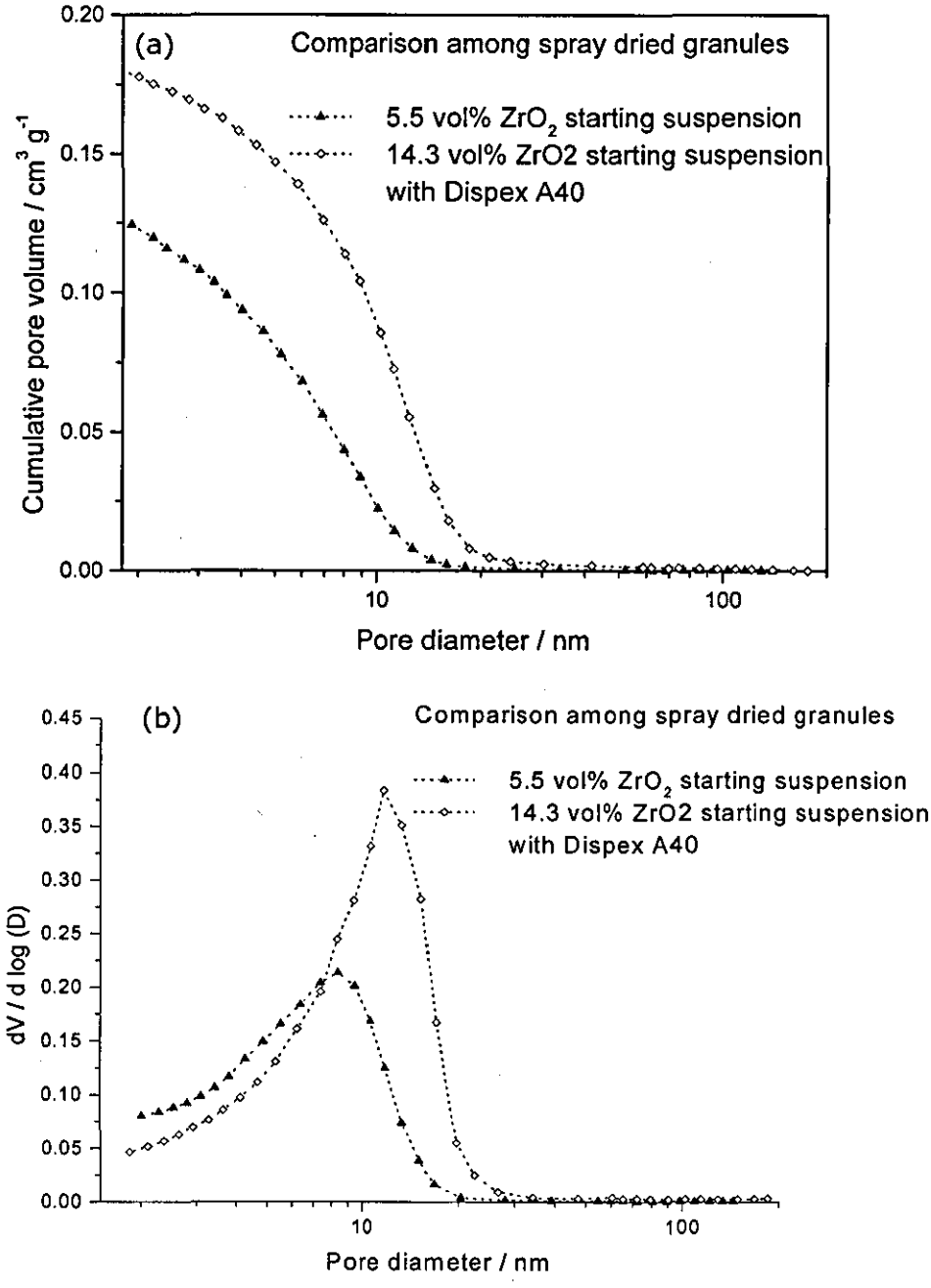

Figure 4-54 Pore size distribution for spray dried granules from different solids content suspensions (a) cumulative and (b) differential showing intra-agglomerate porosity.

4.7.4 Pore size distribution in spray freeze dried granules

The different spray freeze dried powder samples showed different pore size distributions, Figure 4-55a, the pore size being narrower with an increase in the solid content, Figure 4-55b reflecting the reduction in inter-particle distance because of better packing. However, the macropores in the granules, which were seen in the electron microscopy, cannot be analysed using this technique, although at higher pore diameters, the trace showed an increase in differential pore volume, indicating that there are pores of diameter larger than 120 nm.

The tap density of 28 vol% soldis suspension was 1.31 g cm^{-3}, as presented in Table 4-1. This represents a total porosity of about 12.55 $cm^3 g^{-1}$. From the plots, it is clear that the porosity measurements using nitrogen adsorption on uncompacted powders was representative only of a small fraction of the total porosity; the inter-agglomerate pores and the macropores within the granules were not accounted for by these measurements.

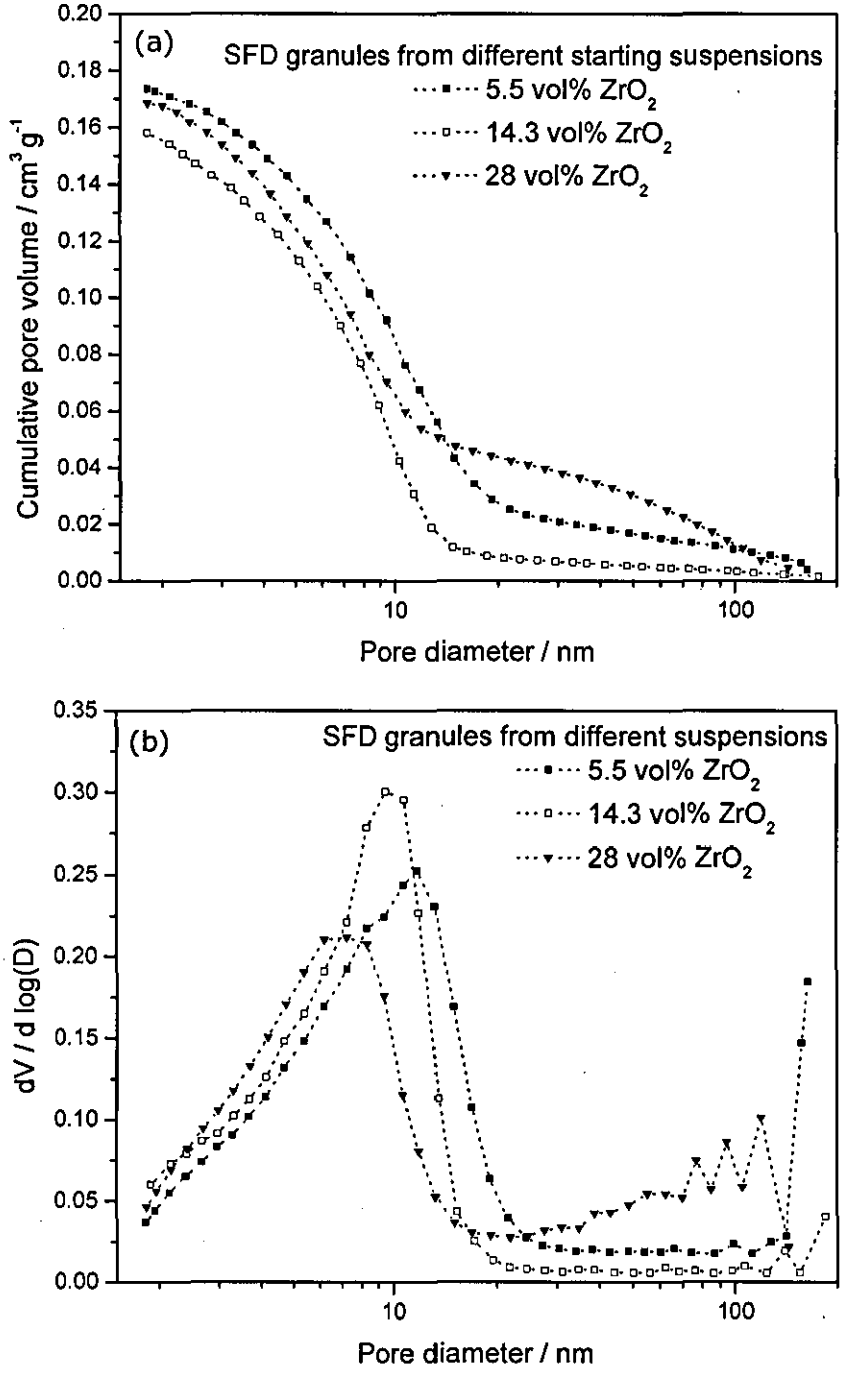

Figure 4-55 Pore distribution for spray freeze dried granules from different solid content suspensions (a) cumulative and (b) differential pore volume.

4.7.5 Pore size in powders from different routes

The powders granulated using different routes from the same starting suspension, e.g. the as-received nanosuspension with 5.5 vol% solids content, showed some interesting features. The spray freeze dried granules had the maximum amount of mesoporosity, whilst the volume of the pores was higher for the oven dried powders than the spray dried granules. This shows that the granules had undergone more shrinkage during spray drying compared to spray freeze drying. As the primary particles become closer, the porosity between them decreased, simultaneously, the pore size also reduced. This is evident in Figure 4-56a and b.

During oven drying, the nanosuspension was taken to 60°C and, as drying proceeded, the liquid phase was slowly depleted and the capillary forces brought the nanoparticles together to form clusters. Consequently, the primary particles are bound closer in this agglomerate.

In spray drying, the fine droplet descended in a hot air stream at about 100°C and dried. The moisture was initially driven off from the surface and water from the core reached the surface through capillary action to replenish for the lost water. During this process, the primary particles were brought closer, essentially forming finer pores. Of course, the particle rearrangement was affected by the viscosity and surface tension of the suspension. In case of nanopowders, the capillaries that were formed would have been thin. Thinner capillaries will have exerted more capillary force and hence more shrinkage.

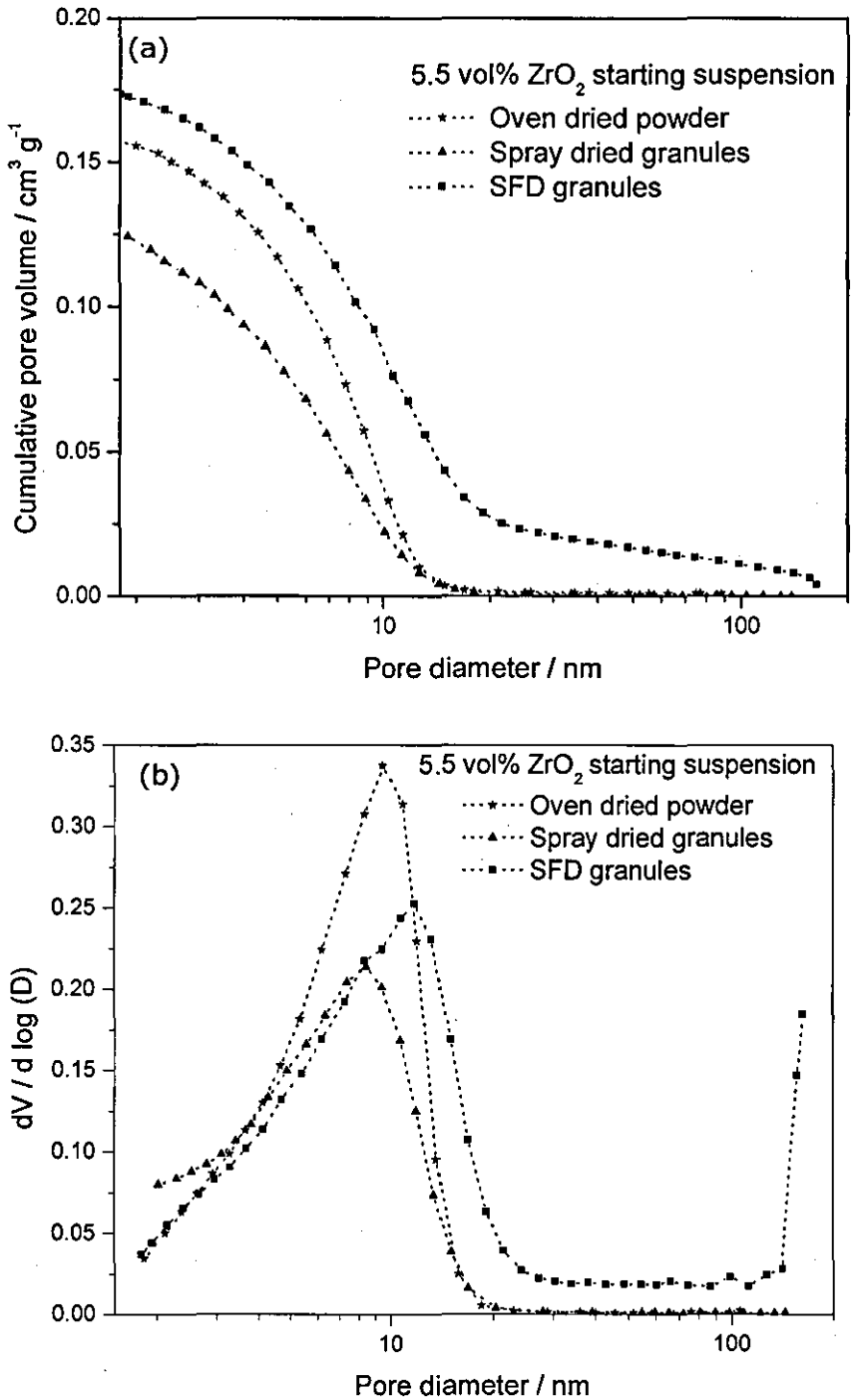

Figure 4-56 Pore size distribution for powders from different routes for a 5.5 vol% ZrO_2 suspension with no dispersant (a) cumulative and (b) differential.

The isotherms of oven dried nanopowder and benchmark submicron granules can be seen in Figure 4-57. In case of the submicron powders the total adsorbed volume of nitrogen was low. Further, the hysteresis loop was small. This represents the lower surface area and absence of mesoporosity in TOSOH powders. The onset of porosity for TOSOH powders at around 100 nm is noticeable in Figure 4-58. As the primary particle size of TOSOH is well over 150 nm, the pore formed between these particles is typically bigger than 120 nm. As a result, there was no capillary condensation and the quantity of adsorbed nitrogen was less.

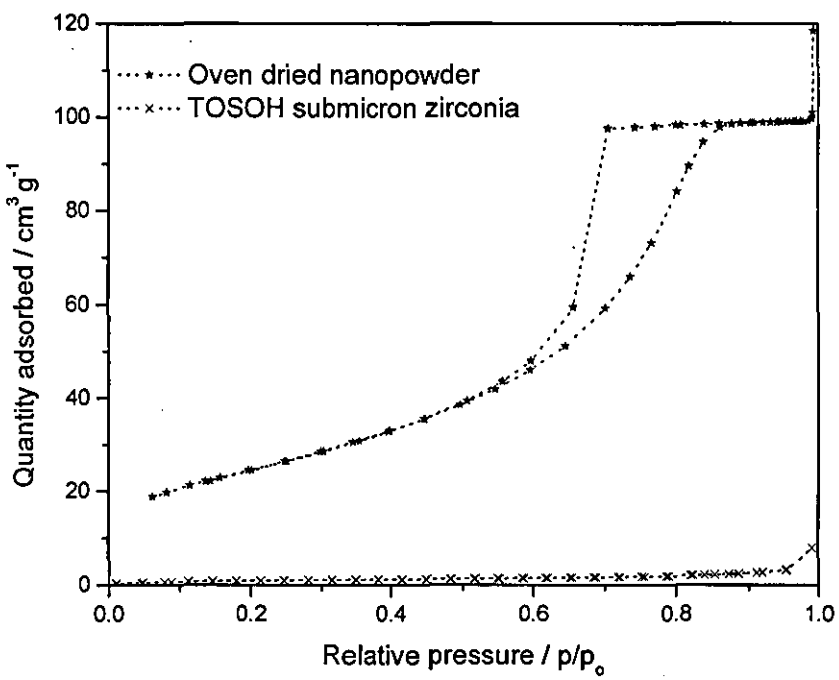

Figure 4-57 Comparison between nitrogen adsorption – desorption isotherms of oven dried nanopowder from5.5 vol% suspension and benchmark TOSOH granules.

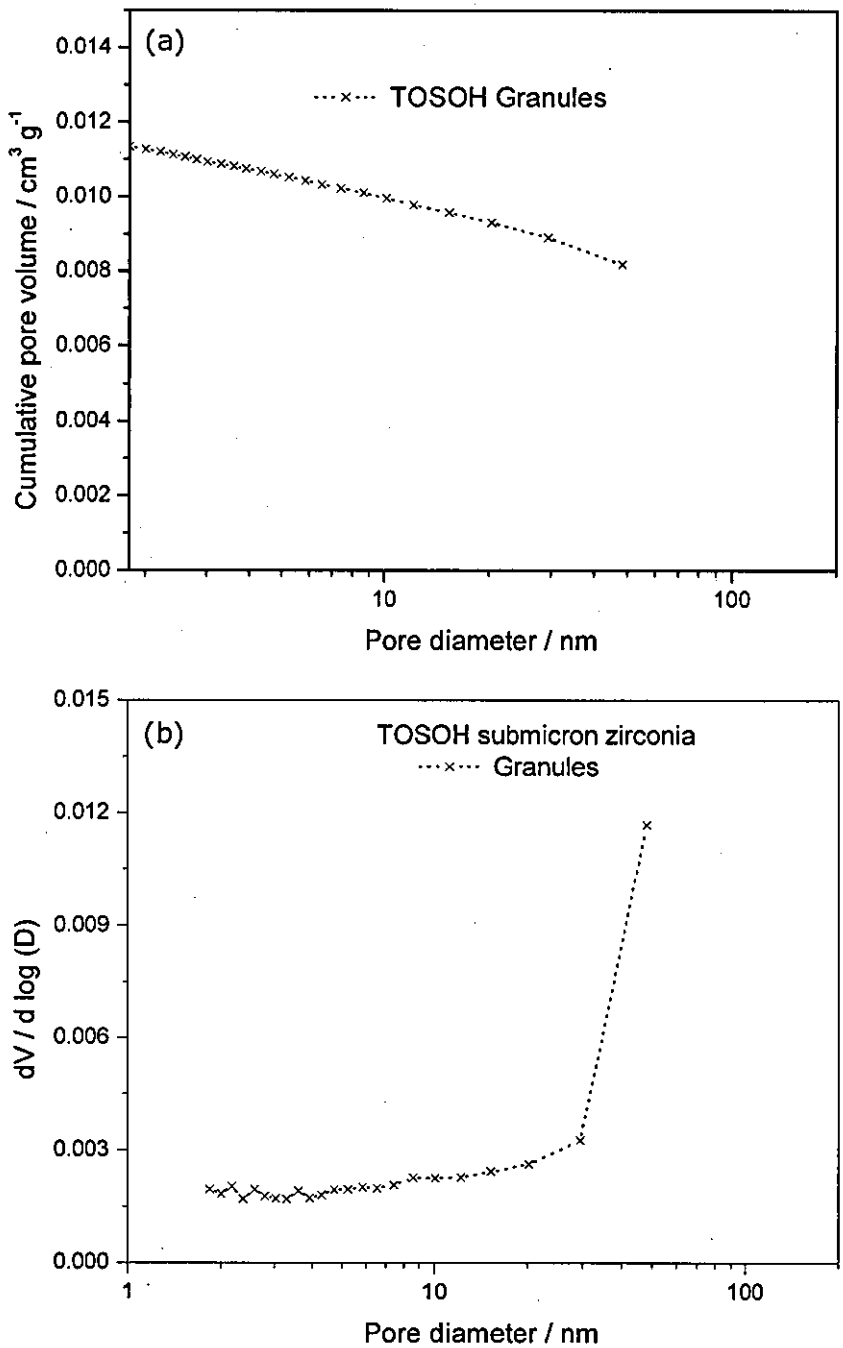

Figure 4-58 Pore size distribution in TOSOH granules (a) cumulative and (b) differential showing very less porosity below 100 nm.

4.7.6 Pore structure evolution during pressing

Interesting trends can be seen in Figure 4-59 regarding the pore structure evolution during die pressing. The arrows indicate the direction in which the partial pressure was either increased during the adsorption leg or decreased in the desorption leg. Through out this section, solid lines have been used to represent compacts pressed at 380 MPa, dashed lines for compacts pressed at 125 MPa and dotted lines for powder samples. All the three traces overlap each other in the low pressure regime. As the pressure was increased, the isotherms differ significantly. If the adsorption branch alone is considered, the total volume of nitrogen adsorbed is higher for the granules than that of the compacts; it was the lowest for powder compacts pressed at higher pressure. The hysteresis loop was broader for the compact pressed at 380 MPa than the one pressed at 125 MPa.

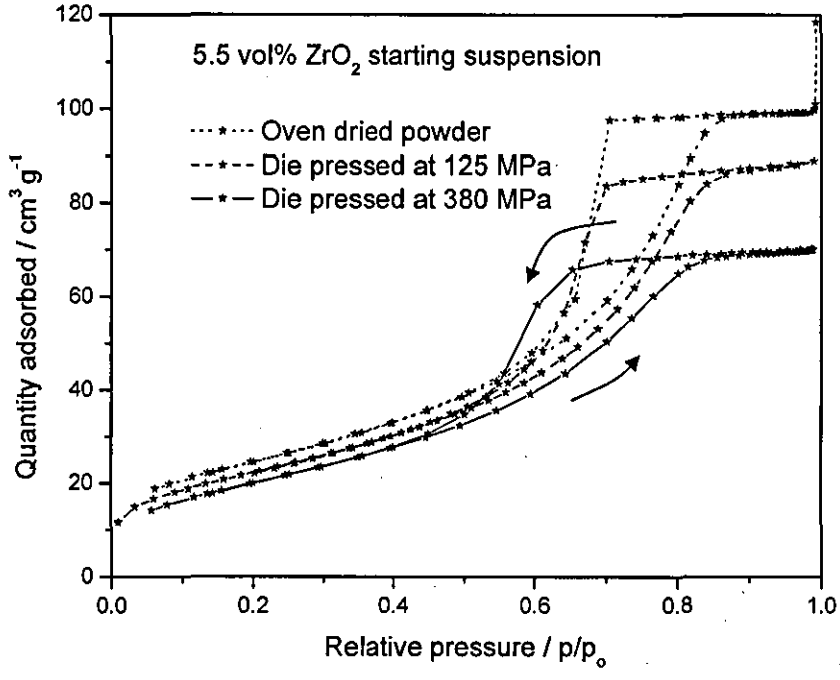

Figure 4-59 Nitrogen adsorption – desorption isotherms for oven dried powder and die pressed compacts made from 5.5 vol% solids starting suspension showing reduction in mesoporosity on consolidation.

In Figure 4-59, the important observations for the oven dried powder were (i) the total amount of adsorbed nitrogen decreased with compaction and (ii) the desorption was delayed with increasing

compaction pressure. These were reflected as a reduction in the cumulative pore volume of the samples after consolidation as in Figure 4-60a. As expected, the particle packing improved with die-pressing and hence the pore size shifted towards the smaller pore sizes, Figure 4-60b. A similar trend was seen for spray dried granules and spray freeze dried granules as illustrated in Figure 4-61 to Figure 4-66.

The BET surface area for the oven dried powder and its compact pressed at 125 MPa and 380 MPa were found to be 84.09, 87.85 and 85.44 m^2g^{-1} respectively. This confirms that there is no loss of surface area as a result of compaction.

The evolution of mesopores is characterised by the change in the shape of the hysteresis loop in the isotherm. As the consolidation pressure was increased, the mesopores narrowed. In other words, the increase in density during this stage of compaction is brought about by the rearrangement of primary particles. As a result, the total pore volume was reduced and hence so was the total volume of adsorbed nitrogen. The widening of the hysteresis loop is ascribed to the formation of narrow channels that are needed to access the pores for condensation to occur. Figure 4-60a and b show these trends in oven dried powder.

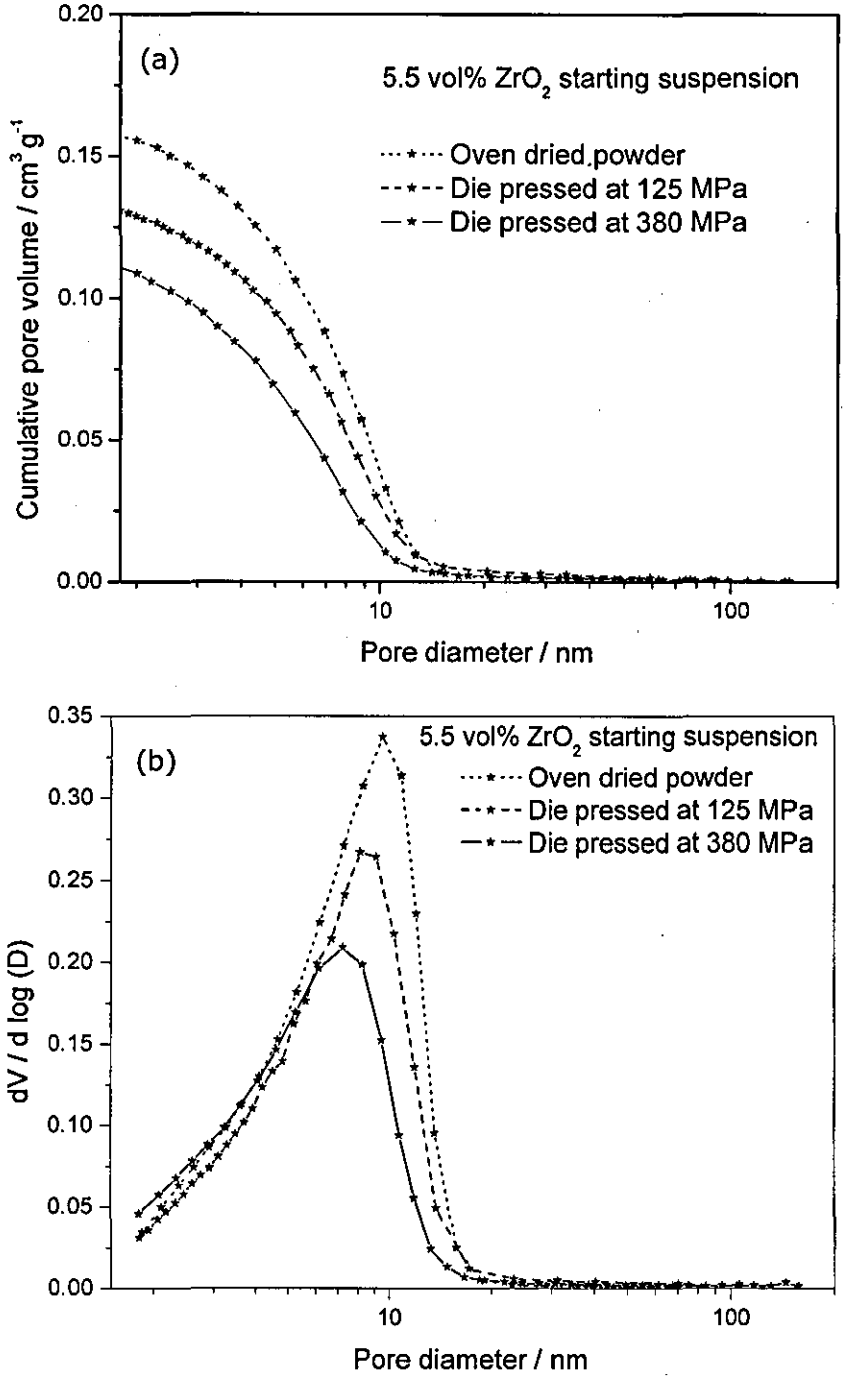

Figure 4-60 Pore size distribution as a function of compaction for oven dried powder from 5.5 vol% suspension (a) cumulative and (b) differential showing reduction in porosity on consolidation.

In the case of the spray dried granules, the same trend as for the oven dried powder may be seen in Figure 4-61 and Figure 4-62. However,

the reduction in pore volume is higher in the case of the SD14 powders. This correlates with the low fill density of the powder and a compact green density comparable with that of SD5 powder compact. As explained in section 4.6, the SD5 granules have a density similar to that of their compacts. As a result, their pore size distribution is similar in the case of Figure 4-62a. Granulation is essentially an intermediate step and the granule structure must be completely destroyed in the transition stage. As expected, this doesn't occur when the granule density is higher, especially if the agglomerates are hard.

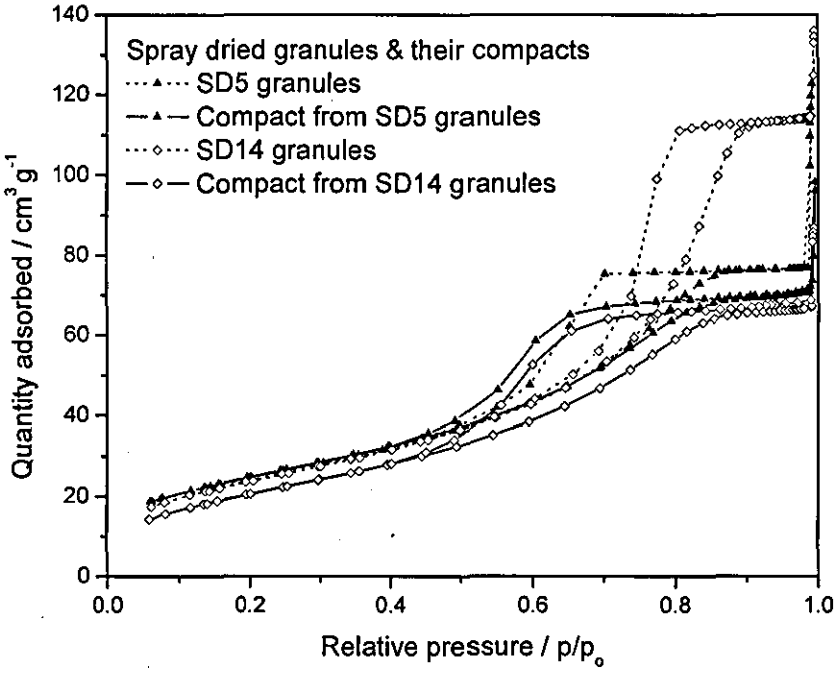

Figure 4-61 Nitrogen adsorption - desorption isotherms for spray dried granules from 5.5 vol% suspension without dispersant and 14.3 vol% suspension with Dispex A40 and their compacts pressed at 380 MPa.

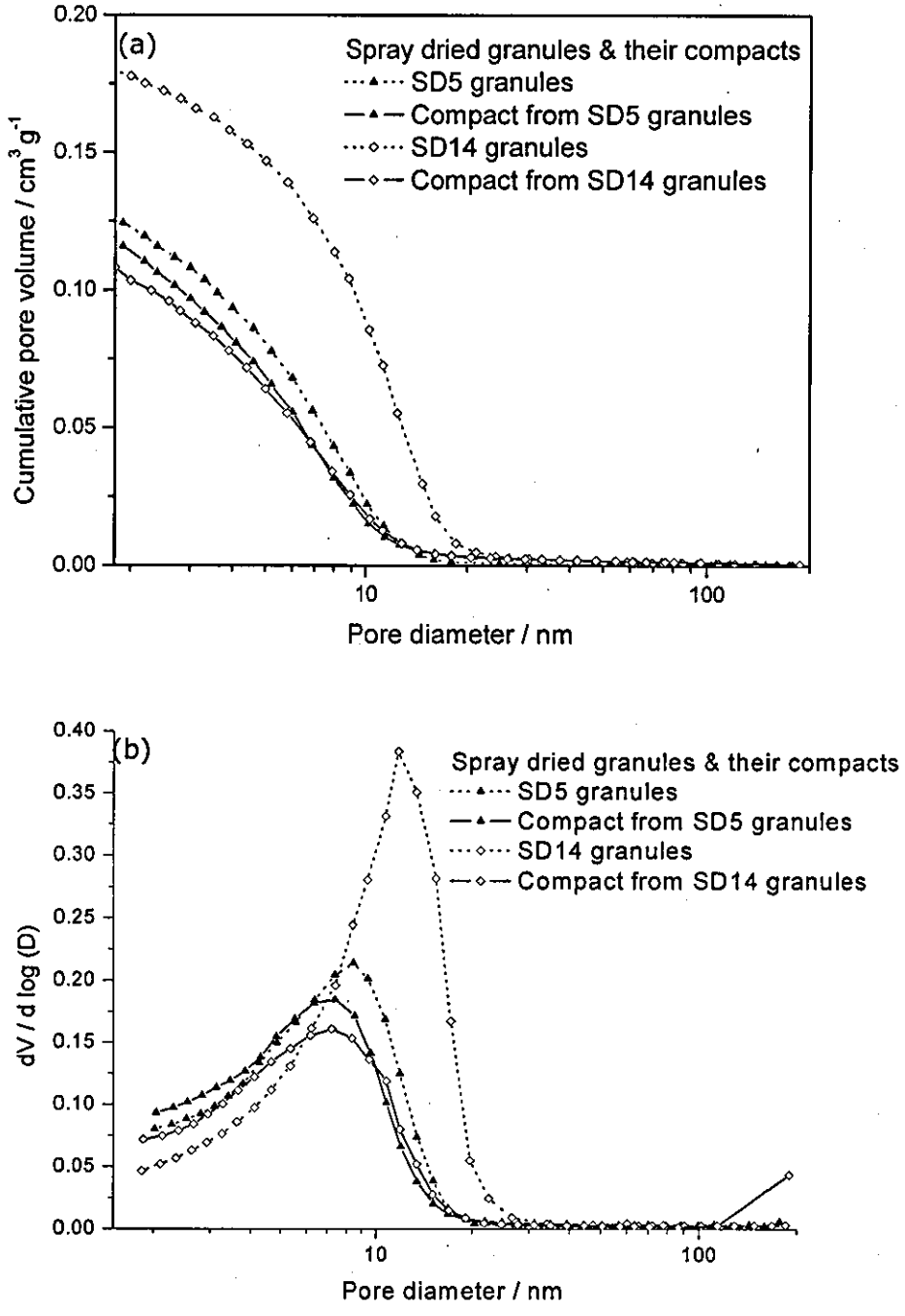

Figure 4-62 Pore size distribution for spray dried granules from 5.5 vol% suspension without dispersant and 14.3 vol% suspension with Dispex A40 and their compacts pressed at 380 MPa (a) cumulative and (b) differential.

4.7.6.1 Porosity in SFD powder compacts

The nitrogen adsorption – desorption isotherms for spray freeze dried powder from the 5.5 vol% ZrO_2 suspension and the compacts die pressed from it are shown in Figure 4-63. A trend similar to the oven dried and spray dried powders can be observed. The SFD5 granules had a lot of macropores, as seen in Figure 4-15, which were eliminated first during consolidation. In Figure 4-64a, it can be seen that the pore size distribution of the granules was similar to that of the compact pressed at 125 MPa. As the consolidation pressure increased further, the total pore volume reduced in line with the density increase on compaction. Figure 4-64 shows the reduction in peak pore diameter on compaction. A similar trend was seen for all the spray freeze dried granules, Figure 4-65 and Figure 4-66.

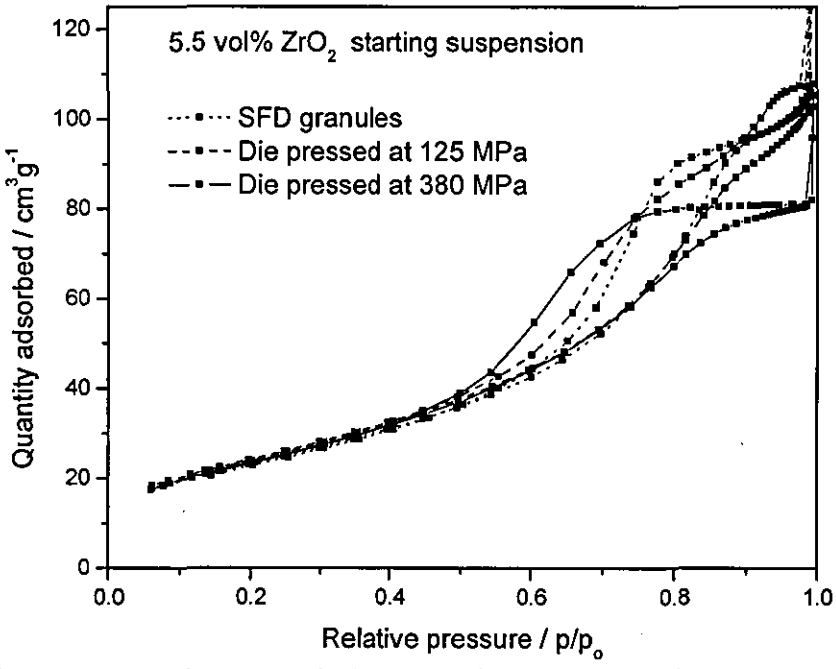

Figure 4-63 Nitrogen adsorption - desorption isotherms for spray freeze dried granules from 5.5 vol% ZrO_2 suspension and its compacts.

A die pressed compact with uniform green microstructure that originated from soft granules will have a narrow and unimodal pore size distribution. With hard granules, a bimodal pore size distribution is common. Figure 4-64 to Figure 4-70 compares the effect of the starting

solid content on the pore size distribution of these powder compacts. It turns out that there is a relation between these two parameters. If the granules are soft, the granules crush down into primary particles and perfect packing is achieved. The residual pore diameter in this case will be <10 nm. In this respect, Figure 4-69 demands special attention. It can be seen that the volume of pores having size greater than 10 nm increases with increase in the solid content of the starting suspension. This is a very important result since it links the various stages, viz. suspension characteristics, drying and compaction, to the properties of the green compact. The differential pore distribution shown in Figure 4-70 shows that there is a considerable proportion of pores >20 nm in size for compacts from 28 vol% ZrO_2 spray freeze dried powder.

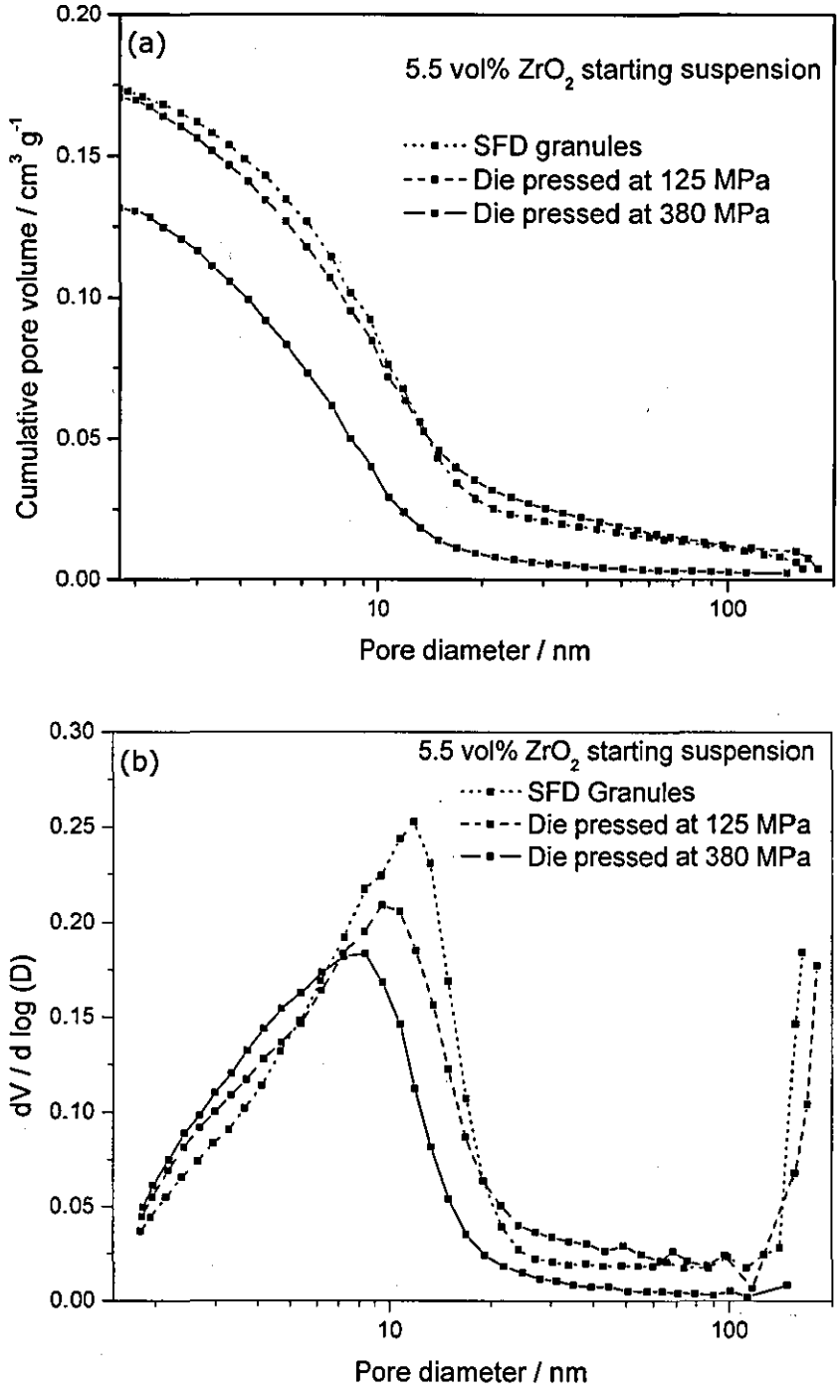

Figure 4-64 Pore size distribution in spray freeze dried granules from 5.5 vol% ZrO_2 starting suspension and compacts pressed at different pressures (a) cumulative and (b) differential showing better packing at high consolidation pressures.

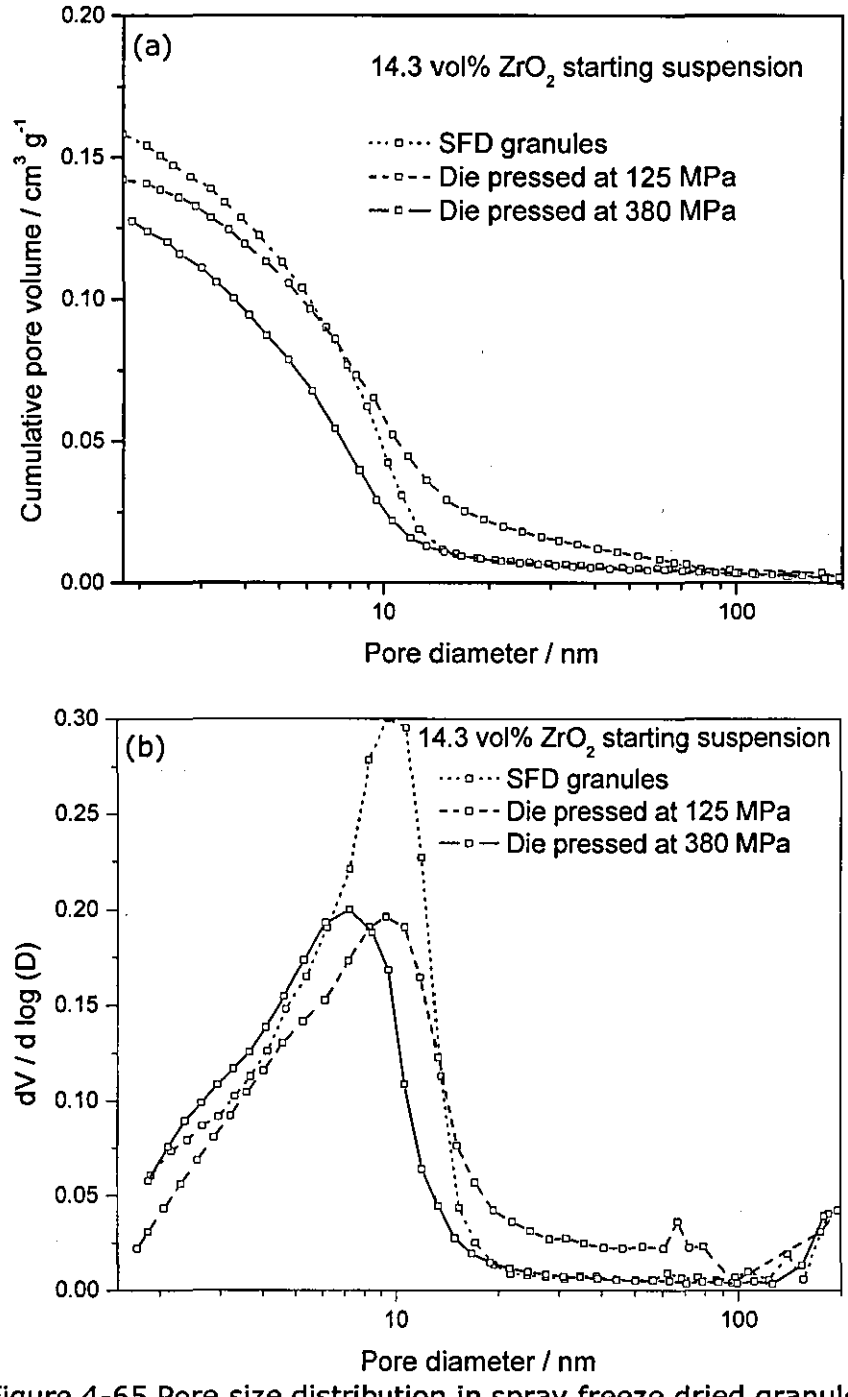

Figure 4-65 Pore size distribution in spray freeze dried granules from 14.3 vol% ZrO_2 starting suspension and compacts pressed at different pressures (a) cumulative and (b) differential.

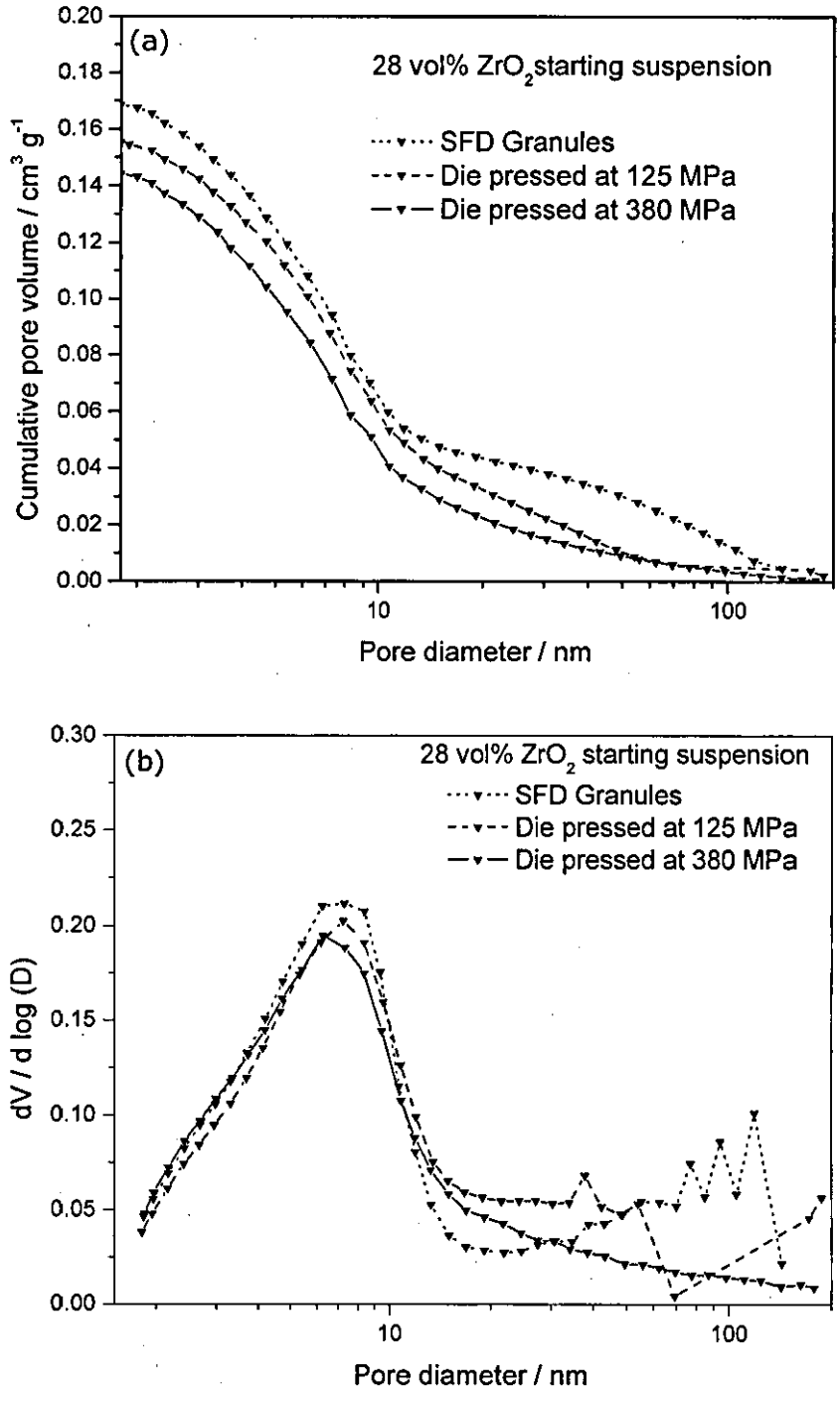

Figure 4-66 Pore size distribution in spray freeze dried granules from 28 vol% ZrO_2 starting suspension and compacts pressed at different pressures (a) cumulative and (b) differential.

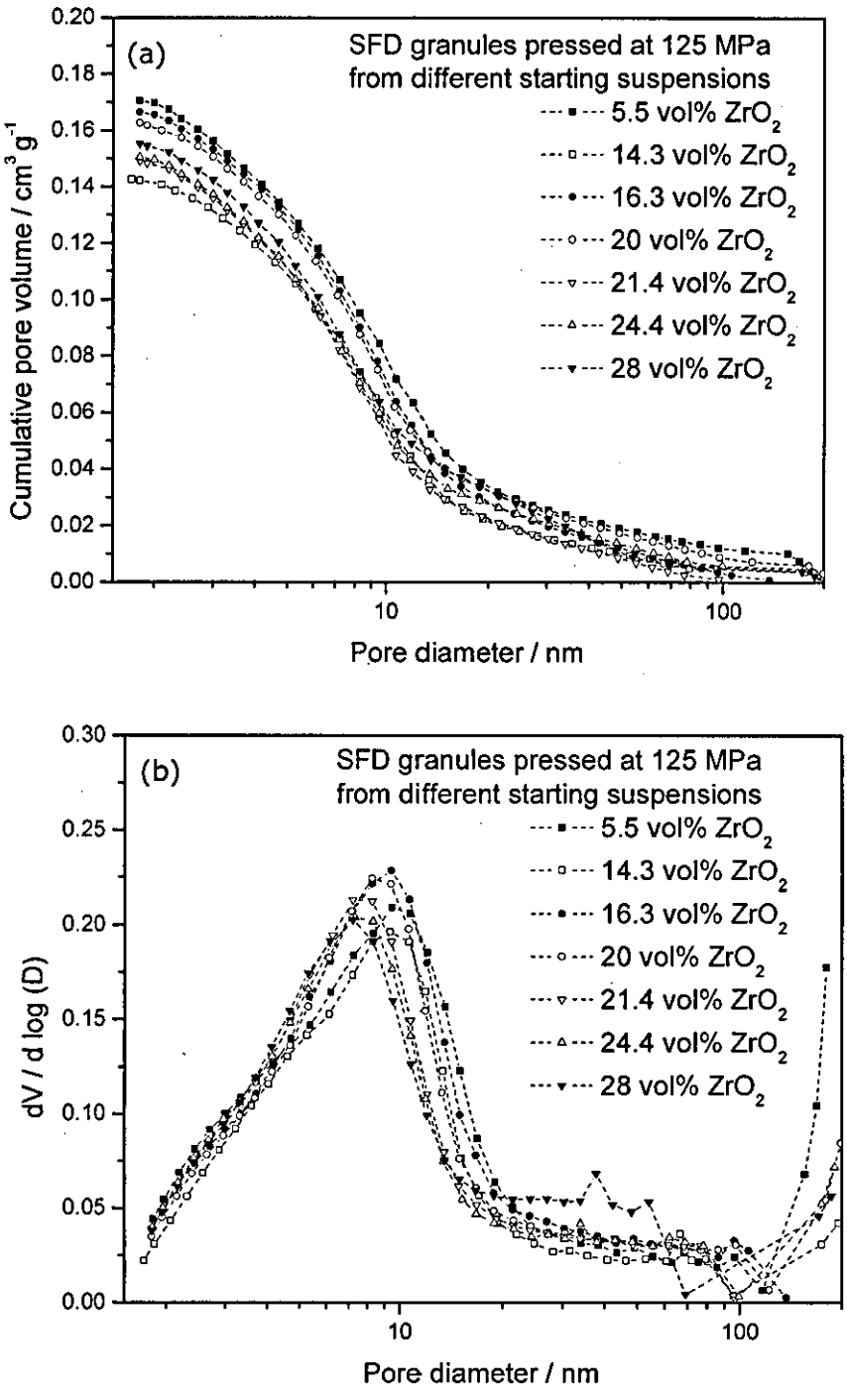

Figure 4-67 Pore size distribution in compacts pressed at 125 MPa from spray freeze dried granules obtained from different vol% ZrO_2 starting suspensions (a) cumulative and (b) differential.

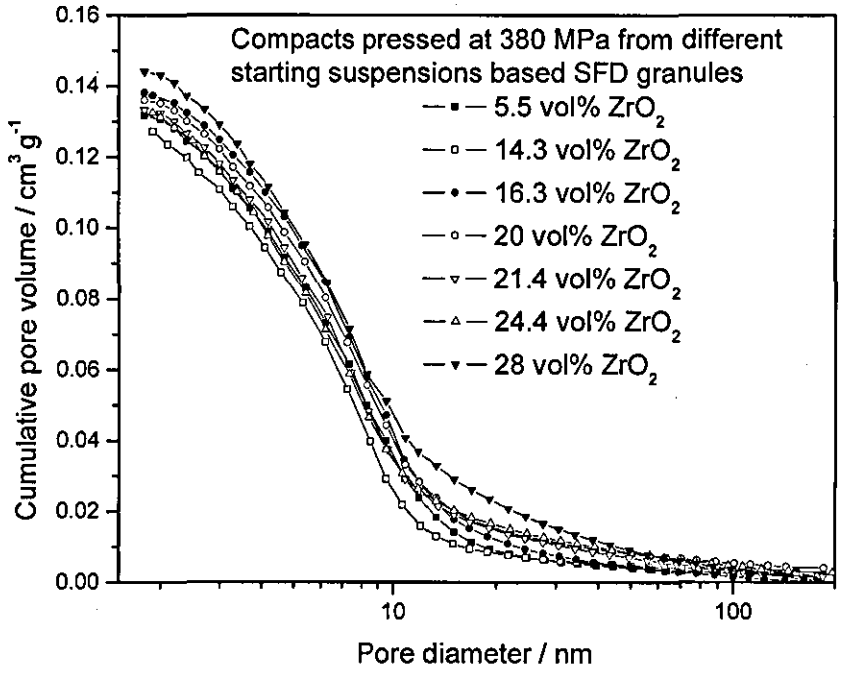

Figure 4-68 Cumulative pore size distribution in compacts pressed at 380 MPa from spray freeze dried granules from different vol% ZrO_2 starting suspensions.

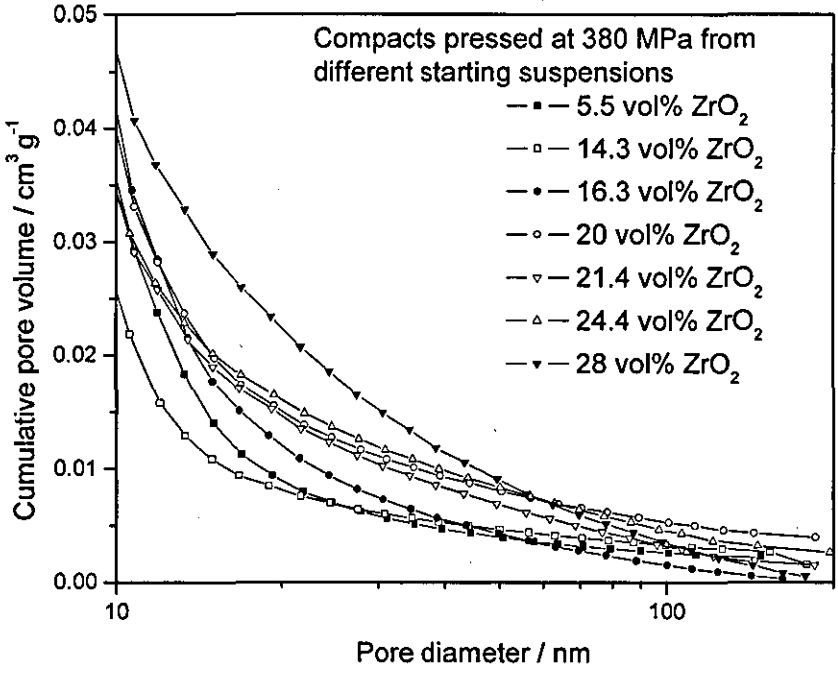

Figure 4-69 Cumulative pore size distribution in green compacts pressed at 380 MPa from spray freeze dried granules from different vol% ZrO_2 starting suspension showing increased porosity above 20 nm as the solid content is increased.

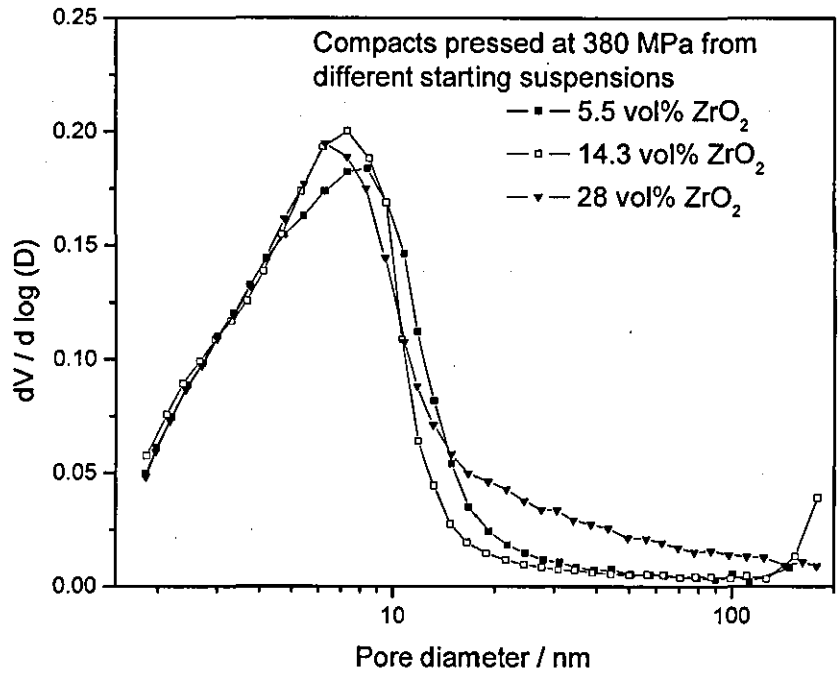

Figure 4-70 Differential pore size distribution in compacts pressed at 380 MPa from spray freeze dried granules obtained from different vol% ZrO_2 starting suspension.

In Figure 4-71a and b, the pore size distribution on die pressed compacts from powders dried using different routes is compared. The SFD5 powder compact shows more porosity since it does not have any inter-granule pores that remain unaccounted for by this technique.

It can be seen in Figure 4-67and Figure 4-71 that the there is an increase in the porosity at pore size greater than 100 nm. This can be attributed to heterogeneous densification in the die pressed compact. It is possible that there are few bigger voids in the centre of the compact as the pressure distribution is not homogeneous during die pressing.

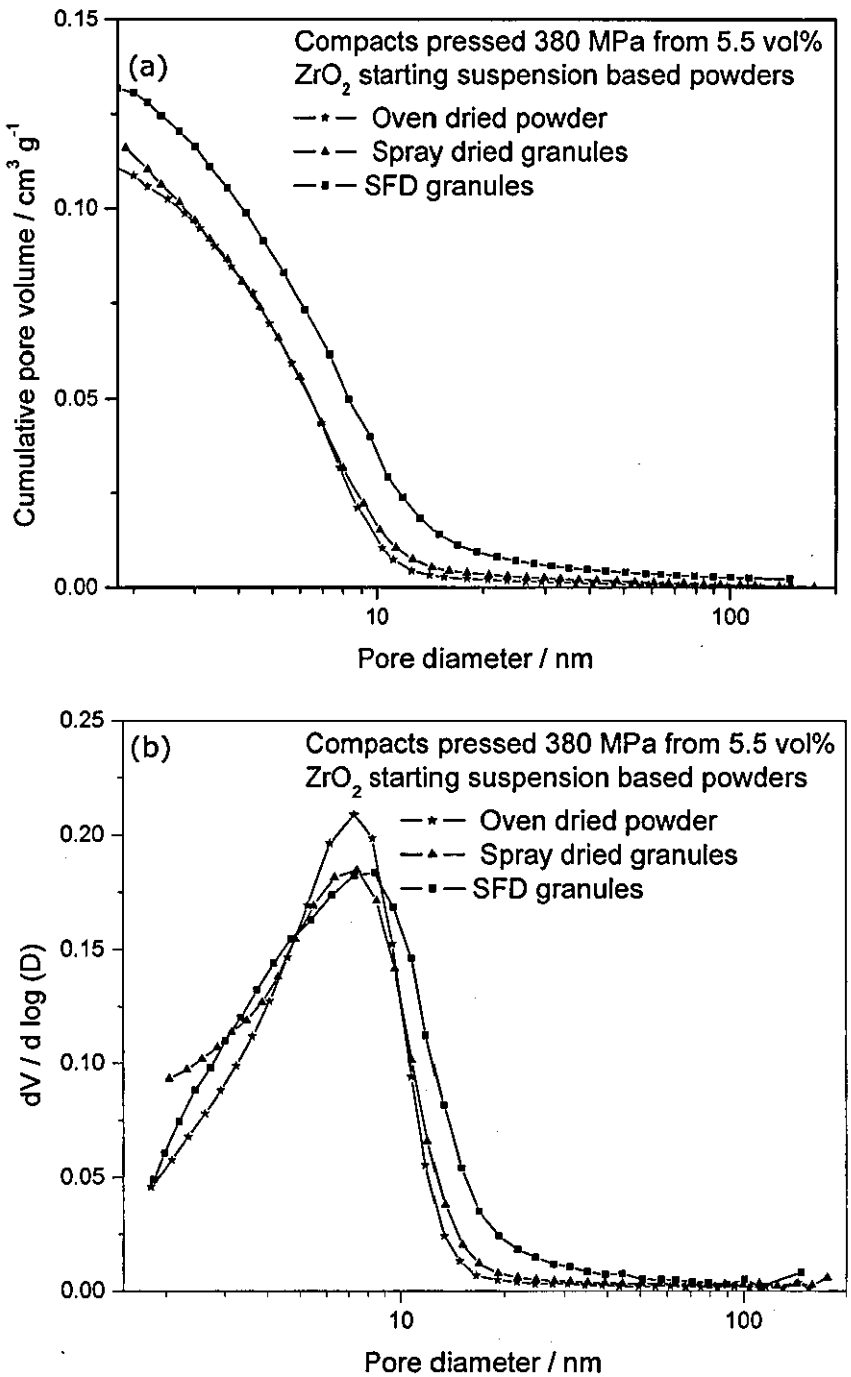

Figure 4-71 Pore size distribution in green compacts pressed at 380 MPa from powders obtained by different drying routes from 5.5 vol% suspension (a) cumulative and (b) differential.

The submicron TOSOH powder has primary particles of ~150 nm. As a result, the inter-particle porosity is not necessarily mesoporous. The granules and the compacts showed much lower adsorption than the

nanopowders and the hysteresis loop was pretty small Figure 4-72. This was manifested as very low porosity detected as in Figure 4-73.

A comparison of the cumulative pore volume between nanopowder and submicron powder compacts dry pressed at 380 MPa, Figure 4-74, showed that, as expected, the mesoporosity was lower in the case of the submicron powder. In case of submicron powder based compact, the trace showed that there is some porosity associated in the range between 20 nm to 100 nm. But, the nanopowder compacts had negligible porosity in this range, but increased below 20 nm. The TOSOH powder compacts shows very low porosity as detected by nitrogen adsorption owing to the limitations of the technique as discussed earlier.

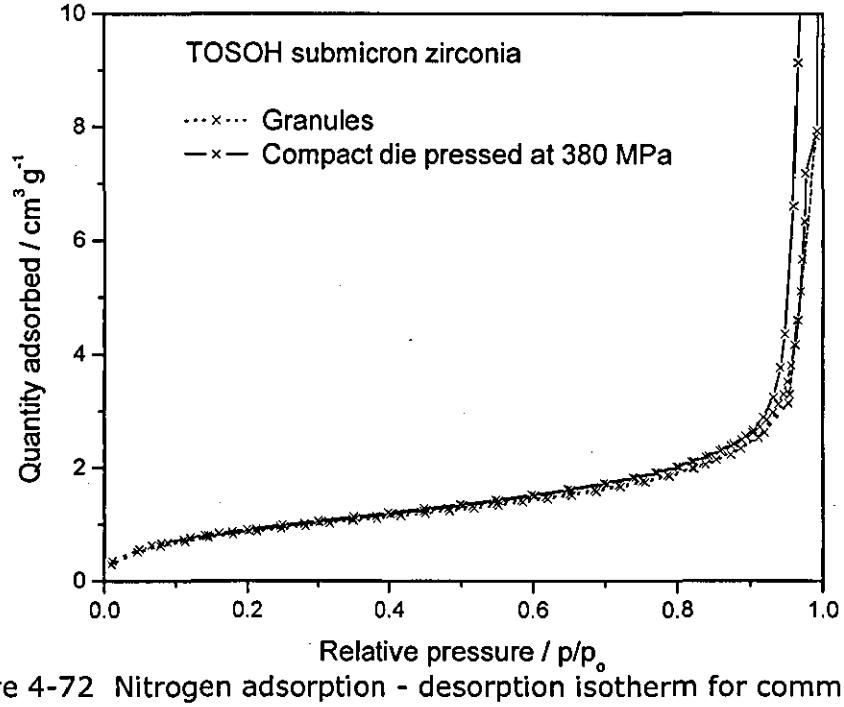

Figure 4-72 Nitrogen adsorption - desorption isotherm for commercial submicron powder and its compact pressed at 380 MPa.

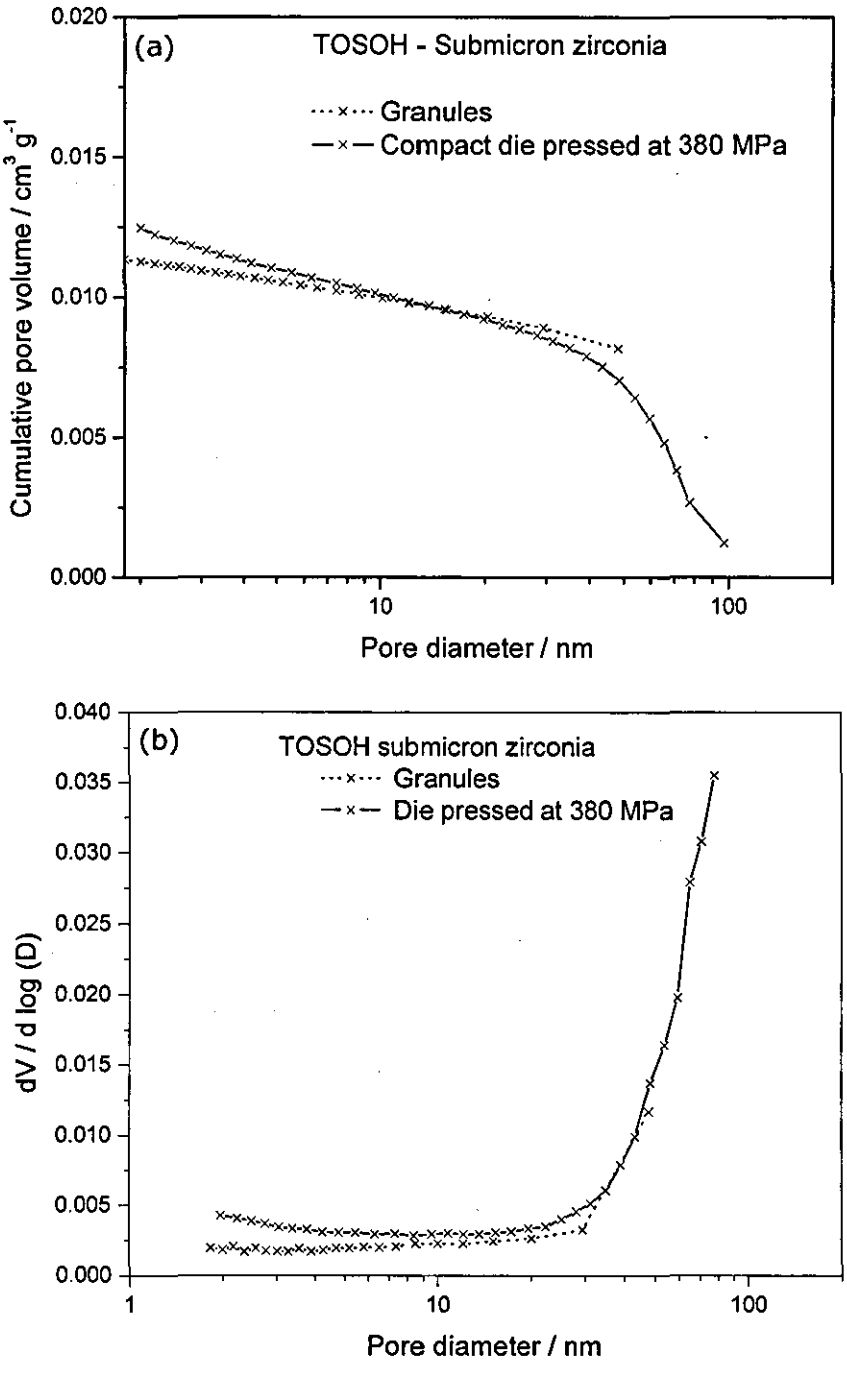

Figure 4-73 Pore size distribution in benchmark submicron granules and its compact pressed at 380 MPa (a) cumulative and (b) differential.

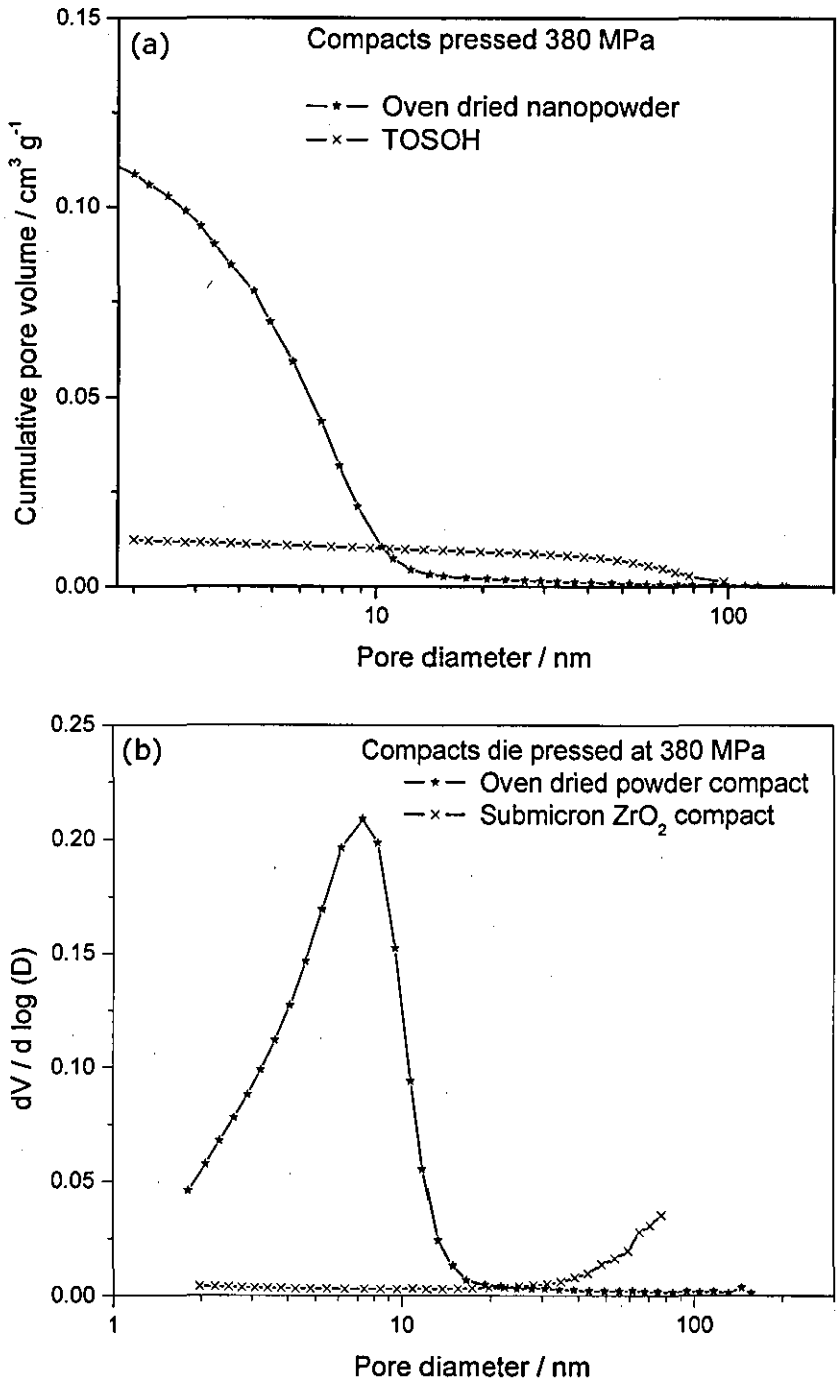

Figure 4-74 Comparision between pore size distribution in oven dried nanopowder and benchmark submicron powder compacts (a) cumulative and (b) differential.

Table 4-4 compares the porosity calculated from the geometrical density of the green compact with that found using nitrogen adsorption. The difference between these values yields the fraction of pores that could not be detected by this technique, which are those that are larger than 120 nm in size. It is noteworthy that the difference between these two values is higher for the spray dried powder compact than the spray freeze dried powder compact from the same, as-received, 5.5 vol% solids suspension, though their green densities were almost the same.

Table 4-4 Cumulative pore volume in green compacts.

Powder description	Compaction pressure /MPa	% Theo. Density	Actual pore volume /cm^3g^{-1}	Cumulative pore volume (from N_2 adsorption)
Oven dried	125	46.8	0.19	0.1307
	380	53.4	0.14	0.1117
Spray dried from 5.5 vol% suspension	125	50.0	0.17	0.1126
	380	55.3	0.13	0.1159
Spray dried from 14.3 vol% suspension	125	45.2	0.20	0.1426
	380	54.9	0.14	0.1081
SFD from 5.5 vol% suspension	125	47.4	0.18	0.1707
	380	55.1	0.14	0.1317
SFD from 14.3 vol% suspension	125	47.1	0.19	0.1426
	380	55.1	0.14	0.1271
SFD from 16.3 vol% suspension	125	45.4	0.20	0.1664
	380	52.5	0.14	0.1381
SFD from 20 vol% suspension	125	45.1	0.20	0.1626
	380	52.8	0.15	0.1360
SFD from 21.4 vol% suspension	125	45.9	0.20	0.1492
	380	54.5	0.14	0.1333
SFD from 24.4 vol% suspension	125	45.9	0.20	0.1504
	380	53.2	0.15	0.1324
SFD from 28 vol% suspension	125	45.7	0.20	0.1552
	380	51.2	0.16	0.1441
TOSOH	380	56.3	0.13	0.0124

4.8 Mercury intrusion porosimetry

Mercury intrusion porosimetry (MIP) was also used to characterise the green bodies that were pressed at 380 MPa. For oven dried powder compacts, the frequency pore size distribution, Figure 4-75 differs from the spray dried powder compact, Figure 4-76, in that there is a peak around 0.4 μm in the latter case. This originated from the heterogeneous packing and non-uniform pore size distribution, i.e. inter- and intra-agglomerate porosity in the spray dried granule based green compacts. The pore size distributions obtained from mercury intrusion porosimetry were always found to be lower than those measured by nitrogen adsorption isotherm for the nanopowder compacts.

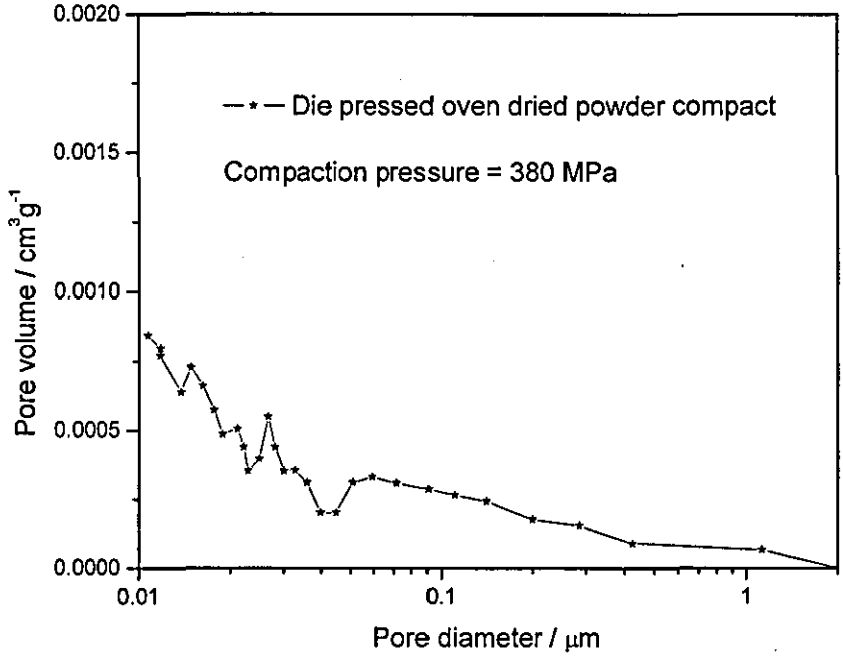

Figure 4-75 Porosity frequency distribution in green compact pressed at 380 MPa from oven dried powder from 5.5 vol% suspension.

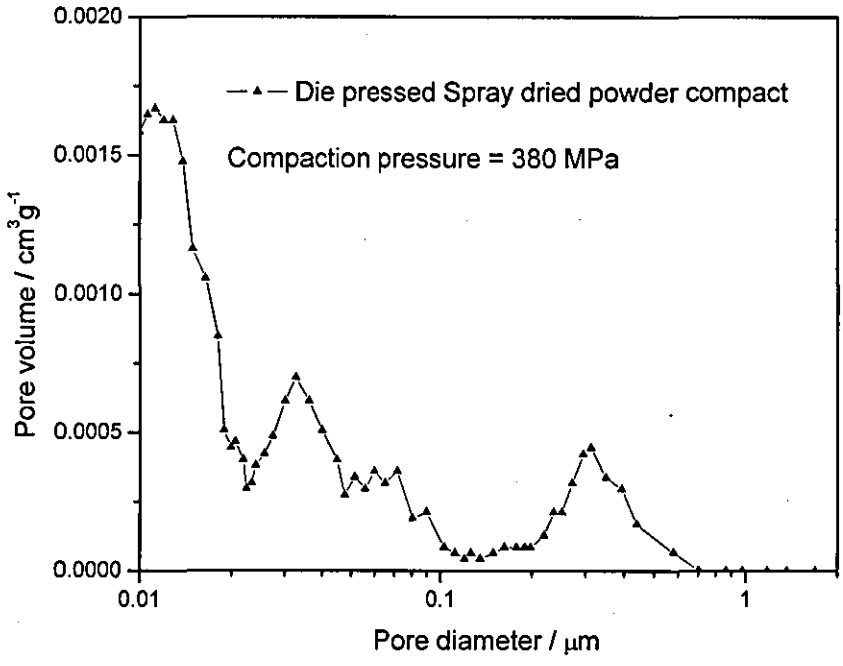

Figure 4-76 Porosity frequency distribution in green compact pressed at 380 MPa from spray dried granules from a 5.5 vol% suspension showing bimodal distribution.

One of the commonly observed features was the sudden increase in intrusion at higher hydraulic pressures; this corresponds to finer pores. For example, in Figure 4-77 the volume of mercury intruded increased from 0.0005 cm^3 g^{-1} to more than 0.0015 $cm^3 g^{-1}$ between 20 nm to 10 nm for the SD14 powder compacts.

Any specific trend in the frequency pore size distribution of the spray freeze dried powder compacts, Figure 4-78, was not immediately evident. However, the cumulative pore volume was higher for compacts made from high solid content spray freeze dried granules, Figure 4-79, a trend matching the one observed in Figure 4-69. Figure 4-80 compares the pore size distribution in compacts for powders obtained through different routes from the as-received 5.5 vol% solids starting suspension. This confirms that the spray freeze dried granules were soft agglomerates. It is worth mentioning that the total pore volume calculated from intruded mercury volume was much less than the actual porosity (calculated from the geometrical density) for nanopowder based compacts, though not for the submicron powder compacts.

As the data was collected in the equilibration mode, it can be assumed that all the accessible pores for the given pressure are filled with mercury. As the pressure is increased in the intrusion step, more and more mercury intake was observed. In Figure 4-81, the pore size distribution in the TOSOH compacts is seen to be unimodal. The total porosity was 0.1149 $cm^3 g^{-1}$, much closer to the actual porosity tabulated in Table 4-4. The mean value of the normal curve was about 100 nm and this corresponds to the typical pore size between the primary particles in TOSOH powders.

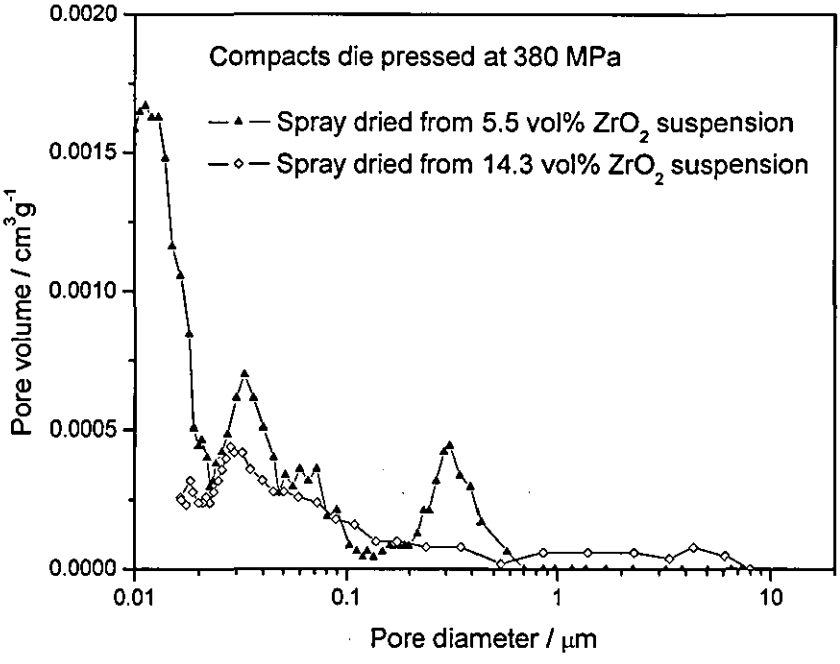

Figure 4-77 Comparision of porosity distribution in spray dried powder compacts compacted at 380 MPa from 5.5 vol% suspension without dispersant and 14.3 vol% suspension with Dispex A40.

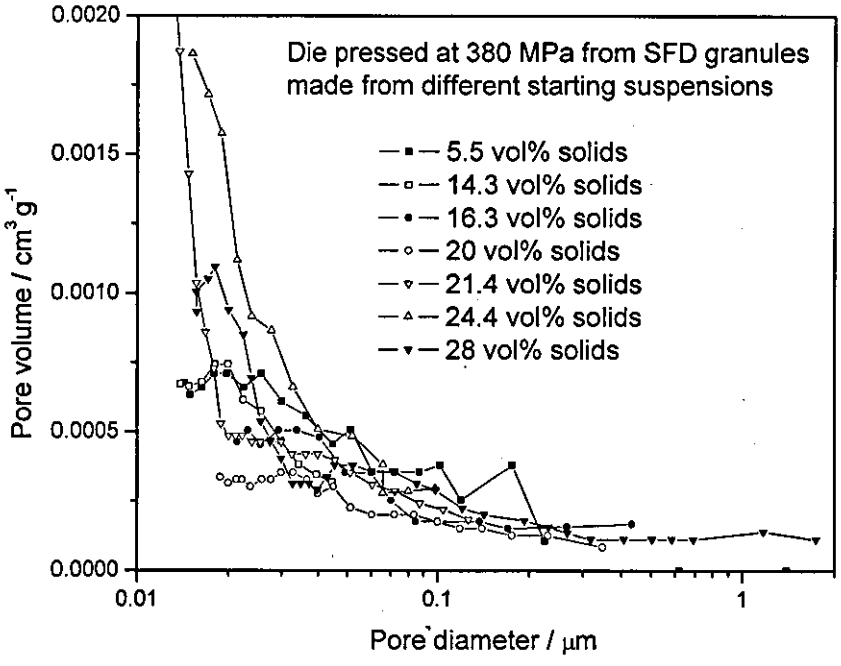

Figure 4-78 Frequency pore size distribution green compacts pressed at 380 MPa from spray freeze dried powder from different solid content starting suspensions.

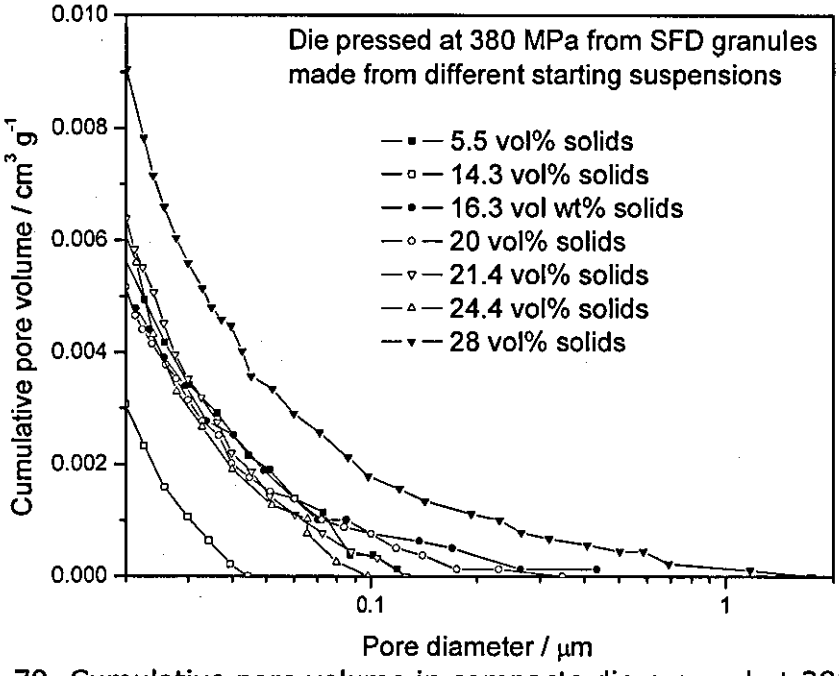

Figure 4-79 Cumulative pore volume in compacts die pressed at 380 MPa from spray freeze dried granules as a function of solid content of the starting suspension.

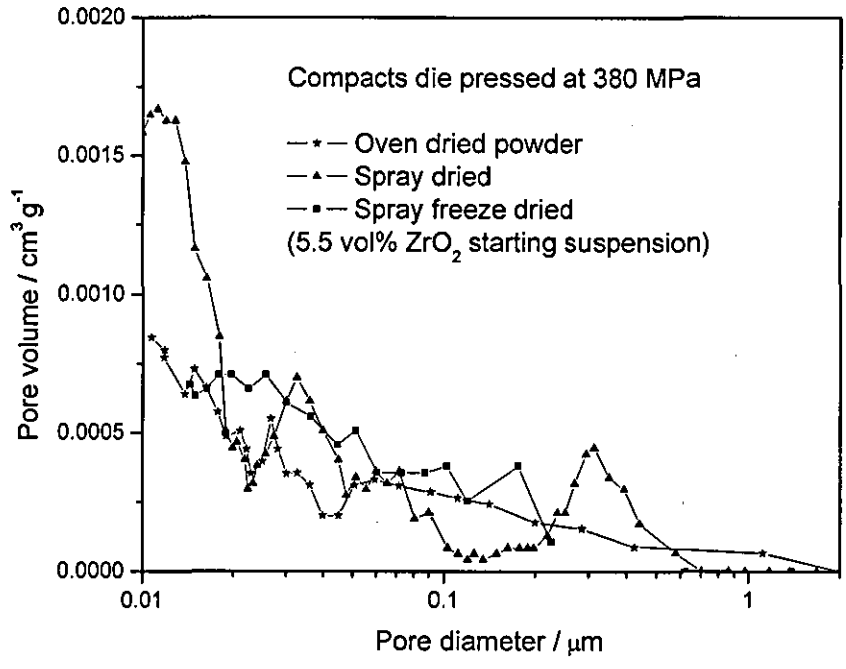

Figure 4-80 Comparison of porosity distribution in green compacts pressed at 380 MPa from powders obtained through different routes for the 5.5 vol% solids starting suspension.

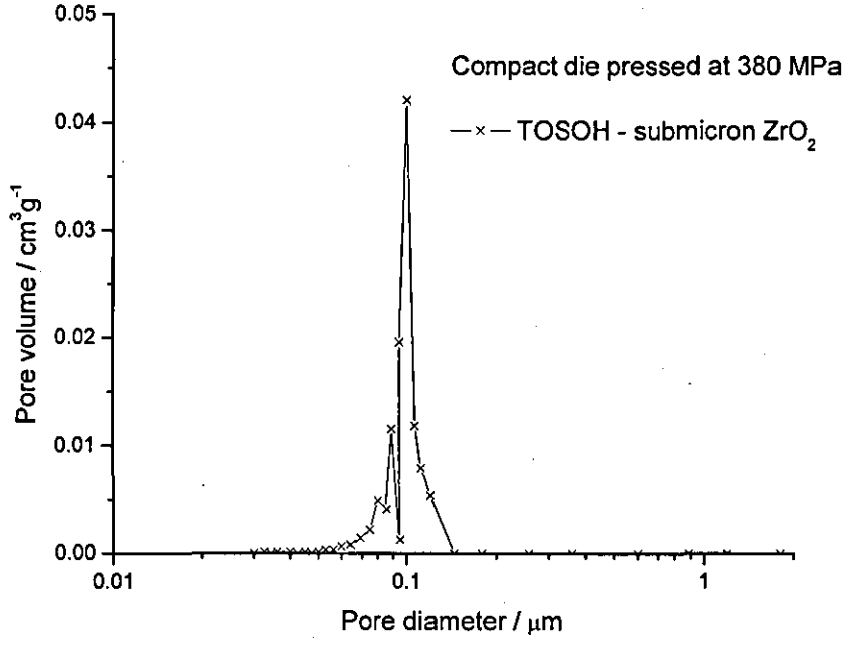

Figure 4-81 Pore size distribution in TOSOH- submicron zirconia powder compacts.

As detailed in the literature [163, 183], if pores have an ink bottle shape, with large pores having a narrow opening, then the observed pore size distribution may not be representative of the actual situation. For the submicron particle based granules, a good comparison with the total volume was observed since the particle-particle channel size was within the experimental range of the MIP equipment. However, owing to the limitations of the MIP equipment used, this was not true for the nanopowder compacts where the minimum pore diameter that could be intruded was about 15 nm. In this case, since the primary pores can be as fine as 7 nm, they remained inaccessible. As a result, the total cumulative pore volume observed in the spray freeze dried granule based compacts was much lower than might have been expected. In case of the 28 vol% solids based spray freeze dried powder compact, for example, the cumulative pore volume was ~0.013 cm^3g^{-1}. This represents only about 10% of the total cumulative porosity as deduced from the geometrically measured density. In contrast, in the case of the spray dried granules, the total cumulative pore volume that was accounted for was about 0.03 $cm^3 g^{-1}$, which was about 25% of the total calculated pore volume. This leads to two conclusions

- The pores were narrower in the spray freeze dried granule based compacts than the spray dried granule based ones.
- The full range of pores was not accounted for in the case of nanopowder compacts owing to equipment limitations

However, the technique shows a clear trend that matches with that observed from the nitrogen adsorption isotherms and acts as a bridge in understanding and interpreting the data obtained from the different powders.

It is possible that in Figure 4-78, the frequency pore size distribution for the spray freeze dried powder based granules is more representative of porosity within the samples' thin outer layer and pores connected to the surface, but not the bulk of it. Despite this, the cumulative pore volume in Figure 4-79 gives the expected trend.

In the case of ink-bottle shaped pores, it is possible to get a quantitative information on volume of bigger pores masked by narrow pore channels using the hysteresis loop. However, this option was prevented by the fact that complete intrusion of mercury into these pores was not possible because the maximum reachable intrusion pressure was lower than that corresponds to the pore channels.

4.9 Relation between agglomerate strength and solid content

From the results, it is clear that the increase in the solid content of the starting suspension not only increased the granule density, but also increased their strength after spray freeze drying, outweighing the favourable increase in flowability.

As the solid content of the suspension increased the inter-particle distance decreased. The mean separation distance between particles in a well dispersed suspension also decreases with the decreasing particle size. Agglomeration and flocculation can occur from such close encounters in this case [79]. In the suspension, the ceramic particles may become more dispersed in a repulsive manner by surface charges. The van der Waals forces of attraction can be overcome by the stronger repulsive forces created of the charged species attached to their surface. These mechanisms are not present in the dried state.

The primary particles of about 20 nm size zirconia make up granules with sizes in the range of few microns to two hundred microns. Consider for example, a typical 150 µm granule. Depending on the porosity of the granule, the number of primary particles would vary from about 5.3×10^9 to 2.1×10^{10} for a porosity of 90% and 60% respectively.

The inter-particle distance in SFD granules can be calculated as shown in Table 4-5 below. In this calculation a simple cubic packing is assumed. As the solid content of the suspension is increased the particles are packed closer. It is worth noting that the primary particle size has an important influence in the interparticle distance. This calculation is based on a 20 nm particle size. Consider for example a 14.3 vol% YSZ

suspension. If the particle size is 2 μm, the distance will be 1 μm; for a 20 nm particle, this distance is 10.7 nm. The reduction in separation distance increases the short range van der Waals forces as per Rumpf's model (Section 2.9.3.3). Substituting these values in Equation 5, it can be inferred that the rupture stress will be ~175 times and ~13 times higher for SFD granules from 28 vol% and 14.3 vol% solids based suspension as compared to a granule from 5.5 vol% solids suspension. However, these forces are too small in magnitude to account for the persistence of the granular structure inspite of the high consolidation pressures used.

Table 4-5 Relation between average inter-particle distance and starting solids content for SFD granules

Vol% of starting suspension	Separation distance between particles, λ nm
5.5	22.8
14.3	10.7
28	4.5

One of the well established reasons for the formation of hard granules in zirconia is bridging by hydrogen bonds as in Figure 4-82. Due to surface hydrolysis, hydroxide is formed on the surface of particles. This reprecipitates on drying and cements the particles together. It can be seen from Figure 4-83 that the surface hydrolysis is higher in the pH range used in this study viz. 9 to 10. Also, yttrium is leached from the YSZ in acidic pH. The as-received suspension was acidic and would have some free yttrium ions in the suspension. But this will have to reprecipitate on drying. A combination of various dissolved species reprecipitating on the particle during drying forms the basis for formation of hard agglomerates, Figure 4-84. As the particles are packed closer, the chances of cementing increases. The microscopy images do not show these precipitated species probably owing to their fine size. TEM did not reveal any necking between particles. A detailed study of chemistry involving x-ray fluorescence or infra red spectroscopy of the surface is beyond the scope of this project.

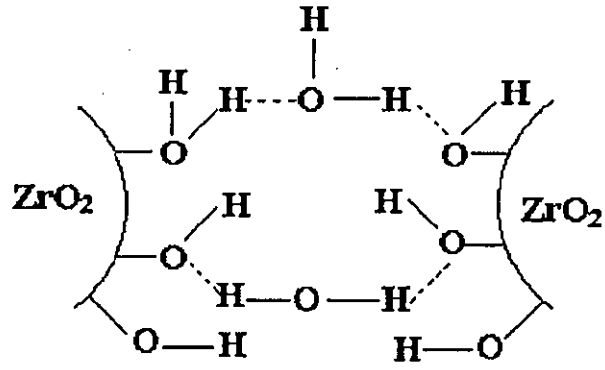

Figure 4-82 Bridging between zirconia particles by hydrogen bonds [124].

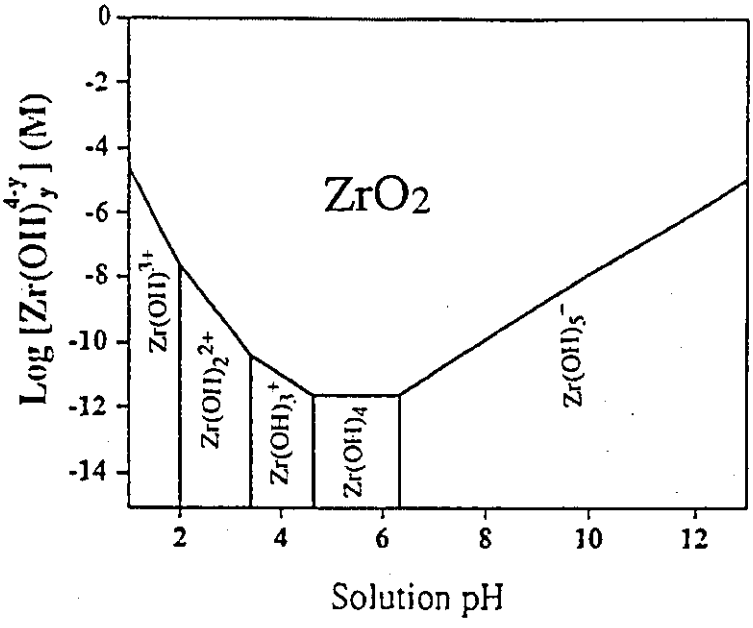

Figure 4-83 Solubility of zirconia at different pH [192].

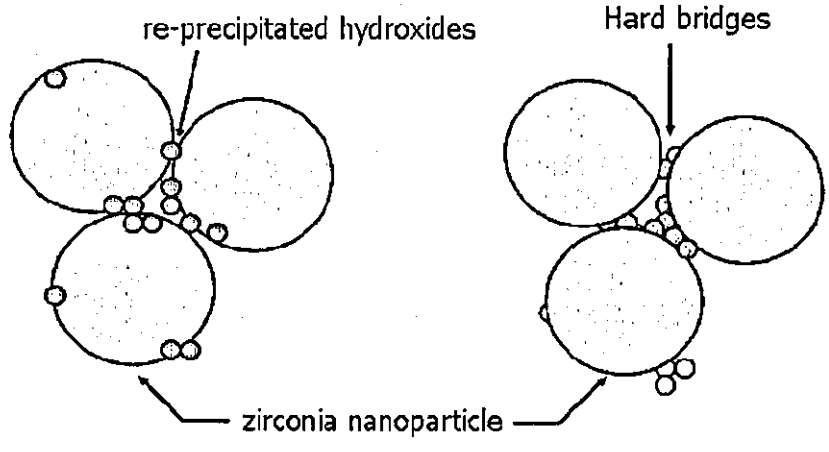

Figure 4-84 Schematic of hard agglomerate formation due to reprecipitation.

4.10 Microstructure of the sintered compacts

Limited sintering trials were carried out to establish the relation between granulation conditions and the microstructural evolution during sintering. As the title implies, the subject of the thesis is to engineer the green state of the nanopowder compacts and the sintering was used rather as a supportive tool; hence, the optimisation of conditions to obtain a fully sintered nanograined ceramic was beyond the scope of this work, though it has been undertaken within the group at Loughborough.

The various powder compacts made in this study were sintered under simple but identical conditions to compare their nanostructure at the end of firing. Depending on the agglomerate characteristics, the sintered density and microstructure varied. In the spray dried powder compacts, Figure 4-85, densification occurred within the granule relics whilst a homogeneous green microstructure was obtained for the compact formed from the SFD14 granules, Figure 4-86. With the increase in granule density, it can be seen in Figure 4-87 and Figure 4-88 that the sintering increased the inter-granular voids and segregation occurred on the uncrushed granule surface. Figure 4-89 shows dense nanograined islands separated by inter-granular cracks; these would act as strength limiting defects in the final ceramic.

The density of these nanostructured compacts were in the range of 90 – 95% of the theoretical value (6 g cm^{-3}). The exact values are not reported as statistically valid data demands many samples to be considered. The grain sizes were less than 100 nm for all nanopowder compacts, probably because grain coarsening had not been initiated.

The microstructure of the TOSOH powder compacts after firing at 1400°C for 1 hour is shown in Figure 4-90. This compact's microstructure also showed circular and horse-shoe shaped structures, the footprint of uncrushed granules at the end of cold compaction.

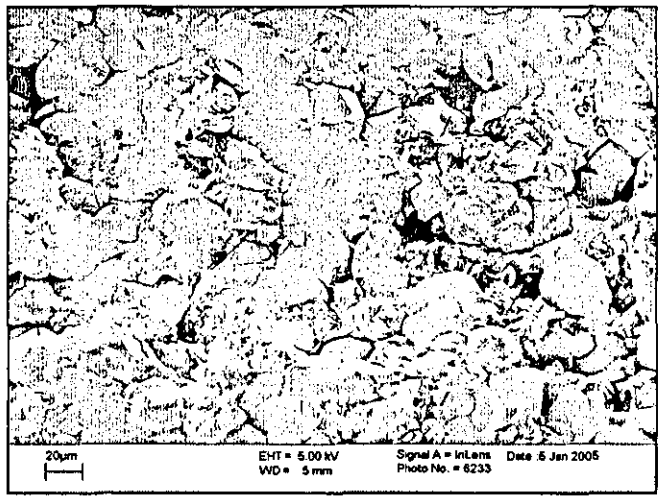

Figure 4-85 Fracture surface of partially sintered SD5 compact.

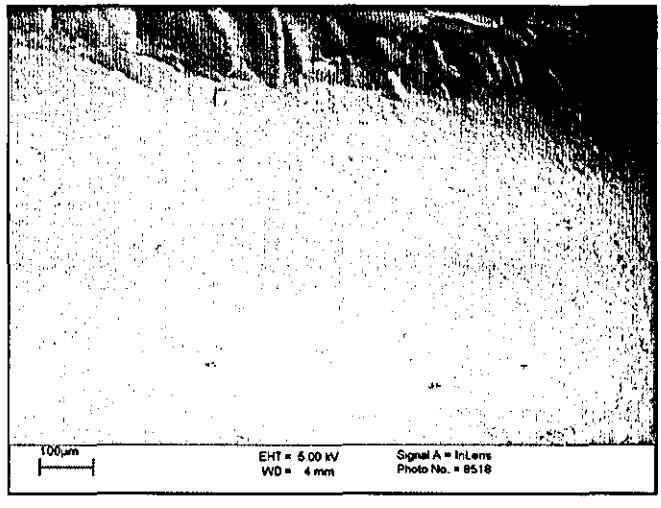

Figure 4-86 Fracture surface of partially sintered SFD14 compact.

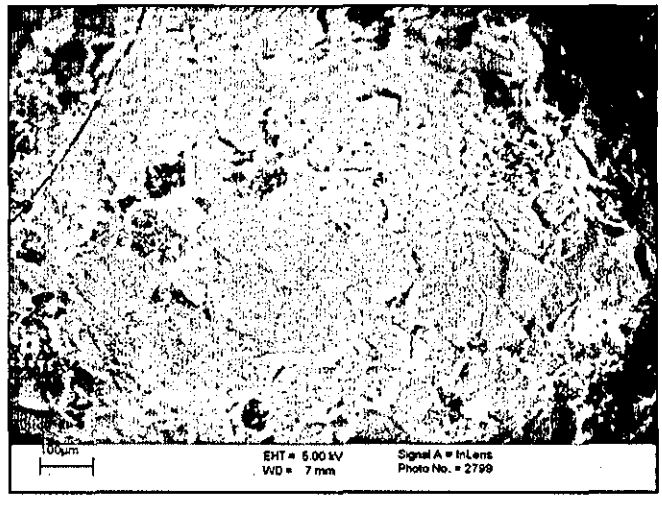

Figure 4-87 Fracture surface of partially sintered SFD24 powder compact.

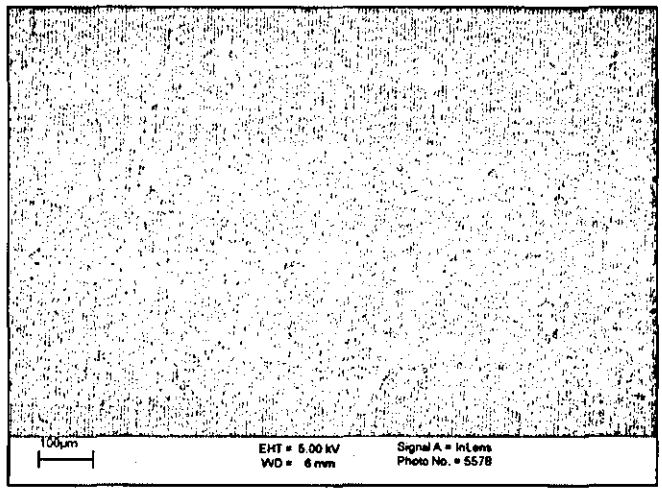

Figure 4-88 Pressed surface of SFD28 powder compact after partial sintering.

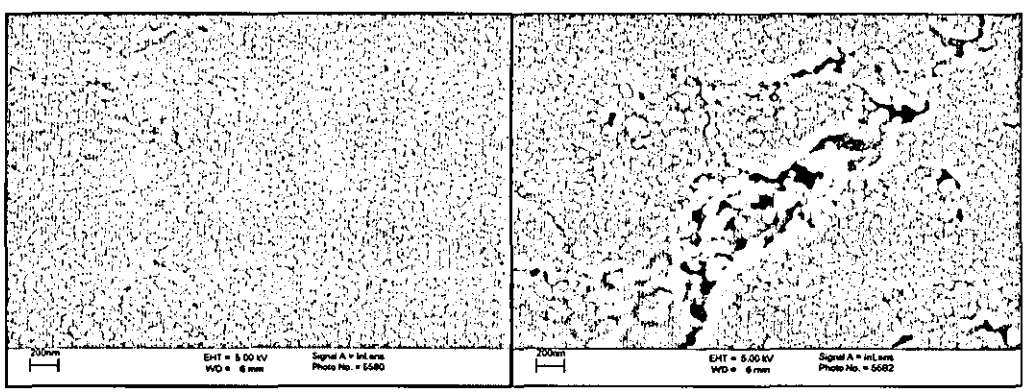

Figure 4-89 Nanostructure in sintered SFD28 powder compact.

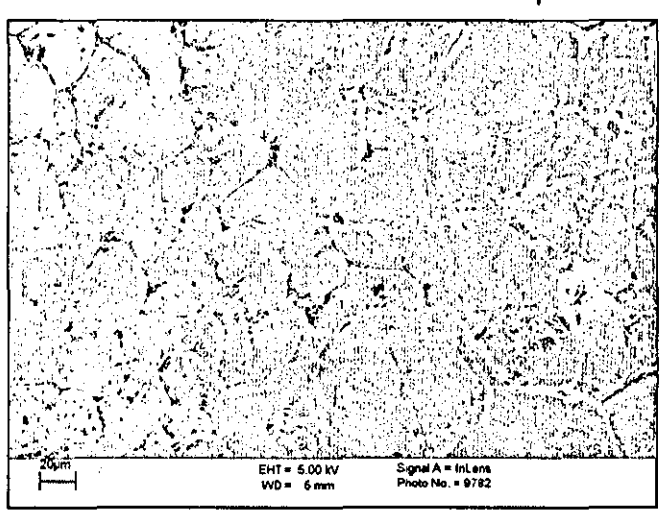

Figure 4-90 Die pressed surface of partially sintered TOSOH compact.

These limited sintering studies show that the SFD5 and SFD14 granules can potentially be sintered to form a completely dense, nano-grained ceramic.

4.11 Comparison among different powders

The overall comparison among these powders needs various parameters to be considered simultaneously. This can be best done by using spider diagrams. The multiple attributes of these powders had certain desired values. The ultimate aim was to have a process to make crushable, flowable granules with high fill density. Crushable granules yield a uniform nanostructure on compaction and have acceptable green density which in turn provides a chance to retain the nanostructure on sintering.

The oven dried powder as indicated in Figure 4-91 has non-existent flowability but an acceptable green microstructure on compaction. The fill density is low, but the tap density is satisfactory. This can be sintered into nanostructured bodies. In contrast, the spray dried powder from the as-received suspension having 5.5 vol% solids content yielded hard agglomerates resulting in a non-homogeneous microstructure which could not be sintered to nanograined ceramics, Figure 4-92.

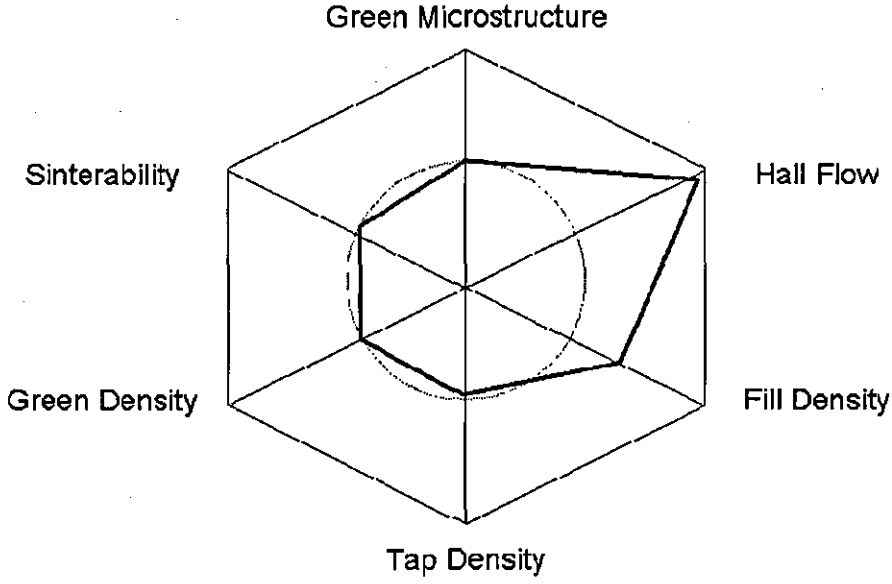

Figure 4-91 Characteristics of the oven dried powder.

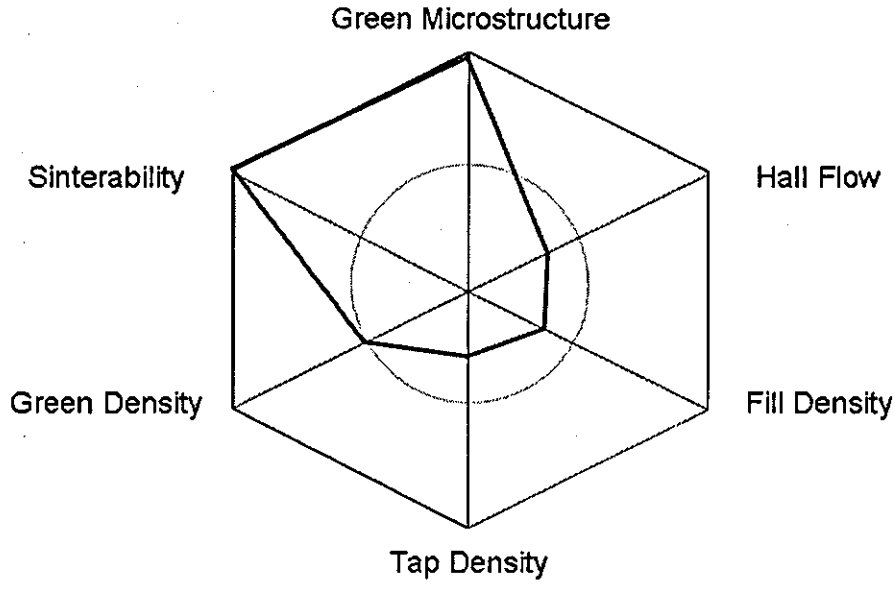

Figure 4-92 Characteristics of the SD5 powder.

The attributes of the spray freeze dried powders from 5.5 vol%, 14.3 vol% and 28 vol% suspensions are depicted in Figure 4-93, Figure 4-94 and Figure 4-95 respectively. It can be seen that the low solid content suspension results in low density granules which have poor flowability. In an attempt to improve upon these unacceptable characteristics, the SFD14 granules were made. It can be seen that the flowability, fill density and tap density are improved with the increase in solid content to 14.3 vol% solids. Fortunately, the green microstructure and sinterability remain acceptable. The effort to improve these parameters further was unsuccessful in the current work. The increase in solid content resulted in dense, hard granules as shown in Figure 4-95. This shows the interdependence between these parameters and that it is probably impossible to achieve all the ideal qualities without a change in the processing strategy. Thus, the best powder which can be produced is a compromise between these parameters. As homogeneous green microstructure is of paramount importance, SFD14 may be called as the best powder with a trade-off of fill density.

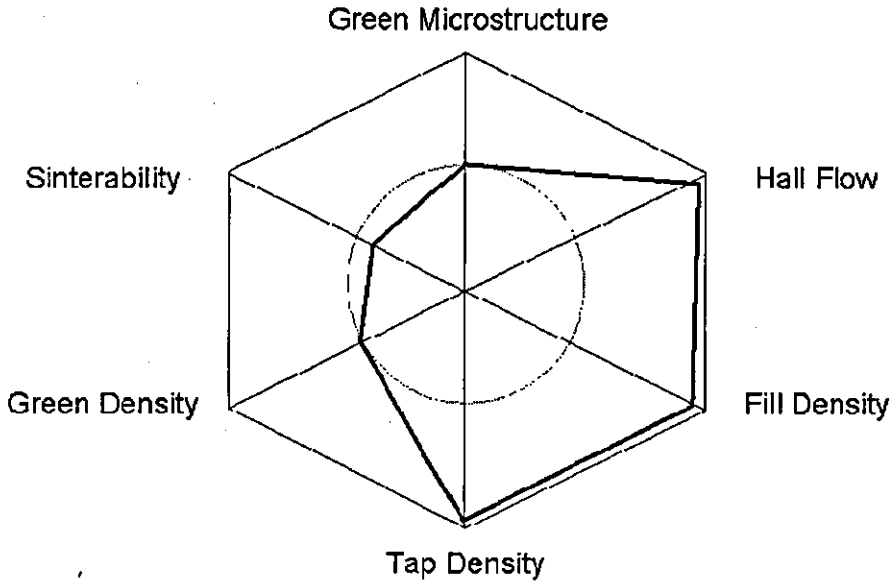

Figure 4-93 Characteristics of SFD5 powder

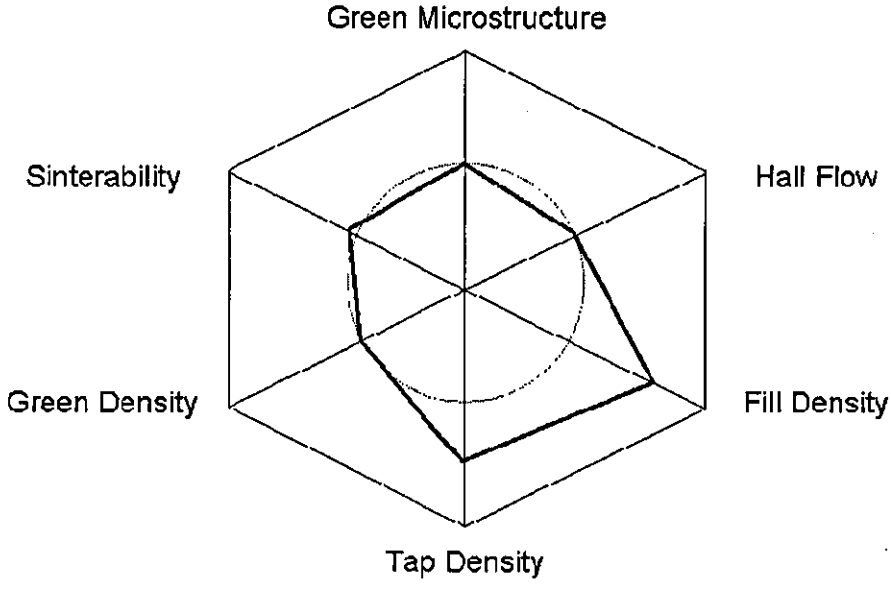

Figure 4-94 Characteristicsof SFD14 powder.

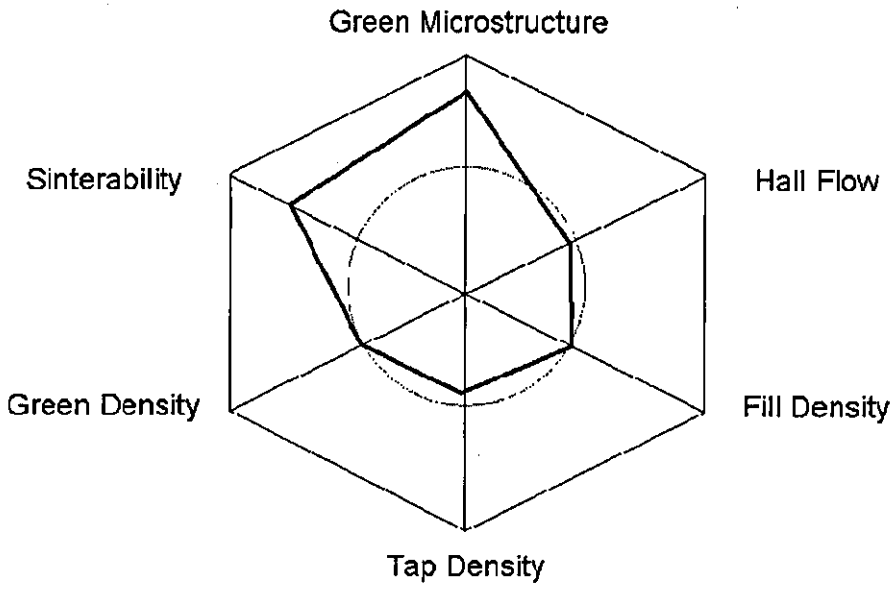

Figure 4-95 Characteristics of SFD28 powder.

Chapter 5

Conclusions

The viscosity of the YSZ nanosuspensions depended on their solid content, pH, dispersant and zeta potential of the particles. As the solid content increased the viscosity increased; the effectiveness of the dispersant depend on its adsorption and pH. It was found that TAC could be used to make low viscosity suspensions with solids content as high as 28 vol% whilst Dispex A40 was not good enough to prepare stable suspensions with oxide content higher than 14.3 vol%. TMAH was found to be a suitable pH modifier for this system.

The powders clearly showed an average primary particle diameter of less than 20 nm from TEM; the calculated d_p is 12.8 nm from XRD line broadening and d_{pBET} is ~12 nm. The match in the primary particle values from TEM and BET confirmed that the particle surface was smooth and nonporous. An agreement between TEM and the XRD values attests the highly nanocrystalline nature of the powders. If the particles had been amorphous, the calculated crystallite size from XRD would have been smaller.

Oven drying followed by micronising led to uncontrolled agglomeration and powders with poor flowability. Controlling the agglomerate size and shape was possible using spray granulation. Spray drying yielded dense, spherical granules with excellent flowability. When the amount of deflocculant was high, the spray dried granules had a donut shape. Spray freeze drying under optimised conditions was used to prepare spherical nano zirconia agglomerates with different granule densities and a targeted granule size of 100 to 250 μm.

Spray freeze drying was used to produce spherical agglomerates with good flowability. These were more porous than the spray dried granules; the granule density was adjusted simply by varying the solid

content of the starting suspension. The fill density and mass flow rate of the powders were directly proportional to the granule density and hence to the solid content of the starting suspension. However, due to the absence of capillary forces that shrank the granule during drying, the spray freeze dried granules had lower density than the spray dried granules.

The flowability of these powders was quantified using Hausner ratio and Hall flow and benchmarked with TOSOH submicron YSZ powder, a powder used widely in industry. With the increase in solids content of the starting suspension, the flowability of the spray freeze dried powder increased. The volumetric flow rate of the 14.3 vol% solids based spray freeze dried powder matched with that of the benchmark. However, its gravimetric flow rate lagged behind, owing to its low granule density.

Both spray drying and spray freeze drying allowed control on the shape and size of agglomerates, thus improving the possibility of die pressing them in an automatic industrial mass production facility. However, crushable granules with low granule strength were obtained only from spray freeze drying. The agglomerates must be weak enough to break down into nanosized primary particles when die pressed. This is important to achieve a homogeneous green microstructure which can then be sintered into fully dense nanograined ceramics.

The granule strength for a range of agglomerates made from zirconia nanopowders was assessed using compaction curves, pore size distribution and microstructural evolution during sintering.

Hard agglomerates resisted deformation during pressing. From the compaction curves, it was found that the strength of the granules decreased with increase in porosity. Spray freeze dried granules made from low solid content (<14.3 vol%) suspensions crushed readily whilst spray dried granules were hard. The compactibility of the nanopowders was less than that of the submicron powders. For a given consolidation pressure, the density of the nanopowder compacts was lower because of the higher surface area, which translated into higher inter-particle friction. The compact density was lower when hard agglomerates were present.

The hard agglomerates left inter-granular voids; a unimodal pore size distribution was achieved when soft agglomerates packed homogeneously in the green compact matrix. Two techniques were used to understand the pore size distribution within the compacts. Mercury intrusion porosimetry was capable of detecting pores between 20 nm to 10 μm whilst nitrogen adsorption isotherms had a range of 1.8 nm to 200 nm.

It was found that the use of MIP was severely limited for the nanopowder compacts. The ink-bottle shaped pores which were inter-granular were only accessible through narrow particle – particle channels. As a result, intrusion into bigger pores was restricted since the pressure available from the equipment was insufficient to achieve intrusion. Correspondingly, the inter-agglomerate pore volume calculated using MIP was underestimated.

Nitrogen adsorption isotherms work by capillary condensation of nitrogen at 77 K at low pressures. Measurement limitations restricted the useable range of this technique to <200 nm. This technique was used to quantify the proportion of intra- and inter- agglomerate pores in green nanopowder compacts. The volume of pores >200 nm was deduced from the geometrically measured compact density minus total cumulative pore volume deducted by nitrogen adsorption. This approach was found to be useful in grading the compacts' microstructural homogeneity.

The key findings using pore size measurements in powder compacts were

(i) the average interparticle distance (and hence the average pore diameter) decreased with increase in the solid content of the starting suspension for spray freeze dried granules

(ii) the primary particles packed closely in the spray dried granules

(iii) the proportion of inter-granular pores in the die pressed, spray freeze dried powder compact increased with the solid content of starting suspension

These results indicate that the granule strength increased when the granule density increased and agreed with the results found using compaction curves.

The two granule properties, viz., flowability and crushability, seem to be related to each other. With the increase in granule density, the fill ratio and flowability improved, but at the cost of crushability. Crushability is of paramount importance if nanostructure is to be maintained after sintering. Hence, a trade-off between these two characteristics was sought in this case. It was found that spray freeze dried granules with 14.3 vol% solids content worked satisfactorily, meeting both the criteria.

Green compacts with fine pores sintered to finer grains. When agglomerates were intact in the pressed bodies, differential sintering occured and grain coarsening started earlier. It was seen that the pores within the granule relics were eliminated before the bigger pores when the granules were hard.

The possible reasons for the formation of hard granules could be

(i) the formation of solid bridges between zirconia particles due reprecipitation of minerals

(ii) bridging between hydroxide formed by surface hydrolysis

(iii) increased van der Waals forces because of the fine particle size and small distance of separation between nanopowders and

(iv) interaction of the dispersant with the particles

It can be concluded that it is possible to have granulated zirconia nanopowder with good flowability and crushability; but the fill density of the spray freeze dried powder was less than that of the spray dried powder; it was essential to use a high solid content starting suspension to get granules with higher fill density but this led to hard granules.

Chapter 6

Future work

The problem associated with the use of organics in producing dispersed high solids content nanosuspension is two fold:

(i) As the organics have a lower density (about 1 g cm^{-3} as compared to 6 g cm^{-3} of zirconia) it reduces the fill density;

(ii) The presence of organics also leads to lower green densities in the die pressed compacts both before and after the binder burnout stage.

It might be possible to improve the green densities for SFD powder compacts by a few percent if the amount of organics was reduced.

At any given consolidation pressure, the green densities obtained by the nanopowders is lower than that of the submicron powders. This is attributed to the higher inter-particle friction which originated from the higher surface area of these powders. The latter lead to more density gradients within the green compacts. A good lubricant system can help in reducing the inter-particle friction by aiding the gliding and sliding of the particles past each other. This will effectively increase the green densities that can be achieved at a given pressure and reduce density gradients within the compact.

Another possible area for improvement is in the way the slurry is atomized. If a system that can atomise higher viscosity suspensions is developed, it will open new avenues for exploration. For example, suspensions with higher solid content and yet low levels of organics, flocculated / suspensions with different (low) zeta potentials (or different levels of dispersion) etc., can be atomized and hence granulated. At this stage, it is not clear if the granules from flocculated slurries will crush more readily than those from dispersed slurries.

Some preliminary tests on single granule strength showed that the granules crush at lower pressures when the amount of organics (TAC and TMAH) was lower. Therefore, fine tuning the dispersant and combining with optimal binders to achieve flowable and crushable granules with high fill density from high solid content starting suspension needs further optimisation on the lab scale.

Industrial adoption of the process would include designing suitable freezing and drying systems. Freeze drying is possible over a wide range of temperatures and pressures. However, for an industrial process the most suitable drying temperature is just below the collapse temperature of the granule. This can be found by carrying out low temperature differential scanning calorimetry. The effect of freezing rate on the granule strength is unknown and needs investigation.

The flowability of the powders depends on their granule size distribution. It is known that the flowability is better when the granules are bigger; the presence of fines reduce the flow rates. In this study, only spray freeze dried granules within the size range 125 to 250 μm were used. Optimisation of the granulation (spraying) conditions depend on the suspension characteristics and a detailed study can be carried out on this front.

Sintering curves using dilatometry can yield quantitative information on the sinterability of these powder compacts. Optimisation of the sintering conditions to retain the nanostructure can be carried out as a separate project.

7.1 Standard XRD file

78-1807 Quality: C
CAS Number:
Molecular Weight: 123.22
Volume[CD]: 140.88
Dx: 5.809 Dm:
Sys: Monoclinic
Lattice: Primitive
S.G.: $P2_1/c$ (14)
Cell Parameters:
a 5.150 b 5.211 c 5.317
α β 99.230 γ
I/Icor: 4.82
Rad: CuKa1
Lambda: 1.54060
Filter:
d-sp: calculated
ICSD #: 062993

Zr O2
Zirconium Oxide
Ref: Calculated from ICSD using POWD-12++, (1997)
Ref: Howard, C.J., Hill, R.J., Reichert, B.E., Acta Crystallogr., Sec. B: Structural Science, 44, 116 (1988)

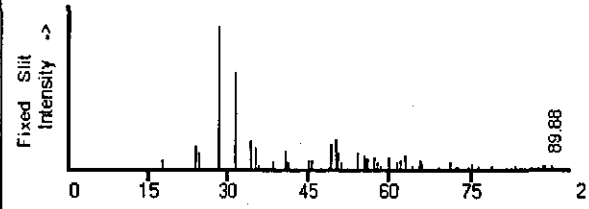

2θ	Int-f	h	k	l	2θ	Int-f	h	k	l	2θ	Int-f	h	k	l
17.430	64	1	0	0	50.090	212	2	2	0	64.054	13	0	2	3
24.044	168	0	1	1	50.540	122	1	2	2	64.252	29	0	3	2
24.440	118	1	1	0	51.168	53	2	2	1	64.252	29	1	2	3
28.166	999 *	1	1	1	54.059	116	2	0	2	64.968	8	2	3	0
31.455	678	1	1	1	54.059	116	3	0	0	65.349	23	1	3	2
34.138	201	0	0	2	54.657	7	1	2	2	65.657	65	2	2	2
34.387	130	0	2	0	55.252	50	2	2	1	65.657	65	3	2	0
35.280	149	2	0	0	55.347	98	0	1	3	65.884	40	2	3	1
35.874	31	1	0	2	55.564	74	1	1	3	68.898	21	1	3	2
38.541	53	0	2	1	55.687	38	0	3	1	69.585	8	1	2	3
39.407	10	2	1	0	55.884	75	1	3	0	70.155	5	2	2	3
39.949	5	1	1	2	57.125	80	3	1	0	71.017	22	3	2	1
40.702	128	2	1	1	57.125	80	3	1	1	71.017	22	3	2	2
41.129	50	1	0	2	57.855	50	1	3	1	71.223	48	1	0	4
41.365	48	1	2	1	58.242	34	2	2	2	71.897	9	0	0	4
43.782	1	1	2	1	59.767	87	1	3	1	72.069	15	2	3	2
44.802	64	1	1	2	59.996	80	3	0	2	72.485	13	0	4	0
45.485	67	2	0	2	61.322	55	1	1	3	72.582	12	2	1	3
45.485	67	2	1	1	61.931	64	2	1	3	73.514	4	3	1	3
48.898	21	2	1	2	62.793	96	3	1	1	74.611	18	4	0	0
49.238	171	0	2	2	62.793	96	3	1	2	75.056	42	0	4	1

79-1769 Quality: C
CAS Number:
Molecular Weight: 123.22
Volume[CD]: 67.04
Dx: 6.104 Dm:
Sys: Tetragonal
Lattice: Primitive
S.G.: $P4_2/nmc$ (137)
Cell Parameters:
a 3.595 b c 5.185
α β γ
I/Icor: 9.87
Rad: CuKa1
Lambda: 1.54060
Filter:
d-sp: calculated
ICSD #: 066787

Zr O2
Zirconium Oxide
Ref: Calculated from ICSD using POWD-12++, (1997)
Ref: Bondars, B et al., J. Mater. Sci., 30, 1621 (1995)

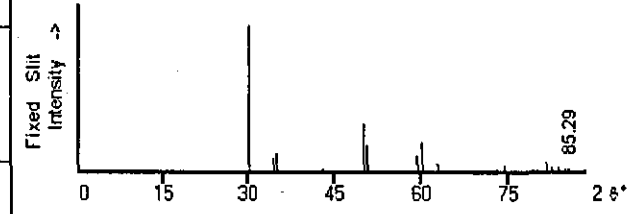

2θ	Int-f	h	k	l	2θ	Int-f	h	k	l	2θ	Int-f	h	k	l
30.222	999 *	1	0	1	59.272	106	1	0	3	81.731	64	2	1	3
34.569	81	0	0	2	60.202	200	2	1	1	82.541	31	3	0	1
35.271	124	1	1	0	62.851	47	2	0	2	83.673	24	1	1	4
42.974	14	1	0	2	68.621	3	2	1	2	84.883	17	2	2	2
50.218	320	1	1	2	72.917	15	0	0	4	85.287	15	3	1	0
50.738	171	2	0	0	74.589	37	2	2	0					
53.933	1	2	0	1	78.347	3	1	0	4					

7.2 Particle size distribution

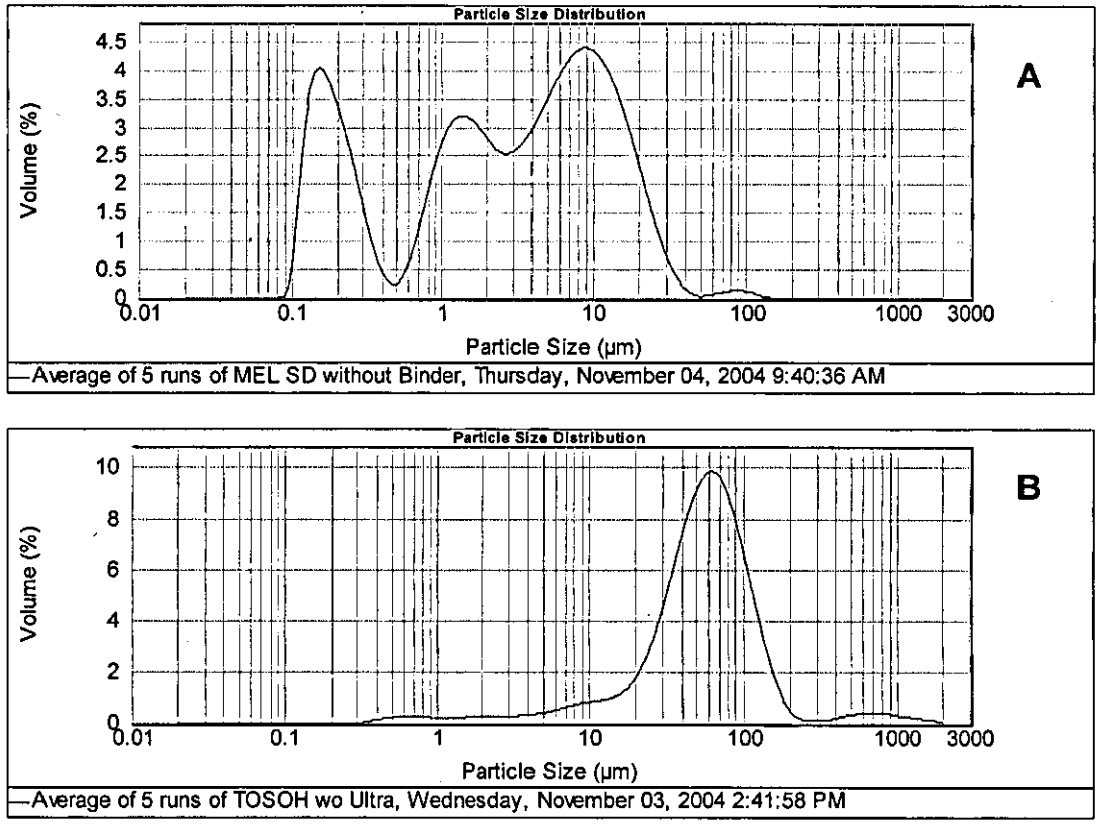

Figure 7-1 Particle size distribution of SD5 and TOSOH powders

7.3 Pore size distribution in powder compacts

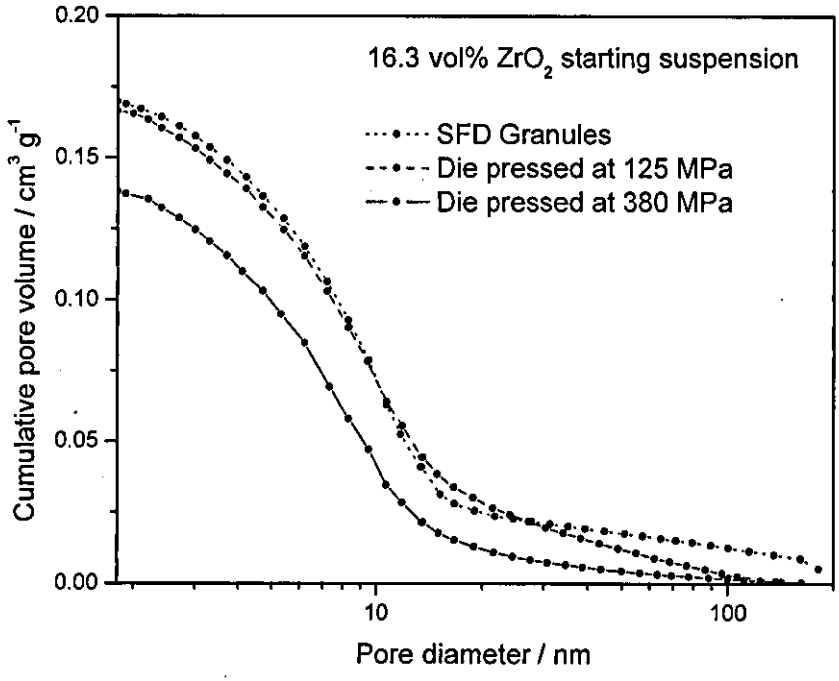

Figure 7-2 Pore size distribution in SFD granules and compacts pressed at different pressures (16.3 vol% ZrO_2 starting suspension).

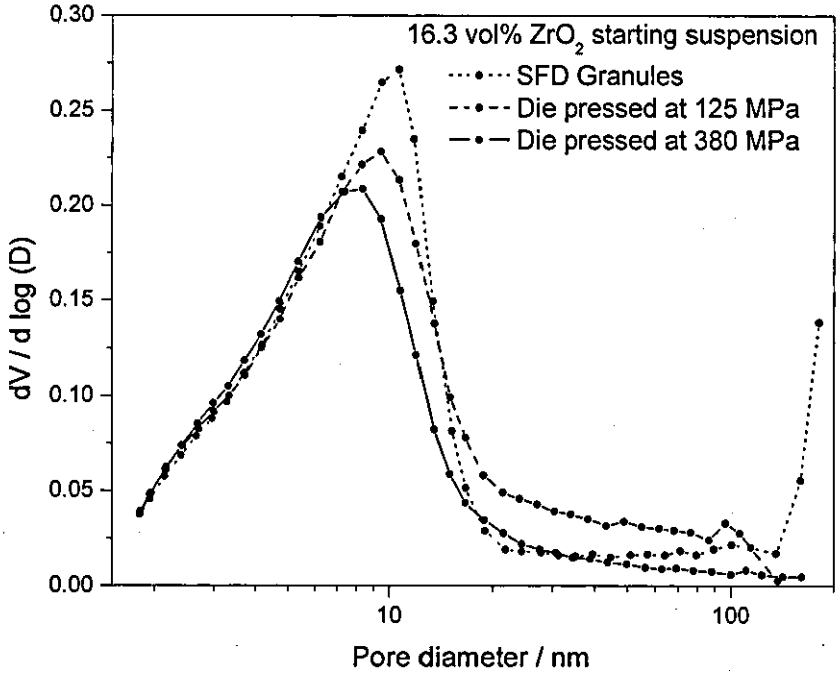

Figure 7-3 Pore size distribution in SFD granules and compacts pressed at different pressures (16.3 vol% ZrO_2 starting suspension).

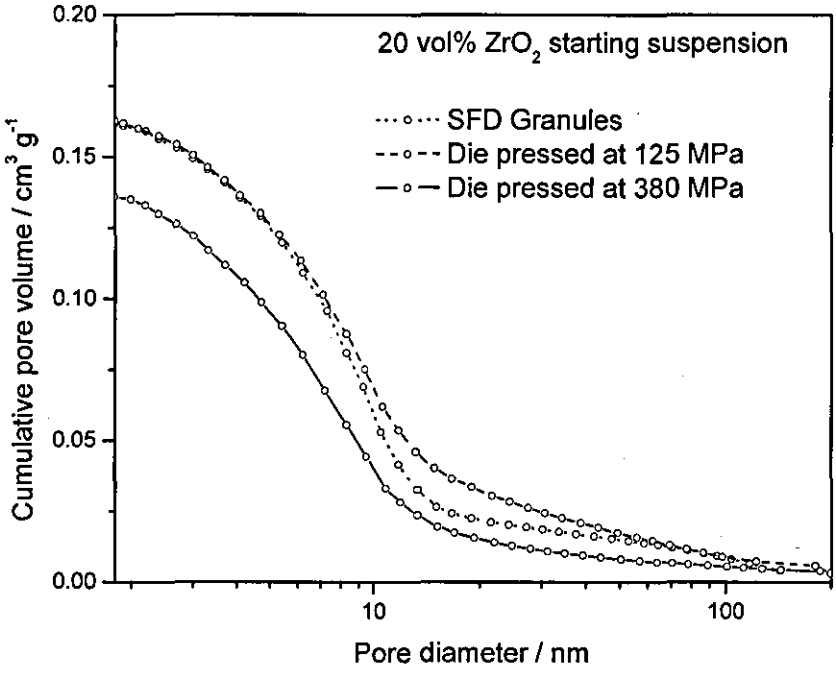

Figure 7-4 Pore size distribution in SFD granules and compacts pressed at different pressures (20 vol% ZrO_2 starting suspension).

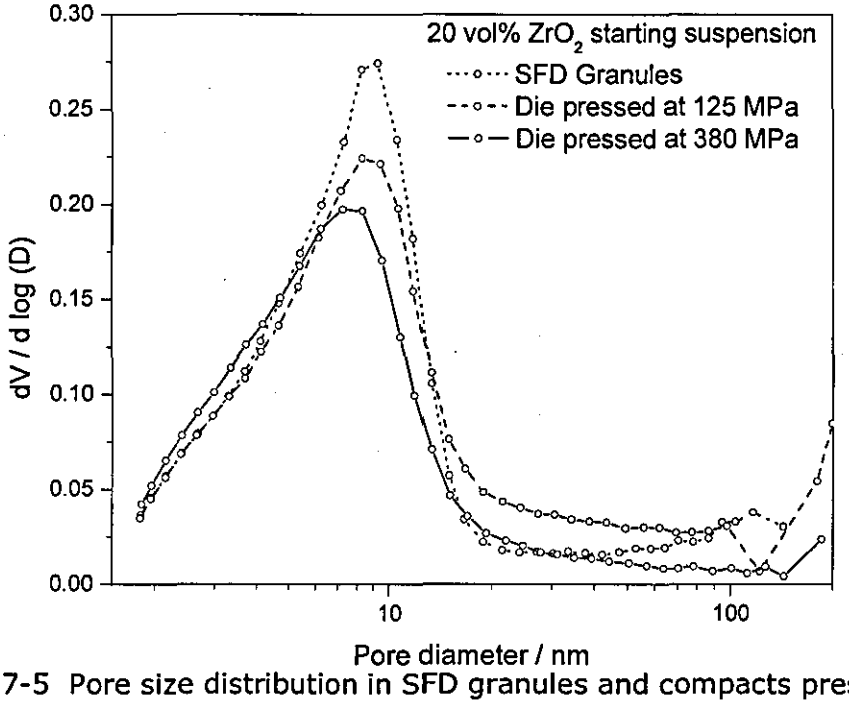

Figure 7-5 Pore size distribution in SFD granules and compacts pressed at different pressures (20 vol% ZrO_2 starting suspension).

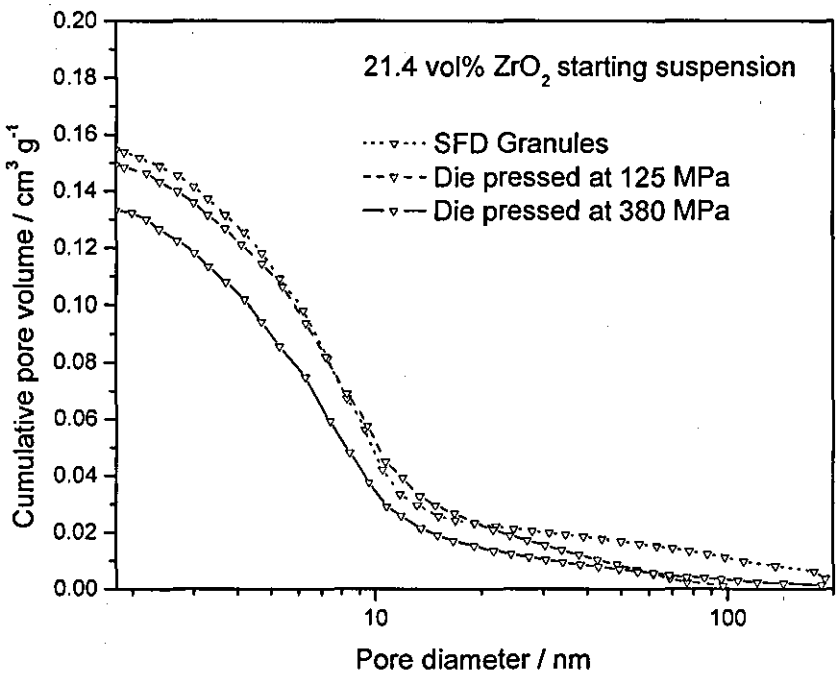

Figure 7-6 Pore size distribution in SFD granules and compacts pressed at different pressures (21.4 vol% ZrO_2 starting suspension).

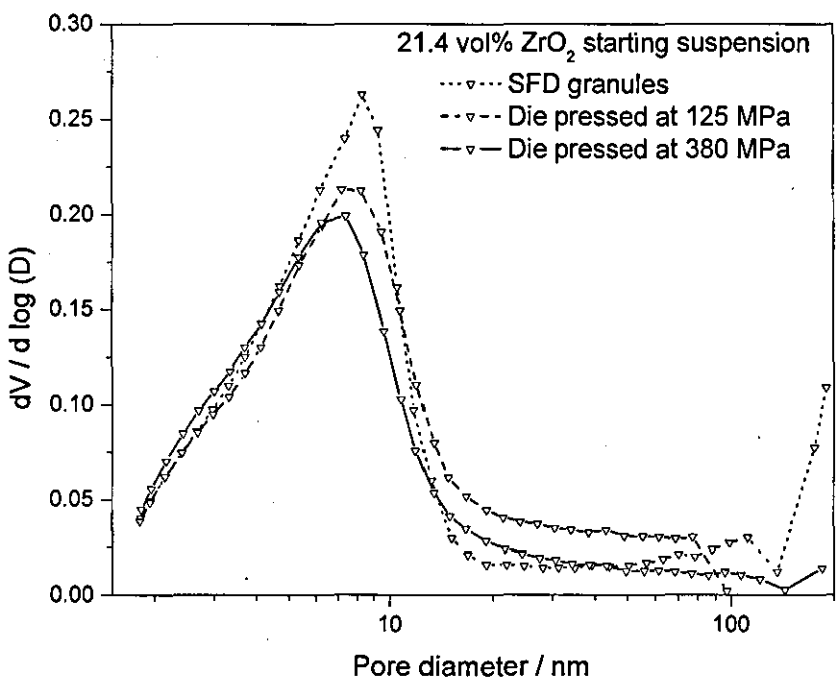

Figure 7-7 Pore size distribution in SFD granules and compacts pressed at different pressures (21.4 vol% ZrO_2 starting suspension).

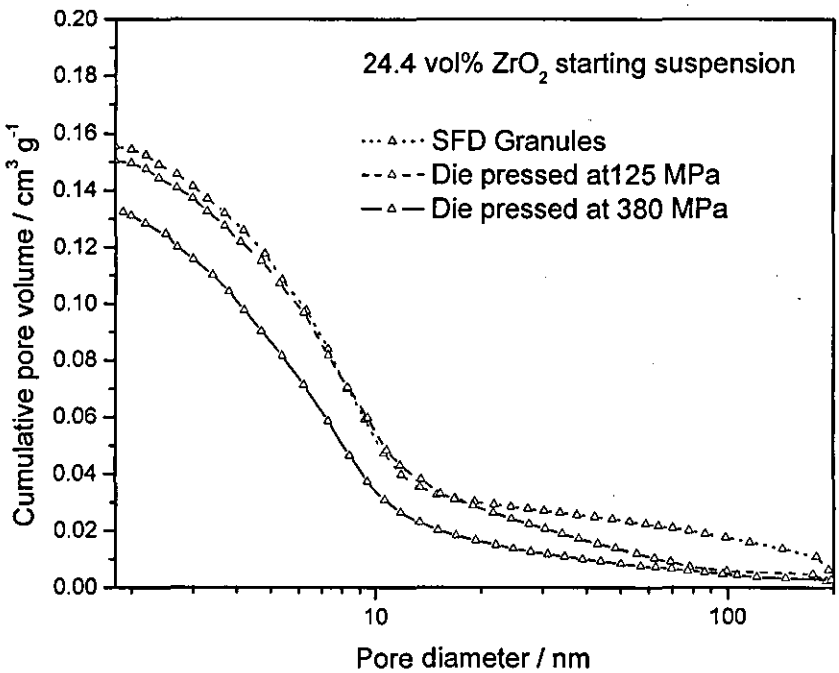

Figure 7-8 Pore size distribution in SFD granules and compacts pressed at different pressures (24.4 vol% ZrO_2 starting suspension).

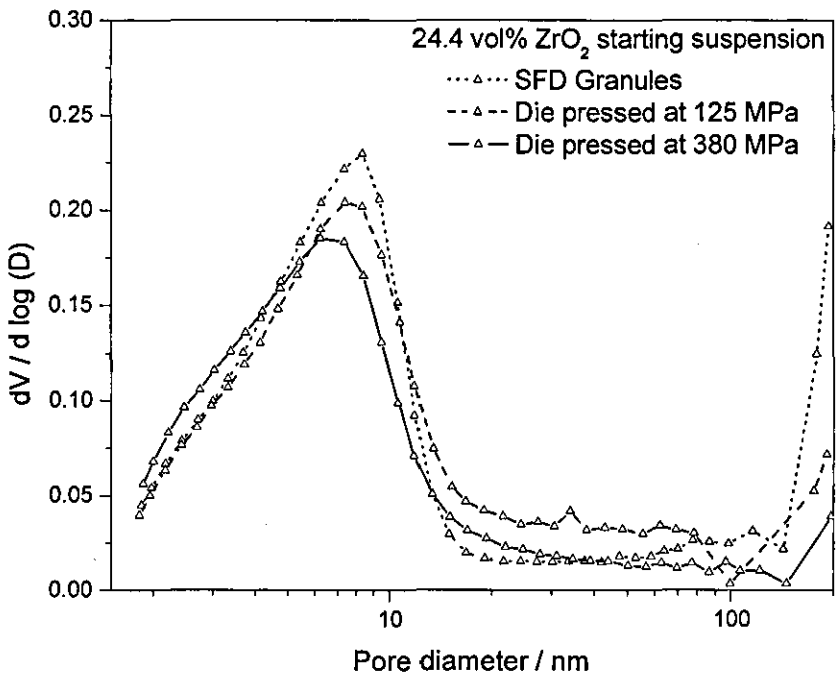

Figure 7-9 Pore size distribution in SFD granules and compacts pressed at different pressures (24.4 vol% ZrO_2 starting suspension).

References

1. R W Rice, "Forming and Pressureless sintering of powder derived bodies", Ceramic fabrication technology, Marcel Dekker publication, 99-141, (2002)
2. N. Lane, "The grand challenges of nanotechnology", *Journal of Nanoparticle Research*, 3, 95-105, (2001)
3. E O Ezugwu, J Bonney, R R da Silva & A R Machado, "Evaluation of the performance of different nano-ceramic tool grades when machining nickel-base, Inconel 718, Alloy", J. of the Braz. Soc. of Mech. Sci. & Eng., XXVI, [1], 12 – 16, (2004).
4. M Cain & RMorrell, "Nanostructured ceramics: a review of their potential", *Appl. Organometal. Chem.*, 15, 321-330, (2001)
5. J R Groza, "Nanocrystalline powder consolidation methods", *Nanostruct Mater.*, edited by C C Koch, Noyes Publications, 115-178, (2002)
6. U Betz & H Hahn, "Ductility of nanocrystalline zirconia based ceramics at low temperatures", *Nanostruct. Mater.*, 12, 911-914, (1999)
7. Nano News Column, "Nanotechnology 10 years out", *Am.Ceram.Soc. Bull.*, 12, 6,(2004)
8. Q Q Zhao, A Boxman & U Chowdhry, "Nanotechnology in chemical industries-opportunities and challenges", *Journal of Nanoparticle Research*, 5, 567-572, (2003)
9. X Zhu, J Xu, Z Meng, J Zhu, S Zhou, Q Li, Z Liu & N Ming, "Microdisplacement characteristics and microstructures of functionally graded piezoelectric ceramic actuator", *Materials and Design*, 21, 561-566, (2000)
10. D W Johnson Jr, "Ceramic materials for electronic, photonic applications", *Am. Cer. Soc. Bull.*, 83, [9], 15-19, (2003)
11. J G P Binner & I A H Al-Dawery, "Microwave melt texturing of bulk YBCO superconductors", *Supercond. Sci. Technol.*, 11, 1230-1236, (1998)
12. M J Lance, E M Vogel, L A Reith & W R Cannon, "Low-temperature aging of zirconia ferrules foroptical connectors", *J. Am. Ceram. Soc.*, 84, [11], 2731-2733, (2001)
13. X Xu, T Nishimura, N Hirosaki, R-J Xie, Y Yamamoto & H Tanaka, "Superplastic deformation of nano-sized silicon nitride ceramics", *Acta Materialia*, 54, 255 -262, (2006)
14. Y Sakka, T S Suzuki, K Morita, K Nakano & K Hiraga, "Colloidal processing and superplastic properties of zirconia- and alumina-based nanocomposites", *Scripta Mater*, 44, 2075-2078, (2001)

15. M Z Berbon & T G Langdon, "An examination of the flow process in superplastic yttria-stabilised tetragonal zirconia", *Acta. Mater*, 47, [8], 2485-2495, (1999)

16. P A Webb & C Orr, "Modern particle characterization methods, Part 2", *Am. Cer. Soc. Bull.*, 85, [9], 24-27, (2006)

17. S H Yoo, T S Sudarshan, K Sethuram, G Subhash & R J Dowding, "Consolidation and high strain rate mechanical behavior of nanocrystalline tantalum powder", *Nanostructured Materials*, 12, 23-28, (1999)

18. L Zych & K Haberko, "Filter pressing and sintering of a zirconia nanopowder", *J. Euro. Ceram. Soc.*, 26, 373-378, (2006)

19. http://www.zircoa.com/e_home/products/fine_grain/dies/tube.intl.reprint.html

20. R C Garvie, "The occurrence of metastable tetragonal zirconia as a crystallite size effect" J. Phys. Chem., 69, 1238 - 43 (1965)

21. F F Lange, "Powder processing science and technology for increased reliability", *J. Am. Ceram, Soc.*, 72, [1], 3-15, (1989)

22. T Abraham, "Powder market update: Nanoceramic applications emerge", *Am. Cer. Soc. Bul.*, 83, [8], 23-25, (2004)

23. D Bortzmeyer, "Dry pressing f ceramic powders", in Ceramic processing, edited by R A Terpstra, P P A C Pex and A H De Vries, Chapman & Hall publishing, (1995)

24. M N Rahaman, in Ceramic processing, CRC press, Chapter 7, 302-306, (2007)

25. http://www.keram.se/eng/pdf/slip_casting.pdf

26. I Santacruz, C Baudin, R Moreno & M I Nieto, "Improved greenstrength of ceramics through aqueous gelcasting", *Advanced Engineering Materials*, 6, [8], 672-676, (2004)

27. http://www.keram.se/eng/pdf/tape_casting.pdf

28. K Lindqvist & E Lidĕn, "Preparation of alumina membranes by tape casting and dip coating", *J. Euro. Ceram. Soc.*, 17, 359-366, (1997)

29. J Davies & J G P Binner, "Plastic forming of alumina from coagulated suspensions", *J. Euro. Ceram. Soc.*, 20, 1569-1577, (2000)

30. J Davies & J G P Binner, "Coagulation of electrosterically dispersed concentrated alumina suspensions for paste production", *J. Euro. Ceram. Soc.*, 20, 1555-1567, (2000)

31. P Sarkar, D De & H Rho, "Synthesis and microstructural manipulation of ceramics by electrophoretic deposition", *J. Mater. Sci.*, 39, 819-823, (2004)

32. J Tabellion & R Clasen, "Electrophoretic deposition from aqueous suspensions for near-shape manufacturing of advanced ceramics and glasses-applications", *J. Mater. Sci.*, 39, 803-811, (2004)

33. I Zhitomirsky & A Petric, "Electrophoretic deposition of ceramic materials for fuel cell applications", *J. Euro. Ceram. Soc.*, 20, 2055-2061, (2000)

34. J R G Evans, "Injection moulding", in Materials Science and Technology– A comprehensive treatment, Edited by R W Cahn, P Haasen & E J Kramer, Volume 17A, VCH Publishers Inc., 268-306, (1996)

35. J R Groza & R J Dowding, "Nanoparticulate materials densification", *Nanostructured Materials*, 7, [7], 749-768, (1996)

36. C C Koch, "Synthesis of nanostructured materials by mechanical milling : Problems and opportunities", *Nanostructured Materials*, 9, 13-22, (1997)

37. D L Bourell, Parimal & W Kaysser, "Sol-Gel synthesis of nanophase yttria-stabilised tetragonal zirconia and densification behavior below 1600 K", *J. Am. Ceram. Soc.*, 76, [3], 705-711, (1993)

38. A L Quinelato, E Longo, L A Perazolli & J A Varela, "Effect of ceria content on the sintering of ZrO2 based ceramics synthesised from a polymeric precursor", *J. Euro. Ceram. Soc.*, 20, 1077-1084, (2000)

39. D W Richerson, in Modern Ceramic Engineering, Second edition, Marcel and Dekker, 418-444, (1992)

40. O L Khasanov, "The Method for Powder Compacting into Articles", PCT WO 03/051561 published on 26 June, (2003)

41. C-Y Wu, A C F Cocks, O T Gillia & D A Thompson, "Experimental and numerical investigations of powder transfer", *Powder Technology*, 138, 216-228, (2003)

42. N Kieffer & R Clasen, "Sintering behavior of pure zirconia powder at low temperatures", Innovative processing and synthesis of ceramics, glasses and composites IV, edited by N P Bansal & J P Singh, Ceramic Transactions, [115], published by ACerS, 305-306,(2000)

43. A P Bromley, "Minimising density variations in die pressed cylindrical compacts", *J. Euro. Ceram. Soc.*, 18, 1539 -1543, (1998)

44. D Holz, P V D Valk, G Kogias, E Eleftheriou & V Zaspalis, "Industrial quantitative control of the pressing behavior of spray dried MnZn-Ferrite granules", *J. Am. Ceram. Soc.*, 90, [6], 1780-1786, (2007)

45. C. L. Feng and A D Yu, "Effect of liquid addition on the packingof mono-sized coarse spheres," *Powder Technol.*, 99, 22-28, (1998)

46. T Moritz & A Nagy, "Spray freeze granulates-from lab scale to pilot production", presented at 7th International conference on nanostructured materials, Wiesbaden, (2004)

47. A Krell, P Blank, H Ma, T Hutzler & M Nebelung, "Processing of high density submicrometer Al_2O_3 for new applications", *J. Am. Ceram. Soc.*, 86, [4], 546 - 53, (2003)

48. Y Yagi, S Hirano, Y Ujihira & M Miyayama, "Analysis of the sintering process of 2 mol% yttria-doped zirconia by positron annihilation lifetime measurements", *J. Mater. Sci. Letters.*, 18, 205-207, (1999)

49. H Ferkel & R J Hellmig, "Effect of nanopowder deagglomeration on the densities of nanocrystalline cermic green bodies and their sintering behaviour", *Nanostruct. Mater.*, 11, [5], 617-622, (1999)

50. J Zheng, W B Carlson and J S Reed, "Dependence of compaction efficiency in dry pressing on the particle size distribution", *J. Am. Ceram. Soc.*, 78, [9], 2527-33, (1995)

51. C Laberty-Robert, F Ansart, C Deloget, M Gaudon & A Rousset, "Dense yttria stabilised zirconia: sintering and microstructure", *Ceram. Int.*, 29, 151-158, (2003)

52. I W Chen & X-H Wang, "Sintering dense nanocrystalline ceramics without final-stage grain growth", *Nature*, 404, 168, (2000)

53. A Cellard, R Zenati, V Garnier, G Fantozzi & G Baret, "Optimization of chromium oxide nanopowders dispersion for spray-drying", *J. Euro. Ceram. Soc.*, 27, 1017-1021, (2007)

54. J Zank, M Kind and E U Schlünder, "Particle growth and droplet deposition in fluidised bed granulation", *Powder Technol.*, 120, 76-81, (2001)

55. G I Tardos, K P Hapgood, O O Ipadeola & J N Michaels, "Stress measurement in high-shear granulators using calibrated 'test' particles : application to scale-up", *Powder Technol.*, 140, 217-227, (2004)

56. H G Kristensen, "Particle agglomeration in high shear mixers", *Powder Technol.*, 88, 197-202, (1996)

57. B N'Dri-Stempfer, D Oulahna, O Eterradossi, A Benhassaine & J A Dodds, "Binder granulation and compaction of coloured powders", *Powder Technol.*, 130, 247-252, (2003)

58. M Bardin, P C Knight & J P K Seville, "On control of particle size distribution in granulation using high-shear mixers", *Powder Technol.*, 140, 169-175, (2004)

59. S Danielsen, P Holm, G H Kristensen & T Schaefer, "Process and an apparatus for agglomeration of a powdery material", *United states patent number* 5, 030, 400, (1991)

60. F Hoornaert, P A L Wauters, G M H Meesters, S E Pratsinis & B Scarlett, "Agglomeration behavior of powders in a Lödige mixer granulator", *Powder Technol.*, 96, 116-128, (1998)

61. S T Keningley, P C Knight & A D Marson, "An investigation into the effects of binder viscosity on agglomeration behavior", *Powder Technol.*, 91, 95-103, (1997)

62. J S Fu, Y S Cheong, G K Reynolds, M J Adams, A D Salman & M J Hounslow, "An experimental study of the variability in the properties and quality of wet granules", *Powder Technol.*, 140, 209-216, (2004)

63. J Werani, M Grünberg, C Ober & H Leuenberger, "Semicontinuous granulation-the process of choice for the production of pharmaceutical granules?", *Powder Technol.*, 140, 163-168, (2004)

64. K Masters, "Spray Drying Handbook", Longman Scientific and technical publishing, Fifth edition, (1991)

65. G E Fair & F F Lange, "Effect of interparticle potential on forming solid, spherical agglomerates during drying", *J. Am. Ceram. Soc.*, 87, [1], 4-9, (2004)

66. W J Walker, J S Reed & S K Verma, "Influence of slurry parameters on the characteristics of spray dried granules", *J. Am. Ceram. Soc.*, 82, [7], 1711 -1719, (1999)

67. G Bertrand, P Roy, C Filiatre & C Coddet, "Spray-dried ceramic powders: A quantitative correlation between characteristics and shapes of granules", *Chem. Eng. Sci.* , 60, 95-102, (2005)

68. G Bertrand, C Filiatre, H Mahdjoub, A Foissy & C Coddet, "Influence of slurry characteristics on the morphology of spray-dried alumina powders", *J. Euro. Ceram. Soc.*, 23, 263-271, (2003)

69. K J Konsztowicz, G Maksym, T Maksym, H W King, W F Caley & E V Butler, "The role of surface tension in the formation of donut-shaped granules during spray-drying", *Ceram. Trans.*, 26, 46-53, (1992)

70. H Mahdjoub, P Roy, C Filiatre, G Bertrand & C Coddet, "The effect of the slurry formulation upon the morphology of spray-dried yttria stabilized zirconia particles", *J. Euro. Ceram. Soc.*, 23, 1637-1648, (2003)

71. H Takahashi, N Shinohara, M Okumiya, K Uematsu, T JunIchiro, Y Iwamoto & H Kamiya, "Influence of slurry flocculation on the character and compaction of spray dried silicon nitride granules", *J. Am. Ceram. Soc.*, 78, [4], 903-908, (1995)

72. S Baklouti, T Chartier & J F Baumard, "Binder distribution in spray dried alumina agglomerates", *J. Euro. Ceram. Soc.*, 18, 2117-2121, (1998)

73. Z Zhang & D J Green, "Fracture toughness of spray-dried powder compacts", *J. Am. Ceram. Soc.,* 85, [5], 1330-32, (2002)

74. S Begum, A Duff, R Puyane & M S J Hashmi, "Evaluation of latex binder in the processing of electronic ceramic powder", *J. Mater. Proc. Technol.*, 77, 108-114, (1998)

75. A Tsetsekou, C Agrafiotis, I Leon & A Milias, "Optimisation of the rheological properties of alumina slurries for ceramic processing applications, Part II: Spray Drying", *J. Euro. Ceram. Soc.*, 21, 493-506, (2001)

76. N Shinohara, S Katori, M Okumiya, T Hotta, K Nakahira, M Naito, Y-I Cho & K Uematsu, "Effect of heat treatment of alumina granules on the compaction behavior and properties of green and sintered bodies", *J. Eur. Ceram. Soc.*, 22, 2841-2848, (2002)

77. D W Whitman, X Tang, D I Cumbers & S A Ibbitson, "Using polymer blends to fine-tune binder performance", *Ceram. Trans.*, 62, 193-200, (1996)

78. S Balasubramanian, D J Shanefield & D E Niesz, "Effect of externally applied plasticizer on compaction behavior of spray dried powders", *J. Am. Ceram. Soc.*, 85, [4], 749-754, (2002)

79. S J Lukasiewicz, "Spray-drying ceramic powders", *J. Am. Ceram. Soc.,* 72, [4], 617-624, (1989)

80. H Leuenberger, "Spray freeze drying-the process of choice for low water soluble drugs?", *J. Nanoparticle. Res.,* 4, 111-119, (2002)

81. X Tang & M J Pikal, "Design of freeze dying process for pharmaceuticals: Practical advice", *Pharm. Res.,* 21, [2], 191-200, (2004)

82. M D Rigterink, "Advances in technology of the cyrochemical process", *Am. Ceram. Soc. Bull.*, 52, [2], 158-161, (1972)

83. http://www.powderpro.se/technology.htm

84. http://www.keram.se/eng/pdf/freeze_granulation.pdf

85. G Chen & W Wang, "Role of freeze drying in Nanotechnology", *Drying Technology,* 25, 29-35, (2007)

86. R M Anklekar, S A Borkar, S Bhattacharjee, C H Page & A K Chatterjee, "Rheology of concentrated alumina suspension to improve the milling output in production of high purity alumina powder", *Colloids Surf., A*, 133, 41-47, (1998)

87. P Badica, G Aldica, A F Alexeev, T Y Gridasova & V V Morozov, "Structural modifications of superconducting phases in Bi(Pb)-Sr-Ca-Cu-O system", *Physica C*, 259, 92 -96, (1996)

88. K Itatani, K Iwafune, F S Howell & M Aizawa, "Preparation of various calcium-phosphate powders by ultrasonic spray freeze drying technique", *Mater. Res. Bull.,* 35, 575-585, (2000)

89. I Amato, F Baudrocco & D Martorana, "Evaluation of freeze drying and spray drying processes for preparing transparent alumina", *Mater. Sci. & Engg.*, 26, 73-78, (1976)

90. C Petot, M Filal, A D Rizea, K H Westmacott, J Y Laval, C Lacour & R Ollitrault, "Microstructure and ionic conductivity of freeze-dried yttria doped zirconia", *J.Euro. Ceram. Soc.*, 18, 1419-28, (1998)

91. O A Shlyakhtin, Y-J Oh & Y D Tretyakov, "Preparation of dense La0.7Ca0.3MnO3 ceramics from freeze-dried precursors", *J. Euro. Ceram. Soc.*, 20, 2047-54, (2000).

92. M A Akbas & W E Lee, "Synthesis and sintering of PLZT powder made by freeze/ Alcohol drying or gelation of citrate solutions", *J. Euro. Ceram. Soc.*, 15, 57-63, (1995)

93. J M McHale, P C McIntyre, K E Sickafus & N V Coppa, "Nanocrystalline BaTiO3 from freeze-dried nitrate solutions", *J. Mater.Res.*, 11, [5], 1199-1209, (1996)

94. S J Visco & J H Kennedy, "Investigation of Na5GdSi4O12 (NGS) NASICON and highly doped NGS NASICON prepared by spray freeze/ freeze dry methods using complex plane analysis", *Solid State Ionics*, 9 & 10, 885-890, (1983)

95. T Tachiwaki, J Sugimoto, T Ito & A Hiraki, "Characterization of freeze-dried powders prepared by alkoxide route for YBCO superconductors", *Appl. Surf. Sci.*, 100/101, 272-276, (1996)

96. P Badica, G Aldica, V V Morozov, S popa & S Mandache, "Influence of sintering environment and intermediate grounding on the scatter of the superconducting characteristics in BSCCO ceramic produced by spray-froze, freeze drying method", *Applied Superconductivity*, 4, [12], 583-589, (1996)

97. C Tallón, R Moreno & M I Nieto, "Synthesis of γ-Al2O3 nanopowders by freeze-drying", *Mater. Res. Bull.*, 41, 1520-1529, (2006)

98. S W Sofie & F Dogan,"Freeze casting of aqueous alumina slurries with glycerol", *J. Am. Ceram. Soc.*, 84, [7], 1459-64, (2001)

99. T Fukasawa, Z Y Deng, M Ando, T Ohji & Y Goto, "Porestructure of porous ceramics synthesized from water-based slurry by freeze-dry process", *J. Mater. Sci.*, 36, 2523-27, (2001)

100. K Araki & J W Halloran, "New Freeze-casting technique for ceramics with sublimable vehicles", *J. Am. Ceram. Soc.*, 87, [10], 1859-1863, (2004)

101. K Araki & J W Halloran, "Room temperature freeze casting for ceramics with non-aqueous sublimable vehicles in the naphthalene-camphor eutectic system", *J. Am. Ceram. Soc.*, 87, [11], 2014- 2019, (2004)

102. T Moritz, H-J Richter, "Ceramic bodies with complex geometries and ceramic shells by freeze casting using ice as mold materials", *J. Am. Ceram. Soc.*, 89, [8], 2394-98, (2006)

103. Y Koh, I Jun, J Sun & H Kim. "Insitu fabrication of a dense bi-layered ceramic composite using freeze casting ofa ceramic-camphene slurry", *J. Am. Ceram. Soc.,* 89, [2], 763-766, (2006)

104. J Song, Y Koh, H Kim, L Li & H Bahn, "Fabrication of a porous bioactive glass-ceramic using room temperature freeze casting", *J. Am. Ceram. Soc.,* 89, [8], 2649-53, (2006)

105. T Fukasawa, M Ando, T Ohji & S Kanzaki, "Synthesis of porous ceramics with complex porestructure by freeze-dry processing", *J. Am. Ceram. Soc.,* 84, [1], 230-232, (2001)

106. K Araki & J W Halloran, "Porous ceramic bodies with interconnected pore channels by a novel freeze casting technique", *J. Am. Ceram. Soc.,* 88, [5], 1108-1114, (2005)

107. T Moritz & A Nagy, "Preparation of super soft granules from nanosized ceramic powders by spray freezing", *J. Nanoparticle Res.,* 4, 439-448, (2002)

108. Y H Koh, J H Song, E J Lee & H E Kim, "Freezing dilute ceramic/ camphene slurry for ultra-high porosity ceramics with completely interconnected pore networks", *J. Am. Ceram. Soc.,* 89, [10], 3089-3093, (2006)

109. J Lee & Y Cheng, "Critical freezing rate in freeze drying nanocrystal dispersions", *J. Controlled Release,* 111, 185-192, (2006)

110. N Uchida, T Hiranami, S Tanaka & K Uematsu, "Spray freeze dried granules for ceramics fabrication", *Am. Ceram. Soc. Bull.,* 81, [2], 57-60, (2002)

111. H Rumpf, "Strength of granules and agglomerates", in Agglomeration, edited by W A Knepper, Wiley-Interscience, New York, 379-418, (1962)

112. W Pyda & M S J Gani, "Microstructural and mechanical properties of spherical zirconia-yttria granules", *J. Mater. Sci.,* 30, 2121-2129, (1995)

113. J R Coury and M L Aguiar, "Rupture of dry agglomerates", *Powder Technol.,* 85, 37-43, (1995)

114. K Kendall, "Agglomerate Strength", *Powder Metall.,* 31, No.1, 28-31, (1988)

115. Jin-Hua Song and Julian R. G.Evans, "A die pressing test for the estimation of agglomerate strength", *J. Am. Ceram. Soc.,* 77, [3], 806-14, (1994)

116. K Kendall & T P Weihs, "Adhesion of nanoparticles within spray-dried agglomerates", *J. Phys. D: Appl. Phys.* 25, A3-A8, (1992)

117. L P Meier, L Urech & L J Gauckler, "Tape casting of nanocrystalline ceria gadolinia powder", *J. Euro. Ceram. Soc.,* 24, 3753-3758, (2004)

118. Y K Leong & D V Boger, "Surface chemistry and rheological properties of zirconia suspensions", *J.Rheol.*, 35, [1], 149-165, (1991)

119. Z Xie, J Ma, Q Xu, Y Huang & Y B Cheng, "Effects of dispersants and soluble counter-ions on aqueous dispersibility of nano-sized zirconia powder", *Ceram. Int.*, 30, 219-224, (2004)

120. Y Liu & L Gao, "Effect of 2-phosphonobutane-1,2,4-tricarboxylic acid adsorption on the stability and rheological properties of aqueous nanosized 3-mol%-yttria stabilized tetragonal zirconia polycrystal suspensions", *J. Am. Ceram. Soc.*, 86, [7], 1106-1113, (2003)

121. A K Nikumbh, H Schmidt, K Martin & F Porz, "Slip casting of partially stabilized zirconia", *J. Mater. Sci.*, 26, 3649-3656, (1991)

122. J Davies & J G P Binner, "The role of ammonium polyacrylate in dispersing concentrated alumina suspensions", *J. Euro. Ceram. Soc.*, 20, 1539-1553, (2000)

123. F Shojai, A B A Pettersson, T Mäntylä & J B Rosenholm, "Electrostatic and electrosteric stabilization of aqueous slips of 3Y-ZrO_2 powder," *J. Euro. Ceram. Soc.*, 20, 277-283, (2000)

124. T Fengqiu, H Xiaoxian, Z Yufeng & G Jingkun, "Effect of dispersants on the surface chemical properties of nano-zirconia suspensions", *Ceram. Int.*, 26, 93-97, (2000)

125. E Ewais, A A Zaman & W Sigmund, "Temperature induced forming of zirconia fromaqueous slurries: mechanism and rheology", *J. Euro.Ceram. Soc.*, 22, 2805-2812, (2002)

126. A J Forsyth, S R Hutton, M J Rhodes & C F Osborne, "Effect of applied interparticle force on the static and dynamic angles of repose of spherical granular material", *Phys Rev E.*, 63, [031302],1-5, (2002)

127. M K Stanford, C DellaCorte & D Eylon, "Effect of particle morphology on flow characteristics of a composite plasma spray powder", *J. Thermal Spray Technol.*, 13, [4], 586-592, (2004)

128. H Takahashi, N Shinohara & K Uematsu, "Influence of spray-dry slurry flocculation on the structure of sintered silicon nitride", *J. Ceram. Soc. Japan.*, 104, [1], 59-62, (1996).

129. Q Tan, "Spray drying dielectric ceramics", *Am. Ceram. Soc. Bull.*, 83, [9], 12-14, (2004)

130. http://www.freemantech.co.uk

131. M Romagnoli & F Bondiali, "Powder Flowability Characterising techniques", *Am. Cer. Soc. Bull.*, online article available at www.ceramicbulletin.org, (2004)

132. L Svarovsky, "Angle of repose and other handling angles", Powder testing guide: Methods of measuring the physical properties of bulk powders, Elsevier Applied Science, 71-77, (1987)

133. R L Carr, "Evaluating flow properties of solids", 1965, *Chem. Eng.*, Jan 18, 163-168, (1965)

134. DD ENV 14312:2002, "Advanced Technical Ceramics-Ceramic Powders-Determination of flowability behaviour of ceramic granules", (2002)

135. BS EN ISO 4490:2002, "Metallic powders-Determination of flow time by means of a calibrated funnel (Hall flowmeter)", (2002)

136. C D Sagel-Ransijn, A J A Winnubst, B Kerkwijk, A J Burggraaf & H Verweij, "Production of defect poor nanostructured ceramics of yttria-zirconia", *J. Euro. Ceram. Soc.*, 17, 831-841, (1997)

137. BS EN ISO 787 -11:1995, "General methods of test for pigments and extenders-Part 11 : Determination of tamped volume and apparent density after tamping", (1995)

138. E C Abdullah & D Geldart, "The use of bulk density measurements as flowability indicators", *Powder Technol.*, 102, 151 -165, (1999)

139. J Staniforth, "powder flow", Pharmaceutics: The science of dosage form design, edited by M E Aulton, 2nd Edition, Churchill Livingstone, 197-210, (2002)

140. http://www.powderandbulk.com/pb_services/ask_joe_archive/flow_properties_testing_jenike_shear_ tester.htm

141. Product catalogue, Aeroflow® TSI powder flowability analyzer

142. B C Hancock, K E Vukovinsky, B Brolley, I Grimsey, D Hedden, A Olsofsky & R A Doherty, "Development of a robust procedure for assessing powder flow using a commercial avalanche testing instrument", *J. Pharm. Biomed. Anal.*, 35, 979- 990, (2004)

143. Aeroflow Application note #9, TSI powder flowability analyzer, Exxon Mobil Chemical

144. R E Freeman, C M Iles, "Rheometer with angled blades", *United States Patent Number* : 6, 065, 330, (2000)

145. C-Y Wu, L Dihoru & A C F Cocks, "The flow of powders into simple and stepped dies", *Powder Technol.*, 134, 24-39, (2003)

146. I C Sinka, L C R Schneider & A C F Cocks, "Measurement of the flow properties of powders with special reference to die fill", *Int. J. Pharm.*, 280, 27-38, (2004)

147. S Jackson, I C Sinka & A C F Cocks, "The effect of suction during die fill on a rotary tablet press", *Eur. J. Pharm. Biopharm.*, 65, 253-256, (2007)

148. L C R Schneider, A C F Cocks & A Apostolopoulos, "Comparison of filling behaviour of metallic, ceramic, hardmetal and magnetic powders", *Powder Metall.*, 48, [1], 77-84, (2005)

149. C-Y Wu & A C F Cocks, "Flow behaviour of powders during die filling", *Powder Metall.*, 47,[2], 127-136, (2004)

150. W A Beverloo, HA Leniger & J Velde, "The flow of granular solids through orifices", *Chemical Engineering Science*, 15, 260 – 269, (1961)

151. A B V Groenou, "Compaction of ceramic powders", *Powder Technol.*, 28, 221-228, (1981)

152. J W Halloran, "Agglomerates and agglomeration in ceramic processing", in Ultrastructure processing of ceramics,glasses and compsites, edited by L L Hench & D R Ulrich, Wiley –Interscience, 404-417, (1984)

153. K Ada, M Őnal & Y Sankaya, "Investigation of the intra-particle sintering kinetics of a mainly agglomerated alumina powder by usingsurface area reduction", *Powder Technol.*, 168, 37-41, (2006)

154. K Kendall, "Influence of powder structure on processing and properties of advanced ceramics", *Powder Technol.*, 58, 151-161, (1989)

155. M Staiger, P Bowen, J Ketterer & J Bohonek, "Particle size distribution measurement and assessment of agglomeration of commercial nanosized ceramic particles", *J. Dispersion Sci. Technol.*, 23, [5], 619-630, (2002)

156. N Shinohara, M Okumiya, T Hotta, K Nakahira, M Naito & K Uematsu, "Variation of the microstructure and fracture strength of cold isostatically pressed alumina ceramics with the alteration of dewaxing procedures", *J. Euro. Ceram. Soc.*, 20, 843-849, (2000)

157. S J Lukasiewicz & J S Reed, "Charater and compaction response of spray-dried agglomerates", *Am. Cer. Soc. Bull.*, 57, [9], 798 - 801, (1978)

158. P R Mort, R Sabia, D E Niesz & R E Riman, "Automated generation and analysis of powder compaction diagrams", *Powder Technol.*, 79, 111-119, (1994)

159. K G Ewsuk, J G Arguello, D N Bencoe, D T Ellerby, S J Glass and D H Zeuch, "Characterising powders for dry pressing, sintering", *Am. Cer. Soc. Bull.*, 82, [5], 41-47, (2003)

160. Y Jorand, M Taha, J M Missiaen & L Montanaro, "Compaction and sintering behavior of sol-gel powders", *J. Euro. Ceram. Soc.*, 15, 469-477, (1995)

161. C D Sagel-Ransijn, A JA Winnubst, B Kerkwijk, A J Burggraaf & H Verweij, "Production of defect poor nanostructured ceramics of yttria-zirconia", *J. Euro. Ceram. Soc.*, 17, 831-841, (1997)

162. P Dúran, M Villegas, F Capel, P Recio & C Moure, "low temperature sintering and microstructural development of nanocrystalline Y-TZP powders", *J. Euro. Ceram. Soc.*, 16, 945-952, (1996)

163. W J Walker Jr. , J S Reed & S K Verma, "Organic additive systems for spray drying and dry pressing silicon nitride", *Ceram. Trans.*, 62, 141-148, (1996)

164. J L Shi, Z X Lin, W J Qian & T S Yen, "Characterisation of agglomerate strength of coprecipitated superfine zirconia powders", *J. Euro. Ceram. Soc.*, 13, 265-273, (1994)

165. V Srdic & M Winterer, "Comparison of nanosized zirconia synthesized by gas and liquid phase methods", *J. Euro. Ceram. Soc.*, 26, 3145-3151, (2006)

166. S K Tadokoro & E N S Muccillo, "Physical characteristics and sinteringbehavior of ultrafine zirconia-ceria powders", *J. Euro. Ceram. Soc.*, 22, 1723-1728, (2002)

167. H Abe, T Hotta, M Naito, N Shinohara, M Okumiya, H Kamiya & K Uematsu, "Origin of strength variation of silicon nitride ceramics with CIP condition in a powder compaction process", *Powder Technol.*, 119, 194-200, (2001)

168. T Hotta, K Nakahira, M Naito, N Shinohara, M Okumiya & K Uematsu, "Origin of the strength change of silicon nitride ceramics with the alteration of spray drying conditions", *J. Euro. Ceram. Soc.*, 21, 603-610, (2001)

169. D-J Kim & J-Y Jung, "Granule performance of zirconia/alumina composite powders spray-dried using polyvinyl pyrrolidone binder", *J. Euro. Ceram. Soc.*, 27, 3177-3182, (2007)

170. X K Wu, D W Whitman, W L Kaufell, W C Finch & D I Cumbers, "Acrylic binders for dry pressing ceramics", *Am. Ceram. Soc. Bull.*, 76, [1], 49-52, (1997)

171. D Liu, J Lin & W H Tuan, "Interdependence between green compact property and powder agglomeration and their relation to the sintering behaviour of zirconia powder", *Ceram. Int.*, 25, 551-559, (1999)

172. J R Groza, "Sintering of nanocrystalline powders", *Int. J. Powder Metall.*, 35, [7], 59-66, (1999)

173. "Gas sorption analysis", Micromeritics, [Online], available at http://www.micromeritics.com/pdf/products/Gas_Sorption_Brochure.pdf, accessed on 14th April, 2008

174. S J Gregg and K. S. W. Sing, "Adsorption, Surface area and Porosity", second edition, Academic press, 173-194, (1982)

175. S Storck, H. Bretinger & W F Maier, "Characterization of micro- and mesoporous solids by physisorption methods and pore-size analysis", *Appl. Catal., A.*, 174, 137-146, (1998)

176. E P Barrett, L G Joyner & P P Halenda, "The determination of pore volume and area distributions in porous substances. I. Computations from nitrogen isotherms", *J. Am. Chem. Soc.*, 73, [1], 373-380, (1951)

177. I Hung, D Hung, K Fung & M Hon, "Effect of calcination temperature on morphology of mesoporous YSZ", *J. Euro. Ceram. Soc.,* 26, 2627-2632, (2006)

178. C Legros, C Carry, P Bowen & H Hofmann, "Sintering of a transition alumina: Effects of phase transformation, powder characteristics and thermal cycle", *J. Euro. Ceram. Soc.,* 19, 1967-78, (1999)

179. M Oya, M Takahashi, Y Iwata, K Jono, T Hotta, H Yamamoto, K Washio, A Suda, Y Matuo, K Tanaka & M Morimoto, "Mercury intrusion porosimetry", *Am. Ceram. Soc. Bull.,* 81, [3], 52-56, (2002)

180. J Zheng & J S Reed, "Study of the bimodal pore structure of ceramic powder compacts by mercury porosimetry", *J. Am. Ceram. Soc.,* 75, [12], 3498-3500, (1992)

181. S P Rigby & R S Fletcher, "Interfacing mercury porosimetry with nitrogen sorption", *Part. Part. Syst. Charact.* 21, 138-148, (2004)

182. S P Rigby, M J Watt-Smith & R S Fletcher, "Integrating gas sorption with mercury porosimetry", *Adsorption*, 11, 201-206, (2005)

183. W C Conner, J F Cevallos-Candau, E L Weist, J Pajares, S Mendioroz & A Cortes, "Characterization of pore structure: Porosimetry and Sorption", *Langmuir*, 2, 151-154, (1986)

184. H H D Lee, "Validity of using mercury porosimetry to characterize the pore structure of ceramic green compacts", *J. Am. Ceram. Soc.,* 73, [8], 2309-2315, (1990)

185. E N S Muccillo, S K Tadokoro & R Muchillo, "Physical characteristics and sintering behavior of MgO-doped ZrO2 nanoparticles", *J. Nanoparticle Research,* 6, 301-305, (2004)

186. www.dynacer.com/zirconia.htm

187. Binner JGP, Annapoorani K & Santacruz I. Patent No. WO 2006/136780 A2, Publ. Date 28/12/06

188. http://www.sono-tek.com/sonodry/index.php

189. F Boulch, M C Schouler, P Donnadieu, J M Chaix & E Djurado, "Domain size distribution of Y-TZP nano-particles using XRD and HRTEM", *Image. Anal. Stereol.,* 20, 157-161, (2001)

190. Micromeritics Tristar 3000, Operator's manual

191. L C R Schneider, I C Sinka & A C F Cocks, "Characterisation of the flow behaviour of pharmaceutical powders using a model die-shoe filling system", *Powder Technol.,* 173, 59-71, (2007)

192. K Sing, "The use of nitrogen adsorption for the characterization of porous materials", *Colloids Surf., A,* 187-188, 3-9, (2001)

193. M J Mayo, J R Seidensticker, D C Hague and A H Carim, "Surface chemistry effects on the processing and superplastic properties of nanocrystalline oxide ceramics", *Nanostruct. Ceram.*, 11, [2], 271 -282, (1999)